

MPP-2003-65

**Measurement of the  $e^+p$  Neutral Current DIS  
Cross Section and the  $F_2$ ,  $F_L$ ,  $xF_3$  Structure  
Functions in the H1 Experiment at HERA**

Dissertation  
an der Fakultät für Physik  
der Technische Universität  
München

vorgelegt von  
ANA DUBAK

München  
10. April 2003



Technische Universität München

Max-Planck-Institut für Physik

–Werner-Heisenberg-Institut–

**Measurement of the  $e^+p$  Neutral Current DIS  
Cross Section and the  $F_2$ ,  $F_L$ ,  $xF_3$  Structure  
Functions in the H1 Experiment at HERA**

ANA DUBAK

Vollständiger Abdruck der von der Fakultät für Physik der Technischen Universität München zur Erlangung des akademischen Grades eines

Doktors der Naturwissenschaften

genehmigten Dissertation.

Vorsitzender: Prof. Dr. Andrzej Buras

Prüfer der Dissertation:

1. Prof. Dr. Gerd Buschhorn
2. Prof. Dr. Stephan Paul

Die Dissertation wurde am 10. 04. 2003 bei der Technischen Universität München eingereicht und durch die Fakultät für Physik am 14. 07. 2003 angenommen.



## Abstract

This thesis presents inclusive  $e^+p$  single and double differential cross sections in the four-momentum transfer  $Q^2$  and in Bjorken  $x$  for neutral current deep inelastic scattering measurements with the H1 detector at HERA. An overview of the phenomenology of the deep inelastic scattering is given. The experimental apparatus is described and the measurement and analysis procedures are detailed. The analysis is based on data taken in 1999 and 2000 at a centre-of-mass energy of  $\sqrt{s} = 319$  GeV and correspond to an integrated luminosity of  $65.2 \text{ pb}^{-1}$ . The cross sections are measured in the range of  $100 < Q^2 < 30\,000 \text{ GeV}^2$  and  $0.0013 < x < 0.65$ . For the inelasticity  $y < 0.6$  the proton structure function  $F_2$  is determined. The neutral current analysis for both the new  $e^+p$  data and the  $e^-p$  data taken in 1998 and 1999 is extended to energies of the scattered electron of  $E'_e > 6$  GeV corresponding to an inelasticity of  $y = 0.75$ , allowing for a determination of the longitudinal structure function  $F_L$  at  $110 < Q^2 < 700 \text{ GeV}^2$ . Clear evidence for an asymmetry between  $e^+p$  and  $e^-p$  cross sections is observed for  $Q^2 > 1000 \text{ GeV}^2$  and the generalised structure function  $x\tilde{F}_3$  is extracted. The results are found to be consistent with the Standard Model expectation, both in terms of QCD and electroweak effects.

## Kurzfassung

Die Dissertation stellt Messungen der tief inelastischen Positron-Proton Streuung mit Neutralen Strom am HERA-Speicherring mit dem H1-Detektor dar. Es werden einfach- und doppeltdifferentielle inklusive  $e^+p$ -Wirkungsquerschnitte in den Variablen quadrierter Viererimpulsübertrag  $Q^2$  und Bjorken  $x$  gezeigt. Ein Überblick über die Phänomenologie der tief inelastische Streuung wird gegeben. Der experimentelle Aufbau, die Messung und die Analyseverfahren werden detailliert beschrieben. Die Analyse verwendet Daten, die im Zeitraum 1999 und 2000 bei einer Schwerpunktsenergie von  $\sqrt{s} = 319 \text{ GeV}$  genommen worden sind und einer integrierten Luminosität von  $65.2 \text{ pb}^{-1}$  entsprechen. Die Wirkungsquerschnitte werden im Bereich  $100 < Q^2 < 30000 \text{ GeV}^2$  und  $0.0013 < x < 0.65$  gemessen. Für den Inelastizitätsbereich  $y < 0.6$  wird die Protonstrukturfunktion  $F_2$  bestimmt. Die Analyse wird sowohl für die neuen  $e^+p$ -Daten wie auch für die  $e^-p$ -Daten aus den Jahren 1998 und 1999 ausgedehnt auf den Energiebereich des gestreuten Elektrons  $E'_e > 6$  GeV. Dies entspricht einer Ausweitung zu hohen Inelastizitäten bis zu  $y = 0.75$  und ermöglicht die Bestimmung der longitudinalen Strukturfunktion  $F_L$  im Bereich  $110 < Q^2 < 700 \text{ GeV}^2$ . Für  $Q^2 > 1000 \text{ GeV}^2$  wird eine Asymmetrie zwischen den  $e^+p$ - und  $e^-p$ -Wirkungsquerschnitten beobachtet und daraus die generalisierte Strukturfunktion  $x\tilde{F}_3$  extrahiert. Die Resultate sind sowohl im Rahmen der QCD wie auch der elektroschwachen Effekte konsistent mit den Erwartungen des Standardmodells.



# Contents

|   |           |
|---|-----------|
| <b>Introduction</b>                                       | <b>1</b>  |
| <b>1 Theoretical Overview</b>                             | <b>3</b>  |
| 1.1 Deep Inelastic Scattering (DIS)                       | 3         |
| 1.2 The Structure of Hadrons                              | 5         |
| 1.3 Quark Parton Model (QPM)                              | 6         |
| 1.4 Quantum Chromodynamics (QCD)                          | 7         |
| 1.5 Neutral Current Cross Section and Structure Functions | 11        |
| 1.6 Charged Current Cross Section and Structure Functions | 13        |
| 1.7 QCD Analysis and Parton Distribution Functions (PDFs) | 13        |
| 1.8 Radiative Corrections                                 | 17        |
| <b>2 HERA and the H1 Detector</b>                         | <b>19</b> |
| 2.1 HERA  | 19        |
| 2.2 H1  | 20        |
| 2.2.1 Calorimeters  | 22        |
| 2.2.1.1 Liquid-Argon Calorimeter                          | 22        |
| 2.2.1.2 SpaCal  | 24        |
| 2.2.2 Tracking System                                     | 25        |
| 2.2.2.1 Central Tracking Detector                         | 25        |
| 2.2.2.2 Forward Tracking Detector                         | 26        |
| 2.2.3 Luminosity System                                   | 27        |

---

|          |  |           |
|----------|--|-----------|
| 2.2.4    | Time of Flight System . . . . .                                | 28        |
| 2.2.5    | Trigger System . . . . .                                       | 28        |
| 2.2.5.1  | The First Trigger Level . . . . .                              | 28        |
| 2.2.5.2  | The Second and the Third Trigger Level . . . . .               | 30        |
| 2.2.5.3  | The Forth Trigger Level and the Event Reconstruction . . . . . | 31        |
| 2.2.6    | The NC Subtriggers . . . . .                                   | 31        |
| <b>3</b> | <b>Monte Carlo Simulation</b>                                  | <b>33</b> |
| 3.1      | Generation of DIS Events . . . . .                             | 33        |
| 3.2      | Generation of Background Events . . . . .                      | 34        |
| 3.3      | Simulation of the H1 Detector . . . . .                        | 35        |
| <b>4</b> | <b>Reconstruction of Kinematic Variables</b>                   | <b>36</b> |
| <b>5</b> | <b>Data Treatment</b>  | <b>39</b> |
| 5.1      | Electron Identification . . . . .                              | 39        |
| 5.1.1    | Electron Cluster in the LAr Calorimeter . . . . .              | 39        |
| 5.1.2    | Electron Cluster Identification Efficiency . . . . .           | 40        |
| 5.1.3    | Validation of Electrons Using Track Information . . . . .      | 42        |
| 5.1.4    | Efficiency of Electron Validation . . . . .                    | 42        |
| 5.2      | Interaction Vertex . . . . .                                   | 44        |
| 5.2.1    | Vertex Reweighting in the MC . . . . .                         | 44        |
| 5.2.2    | Vertex Reconstruction Efficiency . . . . .                     | 46        |
| 5.3      | Electron Angle Measurement . . . . .                           | 47        |
| 5.3.1    | Alignment of the LAr Calorimeter . . . . .                     | 47        |
| 5.3.2    | Azimuthal and Polar Electron Angles . . . . .                  | 49        |
| 5.4      | Electron Energy Measurement . . . . .                          | 51        |
| 5.4.1    | Electron Energy Calibration . . . . .                          | 51        |
| 5.4.2    | Electron Energy Resolution . . . . .                           | 56        |
| 5.4.3    | Cross-check of calibration with QED-Compton Events . . . . .   | 56        |



---

|          |   |            |
|----------|---|------------|
| 5.5      | Hadronic Energy Measurement . . . . .   | 59         |
| 5.5.1    | Calibration of Hadronic Energy . . . . .  | 61         |
| 5.6      | Determination of Trigger Efficiency . . . . .   | 66         |
| 5.6.1    | Trigger Efficiency at Low Electron Energy . . . . .   | 69         |
| 5.7      | Modelling of Time Dependencies in the MC . . . . .  | 72         |
| 5.8      | Rejection of the $ep$ Induced Background . . . . .  | 73         |
| 5.8.1    | Control of $\gamma p$ Background Using Tagged Events . . . . .  | 73         |
| 5.8.2    | Control of Background Rejection . . . . .   | 74         |
| 5.8.3    | Background Subtraction Using Track Information . . . . .  | 75         |
| 5.9      | Rejection of Non- $ep$ Background . . . . .   | 76         |
| <b>6</b> | <b>Selection of NC Events</b>   | <b>79</b>  |
| 6.1      | Run Selection . . . . .   | 79         |
| 6.2      | Luminosity Calculation and Event Yield . . . . .  | 80         |
| 6.3      | Neutral Current Selection Criteria . . . . .  | 81         |
| 6.4      | Neutral Current Data Samples . . . . .  | 82         |
| <b>7</b> | <b>Cross Section Measurement Procedure</b>  | <b>87</b>  |
| 7.1      | Bin Definitions in $x - Q^2$ Plane . . . . .  | 87         |
| 7.2      | Extraction of Cross Section . . . . .   | 90         |
| 7.3      | Systematic Uncertainties . . . . .  | 91         |
| 7.4      | $Q^2$ Bins Combination of $e^-p$ and $e^+p$ Cross Sections for Determination<br>of $F_L$ and $xF_3$ . . . . . | 97         |
| 7.5      | Consistency of H1 High $Q^2$ analyses . . . . .   | 98         |
| <b>8</b> | <b>NC Cross Section Results</b>   | <b>101</b> |
| 8.1      | The $e^+p$ and $e^-p$ Double Differential Cross Section $d^2\sigma/dxdQ^2$ . . . . .                          | 101        |
| 8.2      | The $e^+p$ Single Differential Cross Section $d\sigma/dQ^2$ . . . . .   | 106        |
| 8.3      | The $e^+p$ Single Differential Cross Section $d\sigma/dx$ . . . . .   | 108        |

---

|           |   |            |
|-----------|---|------------|
| <b>9</b>  | <b>Extraction of Proton Structure Functions</b>     | <b>109</b> |
| 9.1       | Proton Structure Function $F_2$ . . . . .           | 109        |
| 9.2       | Longitudinal Structure Function $F_L$ . . . . .     | 111        |
| 9.3       | Structure Function $x\tilde{F}_3$ . . . . .         | 113        |
| <b>10</b> | <b>Electroweak Effects at High <math>Q^2</math></b> | <b>116</b> |
|           | <b>Summary</b>                                      | <b>118</b> |
|           | <b>Appendix</b>                                     | <b>120</b> |
| A         | Details of QCD Analysis                             | 120        |
| B         | Trigger Fiducial Cuts                               | 124        |
| C         | Tables of Results                                   | 125        |
| D         | Events in the H1 Detector                           | 133        |
|           | <b>Bibliography</b>                                 | <b>136</b> |
|           | <b>Acknowledgements</b>                             | <b>145</b> |

---

# Introduction

There are two main tasks of elementary particle physics: the identification of the fundamental building blocks of matter and the investigation of the interactions between them.

In our present knowledge the most fundamental constituents of matter are two types of fermions, spin<sup>1</sup> 1/2 particles: *leptons* and *quarks*. There are three families of leptons electron  $e$ , electron neutrino  $\nu_e$ ; muon  $\mu$ , muon neutrino  $\nu_\mu$ ; tauon  $\tau$ , tau neutrino  $\nu_\tau$ . Quarks also appear in three pairs: up  $u$ , down  $d$ ; strange  $s$ , charm  $c$ ; bottom  $b$ , top  $t$ .

These particles interact with each other by the exchange of integer spin gauge bosons. Existing results show clear evidence of four types of interaction in nature. These are gravitational, electromagnetic, weak and strong. Gravitation is of no significance in subatomic physics, being far too weak to noticeably influence interactions between elementary particles. The electromagnetic interaction is mediated by photons. In the weak interaction heavy gauge bosons,  $Z^0$ ,  $W^+$  and  $W^-$  are exchanged. The carriers of strong interaction are gluons. Each of the interactions is associated with charge: electric charge, weak charge and colour charge of strong interaction. A particle is subject to an interaction if it carries the corresponding charge. Leptons and quarks carry a weak charge, quarks are electrically charged, so are  $e$ ,  $\mu$ ,  $\tau$  leptons. Colour charge is carried by quarks, as well as by the gluon itself.

A field theory of quarks and gluons and their strong interaction, Quantum Chromodynamics, in combination with the unified theory of the electroweak interactions constitutes the Standard Model of elementary particle physics.

Starting with Rutherford's famous experiment [1], the scattering of  $\alpha$  particles on a thin gold foil, scattering experiments have played a crucial role in revealing the structure of matter.

In the late sixties the first experiments on highly inelastic electron scattering were started at the two mile accelerator at the Stanford Linear Accelerator Center (SLAC) using liquid hydrogen targets. The experimental results suggested point-like constituents of the proton, partons, which came to be identified as quarks. In the following years various experiments of lepton nucleon deep inelastic scattering [2–6] have

---

<sup>1</sup>In this work the system of natural units is used, whereby  $\hbar = c = 1$ .

played a significant role in understanding the partonic structure of the proton and constraining the parameters of the electroweak theory.

Since the start of the operation of the electron-proton collider HERA<sup>2</sup> at DESY<sup>3</sup>, Hamburg, the two experiments H1 and ZEUS made possible to probe the structure of the proton at much higher energies and to investigate the electroweak effects at the same time.

The structure of proton is described via three structure functions,  $F_2$ ,  $xF_3$  and  $F_L$ . The structure function  $F_2$  is related to the electromagnetic interaction of electron and quarks in proton. The structure function  $xF_3$  appears due to the weak interaction and the longitudinal structure function  $F_L$  is related to gluon density in the proton. All these three structure functions are accessible at HERA allowing for tests of both components of the Standard Model, electroweak theory and Quantum Chromodynamics.

The aim of this thesis is the measurement of the inclusive cross section of neutral current deep inelastic positron proton scattering at high momentum transfer, and determination of three structure functions  $F_2$ ,  $F_L$  and  $xF_3$ . The thesis is organised as follows: The first chapter gives an introduction to the theory of deep inelastic scattering. Theoretical predictions for the evolution of the DIS cross section and the proton structure functions are discussed. In the second chapter the accelerator and the H1 detector are described. The third and fourth chapter are devoted to Monte Carlo simulation and the reconstruction of the event kinematics, respectively. In the fifth chapter discussion on detailed understanding of detector calibration and efficiency determination, needed for precise measurement of  $e^+p$  interactions, is presented. The sixth chapter describes the selection of the neutral current DIS events. In the seventh chapter the procedure to determine cross section is discussed. In chapters eight and nine the results of the cross section and the structure function measurements, respectively, are presented. In chapter ten the electroweak effects are summarised.

---

<sup>2</sup>Hadron-Electron-Ring-Anlage

<sup>3</sup>Deutsches Elektronen Synchrotron

# Chapter 1

## Theoretical Overview

The scattering of a high energetic electron<sup>1</sup> on a nucleon with large momentum transfer causes an inelastic reaction. In this reaction the nucleon breaks up and numerous strong interacting particles are produced, forming a hadronic final state. This process is known as deep inelastic scattering (DIS).

In this section the theoretical basics of electron proton deep inelastic scattering are discussed. First the process and kinematic variables needed to describe DIS processes are introduced. Further, the cross section and its relation to the structure of proton are discussed. The section concludes with a discussion about the radiative corrections to the cross section. For detailed theoretical overview of DIS see eg. [7,8].

### 1.1 Deep Inelastic Scattering (DIS)

The interaction between a high energetic point-like lepton with a proton is mediated by gauge bosons. In a process when exchanged boson is a neutral particle, i.e. a photon or the neutral vector boson  $Z^0$ , the final state is formed by the scattered electron and hadronic final state. This process is referred to as neutral current (NC) DIS. If the exchanged particle is a charged boson,  $W^\pm$ , an outgoing lepton is (anti-)neutrino. This process is known as charged current (CC) DIS.

Figure 1.1 shows the Feynman graph of DIS. Here  $k$ ,  $k'$ ,  $P$ ,  $P'$  and  $q = k - k'$  are the four-momenta of incoming and outgoing electron, incoming proton, the hadronic final state  $X$  and the exchanged photon. The kinematics of the DIS process is described by the following variables:

---

<sup>1</sup>In the following and through this thesis "electron" refers generically to both electrons and positrons. Where distinction is required the symbols  $e^+$  and  $e^-$  are used.

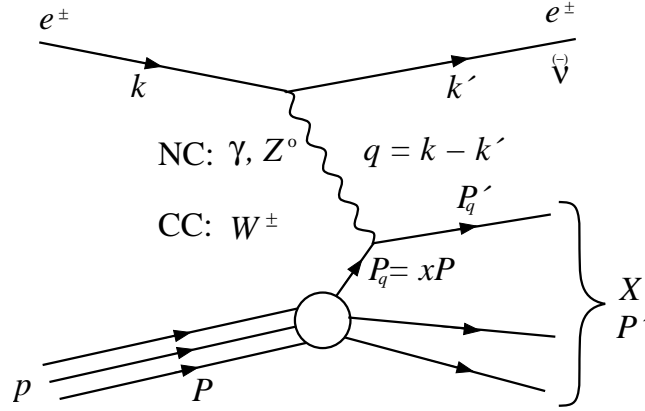


**Figure 1.1:** Feynman graph of the deep inelastic scattering.

- Square of the centre-of-mass energy:

$$s = (k + P)^2 \approx 4E_e E_p, \quad (1.1)$$

neglecting the masses of electron and proton.  $E_p$  and  $E_e$  are the energies of the proton and electron in the HERA accelerator ring.

- Four-momentum transfer squared:

$$Q^2 := -q^2 = -(k - k')^2 \quad (1.2)$$

- Bjorken scaling variable  $x$ :

$$x := \frac{Q^2}{2P \cdot q} \quad (1.3)$$

in the frame of Quark-Parton-Model (QPM), see section 1.3,  $x$  can be interpreted as the momentum fraction of incoming proton carried a struck quark.

- Inelasticity  $y$ :

$$y := \frac{q \cdot P}{k \cdot P} \quad (1.4)$$

$y$  denotes the relative energy transfer of an electron to the hadronic final state in the proton rest frame.

The centre-of-mass energy  $\sqrt{s}$ , four-momentum transfer  $Q^2$ ,  $x$  and  $y$  are related in the following way:  $Q^2 = sxy$ . In the case when the centre-of-mass energy is known, two of the variables  $Q^2$ ,  $x$ ,  $y$  are needed to describe the kinematics of the DIS process; usually,  $Q^2$  and  $x$  are used.

## 1.2 The Structure of Hadrons

The cross section of electron hadron interaction is described via tensor product of the leptonic tensor  $L_{\mu\nu}$  and the hadronic tensor  $W^{\mu\nu}$ .

$$d\sigma \propto L_{\mu\nu} W^{\mu\nu}. \quad (1.5)$$

The leptonic tensor describes the interaction of the electron with the exchanged boson (at the moment only photon exchange is discussed). In the case of unpolarised particles the leptonic tensor depends only on the four-momenta of incoming and outgoing lepton. With the electron defined as a point-like Dirac particle, the leptonic tensor in the Quantum-Electrodynamics (QED) has the following form:

$$L_{\mu\nu} = 4(k_\mu k'_\nu + k'_\mu k_\nu - g_{\mu\nu}(k \cdot k')) \quad (1.6)$$

The hadronic tensor for an a priori unknown structure of proton cannot be calculated from first principles. It is therefore presented in terms of structure functions, the four-momenta at the hadronic vertex,  $P$  and  $q$ , and metric tensor  $g^{\mu\nu}$ :

$$W^{\mu\nu} = -W_1 g^{\mu\nu} + \frac{W_2}{M_p^2} p^\mu p^\nu + \frac{W_4}{M_p^2} q^\mu q^\nu + \frac{W_5}{M_p^2} (p^\mu q^\nu + q^\mu p^\nu) \quad (1.7)$$

The structure function  $W_3$  is related to contribution of  $Z^0$  exchange between electron and hadron and for pure photon exchange it is equal to zero.

Taking into account the conservation of the electromagnetic current at the hadronic vertex:

$$q_\mu W^{\mu\nu} = q_\nu W^{\mu\nu} = 0 \quad (1.8)$$

one obtains the relation between  $W_i$ :

$$W_5 = -\frac{P \cdot q}{q^2} W_2 \quad \text{and} \quad W_4 = \left( \frac{P \cdot q}{q^2} \right)^2 W_2 + \frac{M^2}{q^2} W_1.$$

The hadronic tensor therefore depends only on two functions  $W_i$ , e.g.  $W_1$  and  $W_2$ :

$$W^{\mu\nu} = W_1 \left( -g^{\mu\nu} + \frac{q^\mu q^\nu}{q^2} \right) + W_2 \frac{1}{M^2} \left( p^\mu - \frac{P \cdot q}{q^2} q^\mu \right) \left( p^\nu - \frac{P \cdot q}{q^2} q^\nu \right). \quad (1.10)$$

The functions  $W_1$  and  $W_2$  stand for the parametrisation of the unknown structure of the proton and are therefore called structure functions. The structure functions depend on two, out of three, Lorenz invariant kinematic variables, e.g.  $x$  and  $Q^2$ . Very often, instead of the structure functions  $W_1$  and  $W_2$ , the following notation is used

$$F_1(x, Q^2) = M_p W_1(x, Q^2) \quad (1.11)$$

$$F_2(x, Q^2) = \frac{P \cdot q}{M_p} W_2(x, Q^2). \quad (1.12)$$

With the structure functions defined in this way the NC DIS cross section can be written as

$$\frac{d^2\sigma_{NC}^\pm}{dx dQ^2} = \frac{2\pi\alpha^2}{xQ^4} \left[ \frac{y^2}{2} 2xF_1(x, Q^2) + (1-y)F_2(x, Q^2) \right]. \quad (1.13)$$

The  $ep \rightarrow eX$  interaction can be viewed in a different way, as an interaction of a virtual photon with a proton  $\gamma^*p \rightarrow X$  where the electron serves only as a source of virtual photons. The virtual photon is massive and can therefore be found in all three helicity states,  $\lambda = 0, \pm 1$ . The total cross section of this interaction is given by

$$\sigma_{tot}^{\gamma^*p}(\lambda) = \frac{4\pi^2\alpha}{K} \cdot \epsilon_\lambda^{\mu*} \epsilon_\lambda^{\nu*} W_{\mu\nu}. \quad (1.14)$$

Here  $\epsilon^\mu$  is the polarisation vector of the virtual photons and  $K$  is the photon flux factor in the Hand convention [9].

The cross sections for the proton interaction with transversely and longitudinally polarised photons are defined as follows

$$\sigma_T^{\gamma^*p} = \frac{1}{2} \left( \sigma_{\lambda=+1}^{\gamma^*p} + \sigma_{\lambda=-1}^{\gamma^*p} \right) = \frac{4\pi^2\alpha}{Q^2} \cdot 2xF_1 \quad (1.15)$$

$$\sigma_L^{\gamma^*p} = \sigma_{\lambda=0}^{\gamma^*p} = \frac{4\pi^2\alpha}{Q^2} \cdot (F_2 - 2xF_1) \quad (1.16)$$

The difference:

$$F_L = F_2 - 2xF_1, \quad (1.17)$$

is referred to as the longitudinal structure function.

### 1.3 Quark Parton Model (QPM)

The modern history of DIS experiments started in the early sixties when the first results on the scattering of high energy electrons on nucleus were obtained at the Stanford Linear Accelerator Center (SLAC). In these experiments was observed that the structure function  $F_2$ , measured at  $Q^2 \approx 5 \text{ GeV}^2$ , shows very little dependence on  $Q^2$ , but was depending only on  $x$ . The interpretation of these results lead to the parton model, based on the ideas of Feynman [10] and Bjorken [11]. In this model the proton, as all hadrons, consists of quasi-free point-like particles (partons) which were identified as quarks, particles with spin  $\frac{1}{2}$  and electric charge  $\pm\frac{1}{3}e$  or  $\pm\frac{2}{3}e$ , as proposed by Gell-Mann [12] and Zweig [13]. The proton consists of two  $u$ -quarks with charge  $+\frac{2}{3}e$  and one  $d$ -quark with charge  $-\frac{1}{3}e$ .

In the frame of the QPM the electron-proton deep inelastic scattering is interpreted as elastic scattering of the electron on a quark. The  $ep$  cross section is then incoherent



sum over all electron-quark scattering cross sections. Where incoherent means that the electron scatters on a single quasi-free quark. With these assumptions the structure functions can be expressed as functions of only one variable i.e.  $x$

$$F_1(x) = \frac{1}{2x} \sum_i e_i^2 x q_i(x) \quad (1.18)$$

$$F_2(x) = \sum_i e_i^2 x q_i(x), \quad (1.19)$$

where  $e_i$  is the electric charge of quark and  $q_i(x)dx$  is the probability that the quark  $i$  carries a fraction of the proton momentum in the interval  $[x, x+dx]$ . The independence of structure functions on  $Q^2$  is known as Bjorken scaling and was experimentally confirmed for medium  $x$  values,  $x \approx 0.25$  [14, 15]. For the spin 1/2 partons the Callan-Gross relation [16] holds

$$F_2(x) = 2xF_1(x). \quad (1.20)$$

The Callan-Gross relation implies that the longitudinal structure function (eq. 1.17) is, in the frame of QPM, equal to zero

$$F_L(x) = F_2 - 2xF_1(x) = 0, \quad (1.21)$$

which means that partons cannot interact with longitudinally polarised photons.

## 1.4 Quantum Chromodynamics (QCD)

Further lepton and neutrino nucleon scattering experiments observed a violation of the scaling hypothesis, i.e. a logarithmic dependence of the structure function  $F_2$  on  $Q^2$  and non-zero longitudinal structure function. These effects were explained in the framework of Quantum Chromodynamics (QCD), a non-abelian gauge theory which describes interaction of quarks as mediated by gluons.

Quantum Chromodynamics is based on the following ideas:

- Every quark flavour exists in 3 different colours: red, green or blue.
- The quarks interact via the exchange of one of eight massless gluons.
- The gluons also carry colour charge, resulting in the interaction between gluons themselves.
- The strong interaction is characterised by a strong coupling constant  $\alpha_s$ .

- Only colour neutral ("white") particles can exist as free particles. Quarks and gluons carry colour charge and therefore do not exist as free particles but are bound into hadrons. This effect is called confinement and up to now cannot be fully explained by theory.

### Running coupling constant and asymptotic freedom

Due to possibility of self-coupling of gluons the coupling constant  $\alpha_s$ , calculated according to the renormalisation group equation, is a decreasing function of the characteristic energy scale in the reaction. In the leading order approximation it is given by the equation

$$\alpha_s(\mu^2) = \frac{12\pi}{(33 - 2n_f) \ln(\mu^2/\Lambda_{QCD}^2)} + \mathcal{O}\left(\frac{1}{\ln^2(\mu^2/\Lambda_{QCD}^2)}\right), \quad (1.22)$$

where  $n_f$  is number of active quark flavours ( $m_{quark}^2 < \mu^2$ ),  $\Lambda_{QCD}$  characterises the energy scale at which the coupling constant becomes large. The coupling constant is the one fundamental constant of QCD which has to be determined from experiment. A convenient way of its presentation is to derive its value at fixed-reference scale  $\mu_0 = M_Z^2$ , where  $M_Z$  is the mass of the  $Z^0$  boson. At small distance, large energy scale  $\mu \rightarrow \infty$ , the coupling between quarks and gluons is small  $\alpha_s \rightarrow 0$ . This is known as asymptotic freedom. On the other hand, if  $\mu \rightarrow \Lambda_{QCD}$ , the strong coupling constant increases. This is a sign of breakdown of the perturbative calculations at  $\mu \sim \Lambda_{QCD}$ .

### Factorisation theorem

The applicability of the perturbative QCD (pQCD) calculations to DIS processes follows from the factorisation theorem. It states that the structure functions can be factorised into "short distance" dependences, which can be calculated in pQCD, and into "long distance" dependences, which should be taken from outside the theory, e.g. experiment. Formally, factorisation leads to expression of structure functions as convolution of coefficient functions  $C_a^{V,i}$  given by pQCD for a particular exchanged boson  $V$ , parton  $i$  and a structure function  $a$  with parton distribution  $f_{i/h}$ . For the structure function  $F_2$  the factorisation leads to the expression

$$F_2^{V,h}(x, Q^2) = \sum_{i=q,\bar{q},g} \int_x^1 dz C_2^{V,h}\left(\frac{x}{z}, \frac{Q^2}{\mu^2}, \frac{\mu_F^2}{\mu^2} \alpha_s(\mu^2)\right) f_{i/h}(z, \mu_F, \mu^2), \quad (1.23)$$

where the summation is performed over all partons (quarks, anti-quarks and gluons).

There are two scales in the theorem. The renormalisation scale  $\mu$  defines the separation between the finite and the divergent contributions in the renormalisation procedure. The factorisation scale  $\mu_f$  defines the boundary between perturbative and non-perturbative regions. Both scales,  $\mu$  and  $\mu_F$ , are arbitrary and serve to absorb infrared (ultraviolet) divergences in pQCD.

One has certain freedom in choice of renormalisation scheme. The most commonly used one is the *modified minimal subtraction* ( $\overline{MS}$ ) scheme. Here, the divergent part of the coefficient functions is absorbed into the renormalised quark distributions for  $\mu = \mu_F$ .

### DGLAP evolution equations

The parton distribution functions in the hadrons  $q(x, Q^2)$  cannot be calculated from first principles, but their  $Q^2$  dependence can be calculated within perturbative QCD. The scale dependence of the parton distribution functions in QCD has its origin in the interactions of the quarks and gluons via elementary processes: gluon emission from quarks  $q \rightarrow qg$ , creation of quark-antiquark pairs  $g \rightarrow q\bar{q}$  and gluon emission by gluons.

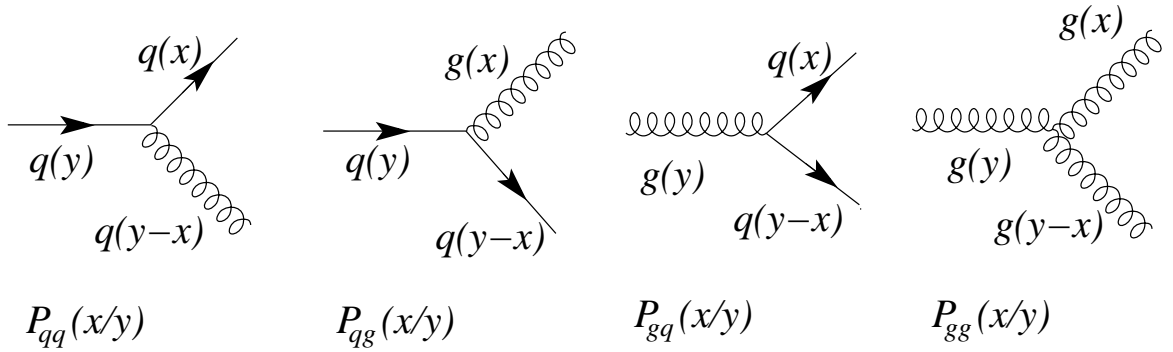


**Figure 1.2:** Splitting function  $P_{ij}$  denotes probability for parton  $j$  with momentum fraction  $y$  to split into a parton  $i$  with momentum fraction  $x$ .

The  $Q^2$  variation of parton distribution functions is described by the DGLAP (Dokshitzer-Gribov-Lipatov-Altarelli-Parisi) evolution equations [17–20]:

$$\frac{\partial q(x, t)}{\partial t} = \frac{\alpha_s(t)}{2\pi} \int_x^1 \frac{dy}{y} \left[ q(y, t) P_{qq} \left( \frac{x}{y} \right) + g(y, t) P_{qg} \left( \frac{x}{y} \right) \right] \quad (1.24)$$

$$\frac{\partial g(x, t)}{\partial t} = \frac{\alpha_s(t)}{2\pi} \int_x^1 \frac{dy}{y} \left[ q(y, t) P_{gq} \left( \frac{x}{y} \right) + g(y, t) P_{gg} \left( \frac{x}{y} \right) \right] \quad (1.25)$$

where  $t = \ln(Q^2/\Lambda_{QCD}^2)$ . The *splitting* functions  $P_{ij} \left( \frac{x}{y} \right)$  represent the probability that by changing the scale from  $Q^2$  to  $Q^2 + dQ^2$  a parton  $i$  with momentum fraction  $x$  is emitted by a parton  $j$  with momentum fraction  $y$  ( $y > x$ ). Figure 1.2 shows the Feynman diagrams of four basic processes which lead to parton evolution. Every diagram corresponds to one splitting function  $P_{ij}$ .

### Longitudinal structure function in QCD

In the naive QPM because of helicity  $H$  and angular momentum  $J$  conservation at hadronic vertex the exchange between electron and proton of longitudinally polarised

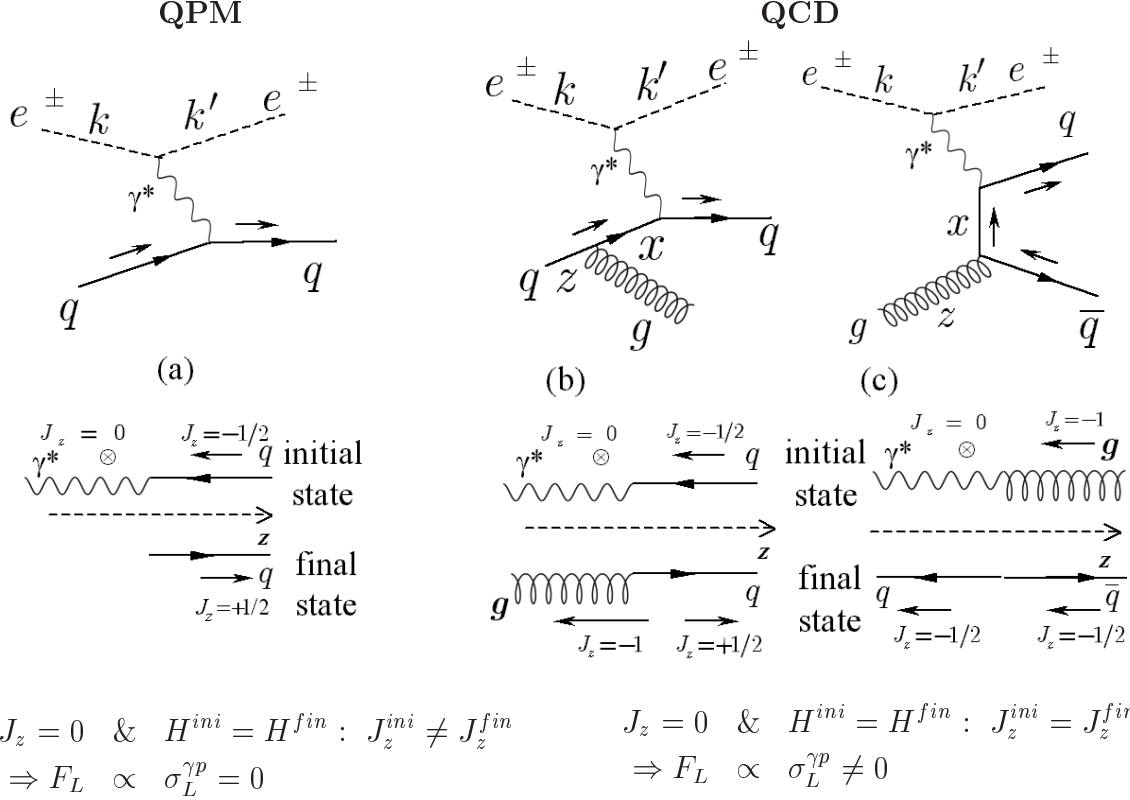


**Figure 1.3:** Helicity and angular momentum conservation at hadronic vertex in Quark Parton Model (QPM) and Quantum Chromodynamics (QCD).

virtual photon is not possible, see figure 1.4(a), which leads to  $F_L = 0$ . On the other hand in QCD, where quark can radiate gluon, figure 1.4(b), or gluon split to quark anti-quark pairs, figure 1.4(c), having three particles in the final state, there is no difficulty to conserve both helicity and angular momentum at the same time. Thus, in framework of QCD, non-zero  $F_L$  is allowed. In NLO it is given by [21, 22]

$$F_L(x, Q^2) = \frac{\alpha_s}{4\pi} x^2 \int_x^1 \frac{dz}{z^3} \left[ \frac{16}{3} \sum_q (q + \bar{q}) + 8 \sum_q e_q^2 \left(1 - \frac{x}{z}\right) \cdot zg \right] \quad (1.26)$$

where the first sum in the integral corresponds to the graph of the gluon radiation off a quark, figure 1.4(b). The second sum corresponds to gluon splitting into quark anti-quark pair, figure 1.4(c), and defines sensitivity of the longitudinal structure function to the gluon distribution function. At low  $x$  the gluon term dominates and the measurement of  $F_L$  can be used for determination of gluon distribution [23, 24].

## 1.5 Neutral Current Cross Section and Structure Functions

Including the  $Z^0$  exchange the neutral current cross sections for electron quark scattering are calculated from the corresponding electroweak matrix elements

$$\sigma \propto \left[ \begin{array}{c} \text{e} \longrightarrow \text{e} \\ \text{q} \longrightarrow \text{q} \end{array} \begin{array}{c} \text{e} \\ \gamma \\ \text{e}_q \end{array} + \begin{array}{c} \text{e} \longrightarrow \text{e} \\ \text{q} \longrightarrow \text{q} \end{array} \begin{array}{c} (v_e, a_e) \\ Z^0 \\ (v_q, a_q) \end{array} \right]^2 \quad (1.27)$$

Here,  $e$  and  $e_q$  are charges of the electron and the quark, and  $(v_e, a_e)$  and  $(v_q, a_q)$  are their vector and axial-vector coupling to the weak neutral current. For a fermion  $f$  the couplings are related to its charge and the  $z$  component of its weak isospin,  $I_{3,f}$ :

$$v_f = \frac{-I_{3,f} + 2e_f \sin^2 \theta_W}{2 \sin \theta_W \cos \theta_W} \quad a_f = \frac{-I_{3,f}}{2 \sin \theta_W \cos \theta_W}. \quad (1.28)$$

where  $\theta_W$  is the weak mixing angle (Weinberg angle).

Finally, the NC cross section for the process  $e^\pm p \rightarrow e^\pm X$  with unpolarised beams can be expressed in terms of generalised<sup>2</sup> structure functions. After correction of QED radiative effects (see section 1.8) the NC cross section is given by

$$\frac{d^2 \sigma_{NC}^\pm}{dx dQ^2} = \frac{2\pi\alpha^2}{xQ^4} \phi_{NC}^\pm (1 + \Delta^{weak}), \quad (1.29)$$

$$\text{with} \quad \phi_{NC}^\pm = Y_+ \tilde{F}_2 \mp Y_- x \tilde{F}_3 - y^2 \tilde{F}_L, \quad (1.30)$$

where  $\alpha \equiv \alpha(Q^2 = 0)$  is the fine structure constant.  $\Delta^{weak}$  are weak corrections, which are not applied to the measured cross section. The NC structure function term  $\phi_{NC}$  was introduced in [25] and is expressed in terms of generalised structure functions  $\tilde{F}_2$ ,  $x\tilde{F}_3$  and  $\tilde{F}_L$ . The helicity dependences of the electroweak interactions are contained in  $Y_\pm \equiv 1 \pm (1-y)^2$ . The generalised structure functions  $\tilde{F}_2$  and  $x\tilde{F}_3$  can be further

<sup>2</sup>Generalised structure functions  $\tilde{F}_i$  include, besides photon exchange, the effects from  $Z^0$  exchange.

decomposed as [26]:

$$\tilde{F}_2 \equiv F_2 - v_e \frac{\kappa Q^2}{(Q^2 + M_Z^2)} F_2^{\gamma Z} + (v_e^2 + a_e^2) \left( \frac{\kappa Q^2}{Q^2 + M_Z^2} \right)^2 F_2^Z, \quad (1.31)$$

$$x\tilde{F}_3 \equiv -a_e \frac{\kappa Q^2}{(Q^2 + M_Z^2)} xF_3^{\gamma Z} + (2v_e a_e) \left( \frac{\kappa Q^2}{Q^2 + M_Z^2} \right)^2 xF_3^Z, \quad (1.32)$$

with  $\kappa^{-1} = 4 \frac{M_W^2}{M_Z^2} (1 - \frac{M_W^2}{M_Z^2})$  in the on-mass-shell scheme [27],  $M_Z$  and  $M_W$  are the masses of  $Z^0$  and  $W^\pm$  bosons. The quantities  $v_e$  and  $a_e$  are the vector and axial-vector weak couplings of the electron to the  $Z^0$  [27].

The electromagnetic structure function  $F_2$  originates from photon exchange only. The functions  $F_2^Z$  and  $xF_3^Z$  are the contributions to  $F_2$  and  $xF_3$  from  $Z^0$  exchange and the functions  $F_2^{\gamma Z}$  and  $xF_3^{\gamma Z}$  are the contributions from  $\gamma Z$  interference. The longitudinal structure function  $F_L$  may be decomposed in a manner similar to  $F_2$ . Its contribution is significant only at high  $y$ .

For the bulk of the kinematic domain at HERA the dominant contribution to the cross section comes from pure photon exchange via  $F_2$ . The contributions due to  $Z^0$  boson exchange only become important at large values of  $Q^2$ . For longitudinally unpolarised lepton beams  $F_2$  is the same for  $e^-$  and for  $e^+$  scattering, while the  $xF_3$  contribution to the cross section changes sign as can be seen in eq. 1.29.

In QPM the structure functions  $F_2$ ,  $F_2^{\gamma Z}$  and  $F_2^Z$  are related to the sum of the quark and anti-quark densities:

$$[F_2, F_2^{\gamma Z}, F_2^Z] = x \sum_q [e_q^2, 2e_q v_q, v_q^2 + a_q^2] \{q + \bar{q}\}. \quad (1.33)$$

The structure functions  $xF_3^{\gamma Z}$  and  $xF_3^Z$  to the difference of the quark and anti-quark densities which determines the valence quark distributions  $xu_v$  and  $xd_v$ :

$$[xF_3^{\gamma Z}, xF_3^Z] = 2x \sum_q [e_q a_q, v_q a_q] \{q - \bar{q}\} = 2x \sum_q [e_q a_q, v_q a_q] q_v. \quad (1.34)$$

The summation here goes over active quark flavours,  $e_q$  is the charge of quarks in units of the electron charge and  $v_q$  and  $a_q$  vector and axial-vector couplings of the quarks.

For the presentation of the subsequent measurements it is convenient to define the "reduced cross section" as

$$\tilde{\sigma}_{NC}^\pm(x, Q^2) \equiv \frac{1}{Y_+} \frac{Q^4}{2\pi\alpha^2} \frac{x}{dx} \frac{d^2\sigma_{NC}^\pm}{dxdQ^2} = Y_+ \phi_{NC}^\pm. \quad (1.35)$$

## 1.6 Charged Current Cross Section and Structure Functions

The charged current cross section is defined as

$$\frac{d^2\sigma_{CC}^\pm}{dx dQ^2} = \frac{G_F^2}{2\pi x} \left[ \frac{M_W^2}{Q^2 + M_W^2} \right]^2 \phi_{CC} \quad (1.36)$$

$$\text{with } \phi_{CC}^\pm = \frac{1}{2}(Y_+ \tilde{W}_2^\pm \mp Y_- x \tilde{W}_3^\pm - y^2 \tilde{W}_L^\pm) \quad (1.37)$$

where  $G_F$  is Fermi coupling constant and  $M_W$  mass of  $W^\pm$  boson. The CC structure functions  $\tilde{W}_L^\pm$ ,  $\tilde{W}_2^\pm$ , and  $x\tilde{W}_3^\pm$  are defined in a similar manner to the NC structure functions [28]. In the QPM (where  $\tilde{W}_L^\pm \equiv 0$ ) they may be interpreted as lepton beam charge dependent sums and differences of quark and anti-quark densities and are given for an unpolarised lepton beam by

$$\tilde{W}_2^+ = 2x(d + s + \bar{u} + \bar{c}) \quad (1.38)$$

$$x\tilde{W}_3^+ = 2x(d + s - \bar{u} - \bar{c}) \quad (1.39)$$

$$\tilde{W}_2^- = 2x(u + c + \bar{d} + \bar{s}) \quad (1.40)$$

$$x\tilde{W}_3^- = 2x(u + c - \bar{d} - \bar{s}) \quad (1.41)$$

where  $u, c, d, s$  are quark distributions and  $\bar{u}, \bar{c}, \bar{d}, \bar{s}$  anti-quark distributions. The structure function terms  $\phi_{CC}^\pm$  are then given by

$$\phi_{CC}^+ = x(\bar{u} + \bar{c}) + (1 - y)^2 x(d + s) \quad (1.42)$$

$$\phi_{CC}^- = x(u + c) + (1 - y)^2 x(\bar{d} + \bar{s}). \quad (1.43)$$

## 1.7 QCD Analysis and Parton Distribution Functions (PDFs)

The Parton Distribution Functions (PDFs) of proton are not predicted by QCD. They are therefore determined by QCD fits. The Standard Model predictions used in this thesis are calculated using PDFs obtained by the H1 PDF 2000 fit [29] which is a fit to the H1 NC and CC data partially including the measurements presented here. More details on the fit procedure are given in appendix A.

The measurements of the neutral and charged current scattering cross sections, via different structure functions provide sensitivity to different quark flavour distributions.

The neutral current structure function terms  $\phi_{NC}^{\pm}$  are dominated by the electromagnetic structure function  $F_2$  which is, according to eq.1.33, below the  $b$  quark mass threshold is given by

$$F_2 = \frac{4}{9}x(u + c + \bar{u} + \bar{c}) + \frac{1}{9}x(d + s + \bar{d} + \bar{s}) \quad (1.44)$$

Defining sums of up, anti-up, down and anti-down quark distributions as:

$$\begin{aligned} xU &= x(u + c) & x\bar{U} &= x(\bar{u} + \bar{c}) \\ xD &= x(d + s) & x\bar{D} &= x(\bar{d} + \bar{s}) \end{aligned} \quad (1.45)$$

the equations 1.42-1.44 can be written as

$$F_2 = \frac{4}{9} \cdot (xU + x\bar{U}) + \frac{1}{9} \cdot (xD + x\bar{D}) \quad (1.46)$$

$$\phi_{CC}^+ = x\bar{U} + (1 - y)^2 xD, \quad (1.47)$$

$$\phi_{CC}^- = xU + (1 - y)^2 x\bar{D}. \quad (1.48)$$

Parametrising the distributions given in eq. 1.45 instead of the traditional way of using the parametrisations of valence and sea quarks [30–33], weakens the influence of necessary assumptions for the flavour decomposition on the sea in the fit. Therefore in the QCD analysis used here the valence quark distributions are not fitted directly but are obtained from the fits to summed distributions:

$$xu_v = x(U - \bar{U}), \quad xd_v = x(D - \bar{D}). \quad (1.49)$$

The fitted parton distributions at the initial scale  $Q_0^2 = 4 \text{ GeV}^2$ , together with the valence quark distributions determined according to eq. 1.49, are shown in figure 1.4. The parton distributions at higher  $Q^2$  are calculated according to DGLAP evolution equations 1.24, 1.25 at the next-to-leading order [34]. The evolved parton densities at  $Q^2 = 10 \text{ GeV}^2$  and  $Q^2 = 1000 \text{ GeV}^2$  are shown in figure 1.5.



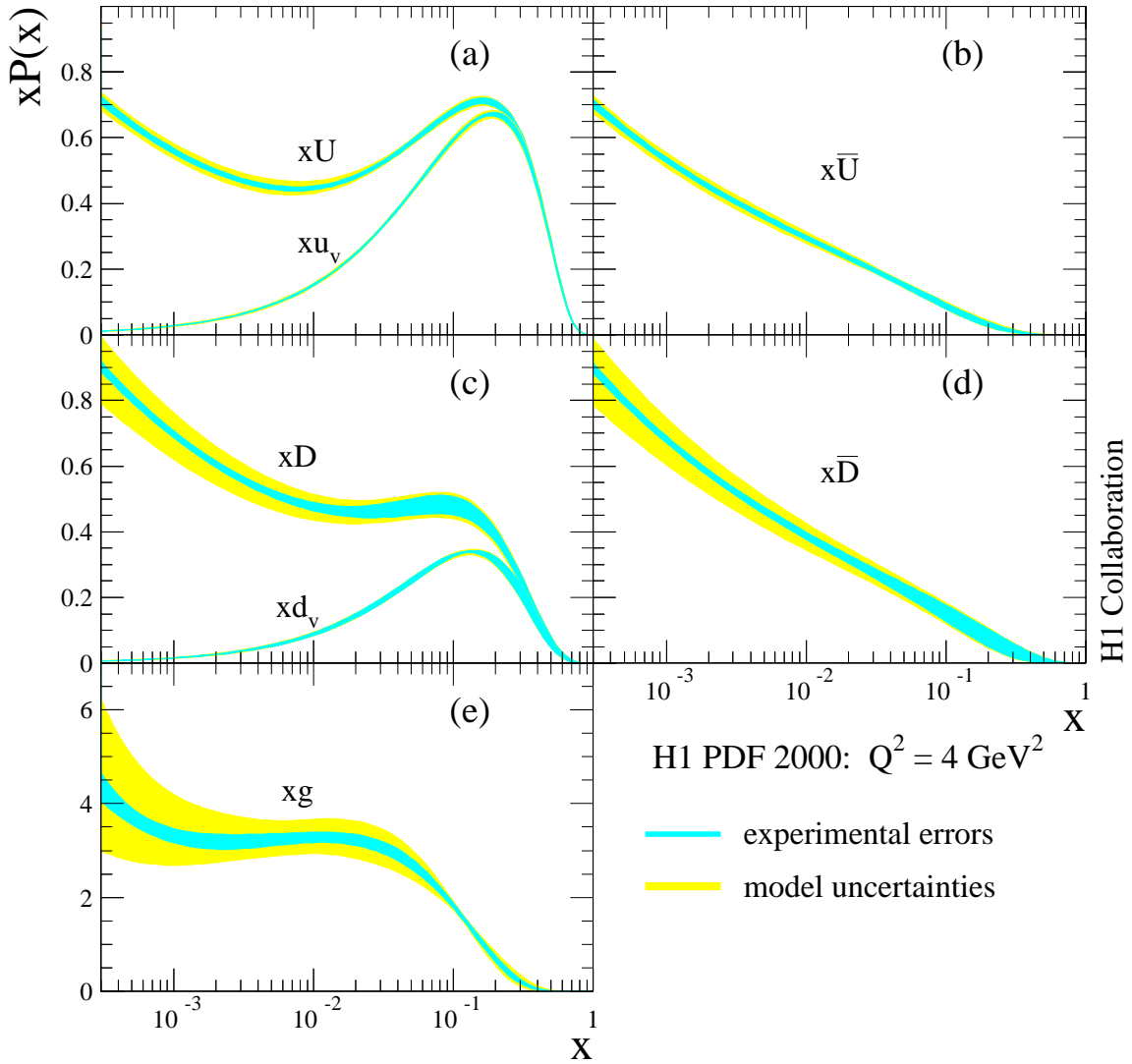


**Figure 1.4:** Parton distributions (a)  $xU$ , (b)  $x\bar{U}$ , (c)  $xD$ , (d)  $x\bar{D}$ , and (e)  $xg$  as determined from the H1 PDF 2000 fit to H1 and data only. The distributions are shown at the initial scale  $Q_0^2 = 4 \text{ GeV}^2$  with experimental and model uncertainties. The valence quark densities  $xu_v$  (a) and  $xd_v$  (c) also shown.

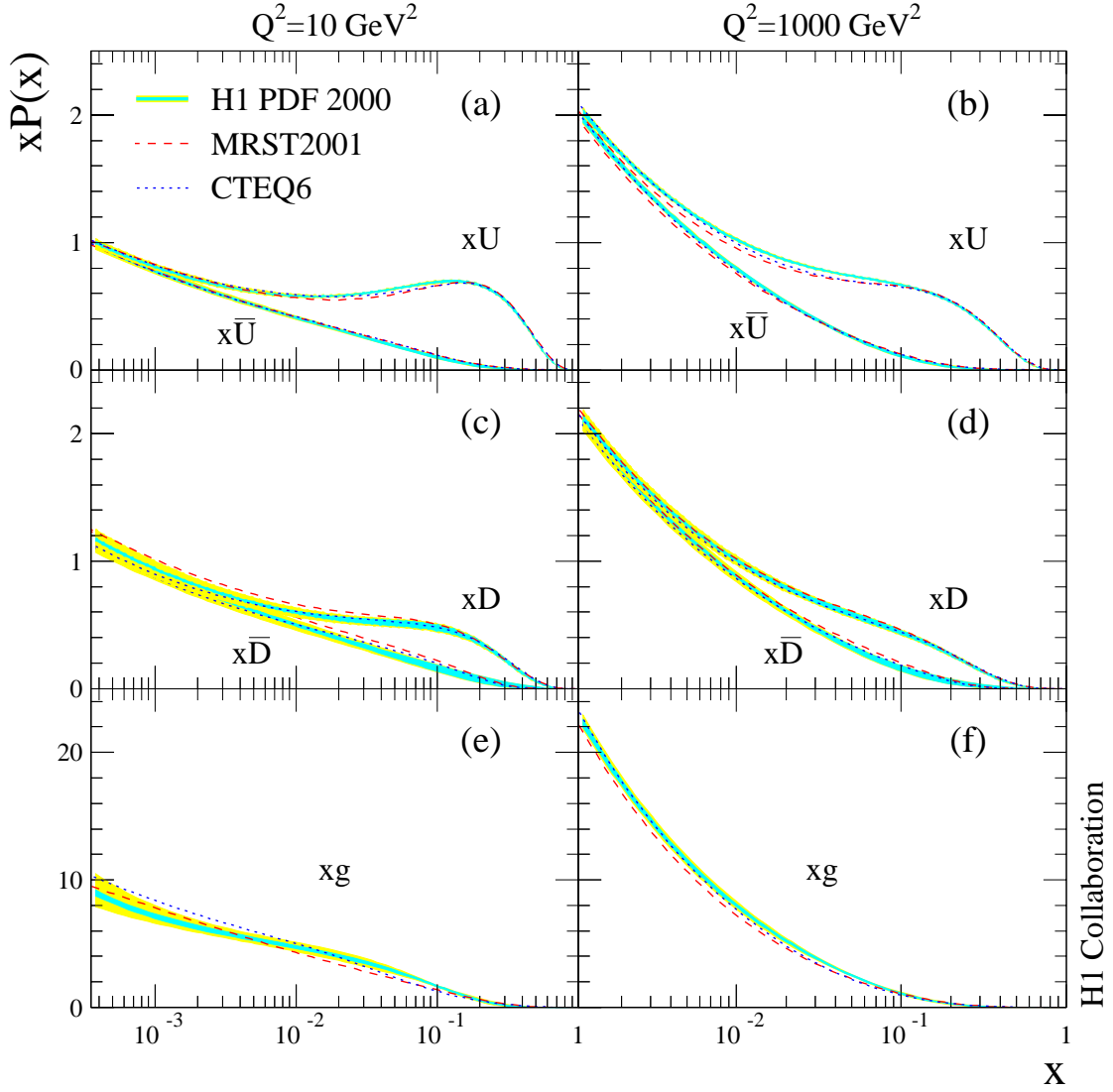


**Figure 1.5:** Parton distributions (a, b)  $xU$  and  $x\bar{U}$ , (c, d)  $xD$  and  $x\bar{D}$ , and (e, f)  $xg$  as determined from the H1 PDF 2000 fit to H1 data. The distributions are shown at  $Q^2 = 10 \text{ GeV}^2$  (a, c, e) and at  $Q^2 = 1000 \text{ GeV}^2$  (b, d, f) with experimental and model uncertainties. For comparison the results of recent global fits from the MRST [30] and CTEQ [31] groups are also shown.

## 1.8 Radiative Corrections

Until now DIS has been discussed in the lowest order  $\mathcal{O}(\alpha^2)$  of the electromagnetic theory (leading order - LO or Born approximation). All higher order processes contribute to the measured cross section as well.

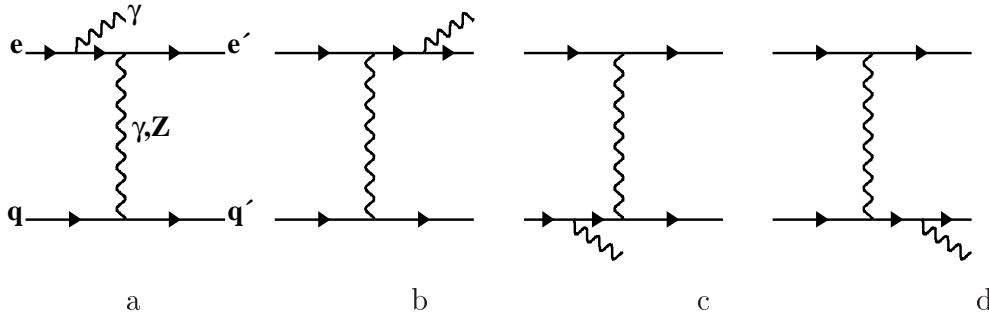


**Figure 1.6:** Feynman graphs of the next-to-leading order (NLO)  $\mathcal{O}(\alpha^3)$  of perturbative theory where an electron (a,b) or a quark (c,d) radiates a real photon giving an additional photon in the final state.

The dominant contribution here arises from the radiation a high energetic photon from the incoming or outgoing electron. When the incoming electron radiates a photon (initial state radiation - ISR), figure 1.6(a), the electron-proton centre-of-mass energy is changed leading to different kinematics with respect to the original process. A process when a photon is radiated from the outgoing electron is called final state

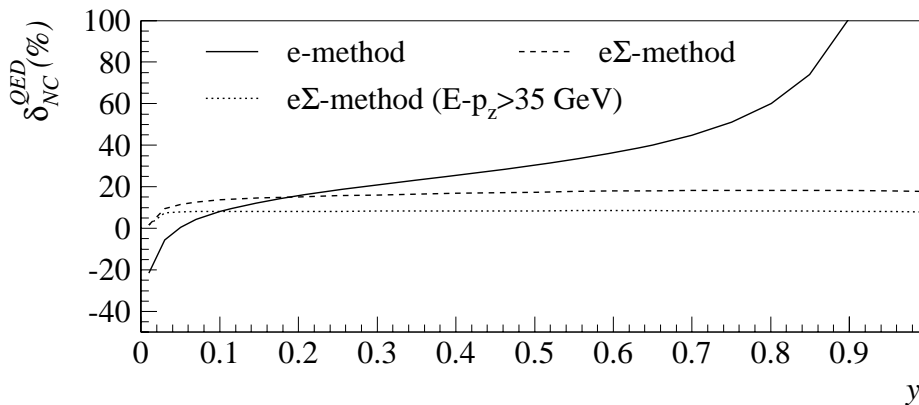


**Figure 1.7:** The radiative corrections for NC electron-proton DIS as function of  $y$  at  $Q^2 = 500\text{GeV}^2$ . The corrections are shown for different methods of reconstructing kinematic variables (section 4), electron-method (solid line) and  $e\Sigma$ -method (dashed line) without kinematic cut on variable  $E - P_z$  and the corrections for  $e\Sigma$  method applying cut  $E - P_z > 35\text{ GeV}^2$  (dotted line) (taken from [35]).

radiation (FSR), figure 1.6(b). Since the photon is emitted under a small angle the electron and the photon are usually detected as one particle. Therefore FSR gives a small contribution. Compared to photon radiation from the electron, the radiation from the quarks, figure 1.6(c,d), is suppressed by the quark mass.

As it was found in [36, 37] and demonstrated in figure 1.7 these contributions are sizeable and have to be corrected for [38]:

$$\left. \frac{d\sigma}{dx dQ^2} \right|_{meas} = \left. \frac{d\sigma}{dx dQ^2} \right|_{Born} (1 + \Delta^{QED}). \quad (1.50)$$

$$(1.51)$$

As shown in the figure 1.7, the size of these corrections can be reduced by different means, i.e. appropriate choice of the method for reconstruction kinematic variables (section 4) and event selection criteria listed in section 6.

Additional corrections,  $1 + \Delta^{weak}$ , arise from the effects of the photon-lepton vertex corrections combined with the self energies of the external fermion lines and the effects of the fermion loops of the exchanged photon self energy. The weak radiative corrections  $\Delta^{weak}$  are defined in [38] with  $\alpha$  and the  $Z$  and  $W$  boson masses (taken here as in [39] to be  $M_Z = 91.187$  GeV and  $M_W = 80.41$  GeV) as the main electroweak inputs. The weak corrections are typically less than 1% and never more than 3% and have not been applied to the measured cross sections.

## Chapter 2

# HERA and the H1 Detector

### 2.1 HERA

The HERA accelerator (*Hadron-Elektron-Ring-Anlage*) consists of two separate storage rings in which the electrons and protons are accelerated [40]. Both rings are situated in the same 6.3 km long tunnel. The beams are in two interaction points brought to collisions at centre-of-mass energy of 319 GeV.

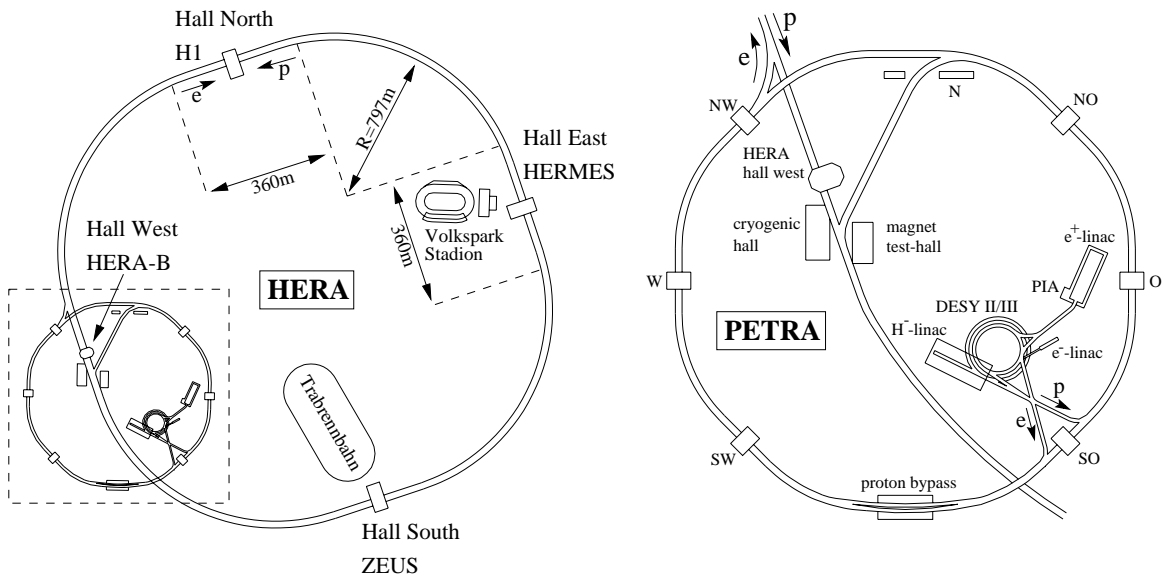


**Figure 2.1:** The electron proton storage ring HERA (left) with the preaccelerators (right).

The schematic overview of the accelerator, together with the preaccelerators is shown in figure 2.1. In the preaccelerators (LINAC, DESYIII, PETRA) the electrons are accelerated to the energy of 12 GeV and protons to 40 GeV. With these energies they are injected into the HERA storage rings where they are accelerated to their nominal

energies. The electron beam energy is 27.6 GeV and it is limited by high energy losses due to synchrotron radiation. In the proton storage ring the superconducting magnets are providing magnetic field of about 5 T. The design proton beam energy is 820 GeV. Both electron and proton rings can accelerate 210 bunches. The spatial distribution of electrons in a bunch is Gaussian with a width of  $\sigma_x \approx 180 \mu\text{m}$ ,  $\sigma_y \approx 60 \mu\text{m}$  transversal to beam direction and of  $\sigma_z \approx 1 \text{ cm}$  in the beam direction. At two experiments, H1 and ZEUS, the bunches are brought to collision, with a time interval between two bunch-crossings (BC) of 96 ns. The periods of data taking with the same filling of electrons and protons in the HERA accelerator ring are referred to as *luminosity fills*. The data in the experiments are collected in so-called *runs* which correspond to running period not longer than 2 hours.

In machine studies it was demonstrated that the superconducting coils of the proton ring can safely operate with 10% increased current. This enabled the increase of the proton energy to 920 GeV and by this centre-of-mass energy to 319 GeV. The first data taken with this increased centre of mass energy were data from electron proton collisions (in 1998 and beginning 1999). From September 1999 till the end of HERA I running in 2000 the data have been taken with positrons and protons accumulating luminosity of about  $65 \text{ pb}^{-1}$ . These data are used in the analysis presented here.

## 2.2 H1

The H1 detector [41, 42] was designed as a general purpose detector to study high-energy interactions of electrons and protons at HERA.

The H1 detector is arranged cylindrically symmetric around the beam axis. The imbalance in the energy of the electron and proton colliding beams implies that the detector is better instrumented in the outgoing proton direction, which, by convention, defines the positive  $z$  direction of the H1 coordinate system. The components of the detector situated on the positive side from the interaction point are referred to as "forward". Similarly, the negative side is referred to as "backward". The region around the interaction point is called "central" part of the apparatus.

The H1 detector (figure 2.2) is composed of a central and forward tracking chambers surrounded by electromagnetic and hadronic calorimeters: Liquid-Argon (LAr) calorimeter in the central and forward part and in backward part a Lead-Fibre calorimeter (SpaCal). A superconducting coil outside the Liquid-Argon calorimeter provides a uniform magnetic field of 1.2 T. The iron return yoke surrounding the whole detector contains several layers of streamer tubes. They are used to detect muons and measure hadronic shower tails. In the forward direction the measurement of muons is performed by drift chambers placed in a toroidal magnetic field.

In the following the most important parts of the H1 detector used in this analysis are described.

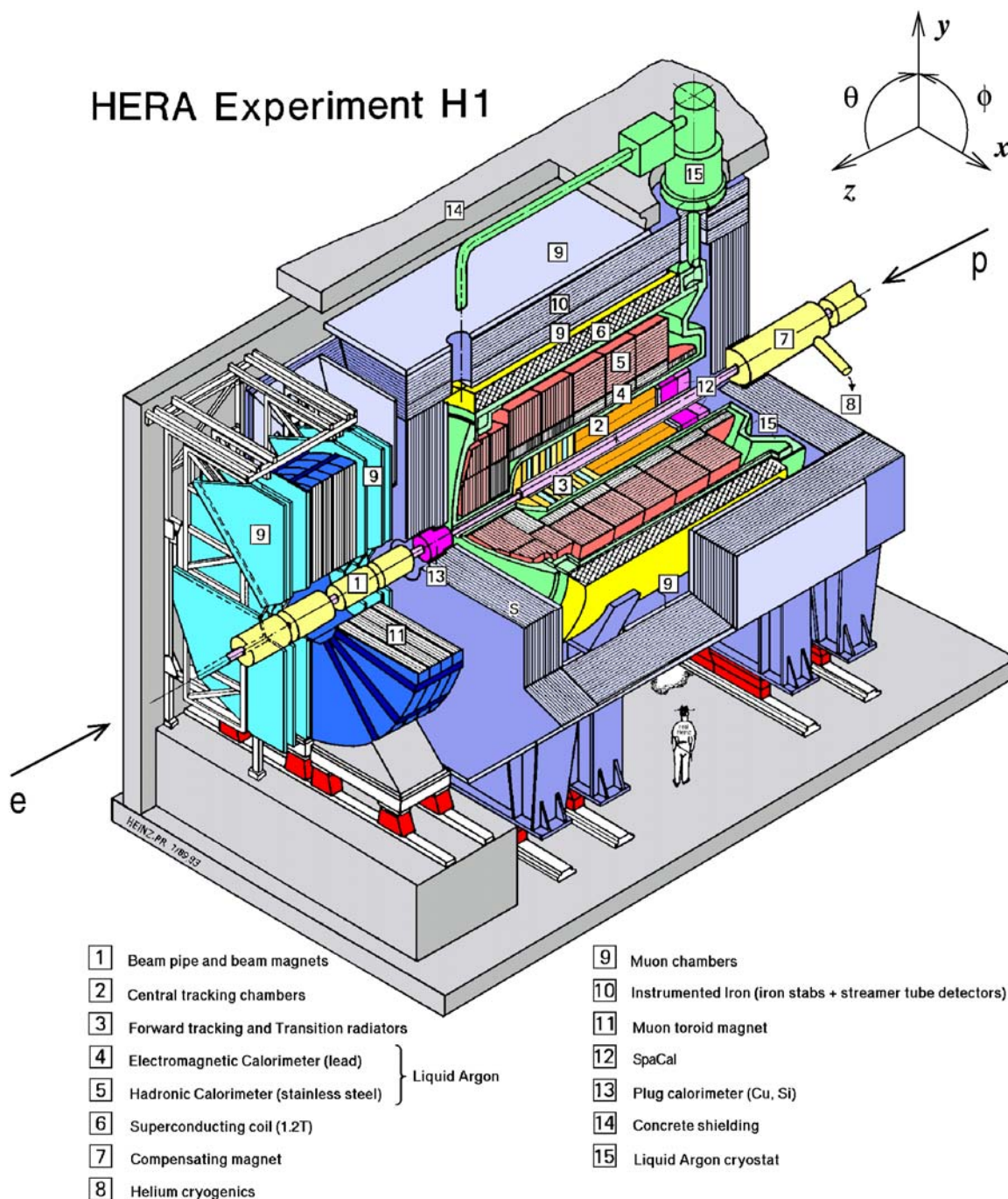


Figure 2.2: Schematic view of the H1 detector

## 2.2.1 Calorimeters

The purpose of the calorimeters is to measure electromagnetic and hadronic energy. They are also used to identify electrons, muons, neutral particles, the hadronic final state and measure their energy. The main calorimeter is the Liquid-Argon calorimeter [43]. It covers the range in the polar angle of  $4^\circ \leq \theta \lesssim 153^\circ$ . In the backward direction,  $153^\circ < \theta < 178^\circ$ , the a spaghetti calorimeter (SpaCal) is installed [44]. In a very backward direction a Wolfram-scintillator calorimeter (VLQ) [45] allows detection of the electrons scattered with very low momentum transfers. The forward part of the detector is closed by a copper silicon calorimeter (PLUG) [46]. The last two calorimeters (VLQ and PLUG) are not of importance for the analysis presented here.

### 2.2.1.1 Liquid-Argon Calorimeter

The characteristics of Liquid-Argon calorimeters are high stability, ease of calibration, possibility of fine segmentation and homogeneity of response [47]. This allows a very good resolution of the measured energy and position of the scattered electron as well as good resolution of hadronic energy measurement.

The LAr calorimeter consists of an inner section for the measurement of electromagnetic showers and an outer section which is needed for measurement of hadronic showers. It is built out of different "wheels" as can be seen in the schematic  $R$ - $z$  view of the calorimeter presented in figure 2.3:

- Backward Barrel Electromagnetic calorimeter (BBE);
- Central Barrel calorimeter modules (CB1,CB2,CB3);
- Forward Barrel calorimeter modules (FB1,FB2);
- Outer and Inner Forward calorimeters (OF,IF).

All wheels apart from the BBE and the OF consist of electromagnetic and the hadronic sections. The BBE consists of an electromagnetic section only, the OF only of hadronic section. The wheels are divided in azimuthal angle  $\phi$  into eight octants (figure 2.3). The shape of the BBE octants is made such that the BBE has a 16-fold symmetry. The regions between the modules are problematic for the measurement due to high energy losses. These gaps between the wheels are called "z-cracks", between the octants "phi-cracks".

The LAr calorimeter is segmented in 45 000 cells to ensure a good spatial resolution of the deposited energy. Each cell consists of absorber plates supplemented by high voltage and readout electrodes. The sampling medium between the absorber plates is liquid Argon. The absorber material is lead in the electromagnetic section and



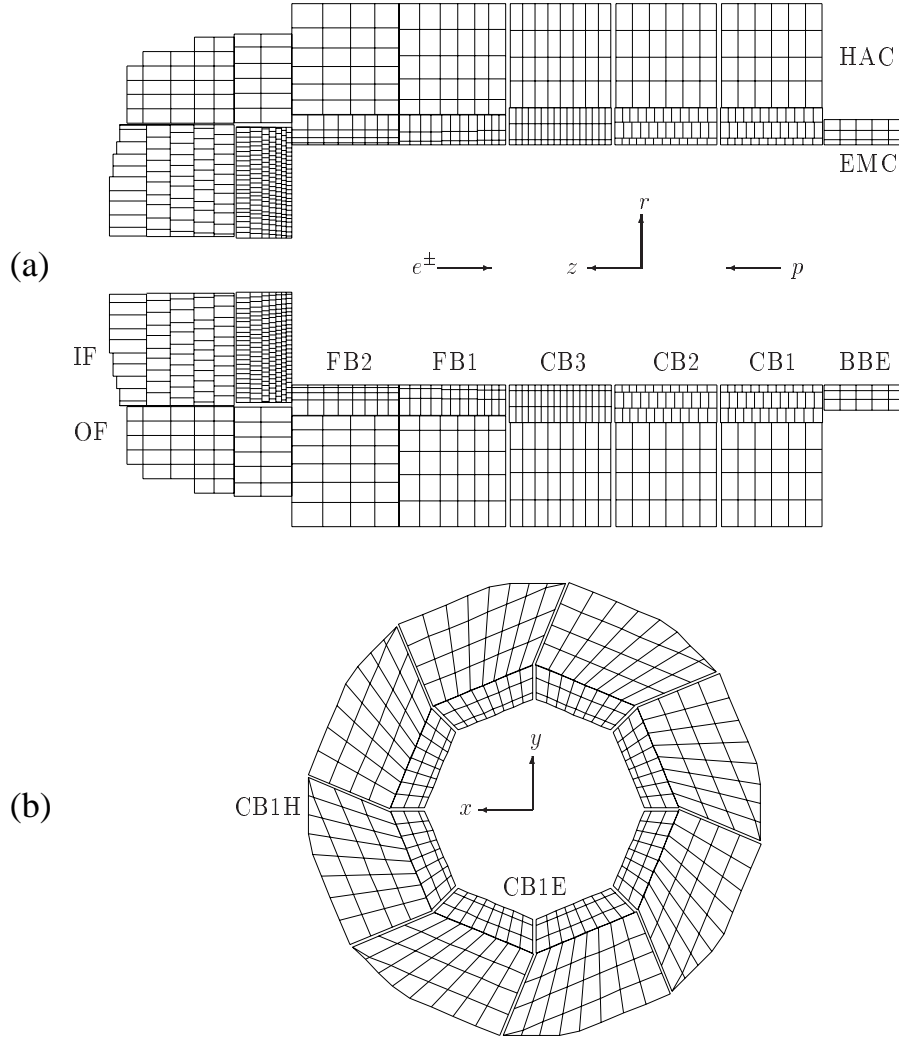


**Figure 2.3:** Schematic view of the wheel and cell structure of the H1 LAr calorimeter (a). Schematic view of the octant structure of the CB1 wheel (b).

stainless steel in the hadronic section. The electromagnetic section consists of three cell layers in the BBE, CB and FB1, four in FB2 and seven in IF. The cell sizes vary and are optimised to measure the longitudinal and transverse extension of electromagnetic showers which are used for the identification of the scattered electron. The depth of the electromagnetic section is  $\approx 20 - 30$  radiation lengths, the total depth of the calorimeter is  $\approx 5 - 8$  interaction lengths.

Test beam measurements [43, 48, 49] of LAr calorimeter modules revealed an energy resolution  $\sigma_{em}(E)/E = 12\%/\sqrt{E/GeV} \oplus 1\%$  for electrons and  $\sigma_{had}(E)/E = 50\%/\sqrt{E/GeV} \oplus 2\%$  for charged pions.

### 2.2.1.2 SpaCal

The SpaCal calorimeter, shown in figure 2.4, is located in the backward region,  $-151 \text{ cm} < z < -244 \text{ cm}$ . It consists of electromagnetic and hadronic sections with an outer radius of 80 cm and inner radius of 5.7 cm. The SpaCal covers the angular range of  $153^\circ < \theta < 178^\circ$ .

The electromagnetic calorimeter is fabricated using grooved lead plates and scintillating fibres. It is composed of 1192 cells, each with an active volume of  $4 \times 4 \times 25 \text{ cm}^3$ . This corresponds to 27.5 radiation lengths ensuring full containment of the deposited electromagnetic energy. The energy resolution of the electromagnetic part of the SpaCal is  $\sigma(E)/E = 7\%/\sqrt{E/\text{GeV}} \oplus 1\%$ .

The hadronic section of the SpaCal consists of 136 cells with a cross section of  $12 \times 12 \times 25 \text{ cm}^3$  which roughly corresponds to the dimension of hadronic showers. The depth of the electromagnetic and hadronic section together is about 2 interaction lengths.

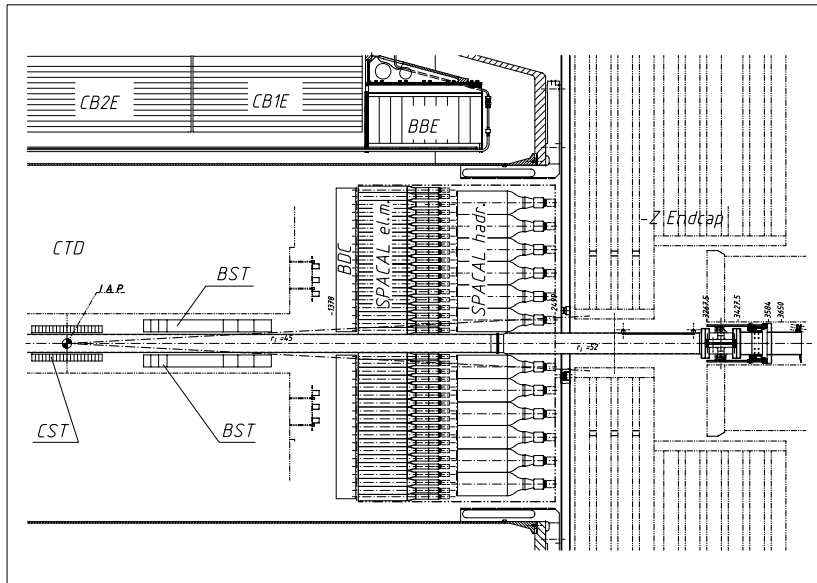


Figure 2.4: Side view of the SpaCal.

The main purpose of the SpaCal is the energy measurement of scattered electrons in the neutral current process at lower momentum transfer ( $Q^2 \leq 120 \text{ GeV}^2$ ). In the analysis presented here the SpaCal is used for the measurement of hadronic activity in the backward region of the detector.

## 2.2.2 Tracking System

The tracking system is surrounding the interaction region, see figure 2.5. It is used for track reconstruction, vertex determination, momentum measurement and particle identification. In order to have high efficiency of the track reconstruction in full angular range the tracking system is divided into two mechanically distinct detector modules, the central tracking detector (CTD) and the forward tracking detector (FTD).

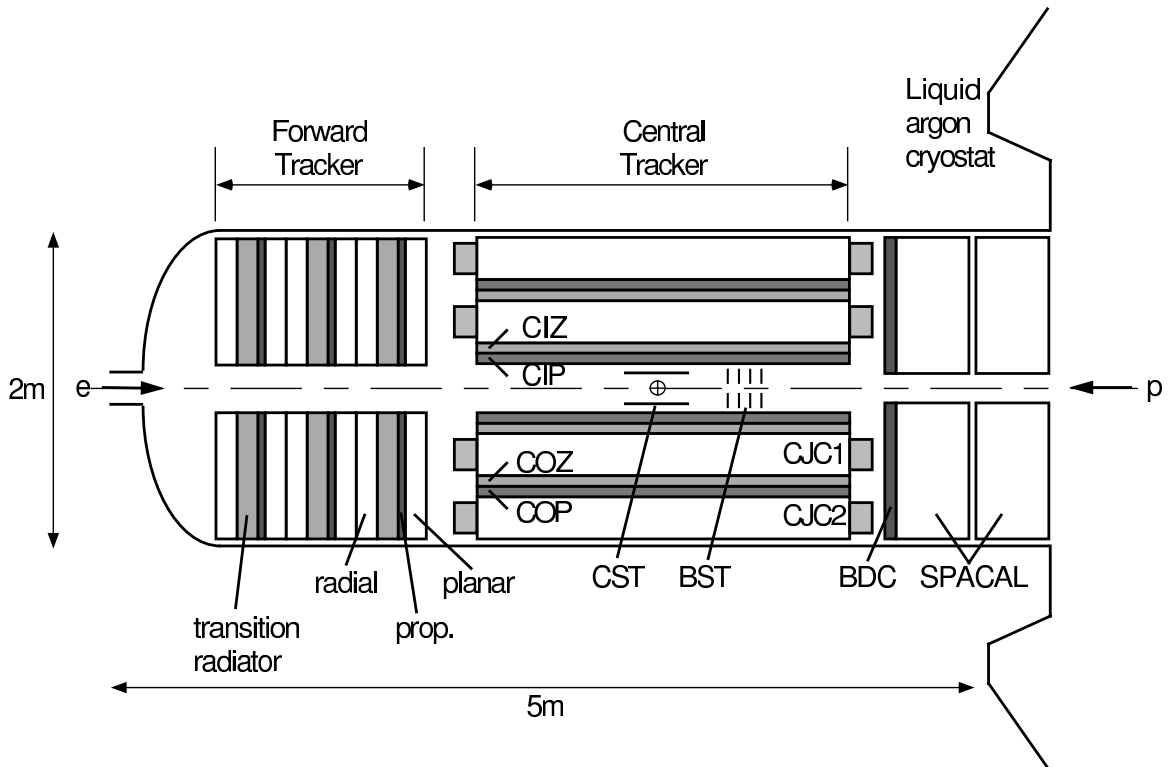
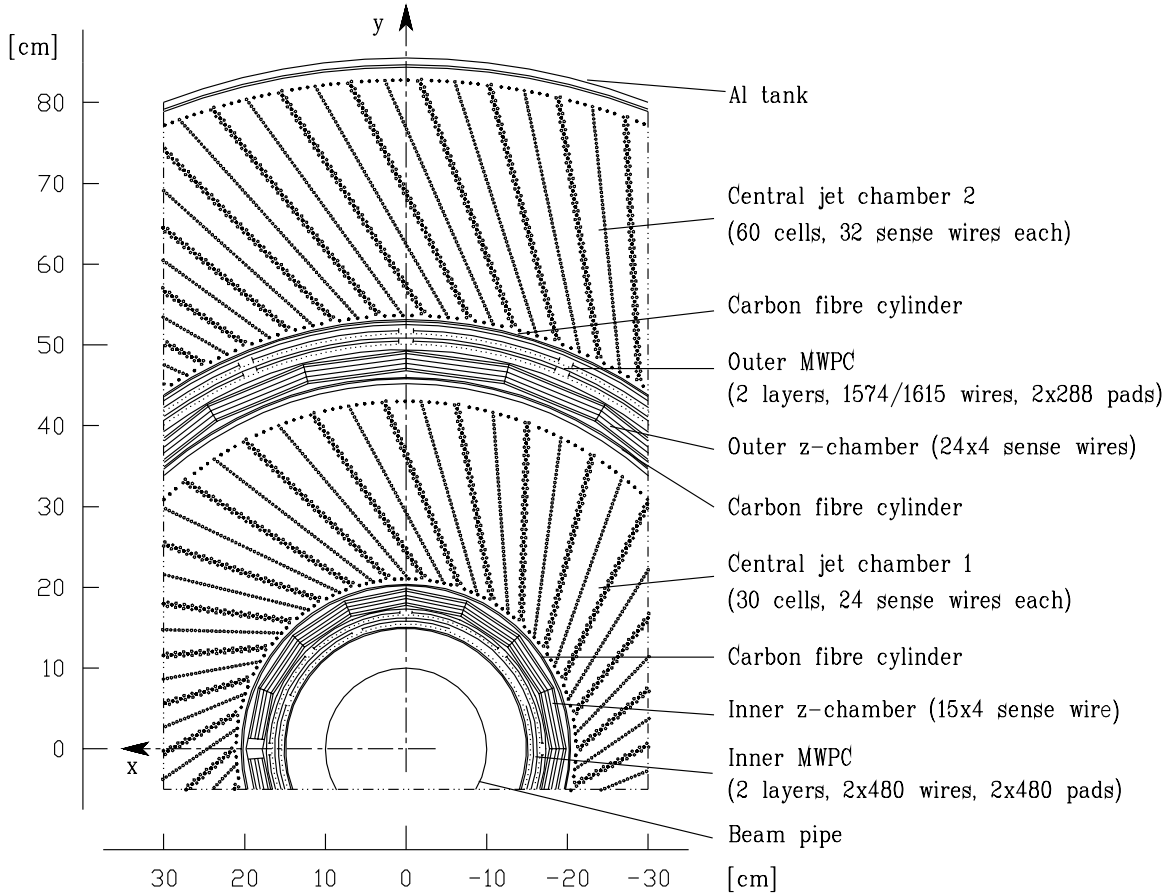


Figure 2.5: The side view of the tracking system.

### 2.2.2.1 Central Tracking Detector

The CTD comprises of six coaxial tracking chambers in the region of  $-110 \text{ cm} < z < 100 \text{ cm}$ , see figure 2.6. The main components of CTD are central jet chambers, CJC1 and CJC2 [50]. The CJC1 consists of 30 cells with 24 sense wires parallel to the  $z$  axis, the CJC2 consists of 60 cells with 32 wires. They are drift chambers which provide a radial resolution of  $\sigma_{r\phi} = 170 \mu\text{m}$  and the precision of the  $z$ -coordinate measurement of about 2 cm.

A precise measurement of the  $z$  coordinate is possible using inner and outer  $z$ -chambers, CIZ and COZ [51]. They are also drift chambers with a drift direction



**Figure 2.6:** The radial view of the tracking system.

parallel to the beam axis. The CIZ is mounted in the inner cylinder of CJC1 and COZ and in between CJC1 and CJC2. The CIZ (COZ) comprises 15 (24) rings of 12 (9) cm length in  $z$  direction with 4 layers of sense wires in each ring. The spatial resolution of the  $z$ -chambers in beam direction is 0.26 mm (CIZ) and 0.20 mm (COZ).

The central proportional chambers, CIP and COP [52,53] are Multi-Wire Proportional Chambers (MWPC) which provide a fast timing signal with a time resolution of 21 ns and thus allowing for a determination of the bunch crossing. The chambers are composed of 60 (CIP) and 18 (COP) sectors in  $z$  direction. In  $\phi$  direction there are 8 (CIP) and 16 (COP) sectors.

### 2.2.2.2 Forward Tracking Detector

The forward tracking detector [54,55] is an integrated system consisting of three identical supermodules. Each supermodule includes three different orientations of planar wire drift chambers designed to provide an accurate  $\theta$  measurements, a multiwire

proportional chamber (FWPC) for fast triggering, a passive transition radiator and a radial wire drift chamber which provides accurate  $R$ - $\phi$  information.

### 2.2.3 Luminosity System

The luminosity is measured by counting Bethe-Heitler (BH) bremsstrahlung events  $ep \rightarrow ep\gamma$  [56] which are detected by the coincidence of a photon and an electron in the luminosity system. Since the cross section of BH is very large and well known, the luminosity can be calculated from the event rate taking into account the detector acceptance. The luminosity system serves several purposes [57, 58]:

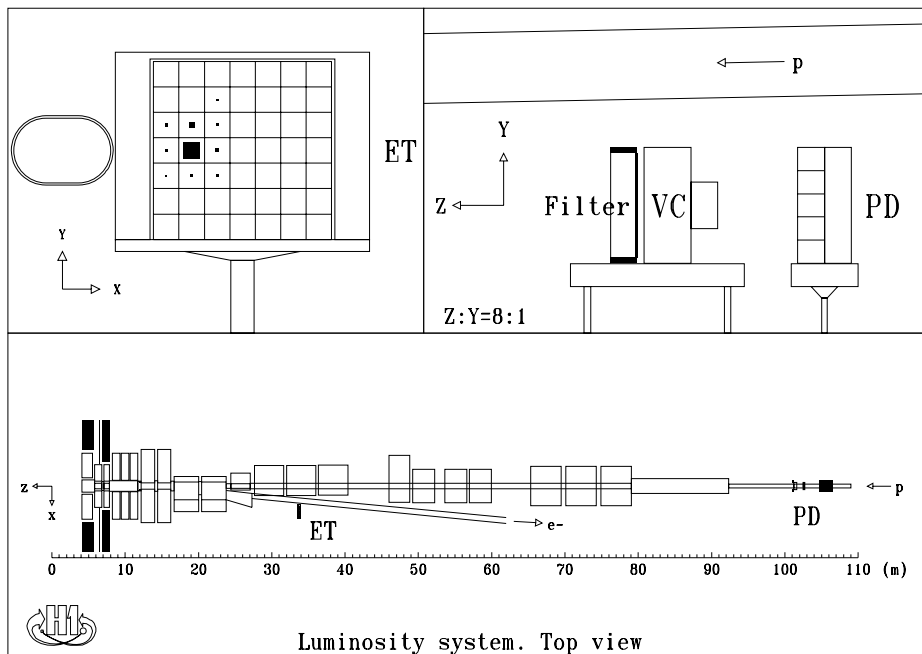


Figure 2.7: The layout of the luminosity system.

- online luminosity measurement by the coincidence method when the  $e$  and  $\gamma$  are simultaneously detected;
- offline luminosity measurement by the single-photon method which counts the photon rate with energy above a certain threshold;
- electron beam monitoring for HERA machine;
- energy measurement for electrons scattered at  $Q^2 < 0.01 \text{ GeV}^2$  (tagging of photoproduction events) using a photon detector as a veto against Bremsstrahlung events;

- measurement of initial state radiation events.

The general view of the luminosity system is shown in figure 2.7. It consists of two small electromagnetic calorimeters, the electron tagger (ET) and the photon detector (PD), situated in the the HERA tunnel at  $z$  positions of  $-34.4$  m and  $-102.9$  m, respectively. The ET consists of  $7 \times 7$  cells covering a total area of  $154 \times 154$  mm<sup>2</sup>. The electrons scattered with energy between 10 and 20 GeV are deflected by the beam optics, pass an exit window at  $z = -27.3$  m and hit the ET. The angular acceptance of the ET is about 5 mrad. The PD consists of  $5 \times 5$  cells covering a total area of  $100 \times 100$  mm<sup>2</sup>. The photons leave the proton beam pipe through a window at  $z = -92.3$  m, where the beam pipe bends upwards, and hit the PD. The angular acceptance of PD amounts to about 0.45 mrad.

## 2.2.4 Time of Flight System

The Time of Flight system (ToF) consists of three scintillators situated at different positions along the beam pipe, the backward ToF (BToF) at  $z = -275$  cm, the forward ToF (FToF) at  $z = 790$  cm and the Plug-ToF (PToF) at  $z = -540$  cm. In addition there are scintillator walls ("Veto Wall") installed at  $z = -810$  cm and  $z = -650$  cm. All these scintillators have a very good time resolution to a precision of 1 ns. They are used to reject beam induced background arriving out-of-time in the H1 detector.

## 2.2.5 Trigger System

The purpose of the H1 trigger system is the fast separation of the interesting physics events from background events. The main background comes from interactions of the proton beam with the wall of the beam-pipe and remaining gas within the evacuated beam pipe. They are called "beam-wall" and "beam-gas" interactions, respectively. The rate of this background is  $\approx 10^4$  times higher than the rate of events coming from the proton electron interactions. The trigger system is operating in several levels in order to filter interesting physics events [59].

### 2.2.5.1 The First Trigger Level

The first trigger level (L1) makes a decision within  $2.3 \mu\text{s}$  on whether to accept or reject an event using the information provided by the different L1 trigger elements (TE). The central trigger logic (CTL) combines these TE into 128 subtriggers. Not all subdetectors can provide this information fast enough to make a decision after each bunch crossing immediately. Therefore the information is sent into pipelines where it is kept until all subdetectors have provided their trigger elements. After 24 bunch

crossings ( $2 \mu\text{s}$ ) the trigger elements are linked logically and the L1 decision is made whether an event is rejected or accepted. If any of the subtrigger conditions is fulfilled by the event, the pipeline is stopped immediately and the signal is passed to the next trigger level [60].

The trigger elements used in this analysis are described in the following.

### The LAr Calorimeter Trigger Elements

The LAr calorimeter provides signals to the central trigger which are used for the triggering of NC events [61]. The analog signals of the neighbouring "trigger towers" (TT) are summed and then digitised using FADCs (flash analog to digital converter). These FADCs are then summed into "Big-Towers" (BTs). Several thresholds are introduced to suppress noise and background, there are so-called AGM-thresholds for the sum of the analog signal and the BT-threshold for summing the digitised signals into big-towers.

The LAr calorimeter trigger elements used in this analysis are:

- **LAr\_electron\_1 and LAr\_electron\_2:** The LAr\_electron TEs are set if the energy in one of the trigger tower exceeds a corresponding threshold value. LAr\_electron\_1 and LAr\_electron\_2 have different thresholds, in the CB and FB region the thresholds are set to about 5 GeV for LAr\_electron\_1 and to about 3.5 GeV for LAr\_electron\_2. In the IF region the thresholds are increased to 32 GeV because of the large beam induced background.
- **LAr\_Etmiss>1:** This TE is set if the missing transversal energy calculated from the BT-energies is above threshold:  $\sqrt{\sum_{BT} E_{BT,x}^2 + \sum_i E_{BT,y}^2} \gtrsim 6 \text{ GeV}$ .
- **LAr\_T0:** The LAR\_T0 provides a timing signal which is determined from the trigger tower signals. The signal of the trigger tower is copied with 500 ns delay. The crossing point of the delayed signal with the original signal determines the trigger tower  $T_0$ . These are combined into the big tower  $T_0$ . The LAR\_T0 is set when a signal in at least one TT exceeds  $T_0$  threshold.
- **LAr\_BR:** The LAr-BigRay TE combines the measurement in one LAr trigger tower and a "ray" information from MWPC-trigger. If the trigger tower exceeds 1 GeV and it is matched in azimuthal and polar angle with a ray from MWPC-trigger this TE provides a signal.

### The Track Trigger Elements

The tracking chambers CJC, CIP/COP and CIZ/COZ all provide information to the CTL:

- **zVtx\_T0, zVtx\_T0\_nextbc and zVtx\_sig>1:** These trigger elements are based on signals from the multi-wire proportional chambers. The MWPC (CIP and COP) send a timing signal when at least one track candidate is found: the zVtx\_T0 is set. The zVtx\_T0\_nextbc is set when MWPC (CIP and COP) send the signal in the next bunch crossing. The zVtx\_sig>1 is set when a vertex can be reconstructed from track candidates.
- **FwdRay\_T0:** This trigger element is similar to zVtx\_T0, but the signal is formed in the FWPC. It is usually used in combination with the zVtx\_T0, the logical OR of these two conditions is called Ray\_T0.
- **DCRPh\_T0 and DCRPh\_Tc:** The  $r\phi$ -trigger makes use of the timing signals from CJC.

### The Veto Conditions

Veto conditions are applied to a large number of subtriggers. They mainly reject the background from beam-gas and beam-wall interactions.

- **Veto-Wall, Forward-ToF, VLQ-ToF:** These scintillators have a very good time resolution and are therefore used to reject beam induced background arriving out-of-time in the detector.
- **RZ-Veto:** Uses information from CIZ and COZ and rejects events for which a vertex is not reconstructed in the region of the nominal vertex position.
- **CIP\_noSPCL and SpaCal-ToF:** The "CIP backward veto and no SpaCal energy" recognises events in which there is no energy deposit in the SpaCal but there is high track multiplicity in the backward region of the CIP. The SpaCal-ToF rejects events in which the energy in the SpaCal is deposited in a time window which does not coincide with the interaction.

#### 2.2.5.2 The Second and the Third Trigger Level

More complex decisions than the first level of the triggering system can be taken at the second level (L2), since here not only trigger elements are available, but also the detailed information which was used to compile them. On L2 the decision is made within 20  $\mu$ s using two independent trigger systems, topological triggers [62] and neural network [63]. Both triggers provide their decision in form of L2 subtriggers. A list of L1 subtrigger is assigned to every L2 subtrigger, which need to fire in coincidence, thus validating the L1 subtrigger. The third trigger level (L3) allows further requirements to be placed on an event within a time of 20  $\mu$ s but has not yet been used.



### 2.2.5.3 The Forth Trigger Level and the Event Reconstruction

On L4 all detector information is available. It is stored in a buffer, which can hold up to 30 events, which are asynchronously processed by a farm of PowerPC computers, so that the time of processing does not contribute to the dead time of the detector. The computers reconstruct parts of the event and recalculate the decisions of previous trigger levels that can be overruled. The events are classified in an analysis dependent way according to their physics properties. Unclassified events are rejected and the selected events are written to a so-called Data Summary Tape (DST) which is the starting point for physics analysis. For monitoring purposes one out of 100 rejected events is written to a separate tape.

### 2.2.6 The NC Subtriggers

The triggering of NC events is based on the signature of high  $Q^2$  NC event in the detector, i.e. highly energetic scattered electron in the LAr calorimeter. The two trigger elements LAr\_electron\_1 and LAr\_electron\_2 are based on this condition. These trigger elements are combined with the timing information from the LAr calorimeter or the central and forward proportional chambers. A more detailed description of the trigger elements and the selection of NC triggers is given in [64]. The subtriggers used in this analysis are ST67, ST75, ST71, ST77<sup>1</sup>:

|              |   |   |
|--------------|---|---|
| <b>ST67:</b> | LAr_electron_1&&<br>((zVtx_T0  FwdRay_T0)  (LAr_T0&&!zVtx_T0_nextbc))&&<br>Veto-Wall&&Forward-ToF&&VLQ-ToF                                | energy criterium<br>time criterium<br>veto conditions   |
| <b>ST75:</b> | (LAr_electron_2&&DCRPh_THig)&&<br>(zVtx_T0) &&<br>Veto-Wall&&Forward-ToF&&VLQ-ToF&&RZ-Veto  | energy and track<br>time requirement<br>veto conditions |
| <b>ST71:</b> | (LAr_BR&&DCRPh_Tc&&(zVtx_sig>1))&&<br>(DCRPh_T0&&(zVtx_T0  FwdRay_T0))&&<br>(Veto-Wall&&Forward-ToF&&VLQ-ToF&&<br>CIP_noSPCL&&SpaCal-ToF) | track criterium<br>time criterium<br>veto conditions    |
| <b>ST77:</b> | (LAr_Etmiss>1)&&<br>((zVtx_T0  FwdRay_T0))&&<br>Forward-ToF&&VLQ-ToF&&RZ-Veto   | energy criterium<br>time criterium<br>veto conditions   |

The decision of subtrigger ST67 is based on the recognition of a local energy deposit through the LAr\_electron\_1 trigger element. Having a high energy threshold the rate

<sup>1</sup>Here && denotes logical AND, || is logical OR.

of this trigger element is low making possible to have for time criterium any of the T0 trigger elements from LAr calorimeter, forward or central tacking chambers. Since the proportional chambers have a better time resolution than the LAr calorimeter the time criterium of LAr calorimeter is valid only if the proportional chambers do not recognise the event in the next bunch-crossing.

The subtrigger ST75 combines the LAr\_electron\_2 trigger, which has in the central part of the LAr calorimeter a lower threshold than LAr\_electron\_1, with requirement that at least one track with high transverse momentum is found. The threshold for the transverse momentum of the track is 0.8 GeV. As time criterium only the zVtx\_T0 trigger element is used.

The subtrigger ST71 is a purely track and vertex trigger. The energy threshold of this subtrigger is 1 GeV, which is much lower than for this analysis interesting electron energy. Therefore as an additional condition it is required that zVtx\_sig>1 is set, that is that in central proportional chambers a track candidate is found. In addition, it is required that the trigger element zVtx\_T0 is set.

Although ST77 is based on the missing energy requirement via LAr\_Etmiss>1 it is efficient trigger for NC events. In the case when an electron energy exceeds the dynamic range of FADC this is interpreted as missing energy. The time criterium is a logical OR of T0 requirements from the forward and central proportional chambers.

All these subtriggers have in addition veto conditions (see section 2.2.5) which are used to reject beam-wall and beam-gas background.

The majority of events is triggered by ST67. The subtriggers ST71 and ST75 add mainly events with lower electron energy. ST77 is interesting as some of the veto options applied to other subtriggers are not present here.

## Chapter 3

# Monte Carlo Simulation

The cross section measurement requires corrections for acceptance, and the resolution of the detector components. Monte Carlo (MC) programs have been established as an important tool to determine these corrections. It is difficult to determine the corrections due to acceptance and smearing in the kinematic variables directly from data, because of the complexity and the correlations between different detector effects. For example, the acceptance depends on the radiative corrections. Therefore the Monte Carlo which includes this effect is used to unfold the cross section from the measured number of events. If the Monte Carlo describes data correctly in every respect the unfolding can be done by using bin-by-bin correction method (section 7.2). Thus the main emphasis in this analysis is to ensure that the detector is correctly simulated. The efficiency of the selection criteria, the detector calibration and the resolution are determined directly from data. When the discrepancy of simulation from data is observed the simulation is adjusted to model the data behaviour.

It is important to stress that the acceptance calculation for the inclusive DIS is almost independent of the choice of the underlying physics assumptions. This is related to the model independent definition of the kinematic variables and redundant information for the measurement of the event kinematics (section 4).

### 3.1 Generation of DIS Events

The deep inelastic scattering events are generated using the DJANGO program package [65]. DJANGO allows the simulation of the complete final state in deep inelastic  $ep$  scattering including electroweak radiative corrections of  $\mathcal{O}(\alpha)$ . The  $\mathcal{O}(\alpha)$  corrected cross section for  $ep \rightarrow e'X(\gamma)$  is generated using HERACLES [66]. The events generated by HEACLES are completely described by the flavour of the scattering quark and the four-momenta of the final electron, final quark and the potentially radiated photon. For the treatment of the QCD dynamics the program package LEPTO [67] is used.

LEPTO uses colour dipole radiation model [68] as implemented in the ARIADNE program [69]. The hadron fragmentation is modelled using the JETSET program package [70]. The parameters for the hadronisation process in JETSET are obtained from fits to  $e^+e^-$  data and are assumed to be the same in DIS.

The events are generated using the MRSH [71] parton density functions (PDF) and then reweighted according to H1 97 PDF Fit [32]. The H1 97 PDF Fit is a NLO-QCD fit performed using H1  $e^+p$  data [32] as well as data from fixed target experiments BCDMS [2] and NMC [3].

## 3.2 Generation of Background Events

For the measurement of DIS cross section it is important to estimate the contribution of non-DIS events which can have signatures in the detector similar to those of DIS events. The main background contribution to DIS arises from the following processes:

- **Photoproduction ( $\gamma p$ ):** Photoproduction is the most important background to the DIS process. This process is an electron-proton interaction at very low four-momentum transfer  $Q^2 \approx 0$  so that exchanged photon is quasi real. The electron is scattered through a very small angle such that it is not detected in the central part of the detector. The events in which electron is detected in the electron tagger (section 2.2.3) are marked as "tagged photoproduction events". The photoproduction events are generated by PYTHIA [72] using GRV LO parton densities for the proton and the photon [73].
- **Low  $Q^2$  DIS:** At DIS process with low four-momentum transfer  $Q^2 \lesssim 60$  GeV the electron is scattered through a small angle, such that it is detected by the backward calorimeter SpaCal (section 2.2.1.2). In the case when a particle from the hadronic final state is misidentified as an electron the event represents a background event to the high  $Q^2$  DIS process.
- **Elastic QED-Compton scattering ( $ep \rightarrow ep\gamma$ ):** The QED-Compton events are treated as background since the exchanged photon has a very small  $Q^2$ , but both the electron and photon can be scattered into the central part of the detector when the virtuality of intermediate electron is high. These events are used for a cross check of the electron energy calibration. For simulation of the QED-Compton process the MC generator COMPTON [74] is used.
- **Lepton-pair production:** The lepton-pair events represent a background to DIS when the produced lepton pair is  $e^+e^-$ :  $e^+p \rightarrow e^+pe^+e^-$  or  $e^+p \rightarrow e^+Xe^+e^-$ . Lepton-pair events are simulated using LPAIR-generator [75, 76].

Besides these  $ep$  induced background processes a significant background contribution arises from non- $ep$  induced background. Here the main sources are:

- 
- Interaction of the proton beam with gas particles or the beam pipe wall called "beam-gas" and "beam-wall" background, respectively
  - muons originating from cosmic rays
  - muons which are produced in beam-wall or beam-gas interactions far upstream of the H1-interaction zone and travel parallel to the beam axis, they are called "beam-halo-muons".

these events do not need to be simulated since they are rejected by the timing and vertex requirements and a special search algorithm developed for rejection of the remaining non- $ep$  background (section 5.9).

### **3.3 Simulation of the H1 Detector**

The detector response to the particles generated in an event is simulated in detail by the H1SIM-package [77] which is based on GEANT-program [78]. The parameters used by this program were determined in test beam measurements and optimised during  $ep$  data taking. For the simulation of the energy response of the calorimeters a fast parametrisation for the development of electromagnetic and hadronic showers as implemented in H1FAST [79,80] is used. Both data and simulated events are then subject to the same reconstruction program (H1REC) and the same analysis chain.

## Chapter 4

# Reconstruction of Kinematic Variables

The cross section determination relies on the precise reconstruction of the kinematic variables. Two kinematic variables are needed to describe the inclusive DIS process. For NC DIS events there are various methods for the reconstruction of the kinematic variables since there is redundant information on the reconstruction from both lepton and the hadronic final state. The choice of the reconstruction method determines the resolution, acceptance, the size of radiative correction as well as the precision of the reconstruction of the kinematic variables. Methods used for the reconstruction of the DIS kinematics are described in following.

### The Electron-method

In the so-called electron-method (e-method) [81] the kinematic variables are reconstructed using the energy  $E'_e$  and the polar angle  $\theta_e$  of the scattered electron:

$$Q_e^2 = 4E_e E'_e \cos^2 \frac{\theta_e}{2} \quad x_e = \frac{E'_e E_e \cos^2 \frac{\theta_e}{2}}{E_p (E_e - E'_e \sin^2 \frac{\theta_e}{2})} \quad y_e = 1 - \frac{E'_e}{2E_e} (1 - \cos \theta_e) \quad (4.1)$$

The resolution in  $x$  and  $Q^2$  as a function of energy and polar angle of scattered electron is given by:

$$\frac{dx_e}{x_e} = \frac{1}{y} \frac{dE'_e}{E'_e} + \tan \frac{\theta_e}{2} \left( x \frac{E_p}{E_e} - 1 \right) d\theta_e \quad \frac{dQ_e^2}{Q_e^2} = \frac{dE'_e}{E'_e} - \tan \frac{\theta_e}{2} d\theta_e \quad (4.2)$$

Due to the  $1/y$  dependence of  $\frac{dx_e}{x_e}$  the resolution in  $x$  is sufficiently good only for  $y$  close to unity. The resolution in  $Q^2$  is, however, excellent over the full kinematic range.

## The Hadron-method

For the hadronic final state the variables  $\Sigma$ , transversal momentum  $P_{T,h}$  and the inclusive hadron angle  $\gamma_h$  are defined by:

$$\Sigma = \sum_i (E_i - P_{z,i}) \quad P_{T,h} = \sqrt{\left(\sum_i P_{x,i}\right)^2 + \left(\sum_i P_{y,i}\right)^2} \quad \tan \frac{\gamma_h}{2} = \frac{\Sigma}{P_{T,h}}. \quad (4.3)$$

Here  $E_i$  and  $P_{z,i}$  are the energy and longitudinal momentum component, respectively, of particle  $i$ .  $P_{x,i}$  and  $P_{y,i}$  the transversal components of the particle momentum. The summation is performed over all hadronic final state particles. Using these variables the kinematic variables can be determined as follows:

$$y_h = \frac{\Sigma}{2 E_e} \quad Q_h^2 = \frac{P_{T,h}^2}{1 - y_h} \quad x_h = \frac{Q_h^2}{s y_h}. \quad (4.4)$$

The hadron-method (the  $h$ -method) [82] is used for the reconstruction of charged current DIS kinematics. For the measurement of NC DIS it is not used due to the degrading  $Q^2$ -resolution with increasing  $y$ :

$$\frac{\delta Q_h^2}{Q_h^2} \Big|_{P_{T,h}} \propto \delta P_{T,h} P_{T,h} \quad \frac{\delta Q_h^2}{Q_h^2} \Big|_{\Sigma} \propto \frac{\delta \Sigma}{1 - y} \quad (4.5)$$

With increasing  $y$  the term  $1/(1 - y)$  becomes increasingly important and severely degrades the resolution in  $Q^2$  and, consequently, in  $x$ .

## The $\Sigma$ -method

The  $\Sigma$ -method [83] makes use of both the electron and the hadronic final state variables:

$$y_{\Sigma} = \frac{\Sigma}{E - P_z} \quad Q_{\Sigma}^2 = \frac{(E'_e \sin \theta_e)^2}{1 - y_{\Sigma}} \quad x_{\Sigma} = \frac{Q_{\Sigma}^2}{s y_{\Sigma}} \quad (4.6)$$

with  $E - P_z \equiv \Sigma + E'_e(1 - \cos \theta_e)$ . In a fully hermetic detector  $E - P_z$  would be equal to twice the energy of incoming electron. The  $y$  and  $Q^2$  determination using this method are independent from the energy of the scattered electron and therefore less sensitive to the initial state radiation of the electron.

## The Electron- $\Sigma$ -method

The electron- $\Sigma$ -method (e $\Sigma$ -method) [84] combines the  $Q^2$  reconstruction from the e-method with the  $x$  reconstruction from the  $\Sigma$ -method:

$$Q_{e\Sigma}^2 = Q_e^2 \quad x_{e\Sigma} = x_{\Sigma} \quad (4.7)$$

and  $y$  is calculated according to

$$y_{e\Sigma} = \frac{Q_e^2}{x_\Sigma s} \quad (4.8)$$

The  $e\Sigma$ -method has good resolution in both  $x$  and  $Q^2$  over the full kinematic range accessible at HERA and is relatively insensitive to radiative corrections.

### The Double-Angle-method

An alternative method which may be used for the reconstruction of kinematic variables in NC DIS events is the Double-Angle-method (DA-method) [81] in which only the angles of the electron and the hadronic final state are used:

$$y_{DA} = \frac{\sin \theta_e \cdot (1 - \cos \gamma_h)}{\sin \gamma_h + \sin \theta_e - \sin(\theta_e + \gamma_h)} \quad Q_{DA}^2 = \frac{4 \cdot E_e^2 \cdot \sin \gamma_h (1 + \cos \theta_e)}{\sin \gamma_h + \sin \theta_e - \sin(\theta_e + \gamma_h)} \quad (4.9)$$

and  $x_{DA} = Q_{DA}^2 / (s \cdot y_{DA})$ . The resolution in  $x$  and  $Q^2$  is determined as  $\frac{\delta \theta_e}{\sin \theta_e} \oplus \frac{\delta \gamma_h}{\sin \gamma_h}$ . Therefore the resolution becomes worse at small and large angles of both the electron and the hadronic final state. It is good at medium  $y$  where all particles are well contained in the central detector.

This method is particularly useful for the calibration of the calorimeters since it is to first order independent of the calorimetric energy. The energy of the scattered electron determined using the DA-method is given by:

$$E_{DA} = \frac{2E_e \sin \gamma_h}{\sin \gamma_h + \sin \theta_e - \sin(\gamma_h + \theta_e)}. \quad (4.10)$$

The scattered electron energy determined in this way is used for the calibration as described in section 5.4



# Chapter 5

## Data Treatment

Precise measurement of the NC inclusive cross section requires a careful treatment of the data. In this chapter the scattered electron identification, measurement of the electron energy and angle, measurement of the hadronic final state properties and the position of the interaction vertex are described. All these quantities are needed for accurate reconstruction of the DIS kinematics. In addition  $ep$  and non- $ep$  background rejection procedures are discussed.

Performance and efficiencies of different detector components are determined directly from data. This is used to adjust the simulation so that MC describes the data behaviour in any respect essential for the analysis. In order to have a good description of the data in the simulation it is also important to model the time dependence of the detector status during the whole running period.

### 5.1 Electron Identification

In the high  $Q^2$  analysis presented here only events with the electron scattered into the LAr calorimeter are considered. The electron identification algorithm is based on properties of electromagnetic shower development in the LAr calorimeter supplemented by information about charged particle trajectories in the H1 tracking system.

#### 5.1.1 Electron Cluster in the LAr Calorimeter

The scattered electron produces an isolated and compact energy deposit (cluster) in the LAr calorimeter. These clusters are found using the QECFWD algorithm [85]. Electron candidates are identified using the information provided by estimators which are related to the shape and size of the electromagnetic shower profile. The estimators used in QECFWD together with the identification criteria are listed in table 5.1.

| Estimator | description   | cut value  |
|-----------|---|--|
| ETOT      | total cluster energy  | $> 3$ GeV  |
| NCEL      | number of cells assigned to electron candidate                | $> 3$  |
| EAEM      | energy fraction in the first 2 (in IF 3) layers of EM section | $> 0.94 + 0.05 \cos(2\theta_e)$<br>in the crack regions $> 0.90$                         |
| EAHN      | hot core fraction (4 hottest cells)                           | $> 0.4 - 0.8$ in fwd - bwd reg.  |
| EATR      | transverse dispersion   | $< 3 - 7.5$ in fwd - bwd reg.  |
| EAIFF     | energy fraction in isolation cone $R = 0.25$                  | $> 0.98$ or<br>$> 0.95$ and $E_{had}^{konus} < 300$ MeV<br>in the crack regions $> 0.90$ |

**Table 5.1:** Estimators and identification criteria used in the electron finding algorithm QECFWD.

For an electron energy measurement all cells in the electromagnetic section and in the first layer of hadronic section, which are inside the shower envelope, are considered. The shower envelope is defined by a cone of  $7.5^\circ$  from the interaction vertex around the centre of gravity of the cluster. The estimators EAEM, EAHN and EATR ensure early development and compactness of the cluster. EAEM is the energy fraction in the first two (in IF three) layers of the electromagnetic section, EAHN is the fraction of energy in the four hottest cells and EATR is the transverse dispersion of the cluster. The estimator EAIFF ensures that the cluster is isolated and not belonging to a hadronic shower. For the calculation of EAIFF all energy depositions around the centre of the cluster within a cone of  $R = \sqrt{(\eta_{clus} - \eta_{cell})^2 + (\phi_{clus} - \phi_{cell})^2} = 0.25$  are summed<sup>1</sup>.

When an electron impact point on the surface of the LAr calorimeter  $z_{LAr}$  is close to a  $z$ -crack between wheels or to a  $\phi$ -crack between octants, the electron energy can be shared between different wheels/octants and partially lost in the dead material of the crack. This causes an inefficiency of the identification algorithm in these regions. To avoid that the estimators EAEM and EAIFF are relaxed in the forward crack regions<sup>2</sup>. The  $z$ -crack between CB1 and CB2<sup>3</sup> and  $\phi$ -cracks<sup>4</sup> are excluded from the analysis.

If more than one electron candidate exists in an event the scattered electron is taken to be the cluster with the highest transverse momentum.

### 5.1.2 Electron Cluster Identification Efficiency

It is important to check whether the efficiency for finding electrons in the data is well described by the simulation. The electron finding efficiency is examined using events rejected by only one criterium of QECFWD and accepted by the others, as described

<sup>1</sup>Here,  $\eta$  is the pseudorapidity defined as  $\eta = -\ln \tan \frac{\theta}{2}$  and  $\theta$  is the polar angle.

<sup>2</sup>Forward cracks:  $z_{LAr} > 260$  cm and  $\theta_{el} > 19^\circ$ ;  $80$  cm  $< z_{LAr} < 120$  cm.

<sup>3</sup> $z$ -crack between CB1 and CB2:  $15$  cm  $< z_{LAr} < 25$  cm.

<sup>4</sup> $\phi$ -cracks:  $|\phi_e - n \cdot 45^\circ| < 2^\circ$ ,  $n = 0, 1, \dots, 7$

in [64]. The  $z_{LAr}$  distribution for these events is shown in figure 5.1(b). The  $z_{LAr}$  distribution of events accepted by QECFWD is shown in 5.1(a) and the fraction of rejected events is presented in figure 5.1(c). Only 1% of the events are rejected by only one criterium at low  $z_{LAr}$  and 2 – 4% at larger  $z_{LAr}$ . The simulation gives good description of the data within an uncertainty of 0.5% for  $z_{LAr} < -5$  cm and 2% for  $z_{LAr} > -5$  cm. This study of efficiency was cross checked using an electron finder based purely on track information [86].

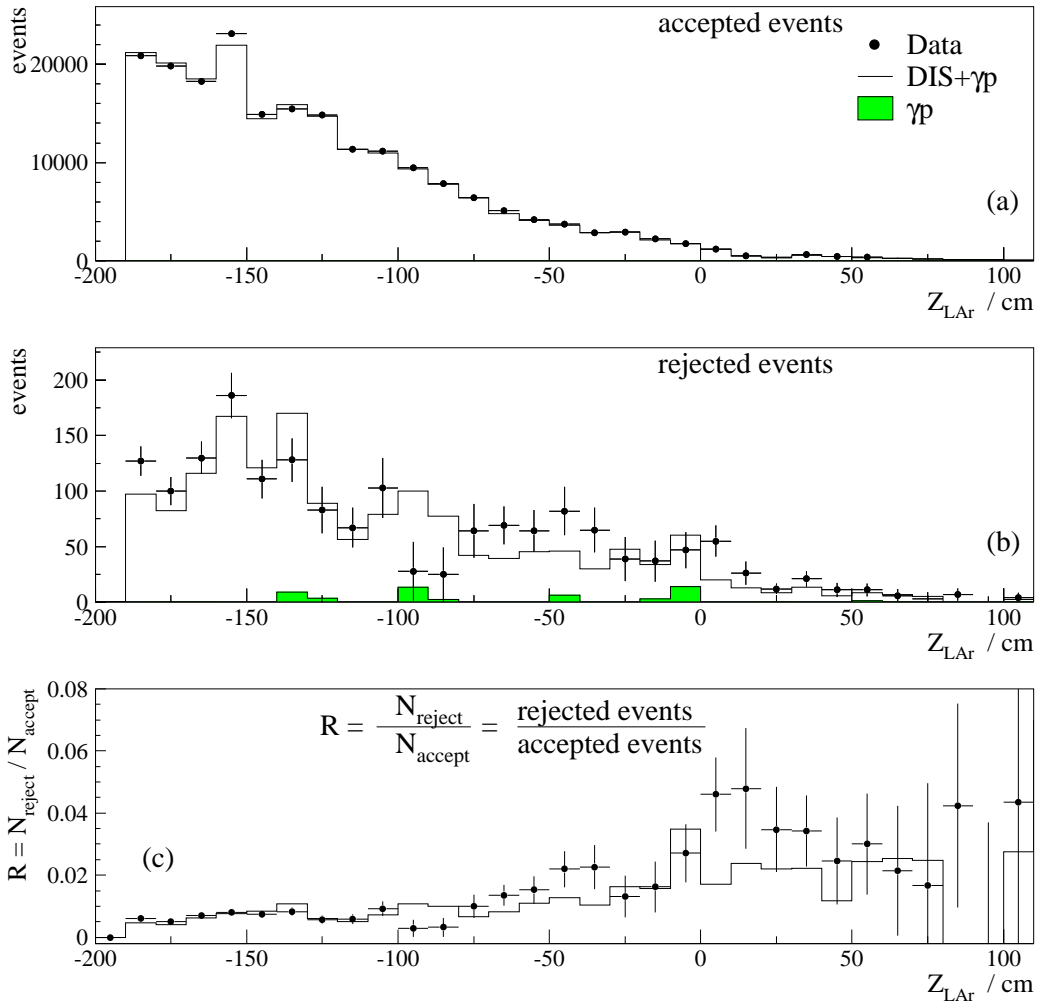


**Figure 5.1:** The  $z_{LAr}$  distribution for scattered electron candidates accepted by QECFWD algorithm (a) and for candidates rejected by only one criterium of the QECFWD algorithm (b). The ratio of rejected and accepted candidates is shown in (c).

### 5.1.3 Validation of Electrons Using Track Information

For the validation of the electron finding, information about the charged particle trajectory in the H1 central tracking system is used. Because of the geometrical acceptance of the central tracker the validation is applied only for electrons with polar angle  $\theta_e > 35^\circ$ . In the validation procedure the tracks fitted to the interaction vertex (DTRA tracks) and tracks which are not connected with it (DTNV tracks) are used.

The track-cluster matching procedure is the following:

- First DTRA tracks are extrapolated into the LAr calorimeter. Among all DTRA tracks the one with the smallest distance of closest approach to the centre of gravity of the electron cluster is considered. If this distance is less than 12 cm the track is assigned to the cluster.
- If a DTRA track is not assigned to the cluster, the DTNV tracks are checked. A distance of closest approach for a DTNV track is defined as the perpendicular distance between the cluster centre and the line connecting the interaction vertex and the end point of the DTNV track. If this distance is less than 20 cm the track is assigned to the cluster.

In the *high y* analysis ( $E'_e \lesssim 11$  GeV, see section 6.4) only electron candidates validated by a vertex fitted track (DTRA) are accepted.

### 5.1.4 Efficiency of Electron Validation

The efficiency of electron validation using track-cluster matching is determined from data. The measured inefficiency is propagated to MC to model the data behaviour.

For the efficiency determination the final NC sample (see section 6.3) is used. In order to reduce the background contribution, namely photoproduction, the cut on electron energy is increased,  $E'_e > 18$  GeV, and stronger cuts in longitudinal and transversal momentum conservation are imposed,  $45 < E - P_z < 80$  GeV,  $0.5 < P_{T,h}/P_{T,e} < 1.2$ .

The efficiency of electron validation by DTRA tracks as a function of  $\theta_e$ , shown in the figure 5.2(a), is about 97% with the uncertainty of 1%. The efficiency of finding DTNV track for electron candidates, if a DTRA track is not found, shown in figure 5.2(b), is about 80%. In both cases the efficiencies are well modelled by MC. The validation efficiency is improved if both DTRA and DTNV tracks are used and the combined efficiency shown in figure 5.2(c) is better than 99%. The efficiency uncertainty in this case is 0.5%.

The combined efficiency as function of  $\phi_e$  is shown in figure 5.2(d). The drop of efficiency in the range  $188^\circ < \phi_{el} < 275^\circ$  is caused by broken wire in CJC at the

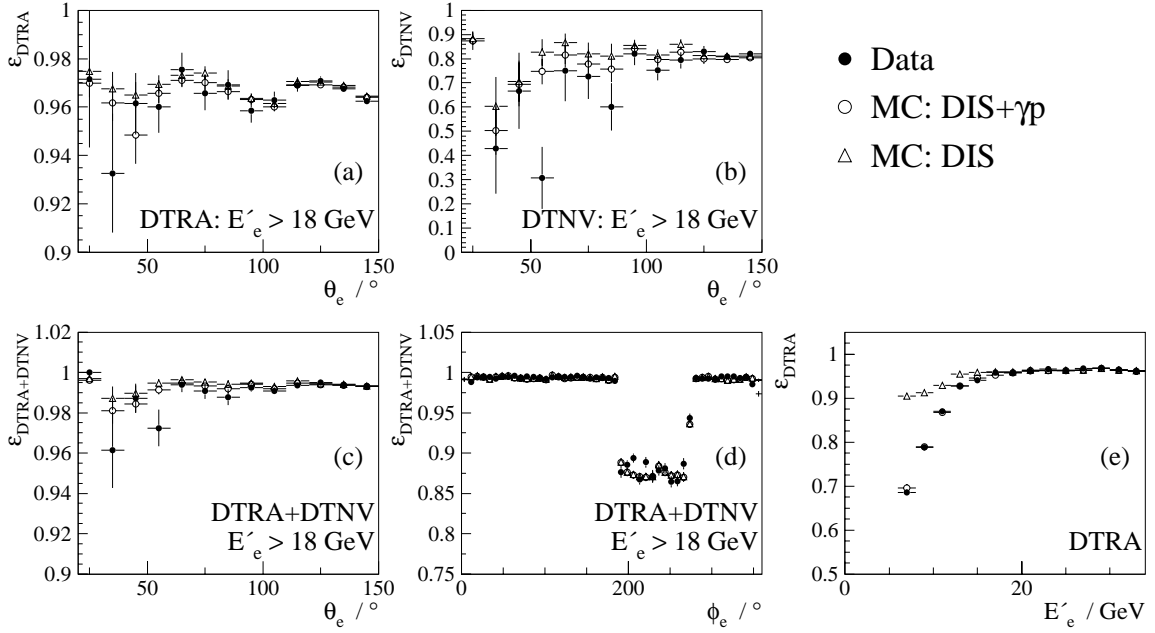


**Figure 5.2:** Efficiency of finding DTRA track (a) and DTNV track if no DTRA is found (b) as a function of polar angle  $\theta_e$ . Combined efficiency of DTRA and DTNV tracks as function of  $\theta_e$  (c) and  $\phi_e$  (d). The drop of efficiency in (d) is caused by a broken wire in CJC. Figure (e) shows the energy dependence of DTRA efficiency.

end of the data taking in 1999. For this time period corresponding track information is suppressed both in data and simulation<sup>5</sup>. All other distributions in figure 5.2 are presented with this  $\phi$  region included only for time period when it was active.

Figure 5.2(d) shows the DTRA finding efficiency as function of the scattered electron energy. The efficiency in the signal (DIS) MC is almost energy independent. A slight decrease of efficiency at low energy is related to the situation when instead of a true electron a hadron is chosen as an electron candidate. The decrease is much more pronounced in the data. It is very well reproduced by MC when the photoproduction background is included in the simulation. This gives confidence in a good understanding of the track finding efficiency down to the lowest electron energies and in the good control of the photoproduction background rejection power of the the cluster-track matching validation.

<sup>5</sup>In simulation this is done for the fraction of luminosity corresponding to the running period with broken wire (see section 5.7).

## 5.2 Interaction Vertex

For an accurate reconstruction of the event kinematics a precise knowledge of the position of the  $ep$  interaction point is needed. In particular the  $z$ -position of the vertex is directly used for the measurement of the polar angle of the scattered electron  $\theta_e$  based on the cluster information. It is therefore important that the vertex position is in detail described by MC. Furthermore it is important that the vertex reconstruction efficiency is well reproduced by the simulation.

### 5.2.1 Vertex Reweighting in the MC

During a luminosity fill the mean position and spread of the  $ep$  interaction points are defined by the beam optics. From fill to fill slight variations in the beam optics bring variations in the mean vertex position as shown in figure 5.3(a). Two periods with different  $\langle z_{vtx} \rangle$  are clearly visible ( $\approx -1$  cm and  $\approx 3$  cm) as indicated by lines in the figure.

The MC events are simulated with a  $z_{vtx}$  spread corresponding to a Gaussian distribution with mean  $\langle z_{vtx} \rangle_{mc} = 0$  and width  $\sigma_{mc} = 15$  cm. Figure 5.3(c) demonstrates that the MC events simulated in this way need additional adjustment to describe the data. Therefore the MC events are reweighted according to the  $z_{vtx}$  distributions obtained from the data.

The  $z_{vtx}$  reweighting of MC is done separately for the two periods (before and after luminosity fill 2360) with different  $\langle z_{vtx} \rangle$ . For each period the following procedure is applied. First all luminosity fills are grouped in ten bins corresponding to ten 2 cm wide slices (from -10 cm to 10 cm) in  $\langle z_{vtx} \rangle$ . For each slice the integrated luminosity,  $\langle z_{vtx} \rangle_{data}$  and  $\sigma_{data}$  from a Gaussian fit are determined using data. Then the MC events are distributed among the slices with a probability corresponding to the fraction of integrated luminosity in each slice. Finally, the MC events in the slice with measured  $\langle z_{vtx} \rangle_{data}$  and  $\sigma_{data}$  are reweighted using the following weights

$$w_{z_{vtx}} = \frac{\frac{1}{\sigma_{data}} e^{-\frac{(z_{vtx} - \langle z_{vtx} \rangle_{data})^2}{2\sigma_{data}^2}}}{\frac{1}{\sigma_{mc}} e^{-\frac{(z_{vtx} - \langle z_{vtx} \rangle_{mc})^2}{2\sigma_{mc}^2}}} \quad (5.1)$$

where  $z_{vtx}$  is the simulated vertex position in the MC event.

How this reweighting works on the slice by slice level is shown in figure 5.3(b). Figure 5.3(d) demonstrates that after applying reweighting procedure the  $z_{vtx}$  distribution for MC events reproduces all details of the data behaviour.

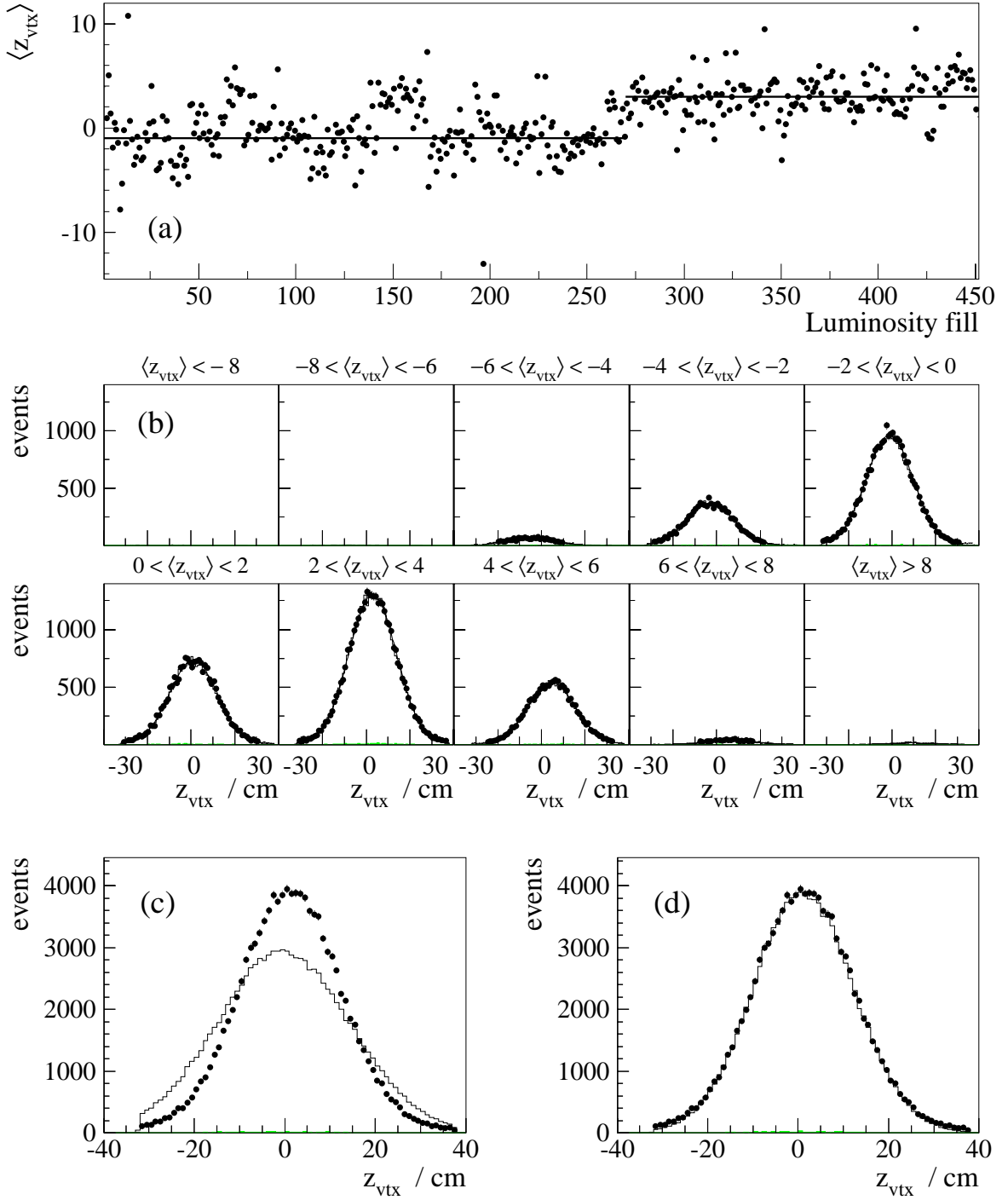


**Figure 5.3:** The variation of the  $\langle z_{\text{vtx}} \rangle$  as function of the luminosity fill (a). The lines indicate the change of the mean  $z$ -vertex position from  $\approx -1$  cm to  $\approx 3$  cm. The vertex distributions in different slices (see text) for data and MC summed over the two periods (b). The  $z_{\text{vtx}}$  distributions for data and MC before (c) and after reweighting (d).

## 5.2.2 Vertex Reconstruction Efficiency

In the vertex reconstruction procedure tracks related to the scattered electron and hadronic final state particles are used. In the analysis it is required that the vertex is reconstructed and its  $z$  position is within 35 cm around the mean value of  $z_{vtx}$  for the full running period  $\langle z_{vtx} \rangle = 2.8$  cm,  $|z_{vtx} - \langle z_{vtx} \rangle| < 35$  cm.

The vertex reconstruction efficiency based on tracks in the central chambers only ("central" vertex) is shown in figure 5.4(a) as function of the the inelasticity  $y$ . In general the efficiency is close to 100%. The decrease of efficiency at low  $y$  for the data is related to the fact that in this case the hadronic final state particles are fully contained in the forward region and the only track in the central chambers is the one from the scattered electron. This behaviour is not reproduced by MC, so the inefficiencies determined from the data are used to adjust the simulation, see figure 5.4(b).

The vertex reconstruction efficiency at low  $y$  is significantly improved if tracks in the central and forward chambers ("forward" vertex) are used in the vertex reconstruction. As shown in figure 5.4(c), the efficiencies in the data and MC are consistent and well above 99%.

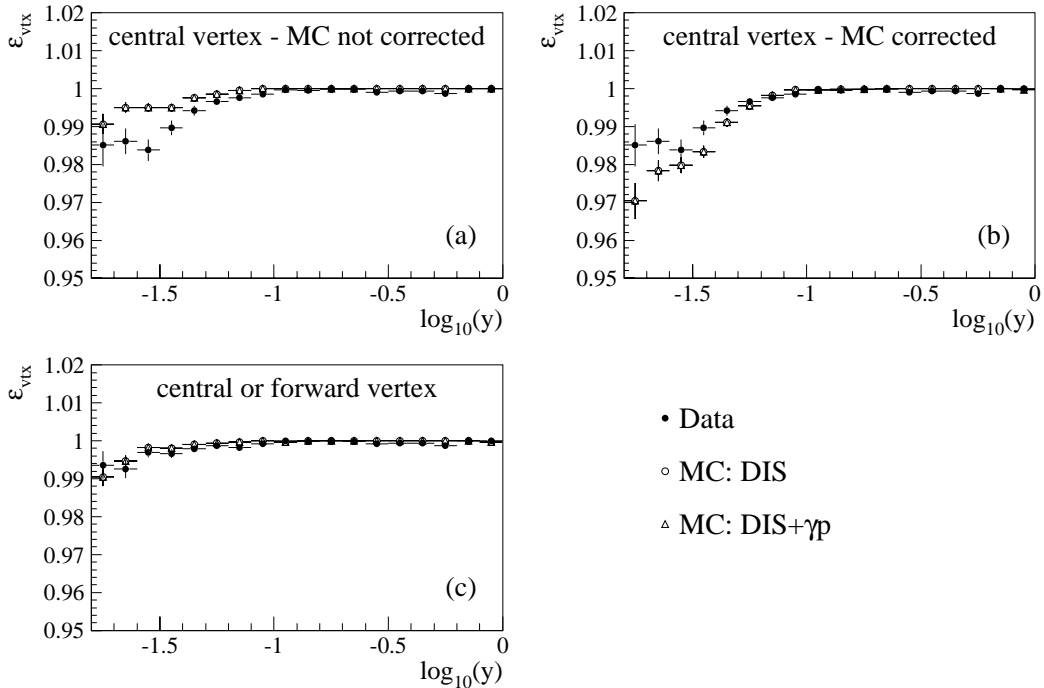


**Figure 5.4:** Efficiency of reconstruction of central vertex before (a) and after (b) adjustment of MC efficiency. The efficiency of reconstruction central or forward vertex (c) is well described by MC.



## 5.3 Electron Angle Measurement

The polar  $\theta_e$  and azimuthal  $\phi_e$  angles of the scattered electron in the interaction vertex can be derived from the parameters of the track associated with the electron (if it exists) or can be calculated from the positions of the electron cluster in the LAr calorimeter and the interaction vertex. For the latter case the LAr calorimeter has to be aligned with the tracking system which defines the H1 coordinates and position of the interaction vertex.

### 5.3.1 Alignment of the LAr Calorimeter

An alignment of the LAr calorimeter relative to the tracking system is performed comparing positions of the track and the cluster after their extrapolation into a reference plane. The reference plane is chosen to be in the depth of 5 cm inside the LAr calorimeter. In the  $x - y$  projection the reference surface has the shape of an octagon with an inner radius of 105 cm, while in the backward region  $z < -157$  cm the shape is a hexagon with the same radius. A projection of the cluster position is done along a straight line from the vertex to the cluster. The track is extrapolated taking into account a curvature in the magnetic field.

The alignment is performed in three steps. First the change of the LAr calorimeter dimensions (shrinkage) due to the low temperature of the liquid Argon is corrected for. Then the position of the LAr calorimeter is adjusted with respect to the H1 coordinate system. These two steps are performed only for the data. Finally for improvement of the LAr calorimeter based polar angle measurement an additional small correction on the  $z$  position of the cluster is applied both in the data and MC.

**Shrinkage of the LAr calorimeter.** The dimensions of the LAr calorimeter have been determined at room temperature. The working temperature of calorimeter is 72 K which causes shrinkage of the LAr calorimeter in the  $z$  direction

$$z_{cold} = 23.67 \text{ cm} + (z_{warm} - 23.67 \text{ cm}) \cdot (1 - 0.0027)$$

It corresponds to 0.7 cm shift in the IF region ( $z = 292$  cm).

**Rotations and shifts of the LAr calorimeter.** Three rotations and three shifts of the LAr calorimeter are defined in the following way:

rotations :

$$\begin{aligned} x_1 &= x_i & x_2 &= x_1 \cos \beta + z_1 \sin \beta & x_3 &= x_2 \cos \gamma - y_2 \sin \gamma \\ y_1 &= y_i \cos \alpha & y_2 &= y_1 & y_3 &= y_2 \cos \gamma + x_2 \sin \gamma \\ z_1 &= z_i \cos \alpha - y \sin \alpha & z_2 &= z_1 \cos \beta - x_1 \sin \beta & z_3 &= z_2 \end{aligned}$$

translations :

$$\begin{aligned} x_f &= x_3 + \Delta x & z_f &= z_3 + \Delta z & y_f &= y_3 + \Delta y \end{aligned}$$

|                         |                                 |
|-------------------------|---------------------------------|
| rotations:              |                                 |
| $\alpha = -0.12$ mrad   | around $x$ axis                 |
| $\beta = -0.24$ mrad    | around $y$ axis                 |
| $\gamma = +1.90$ mrad   | around $z$ axis                 |
| translations:           |                                 |
| $\Delta x = -0.0770$ cm | in $x$ direction                |
| $\Delta y = -0.0087$ cm | in $y$ direction                |
| $\Delta z = +0.2000$ cm | in $z$ direction (w/o CB2, CB3) |
| $\Delta z = -0.0500$ cm | CB2 ( $-60.0 < z \leq 25.0$ )   |
| $\Delta z = +0.3600$ cm | CB3 ( $-25.0 < z < 110.0$ )     |

**Table 5.2:** The parameters for the alignment of the LAr calorimeter.

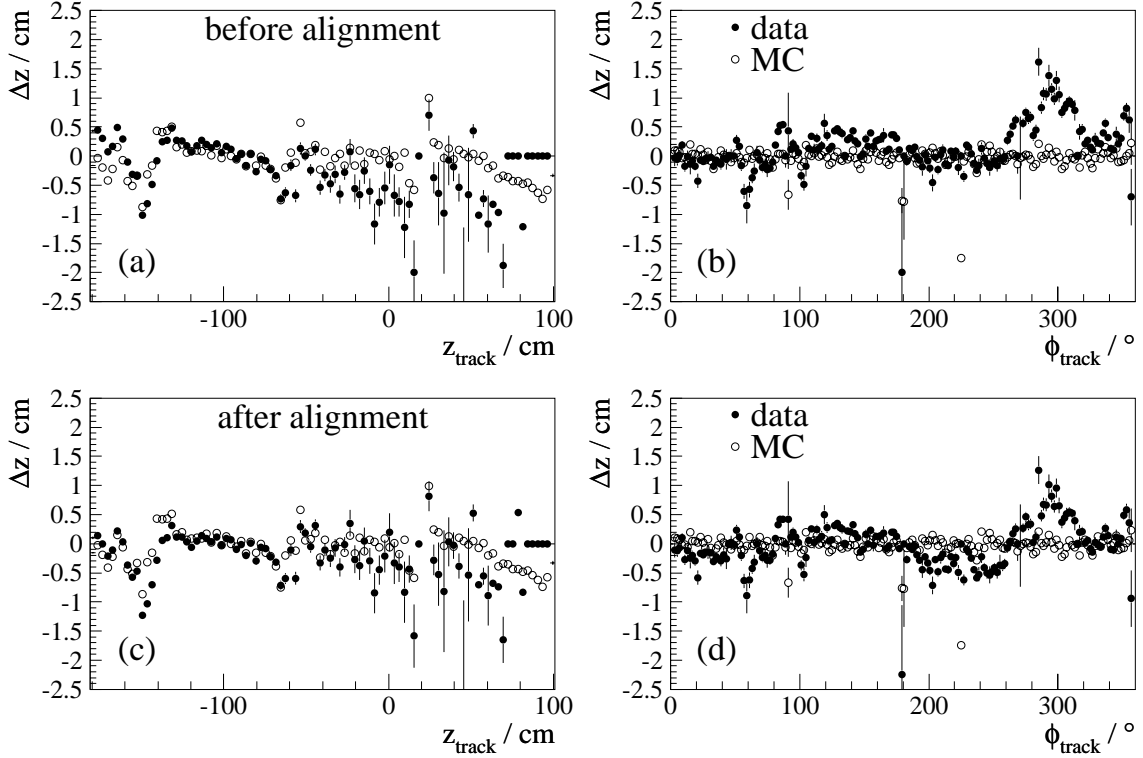


**Figure 5.5:** The difference of  $z$ -position of the impact point determined by the LAr calorimeter and the tracking system ( $\Delta z = z_{LAr} - z_{track}$ ) as function of  $z_{track}$  and  $\phi_{track}$  before, (a) and (b), and after alignment, (c) and (d).

Here,  $\alpha$ ,  $\beta$  and  $\gamma$  are the angles of rotation around the  $x$ ,  $y$  and  $z$  axis, respectively.  $\Delta x$ ,  $\Delta y$  and  $\Delta z$  are translations in  $x$ ,  $y$  and  $z$  directions.

The alignment constants are obtained by comparison of the extrapolations of track and cluster into the reference plane [35] and listed in table 5.2.

In figure 5.5 the effect of the alignment of the LAr calorimeter is shown. The figure shows the  $\Delta z$  difference between the  $z$  positions of track and cluster after extrapolation into the reference plane as functions of  $z_{track}$  and  $\phi_{track}$ .

**Correction of polar angle measurement.** In the MC study a small difference between generated electron polar angle and the polar angle calculated using the LAr calorimeter is observed, figure 5.6(a). After applying the following correction

$$z_{LAr}^{in} = z_{LAr} \cdot 1.006$$

both to the data and the MC, the  $\theta_e$  measurement using the LAr calorimeter is improved as can be seen in figure 5.6(b).

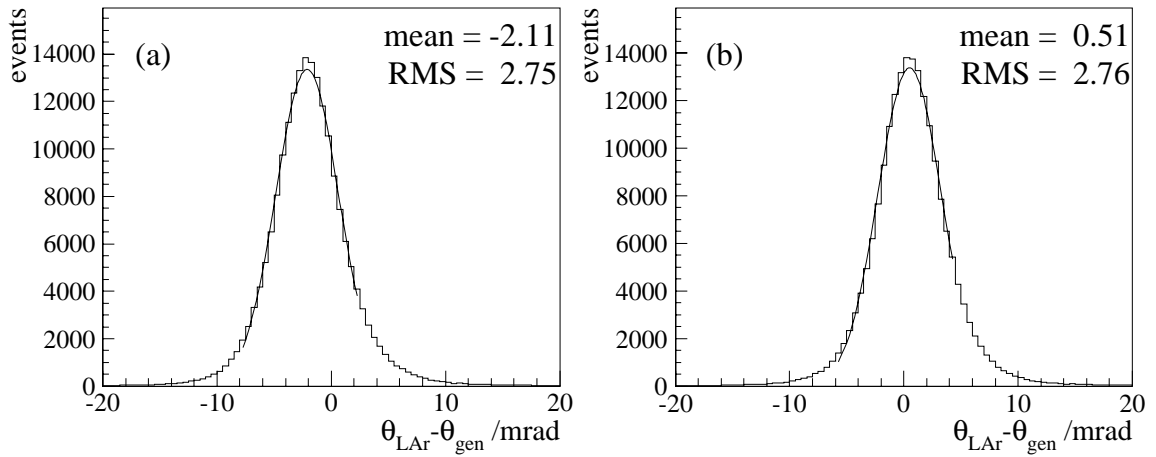


**Figure 5.6:** The difference between generated polar angle and polar angle calculated using the LAr calorimeter before (a) and after (b) applying correction.

### 5.3.2 Azimuthal and Polar Electron Angles

The most accurate measurement of the azimuthal angle  $\phi_e$  is provided by CJC which is optimised for  $r - \phi$  measurements. Therefore if a DTRA track is matched with the scattered electron  $\phi_e$  is taken from this track. When a track does not exist, the azimuthal angle is determined using positions of the cluster in the LAr calorimeter and of the interaction vertex.

The  $z$  information provided by CJC is poor and a polar angle measurement  $\theta_e$  is accurate only when the CJC information is combined with the one from CIZ and COZ. Figure 5.7 demonstrates the spread of the  $z$ -position of tracks after the extrapolation to the surface of the LAr calorimeter for all tracks (a) and for tracks with hits in CIZ and COZ (b). As a reference position the extrapolated position of the cluster is taken.

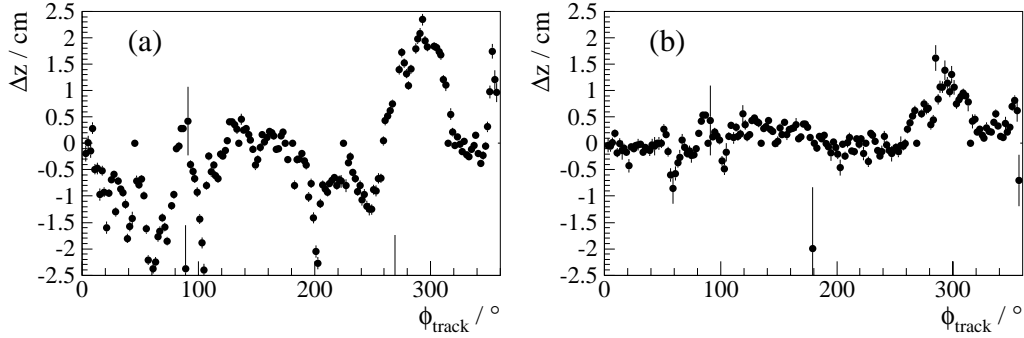


**Figure 5.7:**  $\Delta z = z_{LAr} - z_{track}$  as function of  $\phi_{track}$  for all tracks (a) and for tracks with hits in CIZ and COZ (b).

During 1999-2000 data taking, the CIZ and COZ chambers had unstable performance and low efficiency. For this reason in the the analysis presented here the polar angle is taken as it is calculated using the positions of the cluster and the interaction vertex.

Quality of the  $\theta_e$  determination is checked by comparison with the measurements done using only well measured tracks (with hits in CIZ and COZ). Figure 5.8 shows the average difference of the polar angle determined using the position of the cluster and as measured from the track. This difference is well reproduced in the simulation (solid line) within systematic uncertainty (dashed lines) of 1 mrad for  $\theta_e > 135^\circ$ , 2 mrad for  $120^\circ < \theta_e < 135^\circ$  and 3 mrad for  $\theta_e < 120^\circ$ .

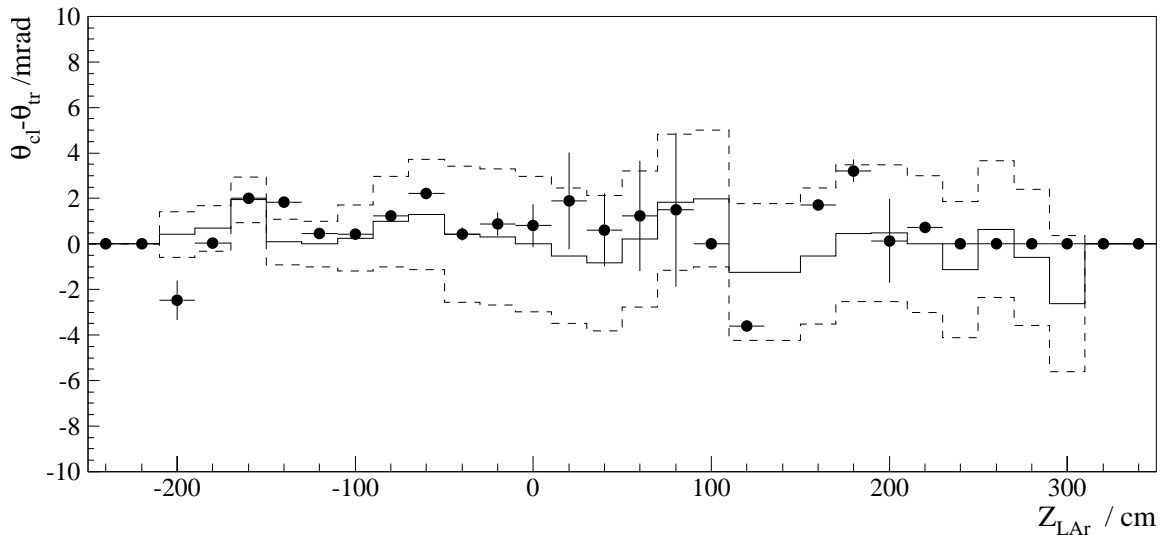


**Figure 5.8:** The average difference between  $\theta_e$  measurement using LAr calorimeter and tracks when at least one hit in CIZ and at least one hit in COZ is found. It is described by MC (solid line) within quoted uncertainty (dashed lines).

**Beam Tilt Correction.** The  $ep$  beam axis does not exactly coincide with the  $z$ -axis of the H1 coordinate system. The beam is inclined by a small angle  $\alpha_x$  ( $\alpha_y$ ) in  $x$  ( $y$ ) direction, so-called “beam tilt”. Figure 5.9 shows these angles as function of time. For the final calculation of the polar and azimuthal angles of the electron this difference between beam axis and the H1 coordinate system has to be taken into account.

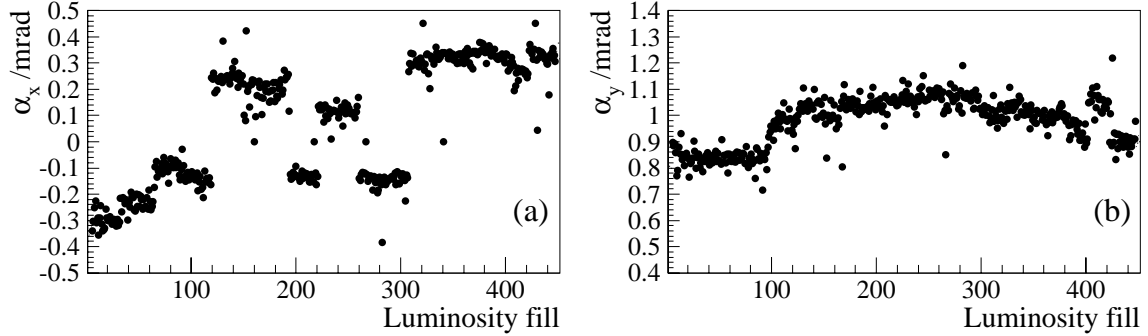


**Figure 5.9:** Beam tilt. The inclination of beam with respect to the H1 coordinate system in  $x$  (a) and  $y$  (b) direction .

For this purpose the tilted coordinate system  $(x', y', z')$  is defined with  $z'$ -axis in the direction of tilted beam. The position of electron  $(x_e, y_e, z_e)$  in the original  $(X, Y, Z)$  coordinate system is then projected into tilted coordinate system  $(x'_e, y'_e, z'_e)$  and the final angles are determined as  $\theta_e = \text{arctg} \left( \frac{z'_e}{\sqrt{x_e'^2 + y_e'^2}} \right)$  and  $\phi_e = \text{arctg} \left( \frac{y'_e}{x'_e} \right)$ .

## 5.4 Electron Energy Measurement

In the NC interactions both the scattered electron and the hadronic final state are measured in the H1 detector. This means that the system is over-constrained and different methods can be used for the reconstruction of the event kinematics (see section 4). The DA method (eq. 4.10) does not rely on the calorimetrically measured energies. Therefore it can be used for the calibration of the calorimeter response.

The calibration is performed separately for the data and MC.

### 5.4.1 Electron Energy Calibration

For the electron energy calibration the cluster energy in the LAr calorimeter is compared to the electron energy calculated in the DA method (eq. 4.10). To ensure sufficient precision of the DA method only the following part of the phase space is

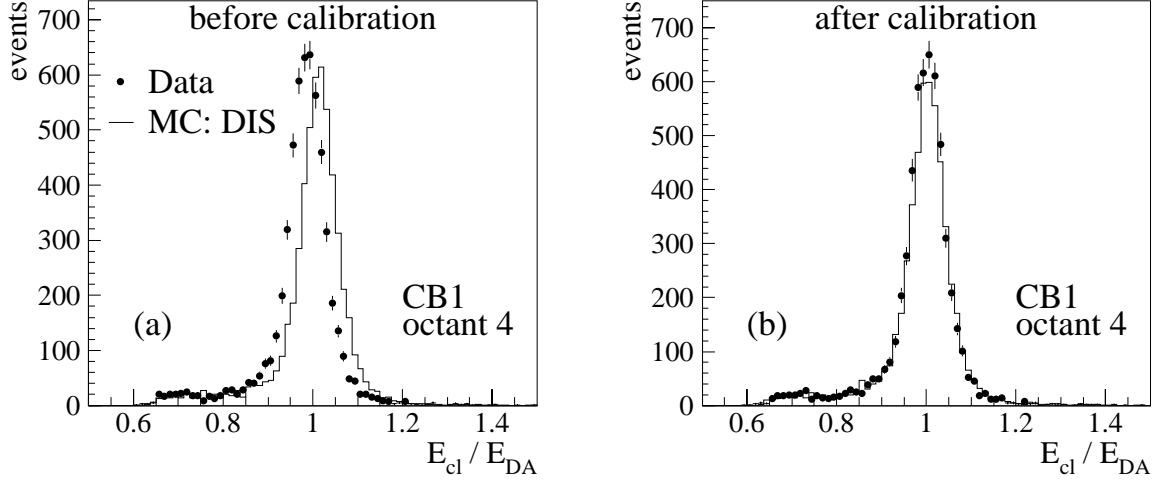


**Figure 5.10:** The ratio of the scattered electron energy measured in the LAr calorimeter and electron energy calculated using DA method before (a) and after (b) calibration.

used  $\gamma_h > 10^\circ$ ,  $y_\Sigma < 0.3(0.5)$  for  $\theta_e \geq 80^\circ (< 80^\circ)$  and  $E'_e > 14$  GeV. All the other selection criteria are as described in section 6.

Figure 5.10(a) shows the ratio  $E_{cl}/E_{DA}$  for octant 4 of CB1 before calibration. Calibration factors  $f_{cal}$  are determined from the  $E_{cl}/E_{DA}$  distributions as  $f_{cal} = 1/\langle E_{cl}/E_{DA} \rangle$ . In order to reduce the influence of tails in the distributions only events with  $0.8 < E_{cl}/E_{DA} < 1.2$  are considered in the averaging.

As a starting point for the present analysis the energy calibration obtained for data collected in 94-97 [32, 35, 87] is used. Further calibration is performed in five steps:

- **The wheel- and octant-wise calibration.** In BBE, CB1 and CB2 the calibration factors are determined for each octant. Because of limited statistics for wheels CB3 and FB only one calibration factor per wheel is determined. Figure 5.11(a) shows the inverse calibration factors as function of module number  $I_{module} = 8 \cdot I_{wheel} + I_{octant}$ .
- **The  $z$ -wise calibration.** Further calibration factors are determined as function of the  $z$  position of the electron impact point in the LAr calorimeter  $z_{LAr}$ . The factors are determined in 1 cm bins for  $z_{LAr} < 0$  and 10 cm bins for  $z_{LAr} > 0$ . Figure 5.11(b) shows the inverse calibration factors as function of  $I_Z$ :

$$I_Z = \begin{cases} 200 + \text{int}(z_{LAr}) & \text{for } -200 \text{ cm} < z_{LAr} < 0 \\ 200 + \text{int}(z_{LAr}/10) & \text{for } z_{LAr} > 0 \end{cases} .$$

- **The  $\phi$ -wise correction.** In this step local effects in  $\Delta\phi_{oct}$  are checked and corrected for.  $\Delta\phi_{oct}$  is defined as the  $\phi$  angle between electron impact point and

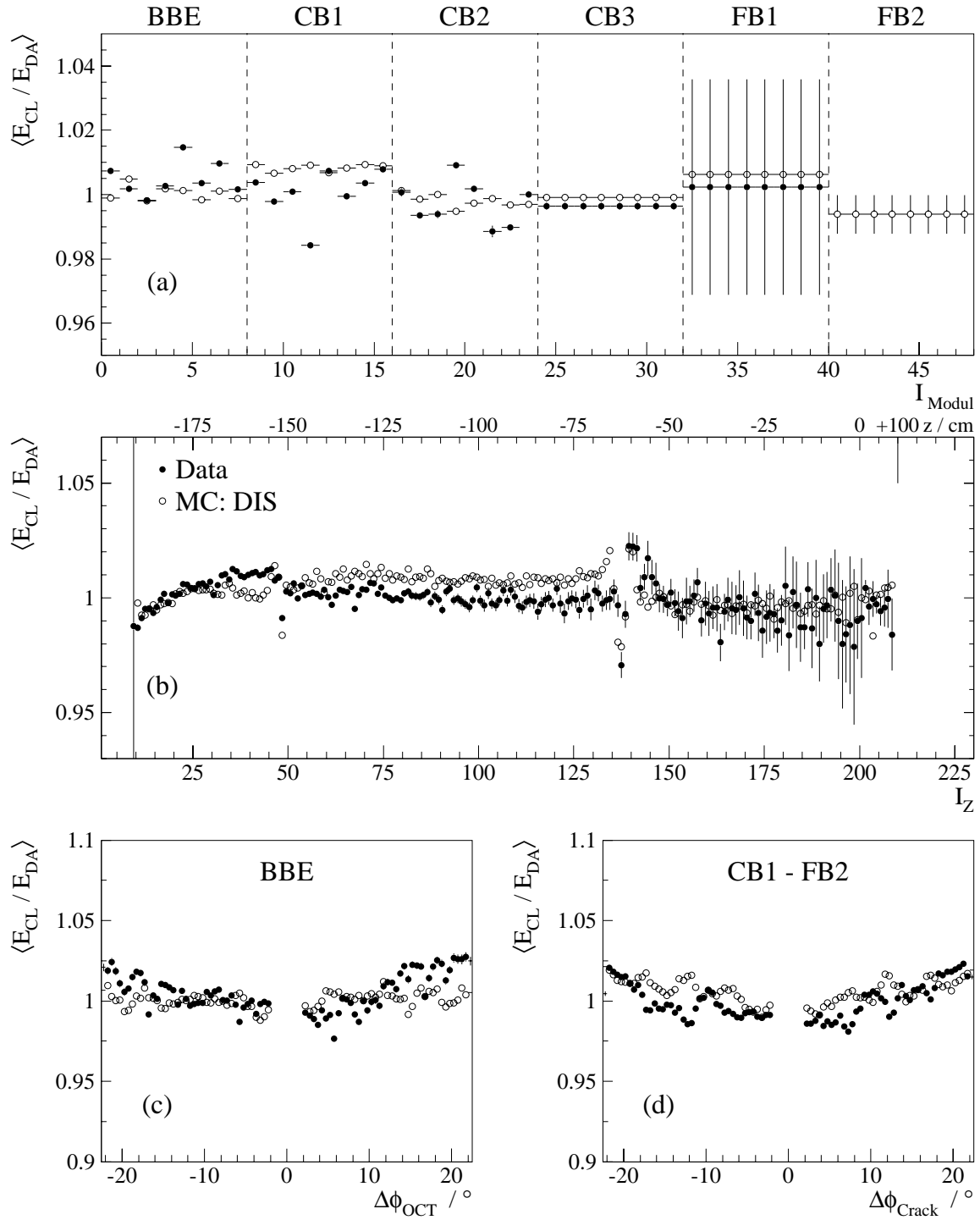


**Figure 5.11:** Electron energy measurement before calibration. Mean values of the ratio  $\langle E_{cl}/E_{DA} \rangle$  as function of module number (see text) (a) and the  $z$  position of electron impact point (b). The ratio  $\langle E_{cl}/E_{DA} \rangle$  as function of  $\phi$  angle between electron impact point and closest crack for BBE (c) and CB1-FB2 (d).

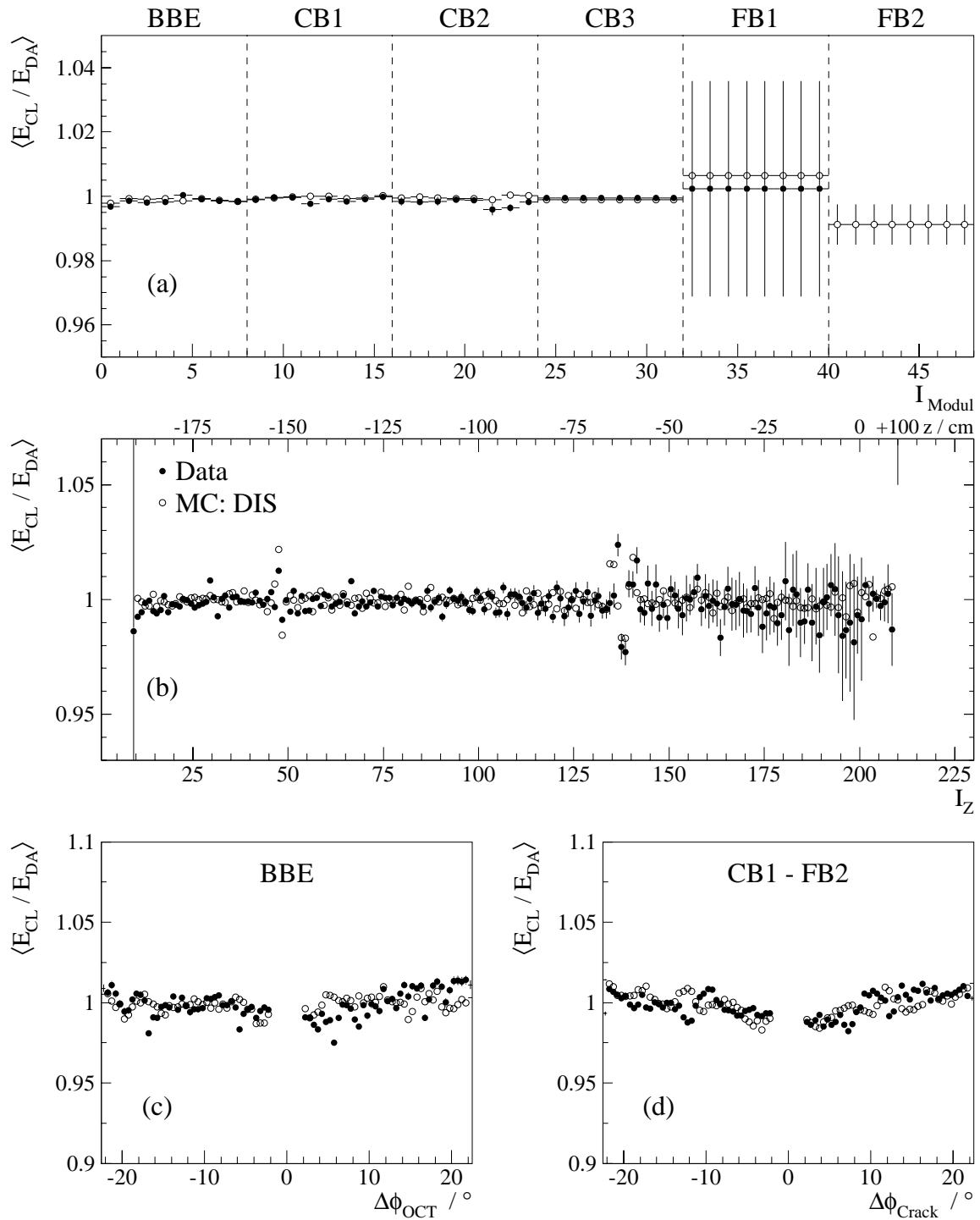


**Figure 5.12:** Electron energy measurement after calibration. Mean values of the ratio  $\langle E_{cl}/E_{DA} \rangle$  as function of module number (see text) (a) and the  $z$  position of electron impact point (b). The ratio  $\langle E_{cl}/E_{DA} \rangle$  as function of  $\phi$  angle between electron impact point and closest crack for BBE (c) and CB1-FB2 (d).



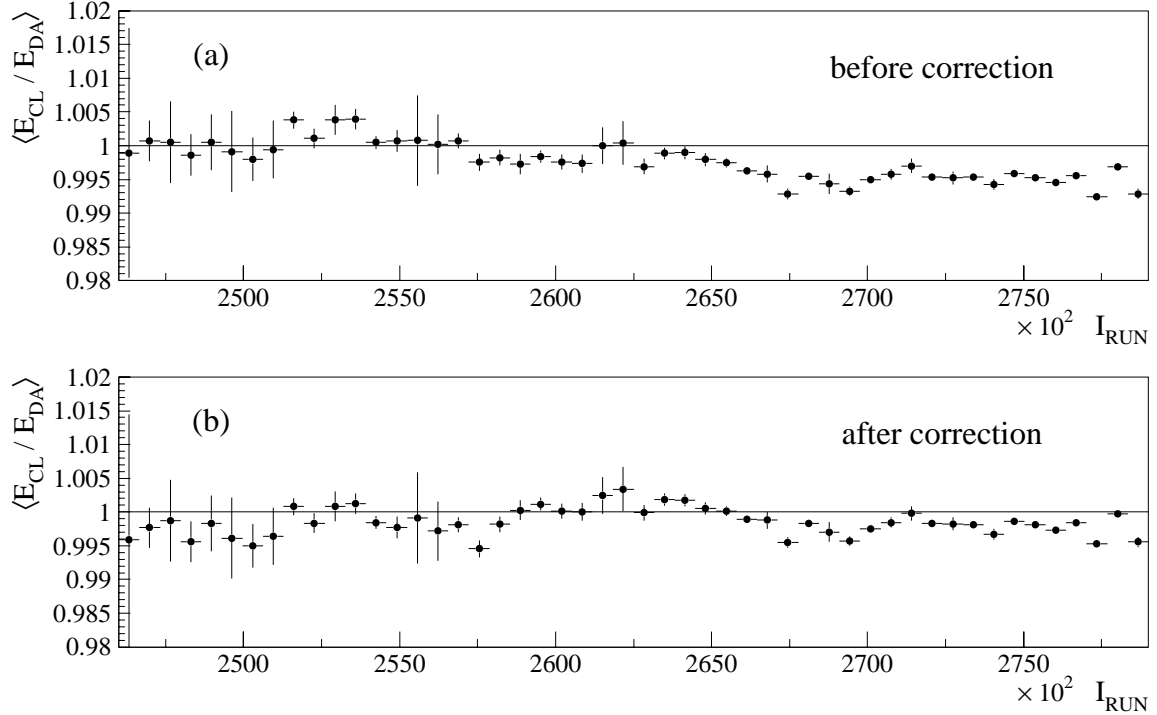


**Figure 5.13:** The ratio  $E_{cl}/E_{DA}$  as function of run number before (a) and after (b) applying time dependent correction.

the closest border between the octants. The corrections applied are  $-1\%$  for  $\Delta\phi_{oct} < -14^\circ$  and  $\Delta\phi_{oct} > 12^\circ$  in BBE and  $-1.5\%$  for  $|\Delta\phi_{oct}| < 18^\circ$  in CB1 to FB2. The effect of this correction can be seen by comparing figure 5.11(c,d), before correction, and figure 5.12(c,d), after correction.

- **The time dependent correction.** The time dependence of the calorimeter energy response is checked. The dependence observed in CB1 (see figure 5.13) is corrected multiplying the electron energy by the factor of 0.997 for the first part of the data taking ( $I_{run} < 258062$ ) and by the factor of 1.003 for the second part of data taking ( $I_{run} > 258062$ ).
- **Final wheel- and octant-wise calibration.** Finally the procedure of first step, wheel- and octant-wise calibration, is repeated.

The ratio  $\langle E_{cl}/E_{DA} \rangle$  after calibration as function of  $I_{Module}$ ,  $I_Z$  and  $\Delta\phi_{oct}$  is shown in figure 5.12.

### 5.4.2 Electron Energy Resolution

In the test beam measurements at CERN [48] the energy resolution of the calorimeter is determined to be

$$\sigma(E)/E = 12\%/\sqrt{E/GeV} \oplus 1\%.$$

The accuracy of the DA method allows an investigation of the electron energy reso-

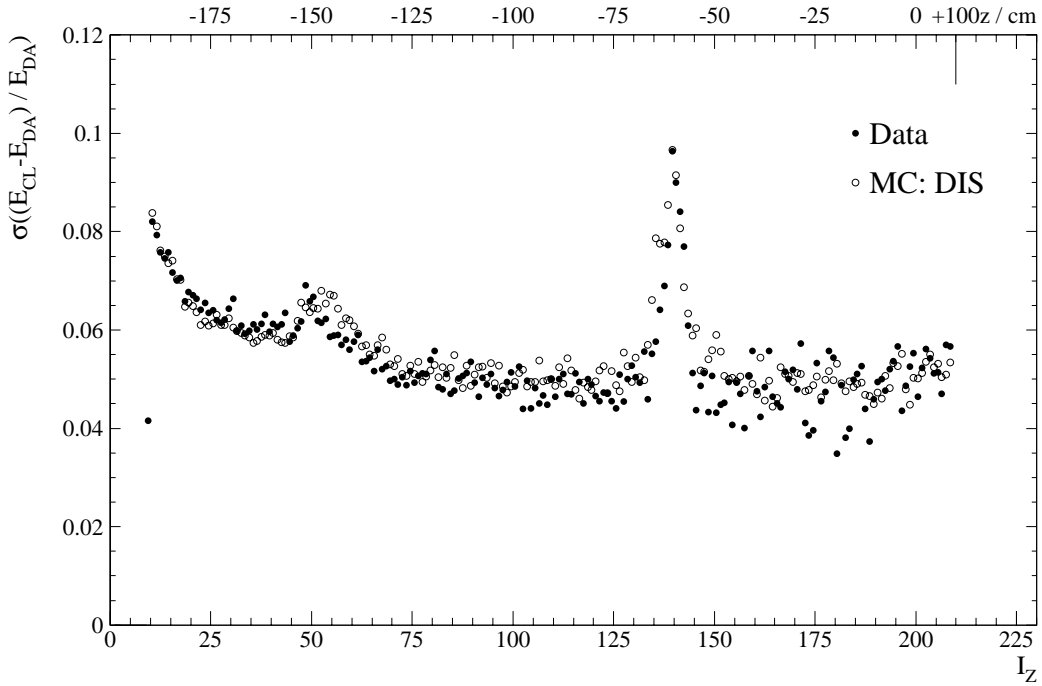


**Figure 5.14:** Resolution of the electron energy as function of  $z$ -position of impact point. The worse resolution at  $-60$  cm and  $-150$  cm

lution of the LAr calorimeter. The results are shown in figure 5.14. The resolution is between 4% and 10% ( $z = -60$  cm). The best resolution of  $\approx 4\% - 6\%$  is observed in the CB region. It is significantly worse in the BBE region where it reaches values higher than 8%. Also in the regions of  $z$ -cracks  $z \approx -60$  cm and  $z \approx -150$  cm the resolution is much worse compared to the rest of the CB region reaching values of 10%. The MC fully reproduces the data behaviour.

### 5.4.3 Cross-check of calibration with QED-Compton Events

The electron energy calibration is cross-checked using elastic QED Compton events. In this sample of events the final state consists of electron and photon only. From the measured electron and photon angles their energies are predicted by the double angle method and compared with calorimetrically measured energies.

The events with both particles scattered in the central region of the detector (LAr-LAr events) are limited to  $E_{e,\gamma} > 11$  GeV, on contrast to events with one particle in the central and one in the backward region of the H1 detector (LAr-SpaCal events) which can access the lowest energies used in this analysis ( $E_{LAr} > 6$  GeV). Therefore the LAr-SpaCal sample is of particular interest for checks of the calibration down to low energies<sup>6</sup>.

Elastic QED Compton events are selected by the following requirements [88–90]:

- Exactly two electromagnetic clusters are found.
- Neither additional energy is deposited in the LAr calorimeter nor in the SpaCal,  $E_{add} < 0.5$  GeV.
- The central vertex is reconstructed within 35 cm around the mean vertex position,  $|z_{vtx} - \langle z_{vtx} \rangle| < 35$  cm.
- The interaction time is within 10 ns from the nominal interaction time,  $\Delta T_{0_{cjc}} < 10$  ns.
- Due to transverse momentum conservation the two electromagnetic clusters are required to have back-to-back position in  $\phi$ ,  $\Delta\phi = |\phi_e - \phi_\gamma| = 180^\circ \pm 15^\circ$ .
- Due to longitudinal momentum conservation  $E - P_z$  is required to have a value close to  $2 \cdot E_e$ , i.e.  $45 \text{ GeV} < E - P_z < 65 \text{ GeV}$ .
- In the tracking chambers no track is found which cannot be assigned to electromagnetic clusters. Due to high photon conversion probability a track may exist also for the photon.
- $\left| \frac{E_{SpaCal} - E_{e,\gamma}^{DA}}{E_{e,\gamma}^{DA}} \right| < 0.05$ . Test of QED-Compton hypothesis for LAr-SpaCal events.

In the figure 5.15(a-f) polar angle and energy spectra are shown. The number of the QED-Compton events is normalised to the luminosity of the  $e^+p$  data set. The simulation describes the data distributions in shape as well as in absolute normalisation.

The distribution  $\Delta E/E = \left| \frac{E_{LAr} - E_{e,\gamma}^{DA}}{E_{e,\gamma}^{DA}} \right|$  (figure 5.15(g-i)) for the cluster with higher transversal momentum  $p_T$  (cluster 1 in LAr-LAr sample) centred around zero. For the cluster with lower transversal momentum  $p_T$  (cluster 2 in LAr-LAr sample) the distribution is systematically negative. This behaviour is very well described by the simulation. In this analysis the SpaCal calibration and alignment are not applied therefore a small disagreement between the data and the MC in the  $\Delta E/E$  distribution is observed.

---

<sup>6</sup>Note that calibration described in section 5.4.1 is performed using events with  $E'_e > 14$  GeV.

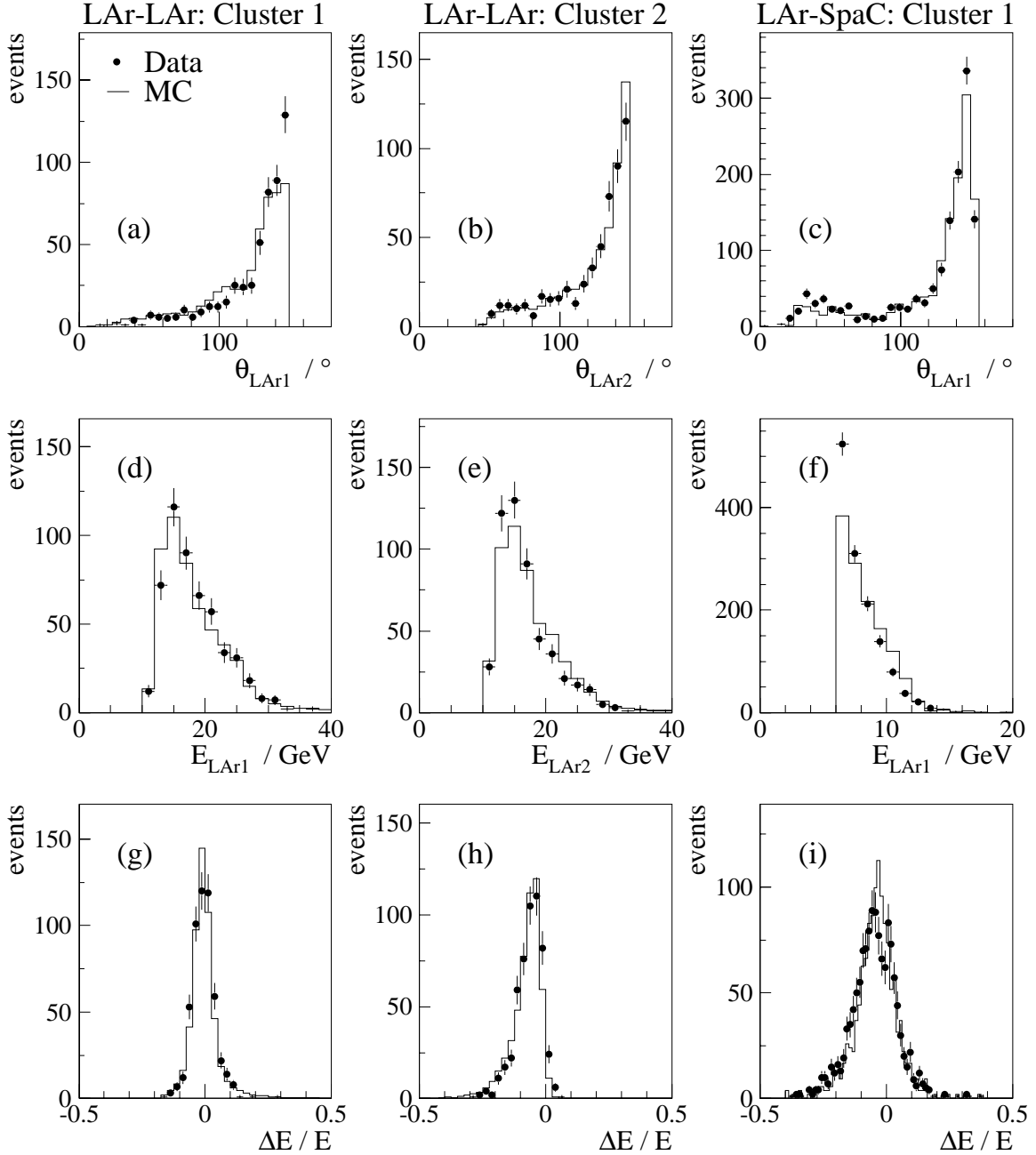


**Figure 5.15:** Cross-check of electron energy calibration with elastic QED Compton events. Shown are polar angle (a,b,c), energy (d,e,f) and deviation of calorimetrically measured energy from energy determined using the DA method (g,h,i). The distributions shown in left (middle) column, marked as *Cluster 1* (*Cluster 2*), correspond to more (less) energetic cluster in the LAr-LAR sample of events. The distributions for LAr cluster in the LAr-SpaCal events are shown in the right column.

The overall good description of the data by the MC demonstrates that the calibration derived for  $E'_e > 14$  GeV is successfully applicable down to low electron energy.

The uncertainty on the electron energy scale is estimated to be 1% in the backward part of the detector,  $z_{LAr} < -150$  cm, 0.7% in the region  $-150 \text{ cm} < z_{LAr} < 20$  cm, 1.5% for  $20 \text{ cm} < z_{LAr} < 100$  cm and 3% in the forward part,  $z_{LAr} > 110$  cm. An uncertainty due to method used for calibration is estimated to be 0.5%.

## 5.5 Hadronic Energy Measurement

For the reconstruction of the DIS event kinematics the following hadronic variables are needed:  $E - P_z$ ,  $P_{T,h}$  and  $\gamma_h$  (eq. 4.3). These variables are calculated summing over particles in the hadronic final state as they are measured in the LAr calorimeter and SpaCal. The measurement can be improved if track information is used as well. Two of these variables,  $E - P_z$  and  $P_{T,h}$ , require a good knowledge of the absolute hadronic energy scale. This scale is calibrated using transverse momentum conservation, which requires  $P_T$  balance between the scattered electron and the hadronic final state,  $P_{T,h}/P_{T,e} = 1$ .

The most important detector for the hadronic energy measurement is the LAr calorimeter. The response of the LAr calorimeter has been extensively tested in 1987-1990 at CERN using charged pion beams with energy from 3 to 205 GeV [49]. The LAr calorimeter is non-compensating, i.e. the response for hadrons is about 30% smaller than that for electrons. Therefore a correction has to be applied to the hadronic signal [91]. To obtain the correct energy measurement for hadrons, a software weighting technique is applied, which was initially proposed by the CCFR Collaboration and used in the CDHS experiment [92]. This method was further developed by H1 on the basis of the CERN test runs [93–96]. The aim of this weighting technique is to equalise the response to the electromagnetic and hadronic components of a hadronic shower. The technique exploits the fact that local energy deposits of high density are mainly of the electromagnetic origin while the hadron component is much more spread out. Thus, in the well segmented LAr calorimeter a separation of electromagnetic and hadronic energy depositions can be done. The weighting technique works well for energies above 10 GeV. For lower energies, simple multiplicative factors corresponding to the effective  $e/\pi$  ratios have been applied [97].

An important issue for the energy measurement in the LAr calorimeter is noise suppression. In events recorded with a random trigger, on average 1100 cells out of 45000 pass a  $+2\sigma$  noise threshold applied online to skip cells with zero signals. The electronic noise per cell varies between 15 and 30 MeV and adding up this energy for the full calorimeter would yield an equivalent energy of 48 GeV. In the simulation, noise patterns recorded in these special runs are overlaid with genuine physics signals. On the reconstruction levels the noise has been removed in several steps, as explained

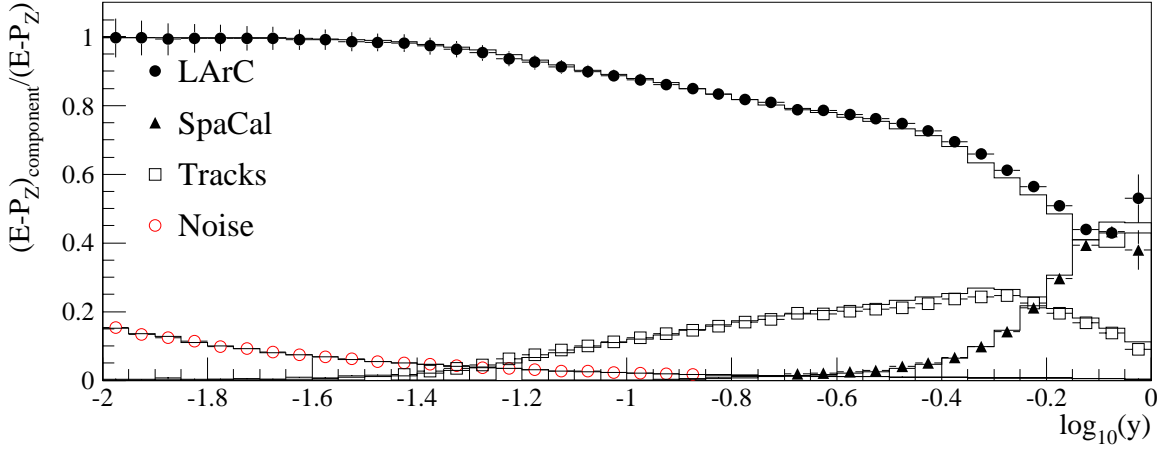


**Figure 5.16:** Relative contributions from LAr calorimeter, tracks and Spacal to the total  $E - P_z$  and the suppressed noise contribution relative to the measured  $E - P_z$ .

in [42]. An additional noise suppression is applied during the analysis. Isolated low energetic clusters are removed from the hadronic final state if the energy inside a cylinder of radius 20 cm (40 cm) around the direction from the interaction point to the cluster is less than 400 MeV (800 MeV) for  $\theta > 15^\circ$  ( $< 15^\circ$ ). A 25% systematic uncertainty on the amount of the equivalent energy of the noise which is removed on this step is assigned.

The H1 central tracking system is used to improve the hadronic energy measurement. Tracks with momentum less than 2 GeV are extrapolated to the LAr calorimeter surface and linked to a cluster. If the energy of the cluster is greater than the mo-

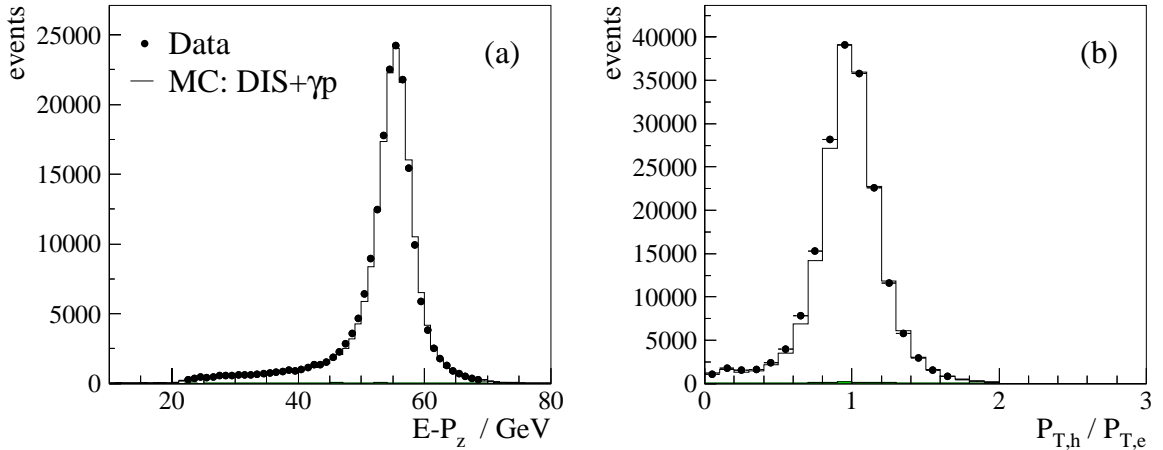


**Figure 5.17:** The longitudinal momentum balance  $E - P_z$  (a) and the transversal momentum balance  $P_{T,h}/P_{T,e}$  (b) after calibration using information from LAr calorimeter and tracks.

mentum of the track linked to it the cluster information is used. The cells of the LAr calorimeter cluster to which the track is linked are masked, i.e. they are not used in the summation over hadronic particles and double counting of energy is avoided.

Figure 5.16 shows the relative contributions of the LAr calorimeter, SpaCal and tracks to  $E - P_z$  as function of the inelasticity  $y$ . The main contribution is coming from the LAr calorimeter. SpaCal is contributing only at high  $y$ . A sharing of  $E - P_z$  between different components is well described by the simulation. The figure shows also the suppressed noise contribution relative to the measured  $E - P_z$ . Figure 5.17 shows resulting  $E - P_z$  (a) and  $P_{T,h}/P_{T,e}$  (b) distributions after applying the calibration discussed in the next section.

### 5.5.1 Calibration of Hadronic Energy

A calibration of the hadronic energy has been performed separately for data and simulated events.

In the first step, an iterative calibration procedure is applied to determine calibration factors  $c_k^i$  for each wheel of the LAr calorimeter using low  $Q^2$   $e^+p$  data [98].  $c_k^i$  are obtained from the Gaussian fit to the  $P_T$  balance ( $R_{P_T} = P_{T,h}/P_{T,e}$ ) weighted by the fraction of  $P_{T,h}$  carried by the wheel,  $w_k$  [99]. Calibration factors are defined as a deviation from unity of the mean value of  $P_T$  balance. For the next iteration they are obtained from relation

$$c_k^{i+1} = c_k^i + \left( 1 - \left\langle w_k^{ev} \cdot \frac{\sum_k P_{T,h}^k (1 + c_k^i)}{P_{T,e}} \right\rangle \right) \quad (5.2)$$

The final tuning of the calibration factors is performed exploiting a  $y$  measurement based on hadrons,  $y_\Sigma$  (eq. 4.6), and the one using the DA ( $y_{DA}$ ) or electron ( $y_e$ ) method. In figure 5.18 the ratios  $y_\Sigma/y_{DA(e)}$  for different wheels are shown. Each event contributes to a wheel distribution with a weight corresponding to the fraction of  $E - P_z$  coming from this wheel. Contributions from SpaCal and from tracks are also shown. The calibration factors are obtained by tuning the wheel response in the data and MC to be the same. The  $P_T$  balance for the different wheels is shown in figure 5.19.

Figure 5.20(a) shows for different wheels the mean values of the  $P_T$  balance distributions obtained by Gaussian fits before and after final tuning of calibration. The values after calibration are closer to unity and the ratios  $\langle R_{P_T}^{data} \rangle / \langle R_{P_T}^{MC} \rangle$  for LAr calorimeter deviate from unity by  $\lesssim 1\%$ , figure 5.20(b). Figure 5.21 shows the mean values of  $P_{T,h}/P_{T,e}$  for  $\gamma_h < 15^\circ$  (a,b) and  $\gamma_h > 15^\circ$  (c,d) as function of  $P_{T,h}$ . The agreement between data and simulation is always better than 2%, figure 5.21(b,d), and for  $12 < P_{T,h} < 50$  GeV and  $\gamma_h > 15^\circ$  it is better than 1%. Figure 5.22 demonstrates the quality of the hadronic energy calibration in the region of  $12 < P_{T,h} < 50$  GeV and

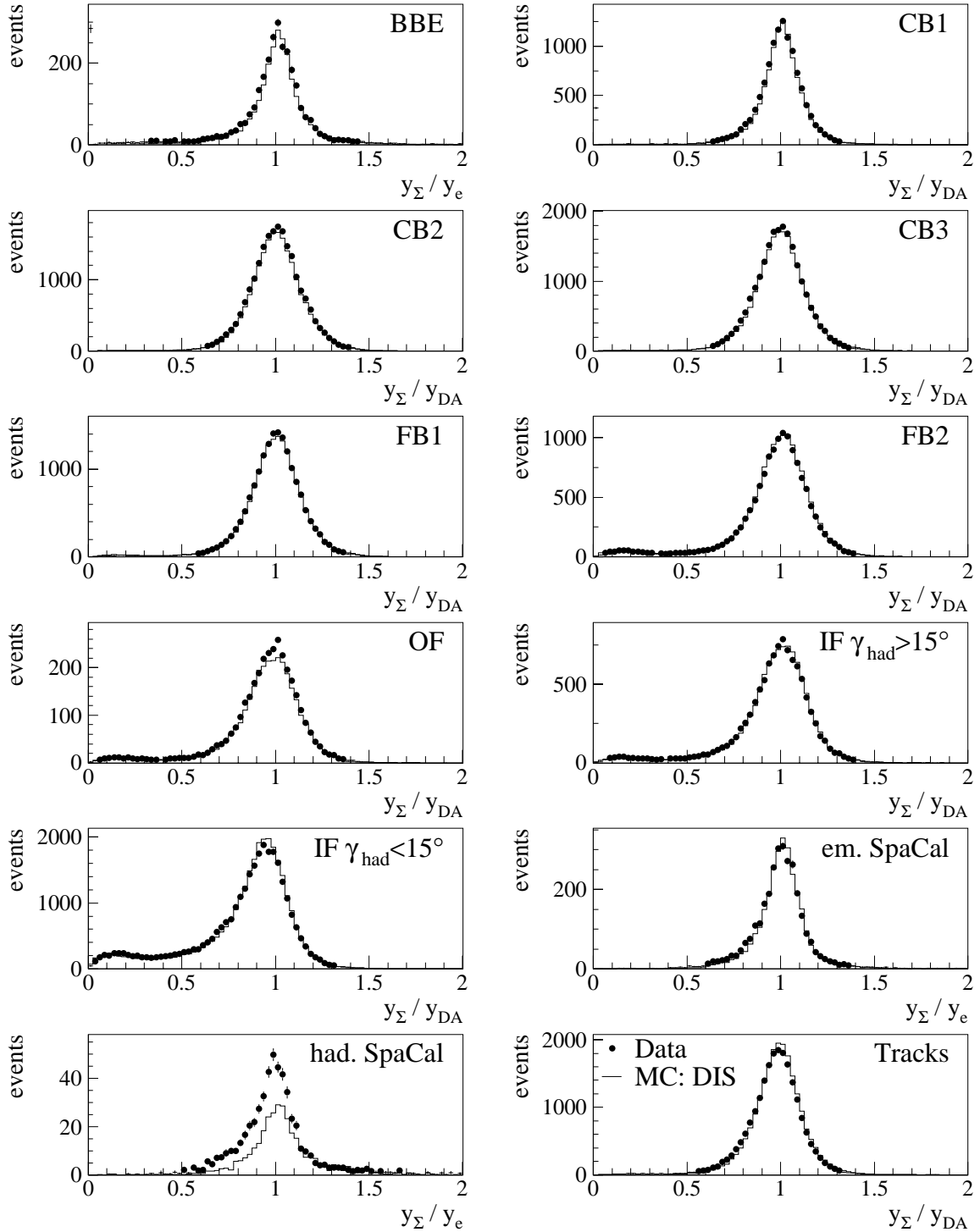


Figure 5.18: The ratio  $y_{\Sigma}/y_{DA(e)}$  for different wheels of the LAr calorimeter.



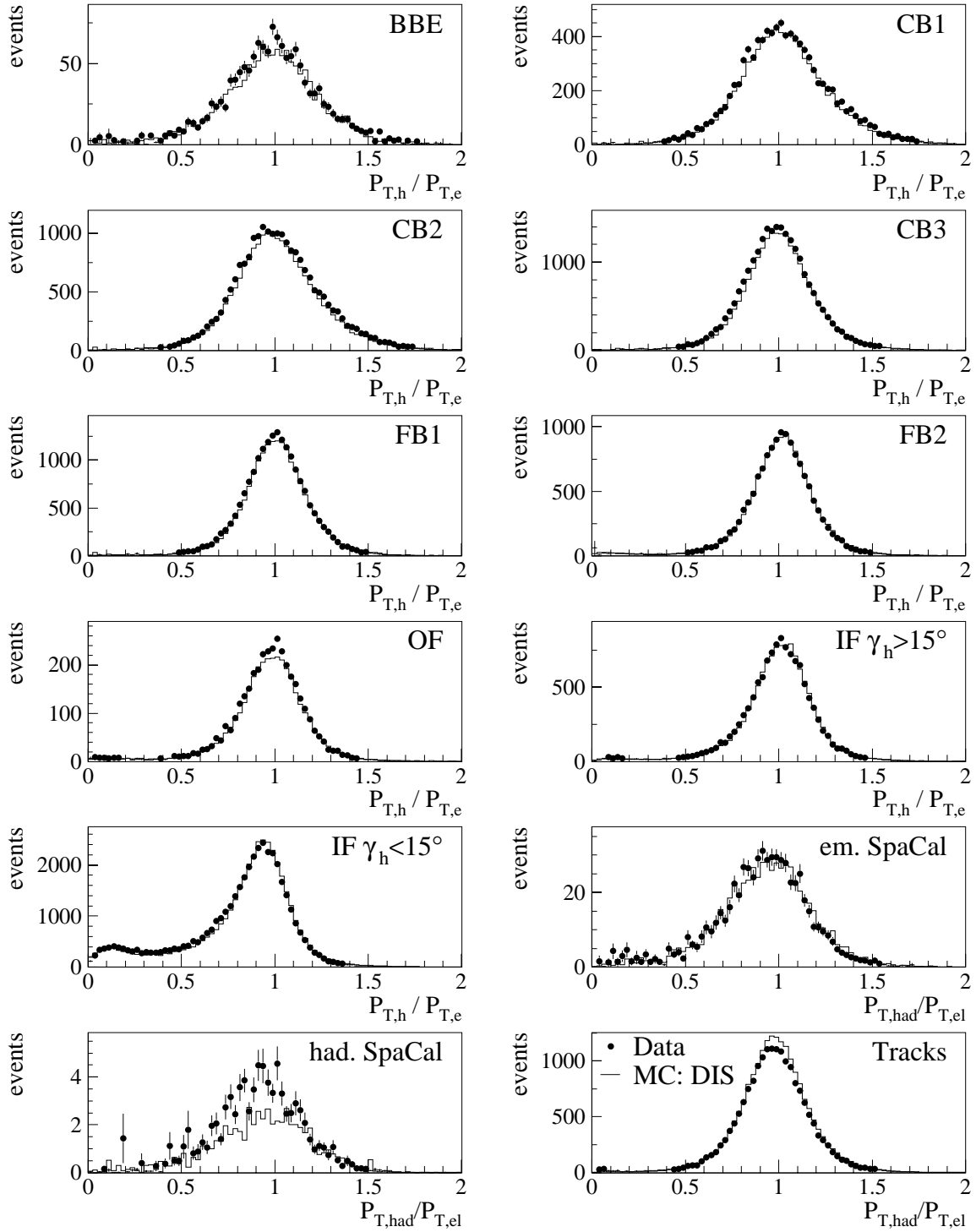
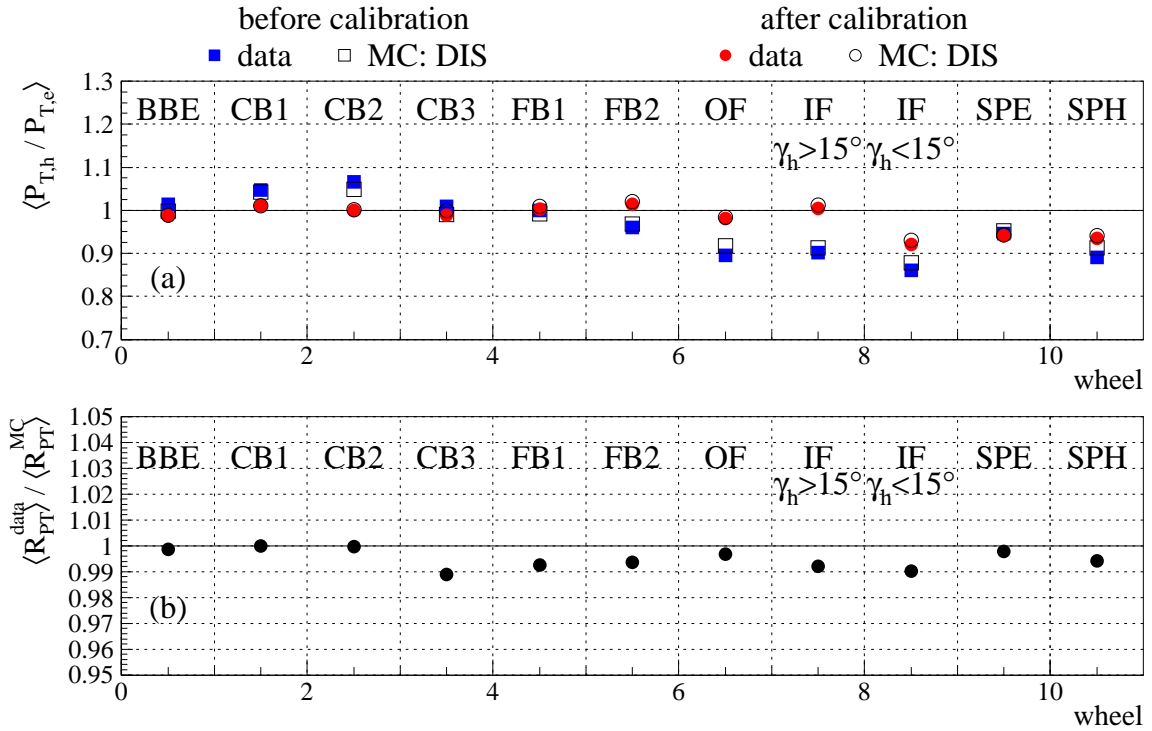
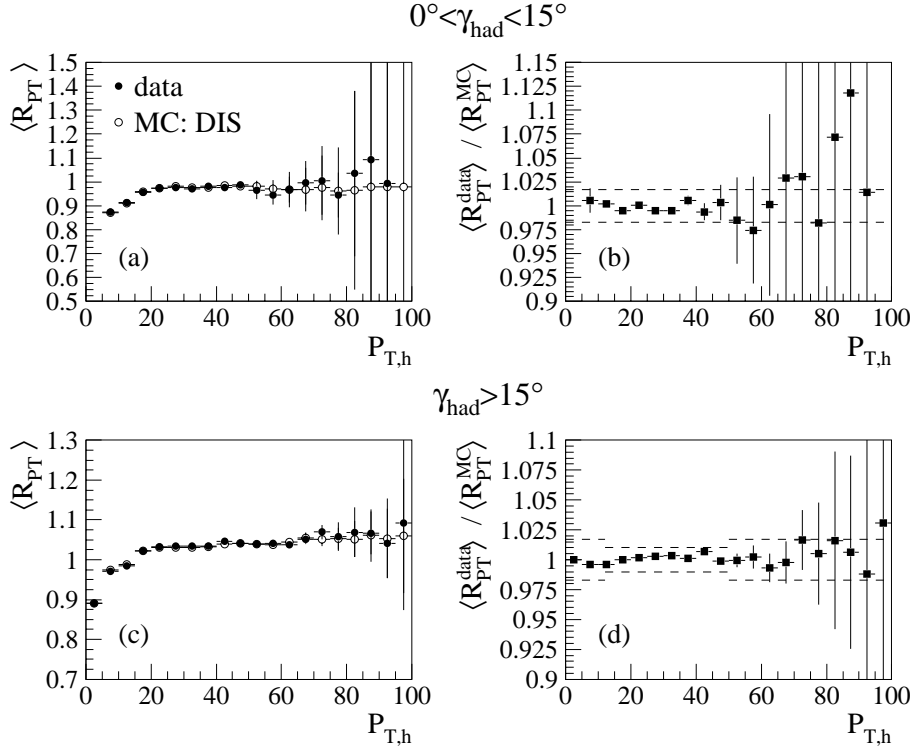


Figure 5.19:  $P_T$  balance for the wheels of the LAr calorimeter.



**Figure 5.20:** Mean values of  $P_{T,h}/P_{T,e}$  obtained by Gaussian fit in different wheels for data and simulation before and after calibration (a). The ratio of  $\langle P_{T,h}/P_{T,e} \rangle$  after calibration of data and MC (b).

$\gamma_h > 15^\circ$  as a function of  $P_{T,e}$  (a) and  $\gamma_h$  (b). Relative differences between data and simulation are used for an estimation of the uncertainty which is taken to be 1% in the region  $12 < P_{T,h} < 50$  GeV and  $\gamma_h > 15^\circ$  and 1.7% outside this region. Additional 1% uncertainty is assigned to account for possible remaining biases in the reference scale used for the calibrations. A 5% uncertainty is attributed to the hadronic energy measurement in the SpaCal and a 3% uncertainty to the tracking system.



**Figure 5.21:** Mean values  $P_T$  balance  $P_{T,h}/P_{T,e}$ , as function of  $P_{T,h}$  for inclusive hadron angle  $0^\circ < \gamma_h < 15^\circ$  (a) and  $\gamma_h > 15^\circ$  (c) and the ratios of  $P_T$  balance of data and MC for  $0^\circ < \gamma_h < 15^\circ$  (b) and for  $\gamma_h > 15^\circ$  (d).

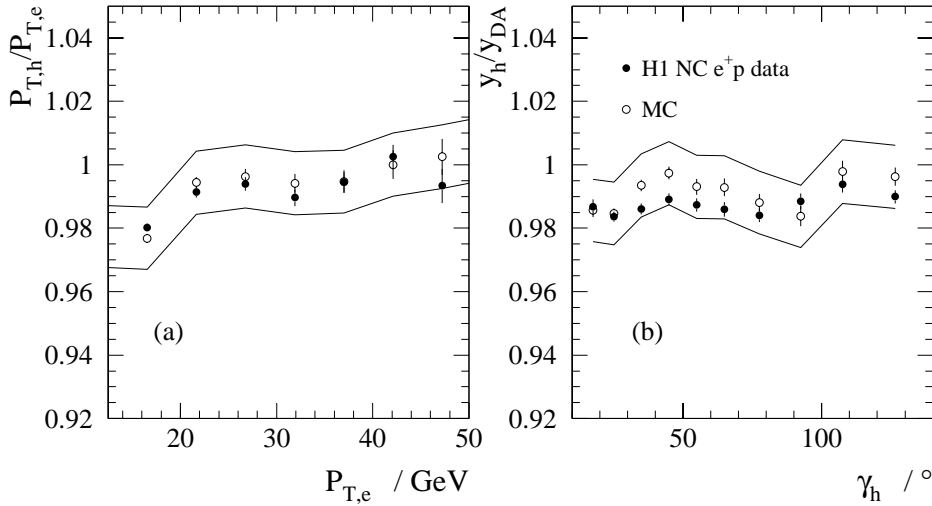


**Figure 5.22:** Mean values of  $P_{T,h}/P_{T,e}$  as a function of  $P_{T,e}$  (a) and of  $y_h/y_{DA}$  as a function of  $\gamma_h$  (b) for data (solid points) and simulation (open points) for  $\gamma_h > 15^\circ$  and  $12 \text{ GeV} < P_{T,h} < 50 \text{ GeV}$ . The curves correspond to a  $\pm 1\%$  variation of the simulation.

## 5.6 Determination of Trigger Efficiency

During data taking the decision whether to record an event for further analysis or not is done through a multi-level trigger system (see section 2.2.5). Since in the high  $Q^2$  NC DIS events the electron is scattered into the LAr calorimeter the most important trigger component for this analysis is the LAr trigger. For  $E'_e > 11$  GeV it is required that the trigger is fully efficient; the regions in which this is not the case are excluded. At lower electron energy the trigger efficiency shows a threshold behaviour. This behaviour is modelled in the simulation.

The efficiency of a trigger element TE, or combination of trigger elements, is defined as follows:

$$\epsilon_{\text{TE}} = \frac{\text{number of events triggered by MT and TE}}{\text{number of events triggered by MT}}, \quad (5.3)$$

where MT is the monitor trigger which is independent of the actual trigger element. The selection of monitor triggers is given in table 5.3.

|   |  |
|---|--|
| LAr trigger elements<br>LAr_electron_1<br>LAr_electron_2<br>LAr_emiss>1   | monitor triggers<br>ST71<br>ST71<br>ST71   |
| T0 criteria<br>LAr_T0<br>zVtx_T0<br>FwdRay_T0   | ST67 && (zVtx_T0    FwdRay_T0)<br>ST67 && (LAr_T0    FwdRay_T0)<br>ST67 && (zVtx_T0    LAr_T0) |
| combinations of trigger elements<br>ST71Rest_L2:<br>ST71 without zVtx<br>ST75Rest_L2:<br>ST75 without zVtx,LAr_electron_2 | ST67 && zVtx<br>ST71 && zVtx && LAr_electron_2   |

**Table 5.3:** NC trigger elements and their monitor triggers

### Trigger Acceptance Volume

For scattered electron energies  $E'_e > 11$  GeV the efficiency of LAr\_electron\_1 is evaluated as function of the electron impact position  $z_{LAr}$  and scattering azimuthal angle  $\phi_e$  as shown in figure 5.23. Over the majority of the  $z_{LAr}$ - $\phi_e$  volume the efficiency is 100%. However there are regions where the trigger efficiency is significantly smaller. These inefficiencies are correlated with trigger cells which have been deactivated due to high noise level. Some of the regions were inefficient only for some time during data taking. These regions with low efficiencies, marked as shaded boxes in figure 5.23 and detailed in appendix B, table B.1, are left out from the analysis. The figure also shows the regions excluded only for  $E'_e < 11$  GeV.

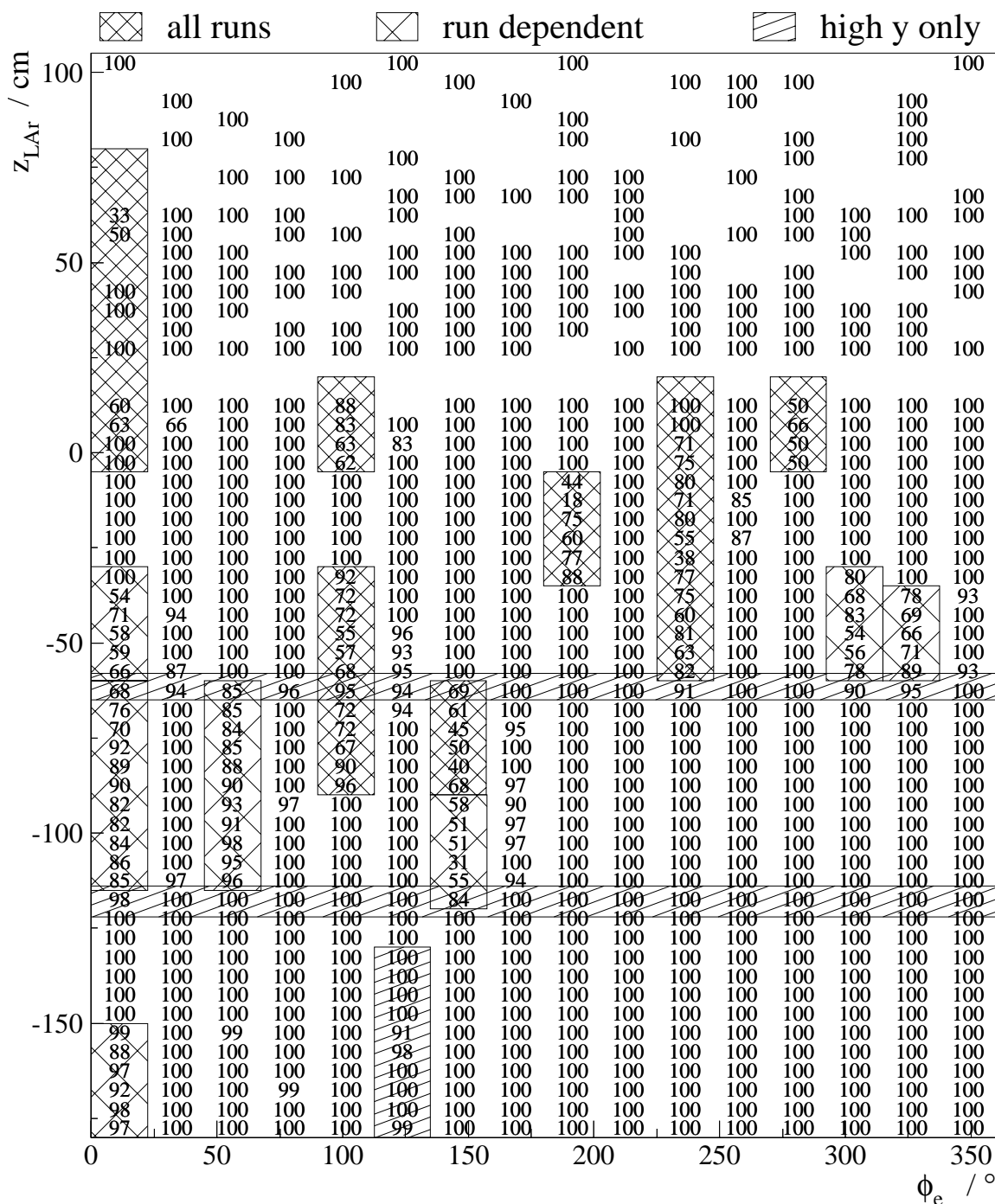


**Figure 5.23:** Trigger acceptance volume. Boxes indicate regions which are excluded because of the low trigger efficiency.

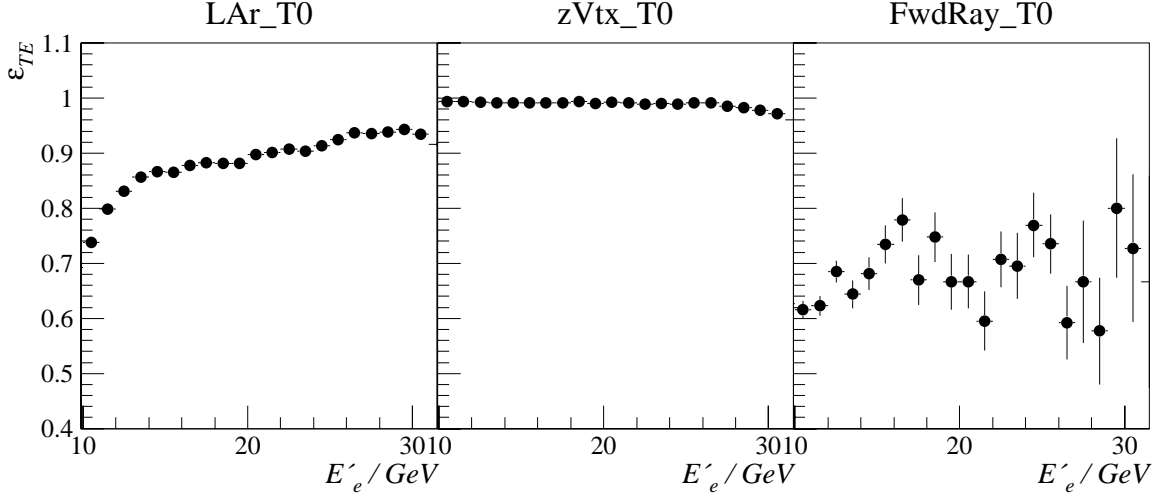


**Figure 5.24:** Efficiency of the trigger elements LAr\_T0, zVtx\_T0 and FwdRay\_T0 as function of electron energy.

### Timing Condition

The T0 trigger elements allow determination of the bunch crossing time. In the sub-triggers the T0 requirements from the LAr calorimeter and the central and forward proportional chambers (LAr\_T0, the zVtx\_T0 and the FwdRay\_T0) are used. The efficiency of T0 trigger elements as function of electron energy is shown in figure 5.24. The efficiency of LAr\_T0 is about 90% and falls at low electron energies below 80%. The combination of the zVtx\_T0 and the FwdRay\_T0 gives the Ray\_T0. The efficiencies of the zVtx\_T0 and the FwdRay\_T0 makes the Ray\_T0 to vary with the track multiplicity in the acceptance region of the proportional chambers and therefore to depend of the inelasticity  $y$ . The efficiency of the Ray\_T0 is above 99.5%.

The combined efficiency of the timing requirements is:

$$\begin{aligned}\epsilon_{T0} &\equiv \epsilon(\text{LAr\_T0} || \text{zVtx\_T0} || \text{FwdRay\_T0}) \\ &= 1 - (1 - \epsilon_{\text{LAr\_T0}}) \cdot (1 - \epsilon_{\text{zVtx\_T0}}) \cdot (1 - \epsilon_{\text{FwdRay\_T0}})\end{aligned}$$

under the assumption that the LAr\_T0, the zVtx\_T0 and the FwdRay\_T0 are independent of each other. The combined efficiency is above 99.9% for full kinematic region.

### Veto Conditions

The veto conditions, described in section 2.2.5 and their inefficiencies are listed in table 5.4. Only the inefficiencies of RZ-Veto and CIP\_noSPCL are significant. However

| System      | Subtrigger             | Monitor-Trigger | Ineff. (%)       |
|-------------|------------------------|-----------------|------------------|
| Veto-Wall   | ST67, ST71, ST75       | ST77            | $0.05 \pm 0.006$ |
| Forward-ToF | ST67, ST71, ST75, ST77 | ST112           | $0.08 \pm 0.04$  |
| VLQ-ToF     | ST67, ST71, ST75, ST77 | ST11,ST2        | $0. \pm 0.008$   |
| RZ-Veto     | ST75, ST77             | ST67 ST71       | $7.0 \pm 0.06$   |
| CIP_noSPCL  | ST71                   | ST71 ST75 ST77  | $1.4 \pm 0.03$   |
| SpaCal-ToF  | ST71                   | ST71 ST75 ST77  | $0.06 \pm 0.006$ |

**Table 5.4:** Inefficiencies of global veto options.

the main subtrigger ST67 does not have these veto options. Since the inefficiency of the veto conditions is either very small or only applied to some of the subtriggers, it is justified to neglect the inefficiency due to the veto requirements. A systematic uncertainty of 0.3% assigned to the trigger efficiency covers these effects.

### 5.6.1 Trigger Efficiency at Low Electron Energy

At low electron energy, i.e.  $6 < E'_e < 11$  GeV, one needs to take into account threshold behaviour of trigger elements listed in table 5.3. It is done separately in three different  $z_{LAR}$  regions: central region CB  $z_{LAR} > -120$  cm, backward region BBE  $z_{LAR} < -157$  cm and transition region between BBE and CB  $-157 \text{ cm} < z_{LAR} < -120$  cm [64]. In this low energy region additional trigger fiducial cuts are imposed (see figure 5.23 and table B.1).

The energy dependence of the efficiency of the LAr trigger elements is parametrised with a threshold function

$$\epsilon(E'_e) = \left[ 1 + \exp\left(\frac{-E'_e + A}{B}\right) \right]^{-1}, \quad (5.4)$$

where  $A$  is the energy at which the efficiency is 50% and  $B$  characterises the width of the threshold function. The other trigger elements are independent of electron energy and can be, within the three  $z_{LAR}$  regions, approximated by a constant.

The total efficiency is calculated taking into account the correlation between the subtriggers. In the backward region  $z_{LAR} < 120$  cm the threshold of LAr\_electron\_2 (ST75) is higher than the threshold of LAr\_electron\_1 (ST75). ST75 has stronger veto requirements and time criterium and therefore ST75 does not significantly contribute to the total efficiency in the backward region.

The total efficiency is obtained in the following way:

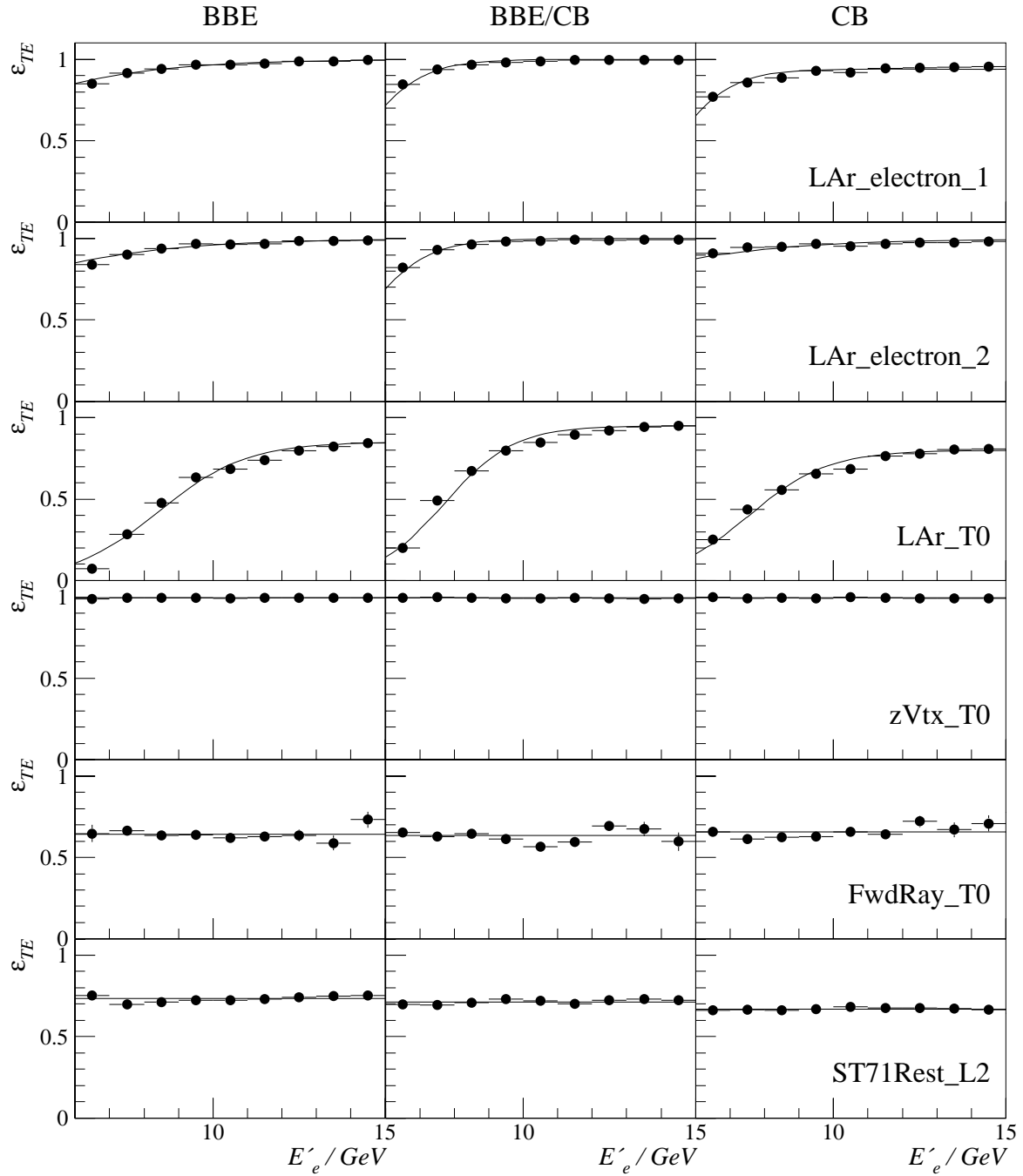


Figure 5.25: The efficiency of the trigger elements as function of energy of scattered electron.



BBE, BBE/CB

$$\begin{aligned}\epsilon_{\text{ST67}} &= \epsilon_{\text{LAr\_elec\_1}}(E'_e) \cdot \epsilon_{T0}(E'_e) \\ \epsilon_{\text{ST71}} &= \epsilon_{z\text{Vtx\_T0}} \cdot \epsilon_{\text{ST71Rest\_L2}} \\ \epsilon_{\text{Total}} &= 1 - (1 - \epsilon_{\text{ST67}}) \cdot (1 - \epsilon_{\text{ST71}})\end{aligned}$$

CB

$$\begin{aligned}\epsilon_{\text{ST67}} &= \epsilon_{\text{LAr\_elec\_1}}(E'_e) \cdot \epsilon_{T0}(E'_e) \\ \epsilon_{\text{ST71,ST75}} &= \epsilon_{z\text{Vtx\_T0}} \cdot (1 - (1 - \epsilon_{\text{ST71Rest\_L2}}) \cdot (1 - \epsilon_{\text{ST75Rest\_L2}} \cdot \epsilon_{\text{LAr\_elec\_2}})) \\ \epsilon_{\text{Total}} &= 1 - (1 - \epsilon_{\text{ST67}}) \cdot (1 - \epsilon_{\text{ST71,ST75}})\end{aligned}$$

To model the threshold behaviour of TE efficiencies the events in the simulation are rejected according to parametrised efficiencies.

In order to estimate the systematic uncertainty of the trigger efficiency the efficiencies of trigger elements are calculated using total number of events and events which are triggered by the SpaCal trigger as monitor samples. In figure 5.26 the envelopes of the efficiencies calculated with alternative methods for both  $e^+p$  and  $e^-p$  data are shown.

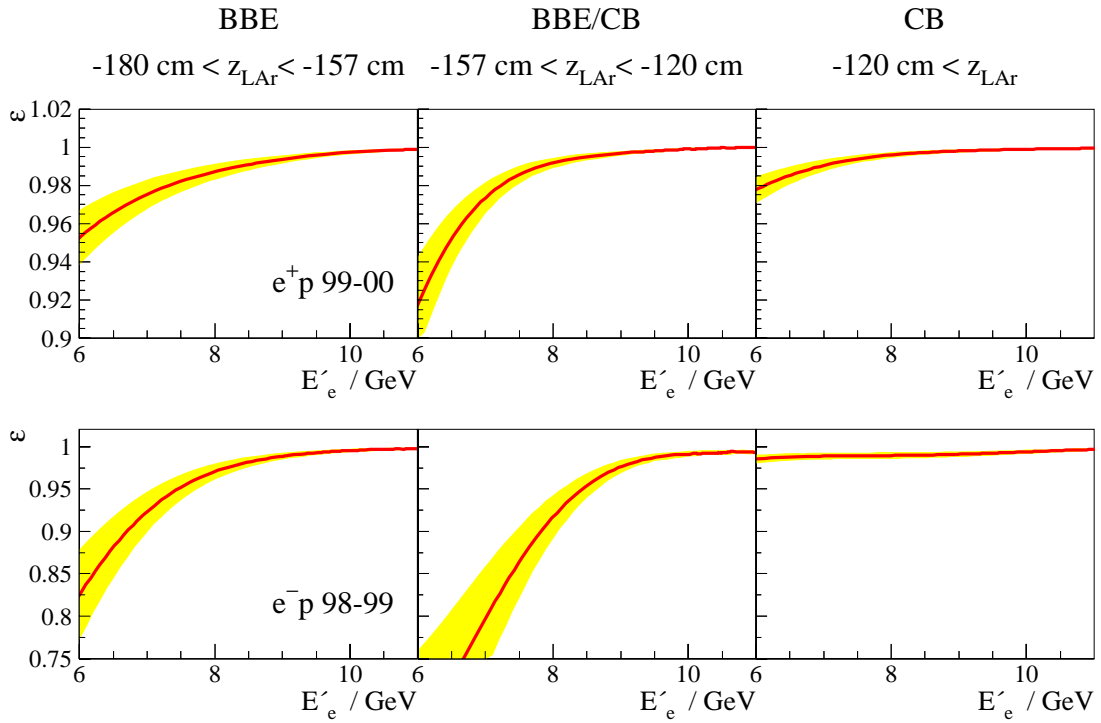


**Figure 5.26:** Parametrisation of trigger efficiencies in the three regions of the LAr calorimeter (BBE, BBE/CB, CB) for the  $e^+p$  and the  $e^-p$  data. Lines show the efficiencies determined by the standard monitor triggers (see table 5.3), bands show the estimated uncertainty of trigger efficiencies.

## 5.7 Modelling of Time Dependencies in the MC

During the 1999–2000  $e^+p$  data taking there were several run periods with significantly different experimental conditions:

- In October 1999 a wire in CJC broke. During shutdown in December 1999 this wire was taken out. The broken wire lead to a degradation of the track reconstruction efficiency in CJC for the run range  $257590 < I_{run} < 261338$ .
- Performance of the LAr trigger was changing with time. This lead to five run ranges with different trigger fiducial cuts, see section 5.6.
- The mean  $z_{vtx}$  position has changed from  $\approx -1$  cm to  $\approx 3$  cm, see figure 5.3.

The time correlation between different conditions is given in table 5.5. This leads to seven different time periods, where the conditions in the first and the third periods are identical. To take into account this time dependence in the simulation the conditions of each of these seven periods are modelled for a fraction of MC events corresponding to the fraction of luminosity in the given period.

| period | track eff.    | trig. fidvol.      | $\langle z_{vtx} \rangle_{data}$ | $\mathcal{L}_i$ [pb <sup>-1</sup> ]    |
|--------|---------------|--------------------|----------------------------------|--|
|        | 244968        | 244968             | 244968                           |  |
| 1      |               |                    |                                  | $\mathcal{L}_1 + \mathcal{L}_3 = 35.1$ |
|        | 257590        |                    |                                  |  |
| 2      | <i>broken</i> |                    |                                  |  |
|        | <i>wire</i>   | $BBE \approx 8\%$  |                                  | $\mathcal{L}_2 = 5.9$                  |
|        | <i>in CJC</i> |                    |                                  |  |
|        | 261338        |                    | $\approx -1$ cm                  |  |
| 3=1    |               |                    |                                  |  |
|        |               | 262031             |                                  |  |
| 4      |               | $BBE \approx 9\%$  |                                  | $\mathcal{L}_4 = 16.6$                 |
|        |               | 265068             |                                  |  |
| 5      |               | $BBE \approx 13\%$ |                                  | $\mathcal{L}_5 = 6.7$                  |
|        |               | 269335             | 269335                           |  |
| 6      |               | $BBE \approx 16\%$ |                                  | $\mathcal{L}_6 = 0.6$                  |
|        |               | 276210             | $\approx 3$ cm                   |  |
| 7      |               | $BBE \approx 18\%$ |                                  | $\mathcal{L}_7 = 0.3$                  |
|        | 279215        | 279215             | 279215                           | $\mathcal{L}_{tot} = 65.2$             |

**Table 5.5:** Run periods with different experimental conditions. The luminosity of each period is given in the last column.

## 5.8 Rejection of the $ep$ Induced Background

The most significant  $ep$  induced background contribution to the NC sample of events is from photoproduction. Smaller contributions come from QED Compton scattering, lepton pair production and low  $Q^2$  DIS events. All these processes are generated and simulated as described in section 3.2.

The background description in the simulation is checked using events with an electron detected in the electron tagger (ET) and using electron candidates rejected by using only one criterium of the electron finder. For the *high  $y$  analysis* ( $6 < E'_e \lesssim 11$  GeV, see section 6.4) the background contribution is estimated directly from data using the information about the electric charge of the electron candidate provided by the tracking system. The control of QED Compton background is already demonstrated in section 5.4.3.

### 5.8.1 Control of $\gamma p$ Background Using Tagged Events

For about 10% of  $\gamma p$  events with  $0.3 < y < 0.7$  the outgoing electron is detected in the electron tagger of the luminosity system. These events can be used for control of description of the  $\gamma p$  background in the simulation.

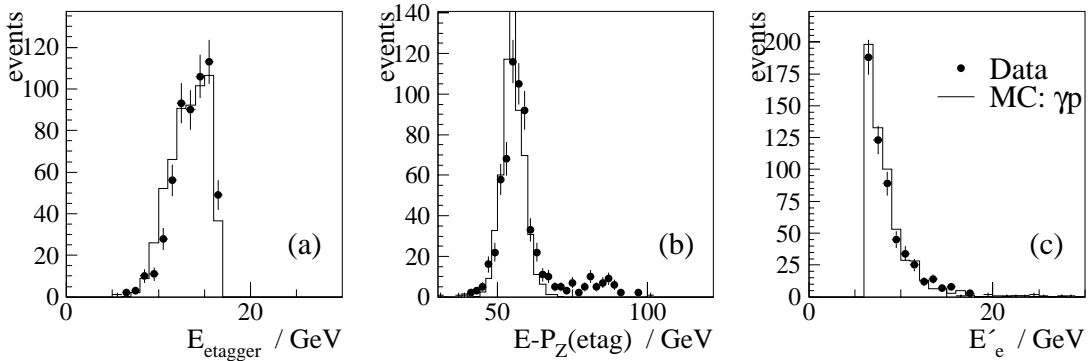


**Figure 5.27:** The control distributions for tagged photoproduction events: energy deposition in tagger (a), longitudinal momentum balance  $E - P_z$  (b) and the energy (c) spectrum of misidentified electron.

The energy spectrum of electrons detected in ET is shown in figure 5.27(a). Figure 5.27(b) shows  $(E - P_z)_{\text{tag}} = E - P_z + 2 \cdot E_{\text{tag}}$ , which includes energy of the electron in ET ( $E_{\text{tag}}$ ). The distribution peaks at 55 GeV as expected; the events in the tail of the  $(E - P_z)_{\text{tag}}$  distribution are due to the overlap of DIS and Bethe-Heitler events. Applying the cut  $45 \text{ GeV} < E - P_z + 2 \cdot E_{\text{tag}} < 70 \text{ GeV}$  the photoproduction events are selected. An energy distribution of *fake electrons* (misidentified electron

candidates) in the LAr calorimeter selected by standard electron identification procedure (see section 5.1) is shown in figure 5.27(c). All the distributions in figure 5.27 are well described by the simulation in terms of shape as well as absolute normalisation, demonstrating good understanding of the photoproduction background.

## 5.8.2 Control of Background Rejection

Another way to check the understanding of the background description by MC is to look on electron candidates rejected by the electron identification algorithm (see section 5.1). Electron candidates rejected by only one criterium of the electron finder and accepted by the others are shown in figure 5.28. The rejected events are mostly due to background processes. The simulation describes the data within 30% normalisation uncertainty which is finally attributed to the systematic error related to the estimation of the background from MC.

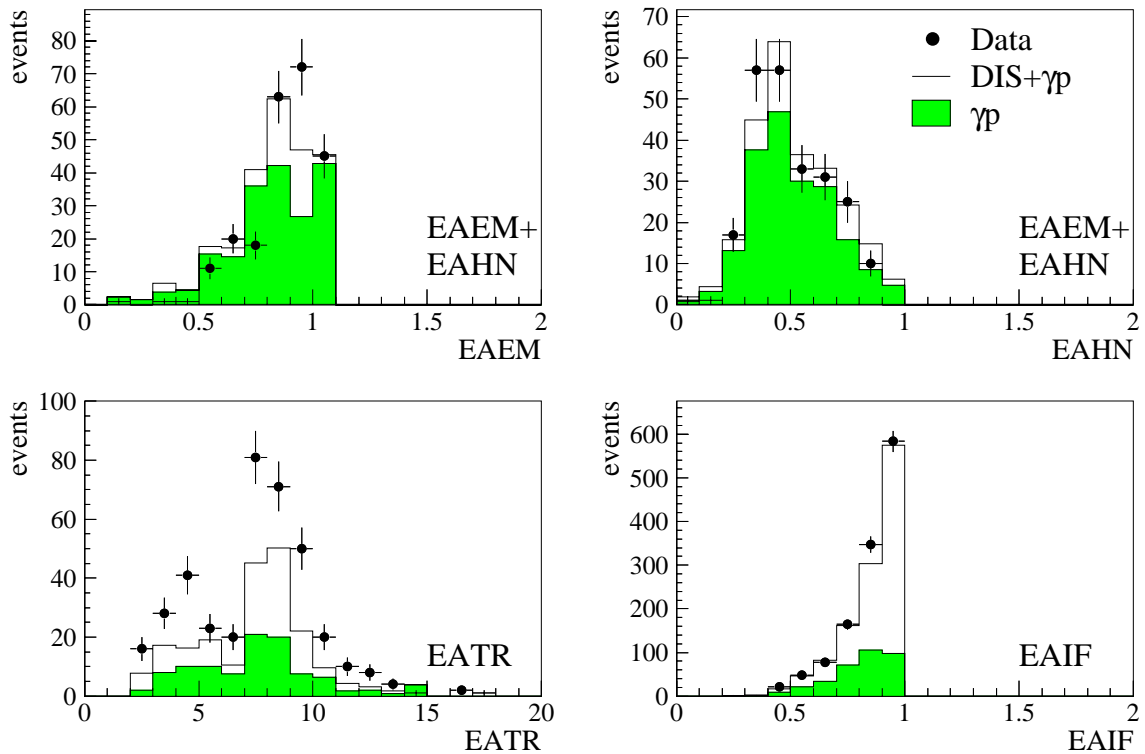


**Figure 5.28:** Estimators of the electron finding algorithm (see section 5.1) for electron candidates rejected by only one criterium. To improve the statistics for the estimators EAEM and EAHN the distributions of events rejected by any of them are shown.

### 5.8.3 Background Subtraction Using Track Information

The contribution of the photoproduction background increases towards low energies of the scattered electron. In view of the 30% uncertainty assumed for the background estimate using MC (see section 5.8.2) this would lead to a large systematic error of the result in this kinematic region. Instead of this, an alternative method to estimate this background is developed for the *high  $y$  analysis*. In this method, based entirely on data itself, the information about the electric charge of the electron candidate is used. If the charge of the electron candidate is opposite to the charge of beam electron the event is clearly originating from a background process. Background identified in this way can be used to estimate remaining background in the sample of "correctly charged" electron candidates.

Thus, the following procedure is used in the *high  $y$  analysis*:

- Only electron candidates validated by a DTRA track are accepted. This ensures a reliable determination of the electric charge of the electron candidate [64].
- Only "correctly charged" electron candidates are kept.

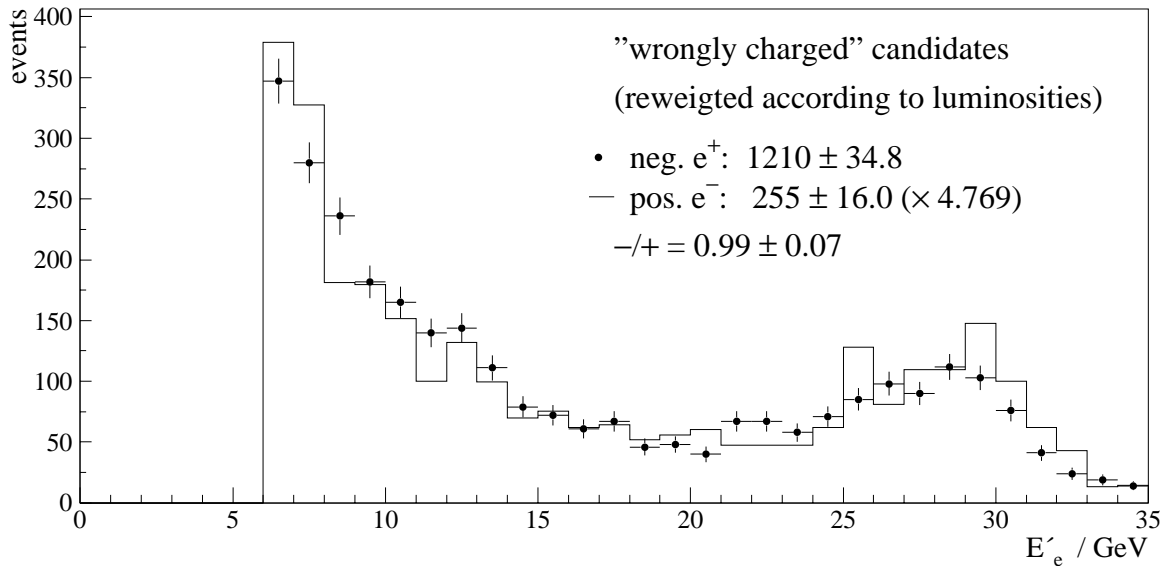


**Figure 5.29:** Energy spectrum of negatively charged candidates in  $e^+p$  data (points) compared to the energy spectrum of positively charged candidates in  $e^-p$  data (line). The  $e^-p$  data are normalised to the luminosity of the  $e^+p$  data set.

- The remaining background is statistically subtracted from the sample. It is estimated directly from data using the sample of events with "wrongly charged" electron candidates. Here it is assumed that the probability to have positive or negative fake electron in the background is the same,  $N_{bg}^-/N_{bg}^+ = 1$ .

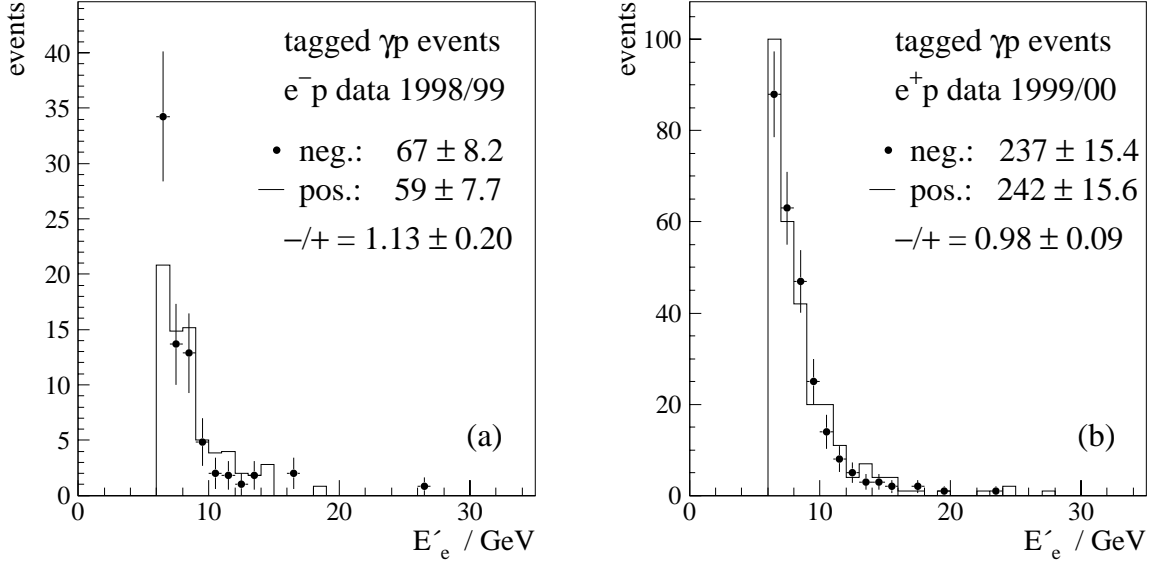


**Figure 5.30:** The energy spectrum of negative (points) and positive (line) fake electrons in tagged photoproduction event samples for  $e^-p$  (a) and  $e^+p$  (b) data sets.

The charge symmetry of fake electrons in the background is checked comparing the numbers of "wrongly charged" electron candidates in  $e^+p$  and  $e^-p$  data sets, figure 5.29. The ratio  $N_{bg}^-/N_{bg}^+$  in the energy range  $6 < E_e' < 11$  GeV is found to be  $0.99 \pm 0.07$ . Further checks are performed using tagged events for  $e^-p$  and  $e^+p$  data, figure 5.30(a,b). The  $N_{bg}^-/N_{bg}^+$  ratio is measured to be  $1.13 \pm 0.20$  ( $0.98 \pm 0.09$ ) for  $e^-p$  ( $e^+p$ ) data. Taking into account the error and the variations from unity of the ratio  $N_{bg}^-/N_{bg}^+$  a systematic uncertainty of 10% for the charge symmetry is assigned.

## 5.9 Rejection of Non- $ep$ Background

Cosmic and beam-halo muons can cause electromagnetic showers which can be misidentified as an electron. In addition, muon itself or some secondary particle from shower can produce a track in the tracking system leading to reconstruction of vertex. Such muon induced background can be identified using special topological background finding algorithms which are listed in the table 5.6 and contained in the program package QBGFIND [100, 101].

Scatter-plots of events found by different background finding algorithms are shown in figure 5.31. Partially these events have been visually scanned. Black (gray) points in the figure correspond to events recognised as background (genuine NC) events.

The NC events, as expected, have  $P_{T,h}/P_{T,e} \simeq 1$ . Therefore an event is rejected if it is found:

| finder        | description   | algorithm |
|---------------|---|-----------|
| halo- $\mu$   |   |           |
| 1             | pure longitudinal pattern in the LAr calorimeter  | HALAR     |
| 2             | longitudinal pattern in the LAr calorimeter matching energy deposit in the backward iron endcap | HAMULAR   |
| cosmic- $\mu$ |   |           |
| 3             | two opposite muon tracks of comparable direction  | COSMUMU   |
| 4             | all LAr calorimeter energy matching the direction of a muon track                               | COSMULAR  |
| 5             | all LAr energy matching the direction of two opposite clusters in the instrumented iron         | COSTALAR  |
| 6             | two CJC tracks with directions exactly opposite in space  | COSTRACK  |

**Table 5.6:** Background finding algorithm for halo-muons and cosmic muons.

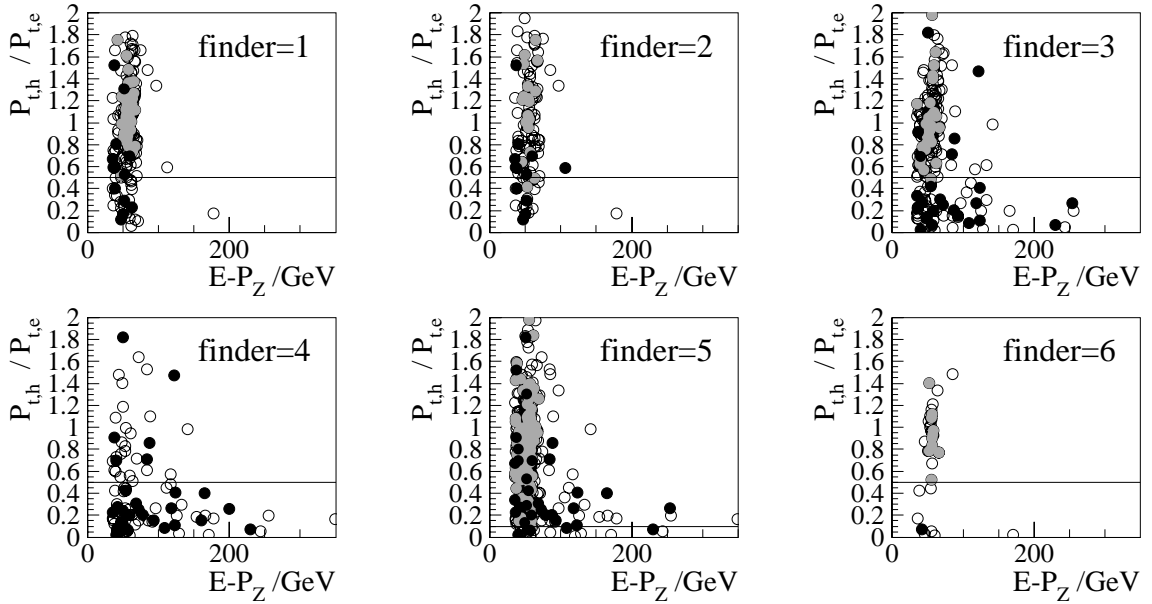


**Figure 5.31:** Events found by background finders 1-6 (open points). Black (gray) points correspond to events recognised by visual scan as background (genuine NC) events.

- by one of the finders 1-4 or 6 and  $P_{T,h}/P_{T,e} < 0.5$ ;
- by finder 5 and  $P_{T,h}/P_{T,e} < 0.1$ ;
- by finders 1 and 2 or by two finders out of 3-5 and  $P_{T,h}/P_{T,e} \geq 0.1$ .

Figure 5.32 shows the events rejected in this restricted scheme. One can see that almost no NC events are lost by applying this scheme.

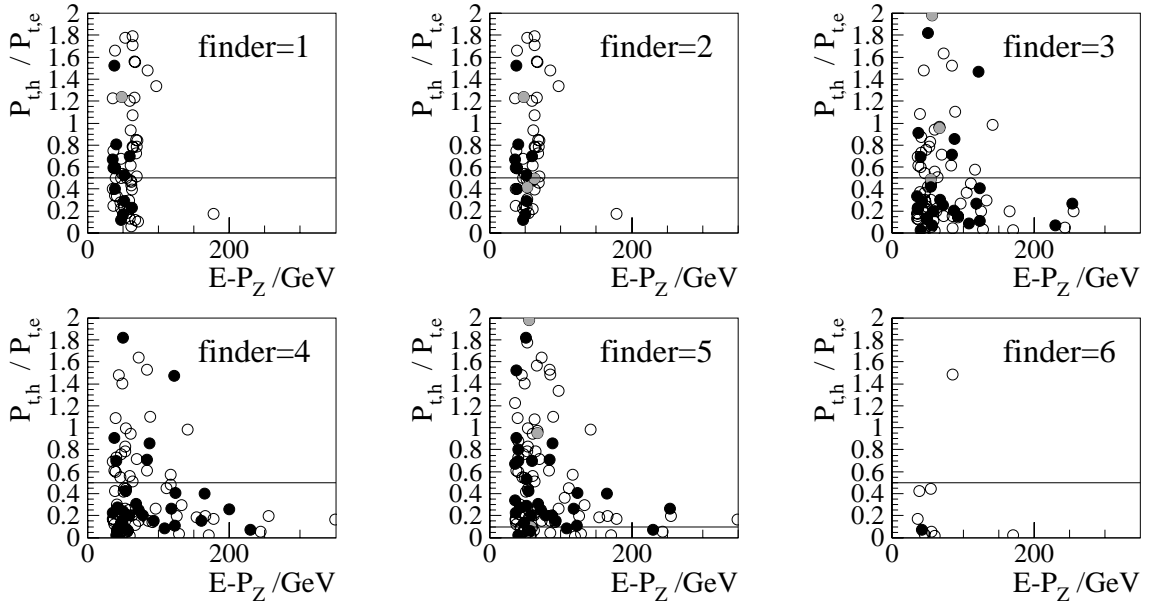


**Figure 5.32:** Events found by background finders which are rejected in the restricted scheme (see text). Black (gray) points in the figure correspond to events recognised by visual scan as background (genuine NC) events.

Finally, all events with  $Q^2 > 10\,000 \text{ GeV}^2$  and one third of the events with  $Q^2 > 5\,000 \text{ GeV}^2$  have been visually scanned and the remaining non- $ep$  background has been removed. The examples of visual scan of the NC DIS events in the highest  $Q^2$  region and cosmic and halo-muon background events are shown in appendix D.



## Chapter 6

# Selection of NC Events

The major part of the data used in this analysis are based on the  $e^+p$  collisions. They are collected in 1999 and 2000 at the centre of mass energy of 319 GeV. The corresponding integrated luminosity is  $65.2 \text{ pb}^{-1}$ . After an upgrade of the LAr trigger electronics in the 1998 winter shutdown it became possible to trigger the scattered electrons down to energy as low as 6 GeV (see section 5.6). This possibility is fully exploited in this analysis both for  $e^+p$  data and  $e^-p$  data. Integrated luminosity of  $16.5 \text{ pb}^{-1}$  of  $e^-p$  data were collected in 1998 and 1999 with  $\sqrt{s} = 319 \text{ GeV}$ . For  $Q^2$  range  $150 \text{ GeV}^2 < Q^2 \leq 890 \text{ GeV}^2$ ,  $y < 0.63$  and  $Q^2 > 890 \text{ GeV}^2$ ,  $y < 0.9$  the inclusive  $e^-p$  cross section measurements were published in [39]. In this analysis this measurement is extended to  $y < 0.9$  for  $Q^2 < 890 \text{ GeV}^2$ .

### 6.1 Run Selection

Depending on the overall detector performance, background situation, problems with readout and so on, all runs are classified as "good", "medium" or "poor". For this analysis only "good" and "medium" runs are selected. Furthermore, for each run it is checked that all important hardware components are fully operational (supplied by high voltage, HV) and included in the readout. These components are the LAr calorimeter and the LAr trigger, the central drift chambers (CJC1 and CJC2) and the proportional chambers (CIP and COP), the luminosity system, SpaCal and the ToF system. The information about the high voltage (HV) status of each hardware component during data taking was stored in the database every 10 s. A run is rejected if any of the relevant detector components was "off" for a large fraction of time. For selected runs an event is accepted only if it appears at a time when all HV were "on".

## 6.2 Luminosity Calculation and Event Yield

For each run the luminosity is measured using events in which the electron and photon from Bethe-Heitler process are detected in coincidence by the H1 luminosity system (section 2.2.3). The typical precision of the luminosity determination is 1–1.3%.

The HERA proton beam has a complicated longitudinal structure, leading to the presence, besides the main interaction region (*main bunch*), of several neighbouring regions (so called *satellite bunches*) [102]. They manifest themselves in the presence of additional peaks in the  $z_{vtx}$  distribution. For the luminosity calculations the most important is the “late satellite bunch” corresponding to an average  $z$  distance of +70 cm with respect to the nominal interaction point [103]. On the other hand, in the analysis only events with an interaction point within 35 cm around the nominal vertex position are selected (see next section). To take this into account for the luminosity calculation, so called satellite bunch correction, is applied [104]. The correction is typically 5 – 10% with an uncertainty of 0.6 – 1%.

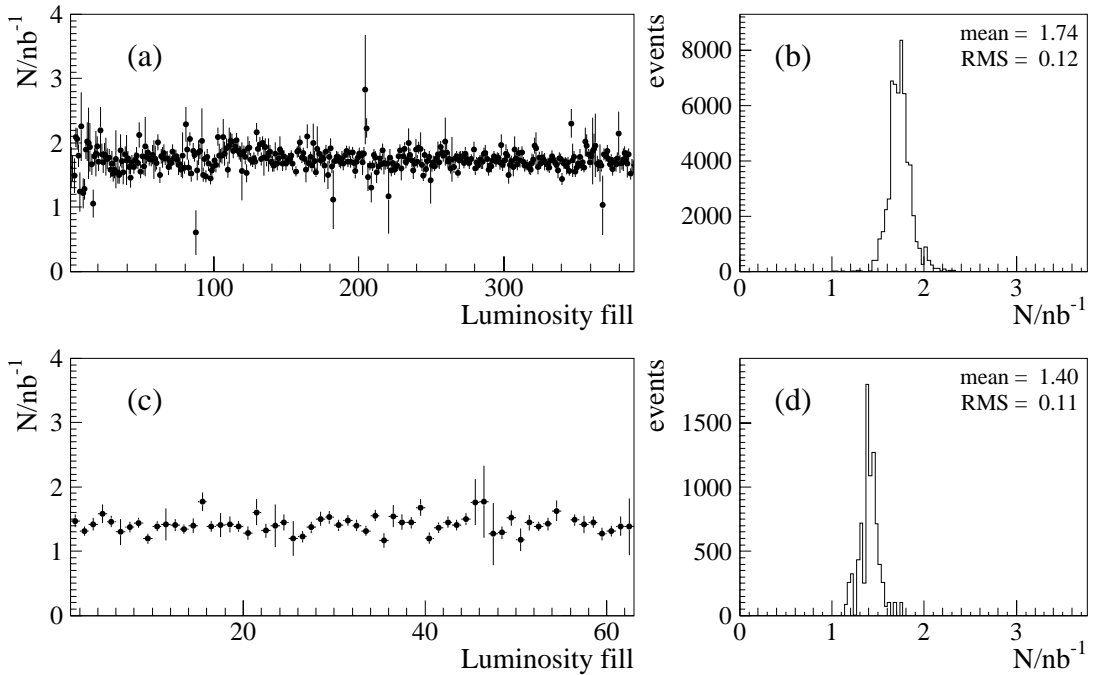


**Figure 6.1:** Number of events per  $nb^{-1}$  as function of luminosity fill (a,c) and projection of event rate of luminosity fill (b,d). On upper plots run range with problems in CJC is excluded, for this run range the event yield and its projection are shown in lower plots.

In the analysis the luminosity corrected for satellite bunches is summed over selected runs and within each run only for periods with all HV “on”. The final uncertainty of the luminosity calculation is 1.5% for the  $e^+p$  sample and 1.8% for the  $e^-p$  sample

[105]. An additional common part of the uncertainty related to the method used for luminosity calculation is taken to be 0.5%.

The event yield, the number of observed events per unity of integrated luminosity ( $\text{nb}^{-1}$ ) after the run and event selection described in section 6.3, is shown in the figure 6.1(a-d) as function of the luminosity fill. The yield is shown for two run ranges. The second run range (c,d) correspond to period with broken CJC wire when a certain  $\phi$  range is excluded from the analysis (see section 5.1.4) causing lower event yield. For both run ranges the event yield is stable over the whole running period.

## 6.3 Neutral Current Selection Criteria

The criteria used for the selection of the NC events are summarised below:

- Run selection.
- Event triggered by the subtriggers ST67, ST77, ST71 or ST75.
- Electron identified by the electron finding algorithm.
- For  $\theta_e > 35^\circ$  electron validated by a DTRA or DTNV track.
- Electron energy  $E_e' > 6$  GeV.
- "Central" or "forward" vertex with  $|z_{vtx} - \langle z_{vtx} \rangle| < 35$  cm.
- Exclude  $z$  and  $\phi$  cracks:  
 $|\phi_e - n \cdot 45^\circ| < 2^\circ$ ,  $n = 0, 1, \dots, 7$ ;  $25 \text{ cm} < z_{LAr} < 15 \text{ cm}$
- Time dependent trigger fiducial volume.
- Cuts against QED Compton and lepton pair events on the basis of their topology, low track multiplicity ( $N_{track} \leq 2$ ), low hadronic energy ( $E_{had}/E_{em} < 0.1$ ) and low activity outside electromagnetic clusters.
- Rejection of cosmic and halo-muon events identified by background finding algorithms.
- Visual inspection of all events with  $Q^2 > 10000 \text{ GeV}^2$  and one third of the events with  $Q^2 > 5000 \text{ GeV}^2$ .
- Transverse momentum balance:  $R_{P_T} = P_{T,h}/P_{T,e} < 2$ .
- Longitudinal momentum balance:  $E - P_z > 35 \text{ GeV}$ .
- $y_e < 0.9$ .

## 6.4 Neutral Current Data Samples

The full kinematic range covered in this analysis is  $90 \text{ GeV}^2 < Q^2 < 30\,000 \text{ GeV}^2$ . Since the photoproduction background increases with increasing  $y$  (low  $E'_e$ ) the analysis is separated into two regions where different techniques to suppress this background are employed (see section 5.8).

### Nominal analysis

The region of the *nominal analysis* is defined as  $y_e < 0.63$  for  $90 \text{ GeV}^2 < Q_e^2 < 890 \text{ GeV}^2$  and  $y_e < 0.90$  for  $Q_e^2 > 890 \text{ GeV}^2$ . For the  $e^-p$  data the results from the analysis in the similar range, with  $Q^2 > 150 \text{ GeV}^2$ , are already published in [39]. For the  $e^+p$  data the nominal data sample consists of about 130 000 events. Figure 6.2 shows the control distributions for the scattered electron energy for  $Q^2 > 100 \text{ GeV}^2$  (a) and  $Q^2 > 5000 \text{ GeV}^2$  (b). The polar and azimuthal angles of the scattered electron are shown in figure 6.3(a) and (b), respectively. All distributions are well described by the simulation. The event kinematics in the nominal analysis are reconstructed using the  $e\Sigma$  method, which uses  $E'_e$ ,  $\theta_e$  and  $E_h - P_{z,h}$  (see section 4) and has the best resolution and least sensitivity to QED radiative corrections over the accessible phase space. Figure 6.4 demonstrates good description of the kinematic variables, the  $Q_e^2$  (a), Bjorken- $x$  (b) and  $y_{e\Sigma}$  (c), by the simulation.

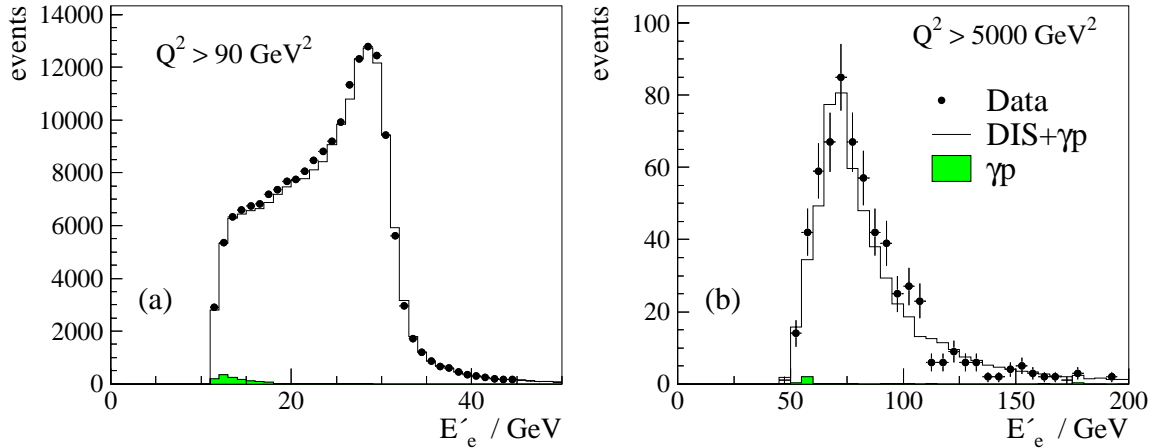


**Figure 6.2:** The scattered electron energy spectra for the 99-00  $e^+p$  nominal analysis,  $Q^2 > 90 \text{ GeV}^2$  (a), and for  $Q^2 > 5\,000 \text{ GeV}^2$  (b).

### High $y$ analysis

The *high  $y$  analysis* is defined by the region of high inelasticity  $y$  for lower  $Q^2$ , i.e.  $E'_e > 6 \text{ GeV}$ ,  $0.63 < y_e < 0.90$  for  $90 \text{ GeV}^2 < Q_e^2 < 890 \text{ GeV}^2$ . Both for previously published  $e^-p$  data and the  $e^+p$  data presented here the analysis is extended to this

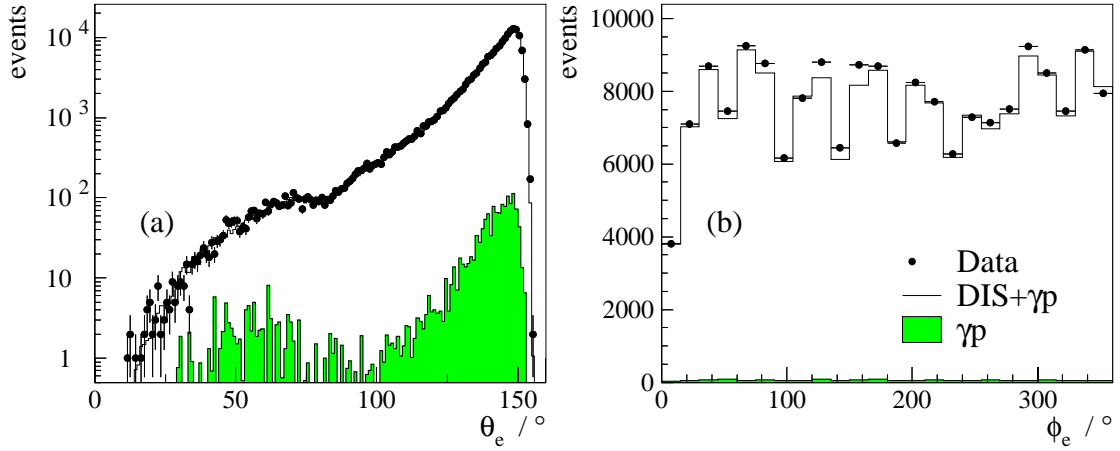


**Figure 6.3:** The polar (a) and the azimuthal (b) angle of the scattered electron for the 99-00  $e^+p$  nominal analysis.

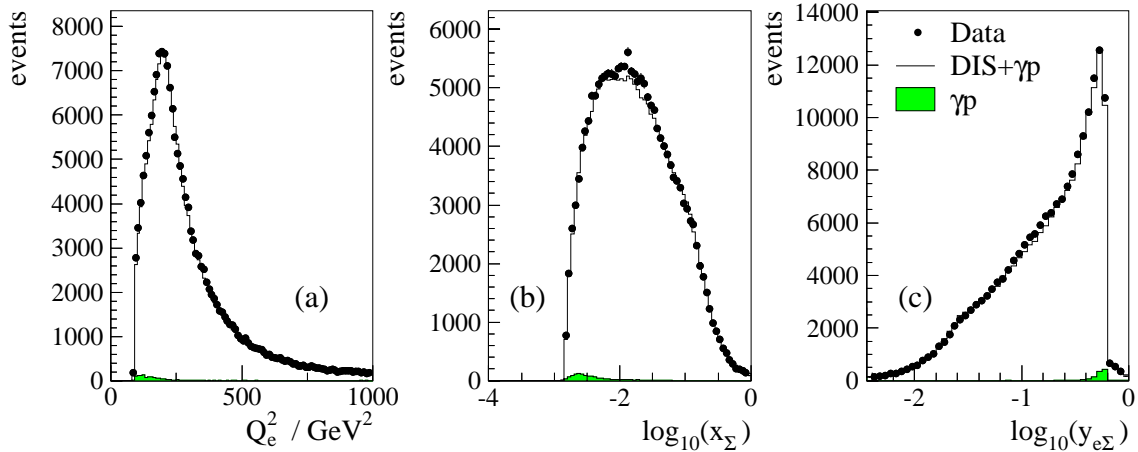


**Figure 6.4:** The distributions of the kinematic variables,  $Q_e^2$  (a),  $x_\Sigma$  (b) and  $y_{e\Sigma}$  (c), reconstructed using the  $e\Sigma$ -method for the 99-00  $e^+p$  nominal analysis.

region<sup>1</sup>.

At high  $y$  which corresponds to the low electron energy the contribution of photoproduction background increases, see figures 6.5(a) and 6.6(a). In order to reduce the uncertainty in the amount of the subtracted background in this region, instead of using MC, the photoproduction background is estimated directly from the data as described in section 5.8.3. For that, in addition to the selection criteria listed in section 6.3 it is required that an electron candidate is validated by a DTRA track,

<sup>1</sup>In the  $e^-p$  data the high  $y$  together with data at  $y < 0.6$  and  $Q^2 < 150 \text{ GeV}^2$  which are not included in [39] are referred to as *extended analysis*.

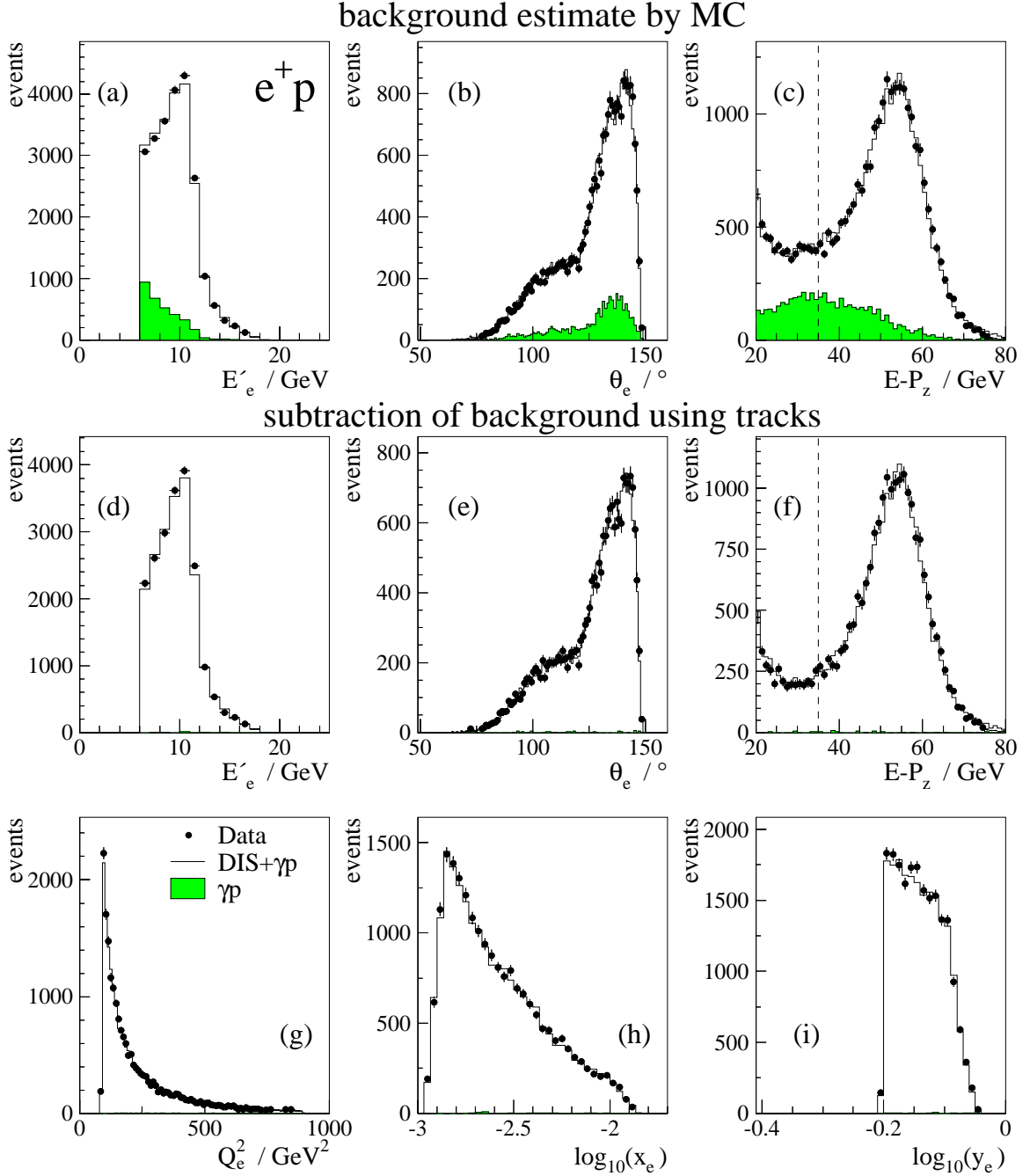


**Figure 6.5:** The control of the data description by the simulation for the 99-00  $e^+p$  high- $y$  analysis. The scattered electron energy  $E'_e$  (a), the electron polar angle  $\theta_e$  (b) and longitudinal momentum balance  $E - P_z$  (c) before subtraction of background (see text). The distributions of  $E'_e$ ,  $\theta_e$  and  $E - P_z$  after subtracting the background using information from tracks are shown in (d), (e), (f), respectively. The dashed line in (c) and (f) indicates the cut  $E - P_z > 35 \text{ GeV}$ . Also shown are the kinematic variables reconstructed using electron method,  $Q_e^2$  (g),  $x_e$  (h) and  $y_e$  (i).

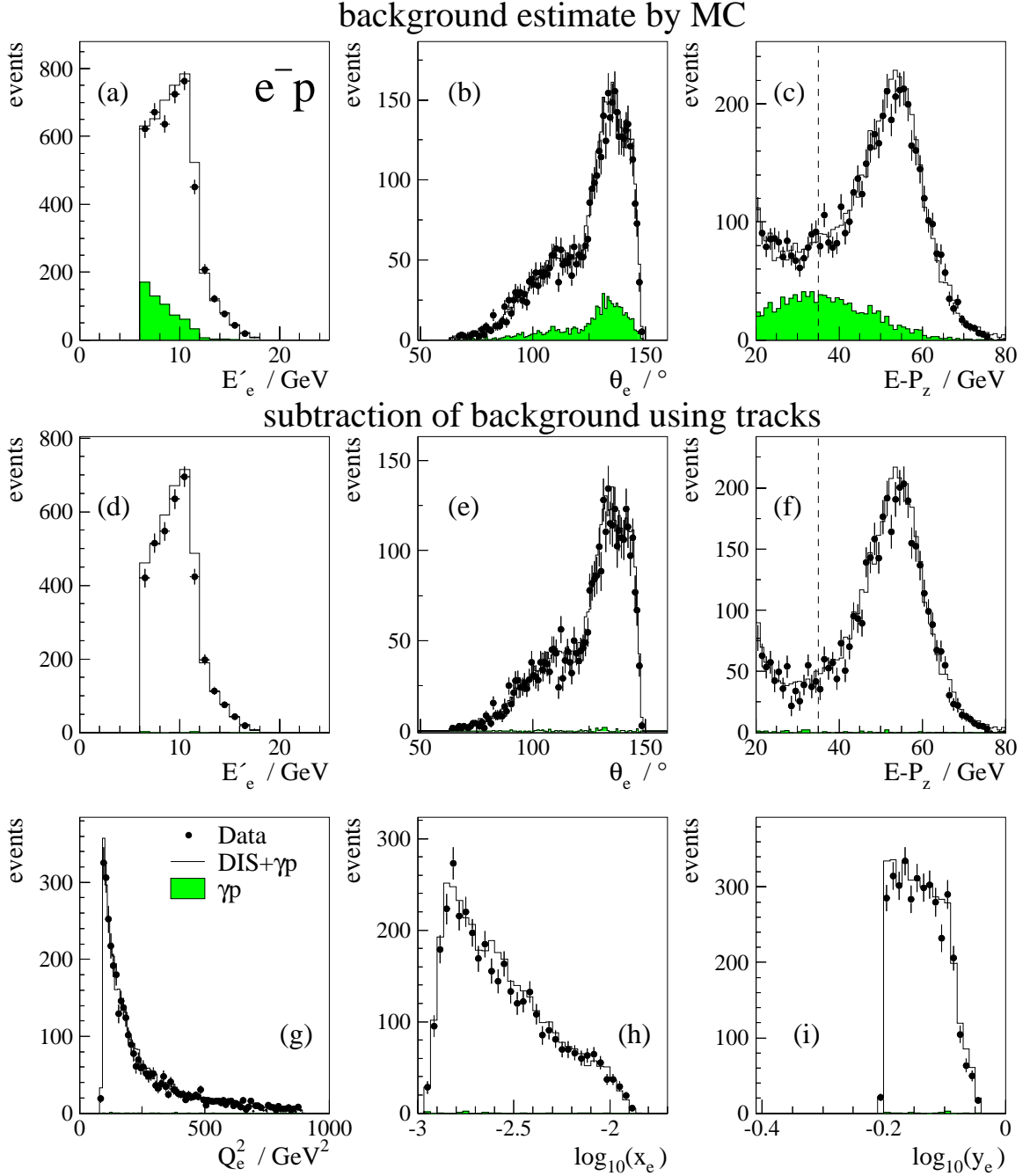


**Figure 6.6:** Control of the data description by MC for the 98-99  $e^-p$  high- $y$  analysis. The scattered electron energy  $E'_e$  (a), the electron polar angle  $\theta_e$  (b) and longitudinal momentum balance  $E - P_z$  (c) before subtraction of background (see text). The distributions of  $E'_e$ ,  $\theta_e$  and  $E - P_z$  after subtracting the background using information from tracks are shown in (d), (e), (f), respectively. The dashed line in (c) and (f) indicates the cut  $E - P_z > 35$  GeV. Also shown are the kinematic variables reconstructed using electron method,  $Q_e^2$  (g),  $x_e$  (h) and  $y_e$  (i).

which is needed for the determination of the electric charge of the particle. Only electron candidates with same charge as the beam electrons are accepted. The remaining background with “right charged” electron candidates is estimated from the amount of “wrongly charged” electron candidates, see section 5.8.3.

In total about 24 000  $e^+p$  events and 5 000  $e^-p$  events are selected in *high-y analysis*. Figures 6.5 and 6.6 demonstrate the data description by MC for the  $e^+p$  and  $e^-p$  *high-y-analyses*. The figures show the distributions of the energy (a) and polar angle (b) of the scattered electron and the longitudinal momentum balance  $E - P_z$  (c) before subtraction of background. The gray histograms indicate the contribution of the background estimated by MC. It can be seen that cut  $E - P_z < 35$  GeV, indicated by dashed line, serves as a powerful cut against photoproduction background. The same distributions after background subtraction using information from the tracking system are shown in figures 6.5(d-f) and 6.6(d-f). The signal in these distributions is as in the distributions for background estimate by MC, figures 6.5(a-c) and 6.6(a-c), but the background is fully suppressed.

In the *high-y analysis* the electron method (see section 4) is used for reconstruction of the event kinematics. The figures 6.5 and 6.6 show the distributions for kinematic variables  $Q_e^2$ , Bjorken- $x$  and inelasticity  $y$  reconstructed using electron-method for  $e^+p$  and  $e^-p$ . The distributions are in both cases well described by the simulation.



## Chapter 7

# Cross Section Measurement Procedure

In this section the procedure for determination of the cross section is described. First, the kinematic plane is divided into  $x$  and  $Q^2$  bins using the resolution, acceptance, stability and purity as criteria for this division. The  $x-Q^2$  bins in which the kinematic plane is divided for the measurement presented here follows the binning used in the previous measurements [32,39]. Then the discussion concentrates on the cross section determination from the measured number of events in each bin and the systematic uncertainties considered in the measurement.

In order to improve statistical precision for the determination of the longitudinal structure function  $F_L$  and the structure function  $xF_3$  the cross section measurements in the neighbouring  $Q^2$  bins are combined. The section concludes with the comparison of the double differential cross section presented here and published in [29].

### 7.1 Bin Definitions in $x - Q^2$ Plane

The cross section measurement in this analysis is performed in bins of  $x$  and  $Q^2$ . The binning is illustrated in figure 7.1 and the bin centres and bin boundaries are given in the table C.1. There are ten bins per decade in  $Q^2$  and five bins per decade in  $x$ . At  $Q^2 \geq 3000 \text{ GeV}^2$  the bin size is doubled due to limited statistics. At  $Q^2 \leq 500 \text{ GeV}^2$  and  $x > 0.1$  the binning is also modified to accommodate to the limited  $x$  resolution. The resolution is always better than the width of bin [35].

For control of the migration of the events from one bin to another due to ISR (see section 1.8) the purity ( $\mathcal{P}$ ), stability ( $\mathcal{S}$ ) and acceptance ( $\mathcal{A}$ ) are used. They are

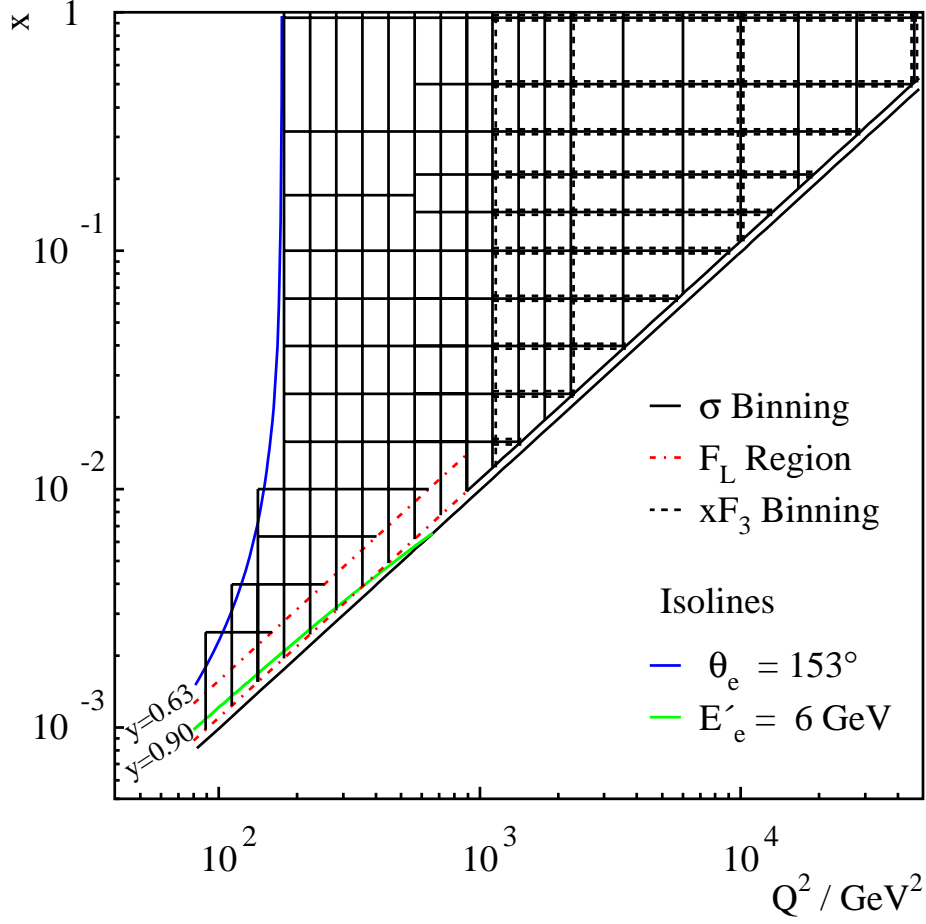


**Figure 7.1:** Division of the kinematic plane in  $Q^2$  and  $x$  bins. The dashed-dotted lines indicate the region of sensitivity to the longitudinal structure function  $F_L$  (high- $y$  analysis). The dashed lines show the combined  $Q^2$  bins for the determination of the structure function  $xF_3$ .

calculated using the MC simulation which includes the radiative effects according to:

$$\mathcal{P}(i) = N_{rec+gen}^{MC}(i)/N_{rec}^{MC}(i) \quad (7.1)$$

$$\mathcal{S}(i) = N_{rec+gen}^{MC}(i)/N_{gen+sel}^{MC}(i) \quad (7.2)$$

$$\mathcal{A}(i) = N_{rec}^{MC}(i)/N_{gen}^{MC}(i) \quad (7.3)$$

where

- $N_{rec+gen}^{MC}(i)$  is the number of events generated and reconstructed in bin  $i$ ;
- $N_{gen}^{MC}(i)$  is the number of events generated in bin  $i$ ;
- $N_{gen+sel}^{MC}(i)$  is the number of events generated in bin  $i$  and passing all selection criteria (i.e. reconstructed in any bin);

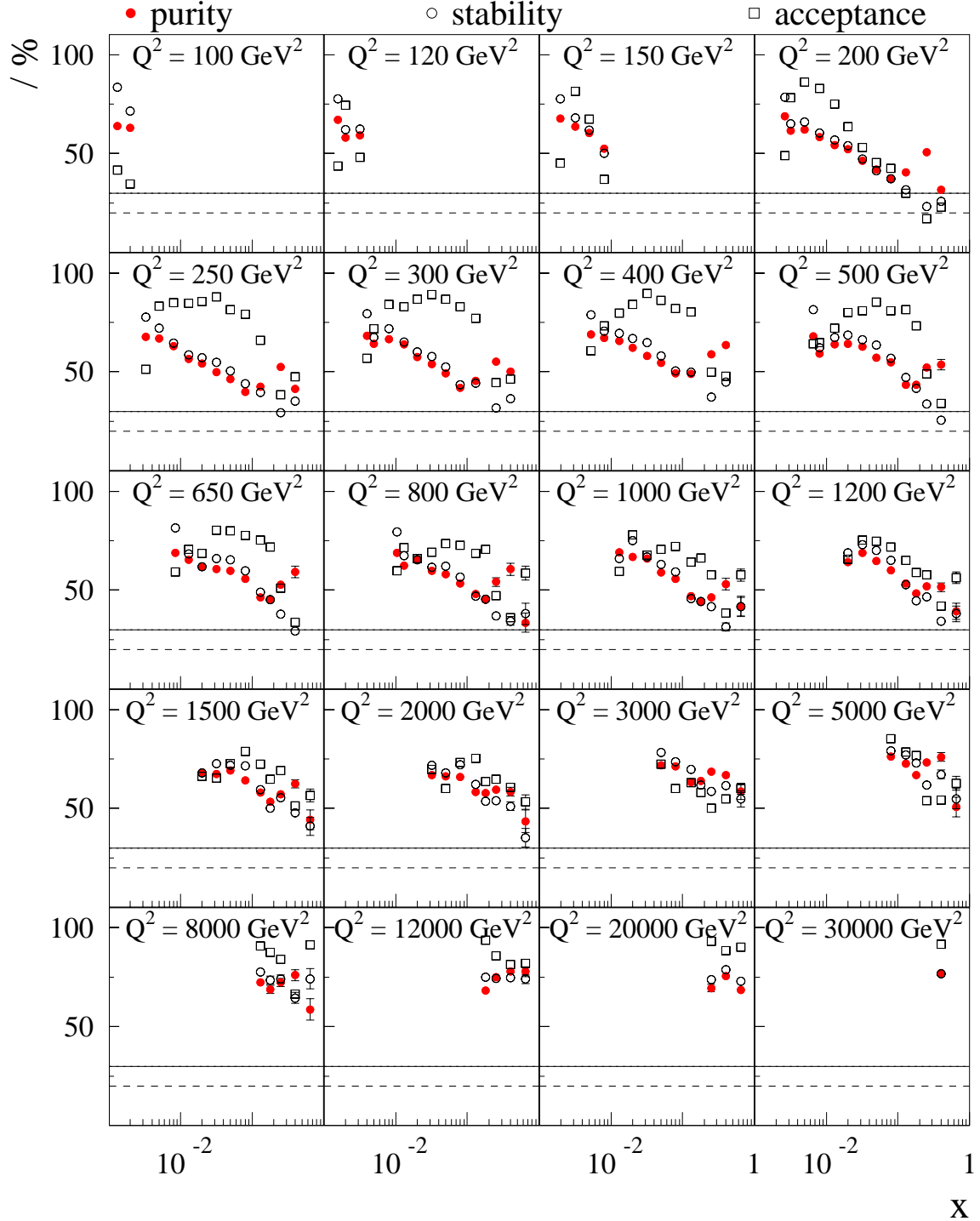


**Figure 7.2:** Purity (solid points), stability (open points) and acceptance (open squares) as function of  $x$  in bins of  $Q^2$ . Solid lines indicate the minimum purity and stability of 30% and the dashed lines the 20% required for the acceptance.

- $N_{rec}^{MC}(i)$  is the number of events reconstructed in bin  $i$ .

The purity, stability and the acceptance in  $x - Q^2$  bins are shown in figure 7.2. The cross section measurement is performed in bins in which the purity and stability are larger than 30% and the acceptance larger than 20%.

## 7.2 Extraction of Cross Section

The cross section measured in a single bin in  $x$  and  $Q^2$  is given by:

$$\frac{d^2\sigma}{dx dQ^2} = \frac{N^{data} - N^{bg}}{\mathcal{L} \cdot \mathcal{A}} \cdot \delta^{bc} \quad (7.4)$$

where

- $N^{data}$  is the number of selected events in a bin;
- $N^{bg}$  is the number of background events;
- $\mathcal{L}$  is the total integrated luminosity;
- $\mathcal{A}$  is the detector acceptance, as defined in equation 7.3, determined from MC which includes radiative corrections;
- $\delta^{bc}$  is the correction from the cross section in a bin of finite size  $\Delta x_i = x_{i,max} - x_{i,min}$  and  $\Delta Q^2_i = Q^2_{i,max} - Q^2_{i,min}$  to the bin centre  $(x_{i,c}, Q^2_{i,c})$ :

$$\delta_i^{bc} = \frac{\left. \frac{d^2\sigma}{dx dQ^2} \right|_{x=x_{i,c}, Q^2=Q^2_{i,c}}}{\int_{x_{i,min}}^{x_{i,max}} \int_{Q^2_{i,min}}^{Q^2_{i,max}} \frac{d^2\sigma}{dx dQ^2} dx dQ^2};$$

The acceptance and the bin centre corrections are obtained from the MC simulation which includes the radiative corrections calculated using the program HERACLES [66] as implemented in DJANGO [106]. In this case formula 7.4 can be simplified to [35]:

$$\frac{d^2\sigma}{dx dQ^2} = \frac{N^{data} - N^{bg}}{N_{rec}^{MC}} \cdot \frac{\mathcal{L}_{MC}}{\mathcal{L}} \frac{d\sigma^{MC}}{d^2x dQ^2}. \quad (7.5)$$

Here  $\mathcal{L}^{MC}$  is the luminosity of the MC sample and  $N_{rec}^{MC}$  the number of MC events reconstructed in a bin.

## 7.3 Systematic Uncertainties

The uncertainties related to the performance of the detector lead to systematic errors on the cross section measurement. A distinction to errors which are correlated between all bins (bin-to-bin correlated errors) and errors which are uncorrelated from bin to bin is made. For instance, a correlated error on the hadronic energy measurement of 1% means that it is possible for the hadronic energy scale to differ from the "true" hadronic energy scale by 1%. The uncorrelated errors are assumed to be due to local fluctuations or deficiencies. The trigger efficiency can be different by 0.5% at low  $Q^2$  in a certain calorimeter region, but this has no impact on the efficiency at high  $Q^2$ . Some sources of errors are treated to be partially correlated and partially uncorrelated. All systematic errors are found to be symmetric to a good approximation and are assumed so in the following.

The total systematic error is formed by adding the individual errors in quadrature. In addition, there is a global uncertainty of 1.5% and 1.8% on the luminosity measurement for the  $e^+p$  and  $e^-p$  data, respectively, of which 0.5% is common to both.

- **The electron energy measurement**

The total uncertainty comes mainly from the possible bias of the calibration method and is estimated to be:

- for  $z_{LAR} < -150$  cm            1%;
- for  $-150$  cm  $< z_{LAR} < 20$  cm    0.7%;
- for  $20 < z_{LAR} < 100$  cm        1.5%;
- for  $z_{LAR} > 110$  cm            3%.

The correlated part of the total uncertainty comes mainly from the possible bias of the calibration method and is estimated to be 0.5% throughout the LAr calorimeter. It results in a correlated systematic error on the NC cross section which is typically below 1%, increasing at low  $y$  to  $\sim 3\%$  for  $Q^2 \lesssim 1000$  GeV<sup>2</sup> and  $\sim 8\%$  for larger  $Q^2$ .

- **The polar angle of the scattered electron**

The correlated uncertainty on the electron polar angle is

- for  $\theta_e > 135^\circ$             1 mrad,
- for  $135^\circ > \theta_e > 120^\circ$     2 mrad,
- for  $\theta_e < 120^\circ$             3 mrad.

This leads to a typical uncertainty on the reduced cross section of less than 1%, increasing up to  $\sim 5\%$  at high  $x$ .

- **The efficiency of the electron identification**

- for  $z_{LAR} < -5$  cm:    0.5% uncorrelated uncertainty in the nominal analysis  
                                  1% uncorrelated uncertainty in the high- $y$  analysis
- for  $z_{LAR} > -5$  cm:    2% uncorrelated uncertainty.

- **Efficiency of electron validation using tracks**

For the efficiency of the scattered electron track-cluster link requirement an uncorrelated error is estimated to be:

- in the nominal analysis 0.5%;
- in the high- $y$  analysis 1%.

- **Hadronic energy measurement**

**LAr calorimeter:**

- for  $12 \text{ GeV} < P_{T,h} < 50 \text{ GeV}$  and  $\gamma_h > 15^\circ$  1% uncorrelated error;
- outside this region 1.7% uncorrelated error.

A 1% correlated component to the uncertainty is added in quadrature. This yields a total uncertainty of 1.4% and 2% for the two regions respectively.

**Contributions from SpaCal and tracking system:**

- SpaCal 5% correlated uncertainty;
- tracking system 3% correlated uncertainty.

The resulting correlated systematic error (from LAr calorimeter, SpaCal and tracks) is typically  $\lesssim 1\%$  but increases at low  $y$  to  $\sim 5\%$ .

- **Noise subtraction in the LAr calorimeter**

A 25% uncertainty on the amount of energy in the LAr calorimeter attributed to noise. This gives rise to a sizeable correlated systematic error in the measurements at low  $y$ , reaching  $\simeq 10\%$  at  $x = 0.65$  and  $Q^2 \lesssim 2000 \text{ GeV}^2$ .

- **Photoproduction background estimated by MC**

In the nominal analysis the photoproduction background is estimated from simulation. A 30% uncertainty on the subtracted photoproduction background is considered. This results in a correlated systematic error of typically  $\lesssim 1\%$ .

- **Charge symmetry of the photoproduction background**

In the high- $y$  analysis the photoproduction background is estimated directly from the data by using wrongly charged scattered electron candidates. A 10% correlated uncertainty on the charge symmetry of the photoproduction background in the high- $y$  analysis is taken into account. The resulting uncertainty on the measured cross sections is found to be  $\lesssim 1\%$ .

- **Trigger efficiency**

A 0.3% uncorrelated error is considered on the trigger efficiency in the nominal analysis.

For the high- $y$  analysis the uncertainty on the cross section is  $\lesssim 2\%$  at low  $Q^2$ , decreasing to 0.5% at the highest  $Q^2$  in the analysis:

|                     |     |     |     |     |     |     |     |     |     |     |
|---------------------|-----|-----|-----|-----|-----|-----|-----|-----|-----|-----|
| $Q^2$               | 100 | 120 | 150 | 200 | 250 | 300 | 400 | 500 | 650 | 800 |
| $\delta_\epsilon\%$ | 2.3 | 1.  | 0.7 | 0.6 | 0.7 | 0.5 | 0.6 | 0.5 | 0.5 | 0.5 |

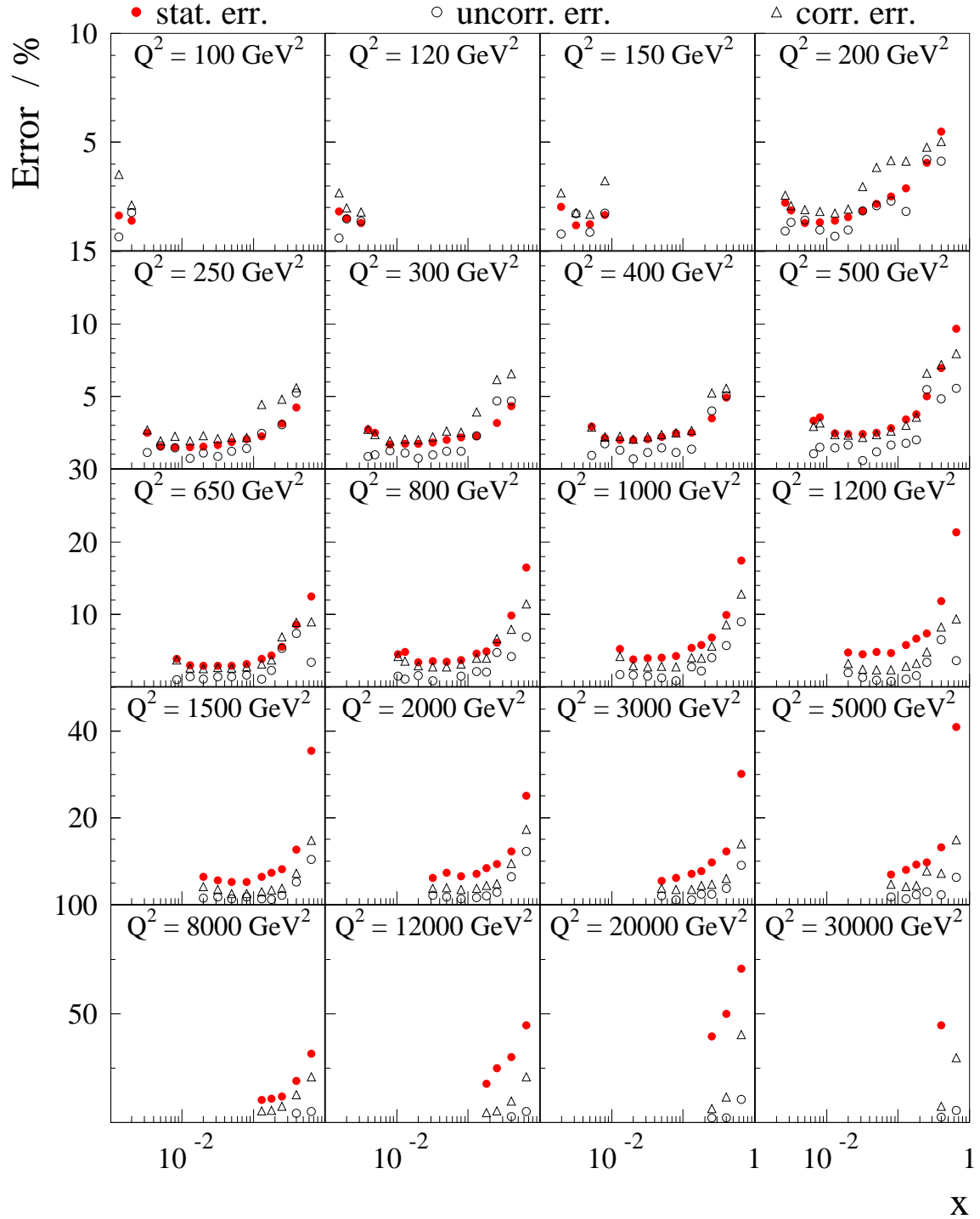


**Figure 7.3:** Statistical (solid points), uncorrelated (open points) and correlated (open triangles) errors of the reduced cross section  $\tilde{\sigma}_{NC}$ .

- **QED radiative corrections**

An uncorrelated error of 1% is estimated on the QED radiative corrections by comparing the radiative corrections used in the Monte Carlo program (DJANGO) with those calculated from HECTOR and EPRC [107]. The error also includes a small missing correction in DJANGO due to the exchange of two or more photons between the lepton and the quark lines.

Figure 7.3 shows statistical, uncorrelated and correlated errors for the measurement of the reduced cross section. For  $Q^2 < 300$  GeV the systematic error is dominant, typically 3-5%. In this region the systematic error is predominantly coming from the uncorrelated part. At high  $x \geq 0.4$  the correlated error becomes important mainly due to the noise contribution at low  $y$ . In the region of  $Q^2 > 1000$  GeV<sup>2</sup> the statistical error dominates in all bins.

The measured cross section should be independent of the the method used for determination of the event kinematics. Therefore the cross section measurement is cross-checked by comparison of the measurements in which different methods for their determination is used. For example, a bad electron energy calibration would lead to disagreement between the electron and  $\Sigma$ -method. Such a disagreement would also point to inconsistencies in the radiative corrections or bad hadronic energy calibration. These two methods, shown in figure 7.4, give consistent picture. In Figure 7.5 the results obtained using the  $e\Sigma$  and DA methods are compared. These two methods are to large extent independent since the DA is independent of the energy scales while the  $e\Sigma$  method largely relies on them. The comparison between these two methods shows no systematic deviations, giving confidence to the final results obtained using  $e\Sigma$  method.



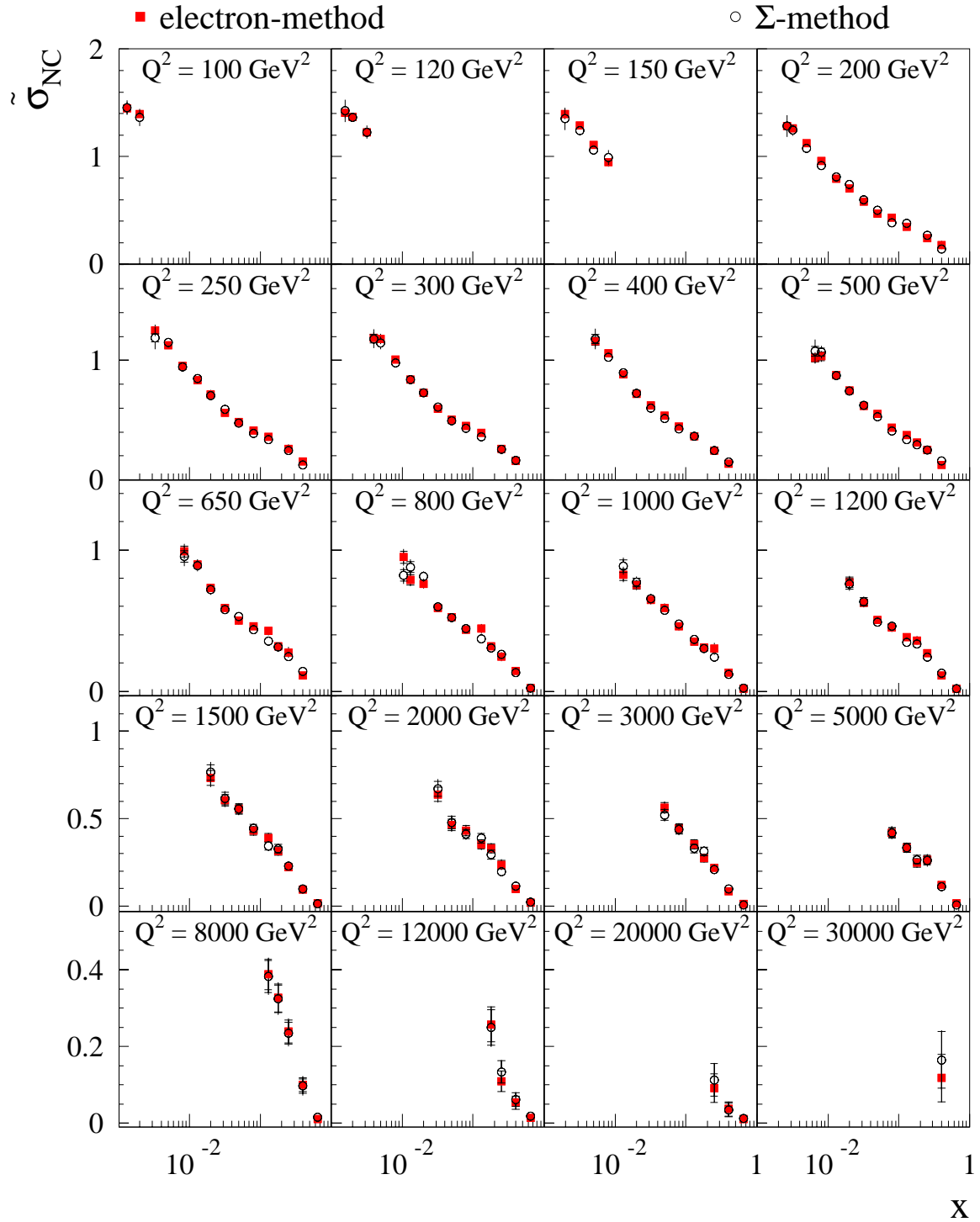


**Figure 7.4:** Comparison of the reduced cross section  $\tilde{\sigma}_{NC}$  measurement obtained using the electron method (solid squares) and  $\Sigma$  method (open points) for the reconstruction of the event kinematics (see section 4).

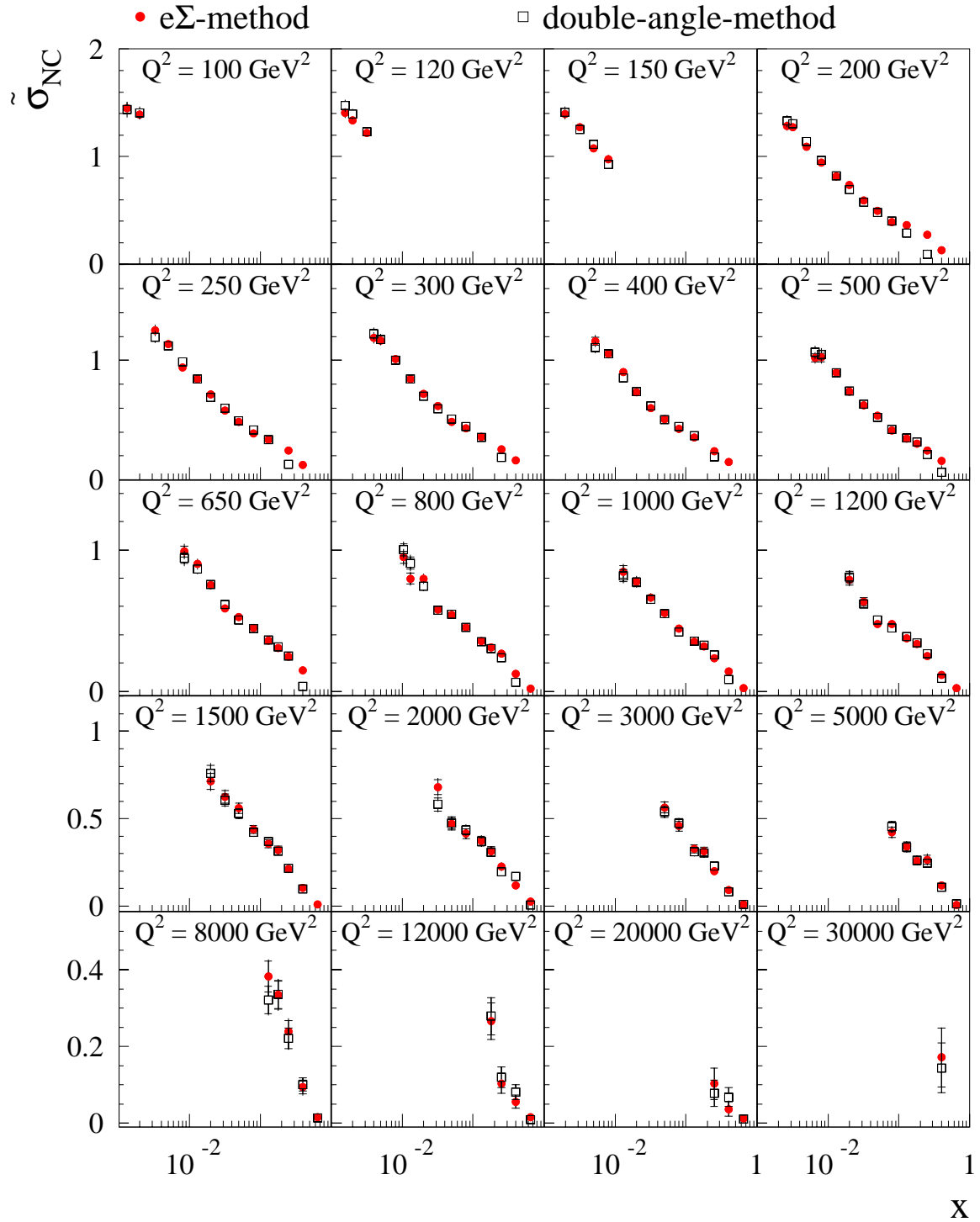


**Figure 7.5:** Comparison of the reduced cross section measurements  $\tilde{\sigma}_{NC}$  using the  $e\Sigma$  method (solid points) and DA method (open squares) for the reconstruction of the kinematic variables method (see section 4).

## 7.4 $Q^2$ Bins Combination of $e^-p$ and $e^+p$ Cross Sections for Determination of $F_L$ and $xF_3$

Because of limited statistics in the region of sensitivity to  $F_L$  (high- $y$ ) and  $xF_3$  (high  $Q^2$ ) the cross section measurements in the neighbouring  $Q^2$  bins are combined. The combination is done using the following formula:

$$\tilde{\sigma}_c = \frac{\sum_i \frac{\int \sigma_i^{th}}{\tilde{\sigma}_i^{th}} \cdot \tilde{\sigma}_i^{data}}{\frac{1}{\tilde{\sigma}_c^{th}} \sum_i \int \sigma_i^{th}} \quad \text{with} \quad \int \sigma_i^{th} = \int_{\text{bin}_i} \frac{d^2 \sigma^{th}}{dx dQ^2} dx dQ^2, \quad (7.6)$$

where  $\tilde{\sigma}_c = \tilde{\sigma}(x_c, Q_c^2)$  is the reduced cross section in the combined bin;  $\tilde{\sigma}_i = \tilde{\sigma}(x_i, Q_i^2)$  is the reduced cross section in the original bins;  $\sigma^{th} = \sigma^{th}(x, Q^2)$  is the NC cross section and  $\tilde{\sigma}_i^{th} = \tilde{\sigma}^{th}(x_i, Q_i^2)$  the reduced cross section calculated using H1 97 PDF Fit [32]. The integration is done within  $y$  range of measured cross section (see figure 7.1). The summation in the formula goes over the bins which are combined. For the determination of the longitudinal structure function  $F_L$ , two neighbouring  $Q^2$  bins are combined (table 7.1) while for the extraction of the structure function  $xF_3$  three  $Q^2$  bins are combined (table 7.2).

The absolute statistical and systematic errors are combined as

$$\delta_c^{stat} = \frac{\sqrt{\sum_i \frac{\int \sigma_i^{th}}{\tilde{\sigma}_i^{th}} \cdot \delta_i^{stat2}}}{\frac{1}{\tilde{\sigma}_c^{th}} \sum_i \int \sigma_i^{th}} \quad \delta_c^{syst} = \frac{\sum_i \frac{\int \sigma_i^{th}}{\tilde{\sigma}_i^{th}} \cdot \delta_i^{syst}}{\frac{1}{\tilde{\sigma}_c^{th}} \sum_i \int \sigma_i^{th}}. \quad (7.7)$$

The Monte Carlo statistical error is combined in the same way as the statistical error from the data and then added to the uncorrelated systematic error.

| $Q_1^2$ GeV <sup>2</sup> | $Q_2^2$ GeV <sup>2</sup> | $Q_c^2$ GeV <sup>2</sup> | $x_c$   | $\Delta\sigma_c$ % |
|--------------------------|--------------------------|--------------------------|---------|--------------------|
| 100                      | 120                      | 110                      | 0.00144 | 0.004              |
| 150                      | 200                      | 175                      | 0.00230 | 0.093              |
| 250                      | 300                      | 280                      | 0.00368 | 0.040              |
| 400                      | 500                      | 450                      | 0.00591 | 0.152              |
| 650                      | 800                      | 700                      | 0.00919 | 0.025              |

**Table 7.1:** The combination of the  $Q^2$  bins for the extraction of longitudinal structure function  $F_L$ . Given are the  $Q^2$  bin centres of the original bins,  $Q_1^2$  and  $Q_2^2$ , and the bin centres of the combined bins  $Q_c^2$ . Also listed are the  $x$  values for combined bins at  $y = 0.75$ .  $\Delta\sigma_c$  denotes the difference of the  $e^+p$  cross section combined using eq. 7.6 and the cross section combined using eq. 7.8.

Since the cross section integrated over the bin  $i$  is proportional to number of events measured in the bin, this method of combining cross sections is very close to the

| $Q_1^2$ GeV <sup>2</sup> | $Q_2^2$ GeV <sup>2</sup> | $Q_3^2$ GeV <sup>2</sup> | $Q_c^2$ GeV <sup>2</sup> | $x$   |
|--------------------------|--------------------------|--------------------------|--------------------------|-------|
| 1200                     | 1500                     |                          | 1500                     | 0.020 |
| 1200                     | 1500                     | 2000                     | 1500                     | 0.032 |
| 1200                     | 1500                     | 2000                     | 1500                     | 0.050 |
| 1200                     | 1500                     | 2000                     | 1500                     | 0.080 |
| 3000                     |                          |                          | 5000                     | 0.050 |
| 3000                     | 5000                     | 8000                     | 5000                     | 0.080 |
| 3000                     | 5000                     | 8000                     | 5000                     | 0.130 |
| 3000                     | 5000                     | 8000                     | 5000                     | 0.180 |
| 3000                     | 5000                     | 8000                     | 5000                     | 0.250 |
| 3000                     | 5000                     | 8000                     | 5000                     | 0.400 |
| 3000                     | 5000                     | 8000                     | 5000                     | 0.650 |
| 12000                    |                          |                          | 12000                    | 0.180 |
| 12000                    | 20000                    |                          | 12000                    | 0.250 |
| 12000                    | 20000                    | 30000                    | 12000                    | 0.400 |
| 12000                    | 20000                    | 30000                    | 12000                    | 0.650 |

**Table 7.2:** The combination of the  $Q^2$  bins for the extraction of the structure function  $xF_3$ . Given are the  $Q^2$  bin centres of the initial bins,  $Q_1^2$ ,  $Q_2^2$  and  $Q_3^2$ , and the bin centres of the combined bins  $Q_c^2$ . The last column lists the bin centres in  $x$ .

direct measurement of the cross section in the combined bin. However, the influence of different cuts, e.g. trigger fiducial cuts, may cause that the number of events in a bin is not proportional to the integrated cross section. This was checked by comparing the cross sections combined using eq. 7.6 and the cross sections combined according to the number of events:

$$\tilde{\sigma}_c = \frac{N_1 \tilde{\sigma}_1^{data} + N_2 \tilde{\sigma}_2^{data}}{N_1 + N_2}. \quad (7.8)$$

As demonstrated in table 7.1 for the combination of bins for  $F_L$  measurement the agreement is found to be within 0.15%.

## 7.5 Consistency of H1 High $Q^2$ analyses

The analysis presented in this thesis has been a part of common efforts of several independent analysis groups in the H1 collaboration which lead to the final results for the high  $Q^2$  data [29]. A very good consistency of the cross section measurements obtained by all analysis groups was achieved.

Figure 7.6 shows the ratios of the  $e^+p$  and  $e^-p$  reduced cross sections as measured in this thesis and on the other side as published in [29]. In the case of the  $e^+p$  cross section for  $Q^2 < 150$  GeV<sup>2</sup> and for  $y = 0.75$  (lowest  $x$ ) at  $Q^2 < 890$  GeV<sup>2</sup> the results

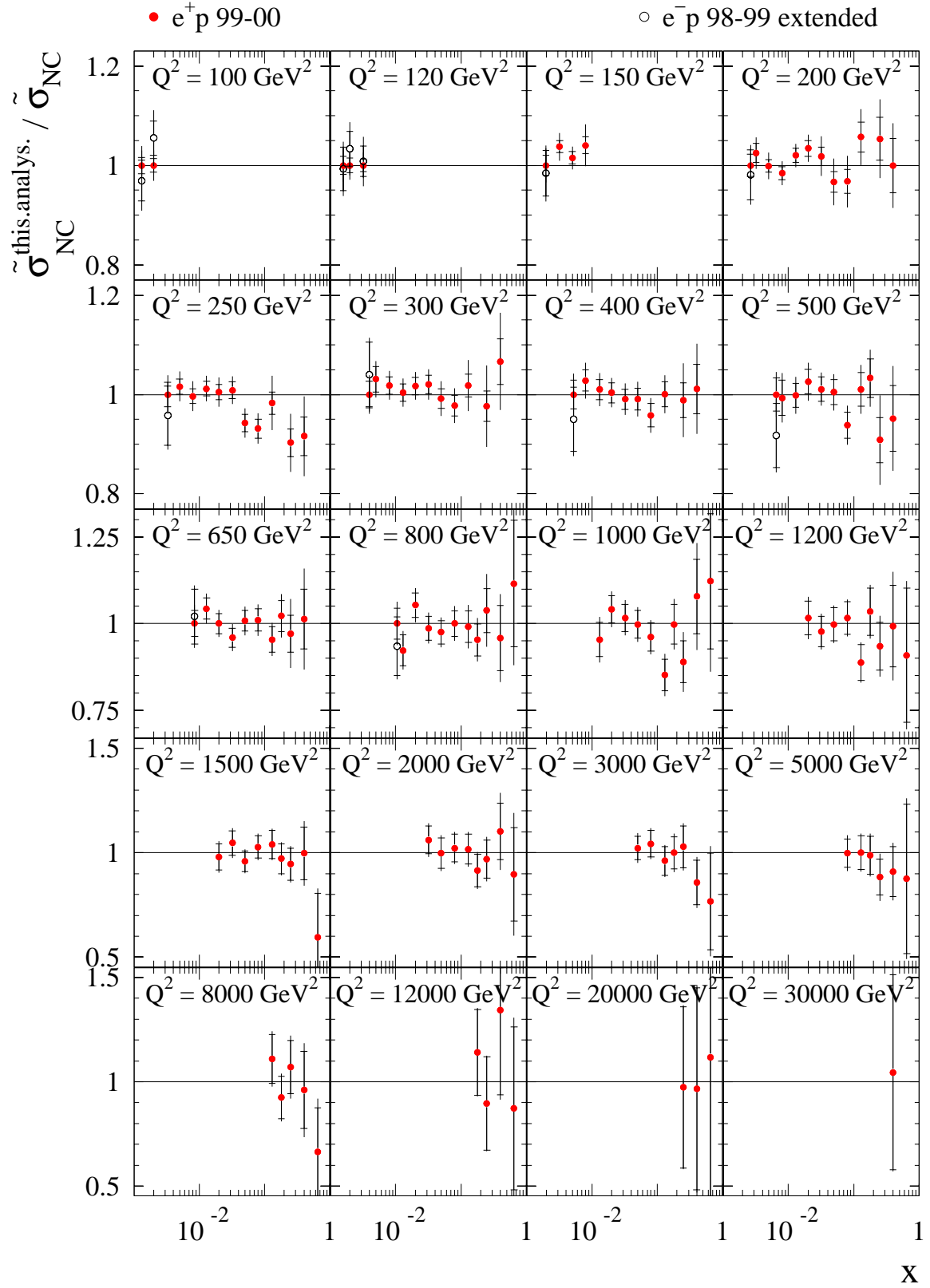


**Figure 7.6:** The ratio of the double differential cross section obtained by the analysis presented here and the results published in [29] for the  $e^+p$  data (solid points) and the  $e^-p$  data (open points). The inner error bars represent the statistical error and the outer the systematic error of this analysis.

of this analysis are taken, therefore the ratio in this region is exactly unity. In the rest of the kinematic domain and for the  $e^-p$  data the differences are within the statistical error of this analysis.

Further discussions of the cross sections and of the structure function measurements in the sections 8 and 9 consider only the results obtained directly in the analysis presented here.

## Chapter 8

# NC Cross Section Results

In this section the results on the neutral current cross section measurements are presented. The cross sections are measured double differentially in  $x$  and  $Q^2$  and single differentially in both of these variables. For the  $e^+p$  data  $d\sigma/dxdQ^2$  is measured in the  $Q^2$  range  $100 < Q^2 < 30000 \text{ GeV}^2$  and  $0.0013 < x < 0.65$  and for the  $e^-p$  data – at highest  $y$  for  $100 < Q^2 < 800 \text{ GeV}^2$ . The  $e^+p$  single differential cross section  $d\sigma/dQ^2$  is measured in the  $Q^2$  range  $200 < Q^2 < 30000 \text{ GeV}^2$ . The measurements of the  $e^+p$  single differential cross section  $d\sigma/dx$  are performed in two  $Q^2$  regions,  $Q^2 > 1000 \text{ GeV}^2$  and  $Q^2 > 10000 \text{ GeV}^2$ . All these measurements are summarised in tables C.2-C.6.

### 8.1 The $e^+p$ and $e^-p$ Double Differential Cross Section $d^2\sigma/dxdQ^2$

The measured  $e^+p$  double differential cross section in the reduced form (see eq. 1.35) is shown in figure 8.1 as a function of  $x$  in bins of  $Q^2$ . The results are compared with previous H1 measurements [32] in a similar kinematic region using, data taken in 94-97 at lower centre of mass energy of  $\sqrt{s} = 301 \text{ GeV}$ . The measurements are in very good agreement over the full kinematic range. The predictions of the H1 PDF 2000 fit (see section 1.7 and appendix A) give good description of both data sets.

The measured cross section is listed in table C.2, where both the reduced cross section and the structure function term,  $\phi_{NC}/Y_+$  (eq. 1.35), are given. The table contains statistical, systematical and total errors. The uncorrelated and correlated parts of the systematical errors together with the contributions from electromagnetic and hadronic energy scales, polar angle measurement, noise and background subtraction are given as well. In the bulk of the kinematic region the statical error is about 1.5 – 3% and the total error is 3 – 4%. The errors are increasing at lowest  $y$ . At high  $Q^2$ ,  $Q^2 > 1000 \text{ GeV}^2$ , the statistical error becomes larger than the systematical error.

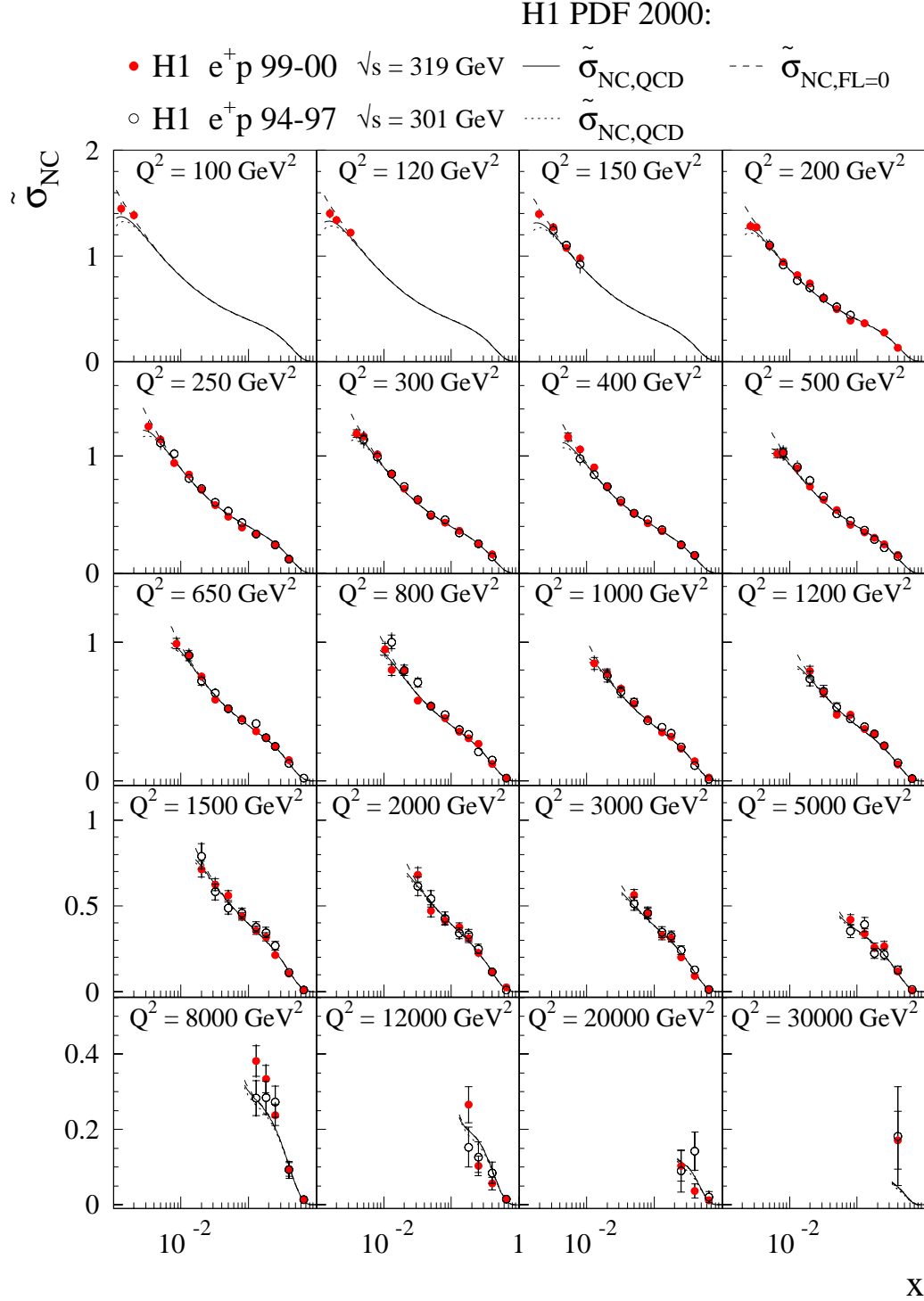


**Figure 8.1:** NC reduced cross section  $\tilde{\sigma}_{NC}$  for the  $e^+p$  99-00 data taken at  $\sqrt{s} = 319$  GeV (solid points) and the  $e^+p$  94-97 data [32] at  $\sqrt{s} = 301$  GeV (open points). The data are compared to the predictions from the H1 PDF 2000 fit (see section 1.7 and appendix A) at  $\sqrt{s} = 319$  GeV (full curve) and  $\sqrt{s} = 301$  GeV (dashed curve). The dotted curve, labelled  $\tilde{\sigma}_{NC,FL=0}$ , represents the expectation obtained from the H1 PDF 2000 fit by excluding the  $F_L$  contribution in the reduced cross section. The inner and outer error bars represent the statistical and total errors, respectively. The 1.5% luminosity uncertainty is not included in the error bars.



With decreasing  $x$ , the data exhibit a strong rise. Because of dominant contribution of the proton structure function  $F_2$ , sensitive to the sea quark distributions (see eqs. 1.31, 1.33), this behaviour can be interpreted to be due to the increase of the sea quark distributions at low  $x$ . This rise of the cross section at lowest  $x$  (highest  $y$ ) departs from the monotonic behaviour of  $F_2$  which indicates a contribution of the longitudinal structure function  $F_L$  to the cross section. In this region of highest  $y$  (lowest  $x$ ) the cross section  $\tilde{\sigma}_{NC}$  is also measured for  $e^-p$  scattering using the data taken in the 98-99 running period. These measurements are shown in figure 8.2 and detailed in table C.6.

The reduced cross section in the high  $x$  region is given in figure 8.3. The figure shows the reduced cross section as a function of  $Q^2$  in different  $x$  bins. The data are

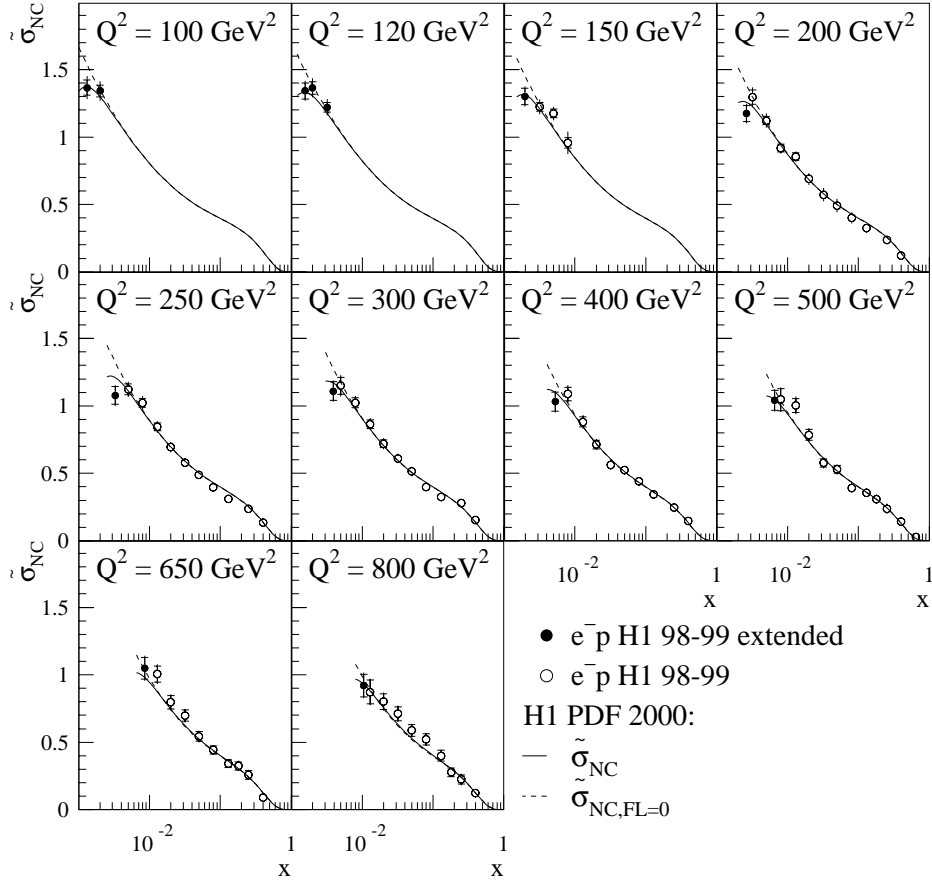


**Figure 8.2:** The NC reduced cross section  $\tilde{\sigma}_{NC}$  from 98-99  $e^-p$  extended analysis (solid points) and previously published results from the same running period (open points) [39]. The full (dashed) curves, labelled  $\tilde{\sigma}_{NC,QCD}$  ( $\tilde{\sigma}_{NC,F_L=0}$ ), show the Standard Model expectations determined from H1 PDF 2000 fit by including (excluding) the  $F_L$  contribution in the reduced cross section. The inner and outer error bars represent the statistical and total error, respectively. The 1.8% luminosity uncertainty is not included in the error bars.

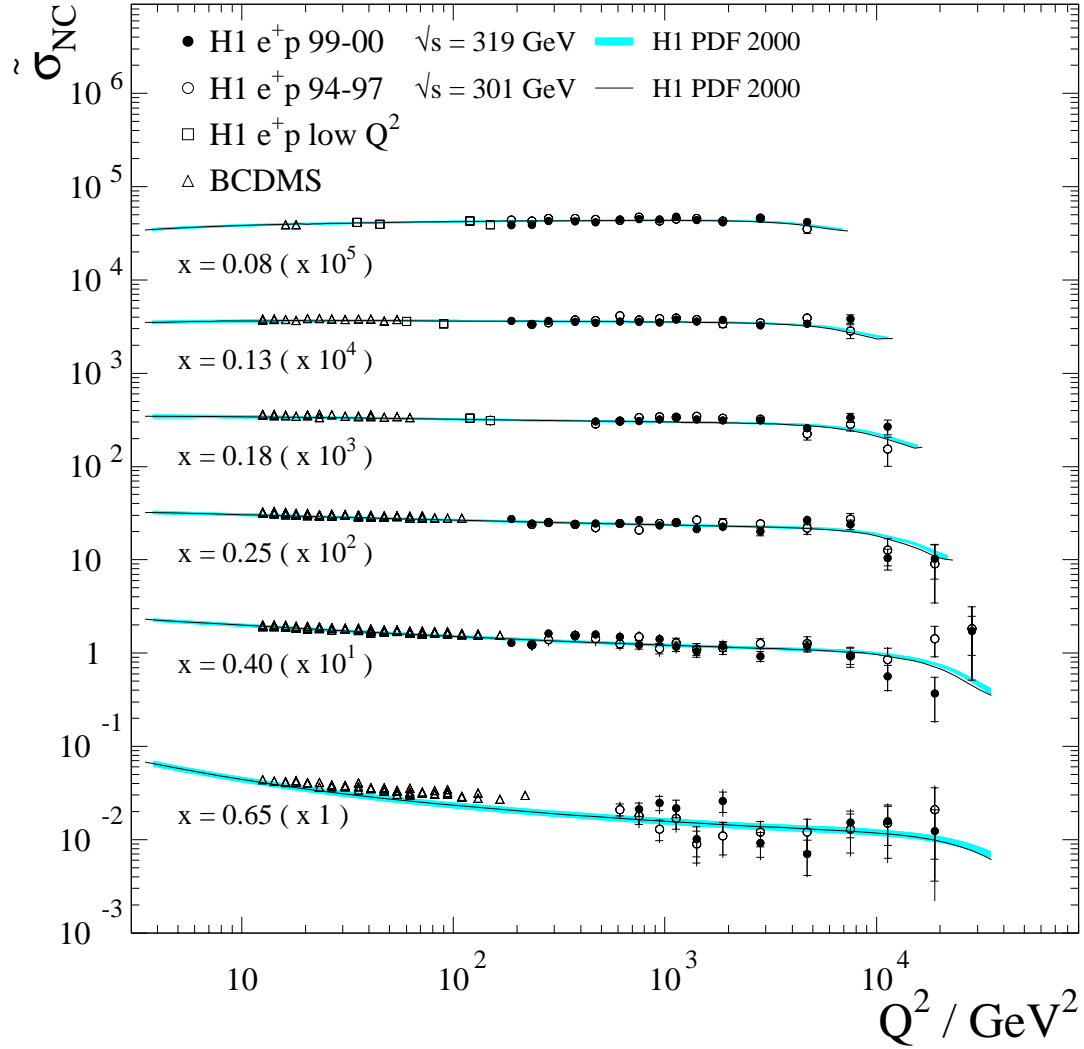


**Figure 8.3:** NC reduced cross sections  $\tilde{\sigma}_{NC}$  at high  $x$  from the 99-00 data (solid points) taken at  $\sqrt{s} = 319$  GeV and 94-97 data at  $\sqrt{s} = 319$  GeV [32] (open points) compared to the H1 PDF 2000 fit. The cross sections measured using the H1 data at low  $Q^2$  [98] (open squares), as well as the results from the fixed-target experiment BCDMS [2] (open triangles) are also shown. The inner and outer error bars represent the statistical and total errors. The luminosity uncertainty is not included in the error bars. The error bands and lines represent the Standard Model expectation based on the H1 PDF 2000 fit for  $\sqrt{s} = 319$  GeV and  $\sqrt{s} = 301$  GeV, respectively.

compared with previous measurements [32]. Both measurements show good agreement with the prediction from the H1 PDF 2000 fit. The figure also shows the H1 results at low  $Q^2$  [98] and BCDMS results from  $\mu$ -proton and  $\mu$ -Deuteron scattering [2]. A fit description of the BCDMS data, which are not used in the fit, is remarkably good except at very large  $x = 0.65$ .

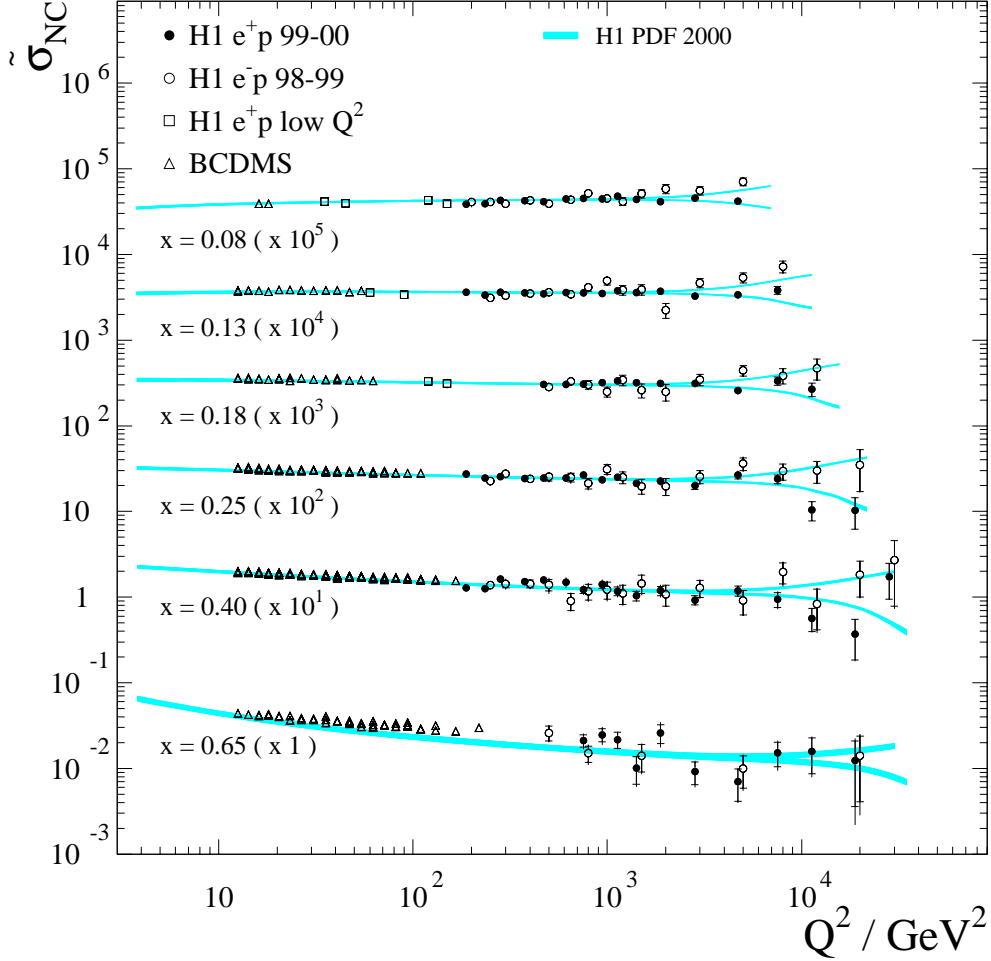


**Figure 8.4:** The NC reduced cross sections  $\tilde{\sigma}_{NC}$  from the  $e^+p$  99-00 data (solid points) and  $e^-p$  98-99 data [39] (open points) at high  $x$  compared to the H1 PDF 2000. The H1 low  $Q^2$  data [98] (open squares) and BCDMS data [2] (open triangles) are also shown. The error bars and bands are defined as for figure 8.3.

A comparison of the  $e^+p$  and  $e^-p$  [39] reduced cross sections at high  $x$  is shown in figure 8.4. At lower  $Q^2$  the measured cross sections are comparable. At the highest  $Q^2$  the effects of  $Z$  exchange become significant mainly via the structure function  $x\tilde{F}_3$ , resulting in decrease (increase) of the  $e^+p$  ( $e^-p$ ) cross section (see eq. 1.29).

## 8.2 The $e^+p$ Single Differential Cross Section $d\sigma/dQ^2$

The single differential cross section  $d\sigma/dQ^2$  for  $y < 0.9$  is shown in figure 8.5 and listed in table C.3. For  $Q^2 < 400 \text{ GeV}^2$  a small correction for a part of the cross section that is unmeasured because of kinematic cut  $E'_e > 6 \text{ GeV}$  (see figure 7.1) is applied

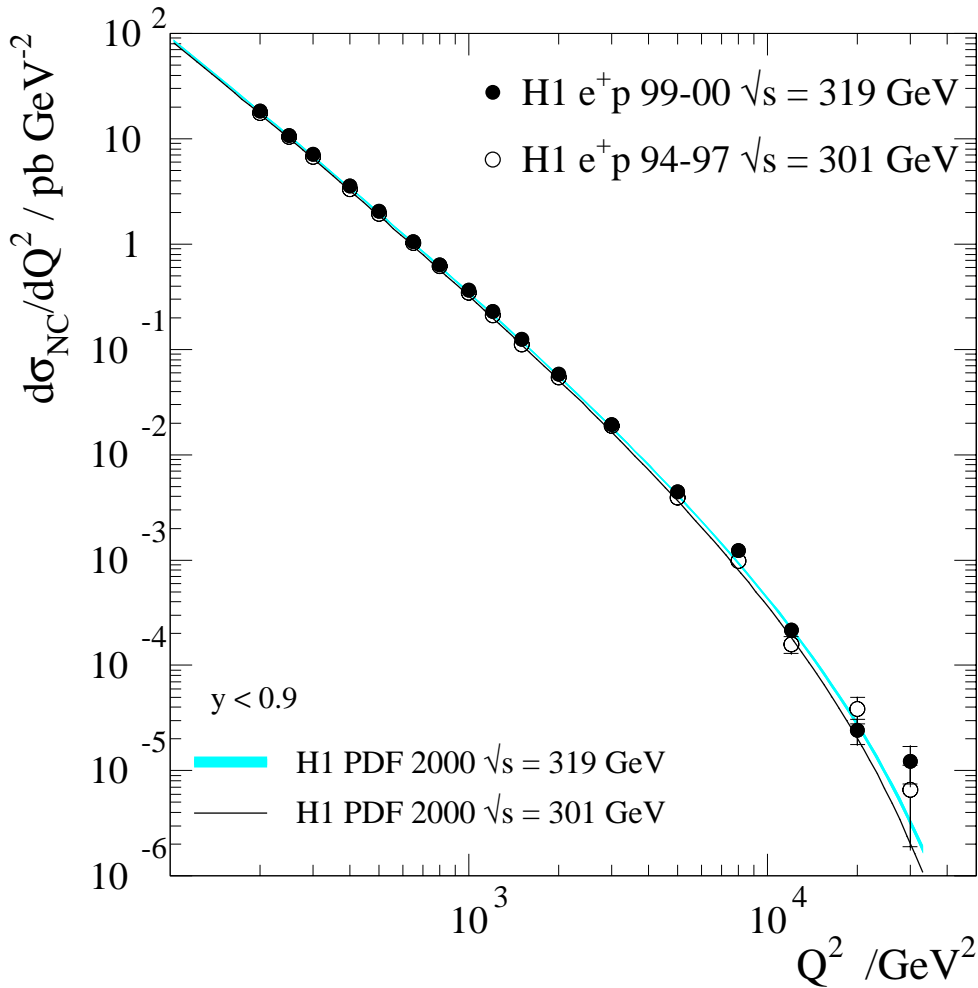


**Figure 8.5:**  $Q^2$  dependence of the NC cross sections  $d\sigma/dQ^2$  for the  $e^+p$  99-00 data at  $\sqrt{s} = 319 \text{ GeV}$  (solid points) and the 94-97  $e^+p$  data at  $\sqrt{s} = 301 \text{ GeV}$  [32] (open points). The error band and line represent the Standard Model expectations determined from the H1 2000 PDF fit for  $\sqrt{s} = 319 \text{ GeV}$  and  $\sqrt{s} = 301 \text{ GeV}$ . The inner and outer error bars represent the statistical the total error, respectively. The 1.5% normalisation uncertainty is not included in the error bars.

according to the Standard Model expectation from the H1 PDF 2000 fit. The results are compared with the previous measurement at  $\sqrt{s} = 301$  GeV. The difference of about 7% is due to the different centre-of-mass energy. Both cross sections, falling by over six orders of magnitude for the measured  $Q^2$  region between  $200 \text{ GeV}^2$  and  $30\,000 \text{ GeV}^2$  are well described by the H1 PDF 2000 fit.

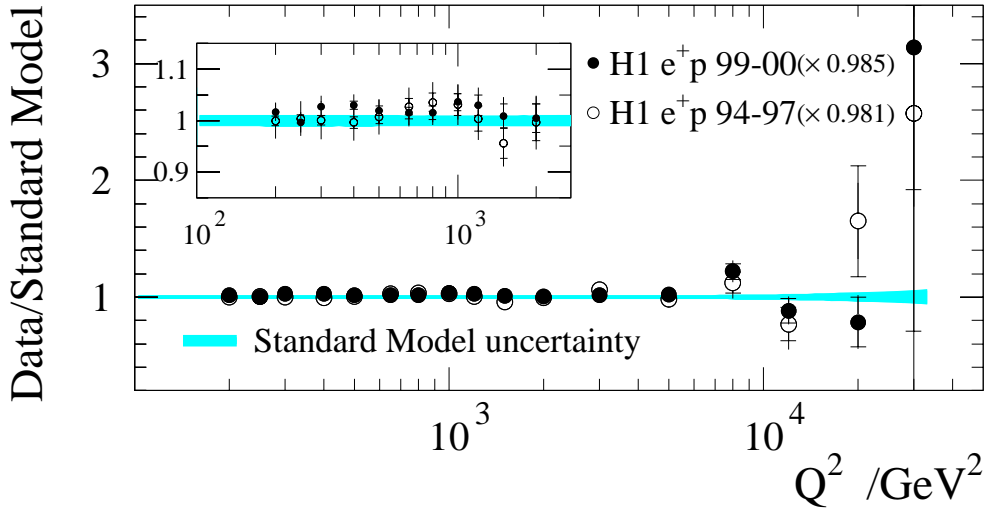


**Figure 8.6:** The ratio of the 99 – 00 and 94 – 97 data to their respective the Standard Model expectations. The normalisation and systematic shift as determined from the QCD analysis is applied to the data (see appendix A, table A.3). The Standard Model Uncertainty is shown as the shaded band. The 1.5% normalisation uncertainty is not included in the error bars.

Figure 8.6 shows the ratios of the measurements using 99-00 and 94-97 data to their corresponding Standard Model expectations obtained from H1 PDF 2000 fit, where the normalisation shifts as determined from the fit (see appendix A, table A.3) are applied to the data. The Standard Model uncertainty represents the fit uncertainty due to assumptions made in the H1 PDF 2000 fit and the experimental errors of the data entering the fit, see appendix A, table A.3. The prediction gives good description of the measured cross section.

### 8.3 The $e^+p$ Single Differential Cross Section $d\sigma/dx$

The single differential  $e^+p$  cross section  $d\sigma/dx$  measured for  $Q^2 > 1000 \text{ GeV}^2$  and for  $Q^2 > 10000 \text{ GeV}^2$ , tables C.4 and C.5, are shown in figure 8.7. The drop in the cross sections at  $x \approx 3 \cdot 10^{-2}$  is due to the restriction  $y < 0.9$ . The figure also shows  $d\sigma/dx$  measured using 94-97 data [32]. The difference between the measurements is due to the difference in the centre-of-mass energy ( $\sqrt{s} = 319 \text{ GeV}$  and  $\sqrt{s} = 301 \text{ GeV}$ ). Both results are well described by the prediction from the H1 PDF 2000 fit.

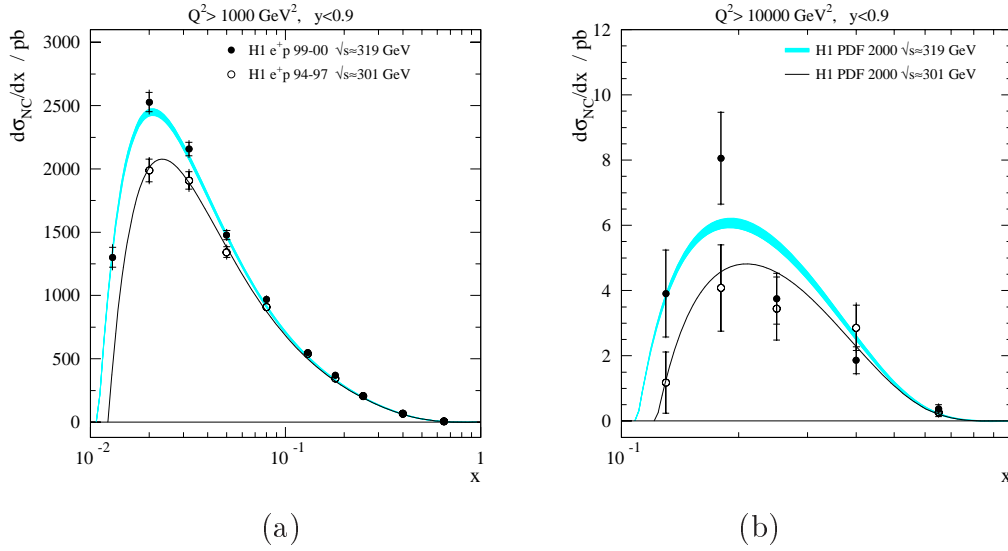


**Figure 8.7:**  $x$  dependence of the NC cross section  $d\sigma/dx$  for  $Q^2 > 1000 \text{ GeV}^2$  (a) and for  $Q^2 > 10000 \text{ GeV}^2$  (b) for the  $e^+p$  99-00 data (solid points) and  $e^+p$  94-97 data [32] (open points). The data are compared to the Standard Model expectation determined from the H1 PDF 2000 fit. The shaded band corresponds to a centre-of-mass energy of  $\sqrt{s} = 320 \text{ GeV}$ . The full line corresponds to a centre-of-mass energy of  $\sqrt{s} = 301 \text{ GeV}$ . The 1.5% luminosity uncertainty is not included in the error bars.

## Chapter 9

# Extraction of Proton Structure Functions

The neutral current cross section is defined by three structure functions  $F_2$ ,  $xF_3$  and  $F_L$ . In the major part of the kinematic range the contribution of the proton structure function  $F_2$  is dominant, the contribution of the longitudinal structure function is enhanced at high  $y$  and  $xF_3$  becomes important at  $Q^2$  comparable to the mass of  $Z^0$ . Using the measured double differential cross section all three structure functions are determined in regions of the phase space where their contributions are enhanced.

### 9.1 Proton Structure Function $F_2$

The NC reduced cross section is dominated by the electromagnetic component of the proton structure function  $F_2$  in most of the HERA kinematic domain. The structure function  $F_2$  is extracted using

$$F_2 = \frac{\phi_{NC}}{Y_+} (1 + \Delta_{F_2} + \Delta_{F_3} + \Delta_{F_L})^{-1}. \quad (9.1)$$

Here the correction term  $\Delta_{F_2}$  accounts for the relative contribution of pure  $Z^0$  exchange and  $\gamma Z^0$  interference to  $\tilde{F}_2$  (see eq. 1.30).  $\Delta_{F_3}$  corresponds to the contribution of  $x\tilde{F}_3$  and  $\Delta_{F_L}$  to the contribution of the longitudinal structure function  $\tilde{F}_L$ . These corrections, shown in table C.2, are determined using the H1 PDF 2000 fit (see section 1.7). At high  $y$  and  $Q^2 \lesssim 1000 \text{ GeV}^2$   $\Delta_{F_L}$  is sizeable. Therefore the extraction of  $F_2$  in this  $Q^2$  region is restricted to the kinematic range  $y < 0.6$ . At larger  $Q^2$  the contribution of  $\tilde{F}_L$  is expected to be small.

The extracted  $F_2$  is presented in figure 9.1 and listed in table C.2. The figure also shows the H1  $F_2$  data at low  $Q^2$  [98] and structure function data from fixed-target

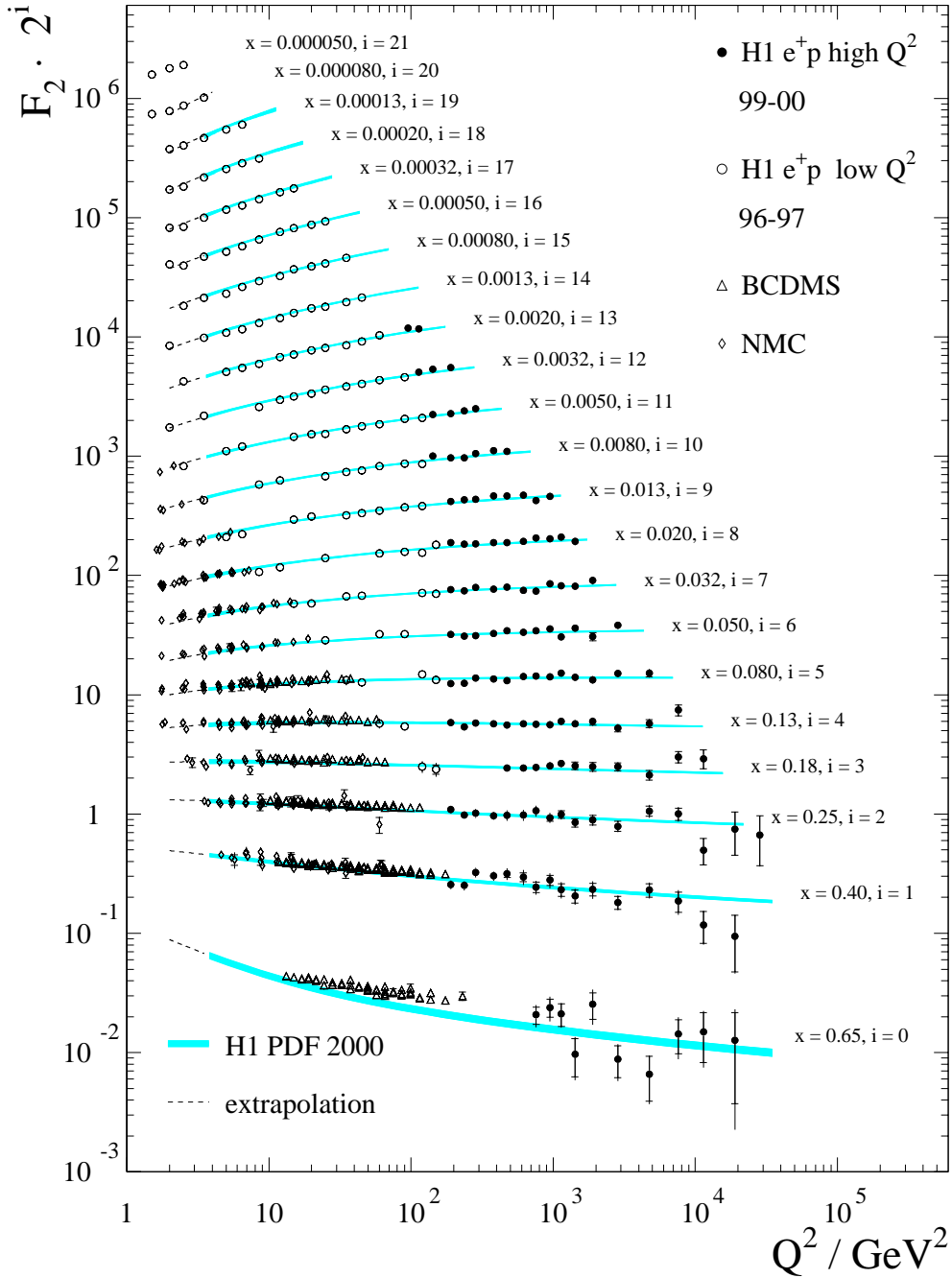


**Figure 9.1:** The proton structure function  $F_2$  from the  $e^+p$  99-00 data solid points. Also shown are the results from the H1 low  $Q^2$  data [98] and the results from the fixed-target experiments BCDMS [2] and NMC [3]. The data are compared with the corresponding Standard Model expectation determined from the H1 PDF 2000 fit (error bands). The dashed curves show the backward extrapolation of the fit to  $Q^2 < Q_{min}^2$ .



experiments BCDMS [2] and NMC [3], which are not used in the QCD fit. The H1 data extend the  $F_2$  measurement with improved precision to higher  $Q^2$  by two orders of magnitude. The H1 PDF 2000 fit provides a good description of the data over the whole region, except for BCDMS data at  $x = 0.65$ .

At  $x \approx 0.1$   $F_2$  does not depend on  $Q^2$ , i.e. so called Bjorken scaling. At larger and lower  $x$  the structure function  $F_2$  departs from the scaling behaviour, which is known as scaling violation. At larger  $x$ ,  $F_2$  is decreasing due to enhanced contribution of gluon emission with increasing  $Q^2$ . The emitted gluon "takes away" some of the initial quark's momentum, so that the quark as it is "seen" by the exchanged photon has a lower  $x$  value. At low  $x$  the structure function  $F_2$  is increasing with  $Q^2$ . This increase is understood to be due to the fact that with increasing  $Q^2$  there are more gluons and thus more sea quarks which enhance the small  $x$  region. All data are well described by the QCD fit, thereby showing that the DGLAP equations are applicable over five orders of magnitude in  $Q^2$ .

## 9.2 Longitudinal Structure Function $F_L$

The contribution of  $F_L$  to the cross section is enhanced at high  $y$  ( $y = 0.75$ ) and  $Q^2 < 1000 \text{ GeV}^2$ . For statistical reasons, the measured  $e^+p$  and  $e^-p$  cross sections in two neighbouring bins are combined as explained in section 7.4. The resulting structure function term  $\phi_{NC}/Y_+$  is given in table C.7. It is used to determine the longitudinal structure function  $F_L$  according to

$$\tilde{F}_L = \frac{1}{y^2} \left[ Y_+ F_2 \mp Y_- x \tilde{F}_3 - \phi_{NC}^\pm \right]. \quad (9.2)$$

Neglecting the small electroweak contribution in the region of this extraction, it reduces to the expression

$$F_L = \frac{1}{y^2} \left[ Y_+ F_2 - \phi_{NC}^\pm \right]. \quad (9.3)$$

The  $F_L$  extraction relies upon the extrapolation of  $F_2$  into the region of high  $y$ , that is larger  $Q^2$  for given  $x^1$ . For this purpose a dedicated QCD analysis is performed using H1 data restricted to  $y < 0.35$  (H1 2000 Low  $y$  Fit). The results are extrapolated using the DGLAP evolution equations. This method was introduced in [109]. The fit follows the same procedure as H1 PDF 2000 fit (see appendix A) and agrees well with it over the full  $y$  range.

In the extraction of the longitudinal structure function, the experimental cross sections are renormalised using the results of the H1 Low  $y$  fit. In addition small shifts from the correlated uncertainties common to the low  $y$  and high  $y$  are applied. The statistical

---

<sup>1</sup>The longitudinal structure function can be measured directly by varying  $y$  for fixed  $x$  and  $Q^2$ . According to relation  $Q^2 = sxy$  this can be achieved by varying centre of mass energy [108].

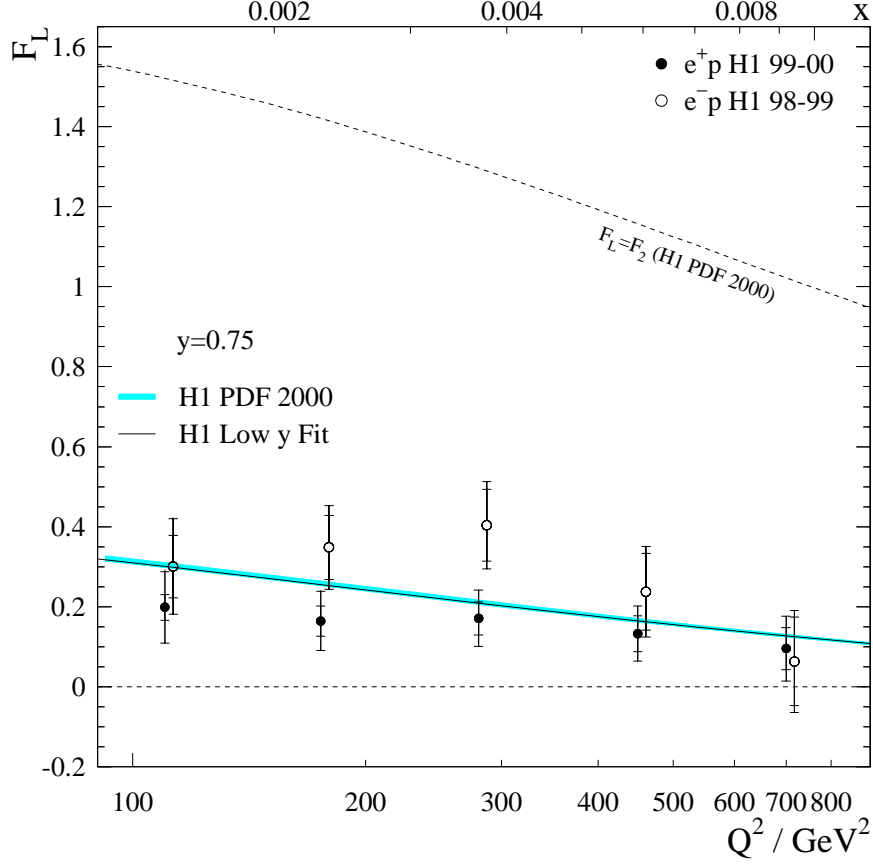


**Figure 9.2:** Determination of  $F_L$  for  $e^-p$  and  $e^+p$  data at fixed  $y = 0.75$  as a function of  $Q^2$  (lower scale), or equivalently  $x$  (upper scale). The inner error bars represent the statistical error, the intermediate error bar shows the systematic uncertainty contribution, and the outer error includes the uncertainty rising from the extrapolation of  $F_2$ . The shaded band (solid line) shows the expectation of  $F_L$ , and its uncertainty, from the H1 PDF 2000 (H1 Low  $y$ ) fit. The upper and lower dashed curves are the maximum and minimum values allowed for  $F_L$ .

and uncorrelated systematic uncertainties of  $F_L$  are directly propagated from cross sections measured at high  $y$ . The correlated errors which are relevant at high and low  $y$  are determined during the fitting procedure since they simultaneously influence both the measured cross sections and the extrapolated structure functions. Additional source of correlated uncertainty is the charge symmetry assumption (section 5.8.3) of the subtracted photoproduction background since this procedure is applied only at high  $y$ . Model uncertainty related to the extrapolation of  $F_2$  from the low  $y$  to the high  $y$  region is estimated by varying fit parameters (see appendix A, table A.2).

In figure 9.2 the measurements of  $F_L$  are shown at fixed  $y = 0.75$  for both the  $e^+p$  and the  $e^-p$  data sets. The extreme values allowed for  $F_L$  ( $F_L = 0$  and  $F_L = F_2$ )

are clearly excluded by the data. Both data sets are mutually consistent and are in agreement with QCD calculations which rely on the gluon distribution as it is defined in the H1 PDF 2000 fit and in the H1 Low  $y$  Fit.

### 9.3 Structure Function $x\tilde{F}_3$

The difference of the  $e^+p$  and  $e^-p$  cross sections (figure 8.4) has been used to determine the structure function  $x\tilde{F}_3$ . In order to optimise the sensitivity to  $x\tilde{F}_3$ , both the  $e^+p$  and the  $e^-p$  cross section results are rebinned into three  $Q^2$  bins as explained in section 7.4. The reduced cross sections  $\sigma_{NC}^\pm$  measured in these bins together with the expectations determined from the H1 PDF 2000 fit are shown in figure 9.3(a). The structure function  $x\tilde{F}_3$  is then evaluated according to

$$x\tilde{F}_3 = \frac{1}{2Y_-} [\phi_{NC}^- - \phi_{NC}^+]. \quad (9.4)$$

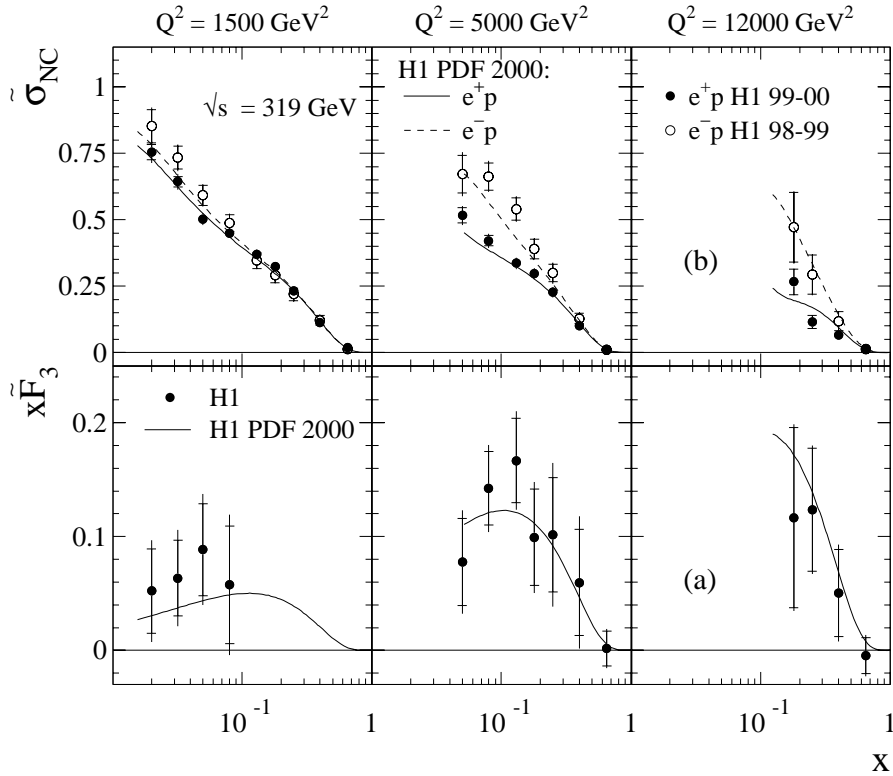


**Figure 9.3:** The measured NC reduced cross sections  $\tilde{\sigma}_{NC}^\pm(x, Q^2)$  (a) and the measured structure functions  $x\tilde{F}_3$  (b) for three different  $Q^2$  values. The results are compared with the corresponding Standard Model expectations determined from the H1 PDF 2000 fit. The normalisation uncertainties of the  $e^-p$  and  $e^+p$  data sets are included in the systematic errors.

Previous determinations of  $x\tilde{F}_3$  by the H1 and ZEUS collaborations [39, 110] are based on  $e^+p$  and  $e^-p$  data taken at different centre of mass energy,  $\sqrt{s} = 301$  GeV and  $\sqrt{s} = 319$  GeV, applying additional corrections for this difference. The extraction of  $x\tilde{F}_3$  presented here is performed using  $e^+p$  and  $e^-p$  data at the same centre of mass energy,  $\sqrt{s} = 319$  GeV, and is therefore free of any theoretical inputs.

The resulting generalised structure function  $x\tilde{F}_3$ , listed in table C.8 is shown in figure 9.3(b) as a function of  $x$ . As expected  $x\tilde{F}_3$  rises with  $Q^2$  for the same values of  $x$  due to the  $Z^0$  propagator factor. At  $Q^2 = 1500$  GeV<sup>2</sup> and  $x > 0.1$  the expected sensitivity to  $x\tilde{F}_3$  is smaller than the luminosity uncertainty, therefore the measurement in this region is not performed.

The dominant contribution to  $x\tilde{F}_3$  arises from  $\gamma Z$  interference. This allows  $xF_3^{\gamma Z}$  to be extracted (eq. 1.32) according to  $xF_3^{\gamma Z} \simeq -x\tilde{F}_3(Q^2 + M_Z^2)/(a_e\kappa Q^2)$  by neglecting the pure  $Z$  exchange contribution which is suppressed by the small vector coupling  $v_e$ . This structure function has little dependence on  $Q^2$  as illustrated in figure 9.4. The

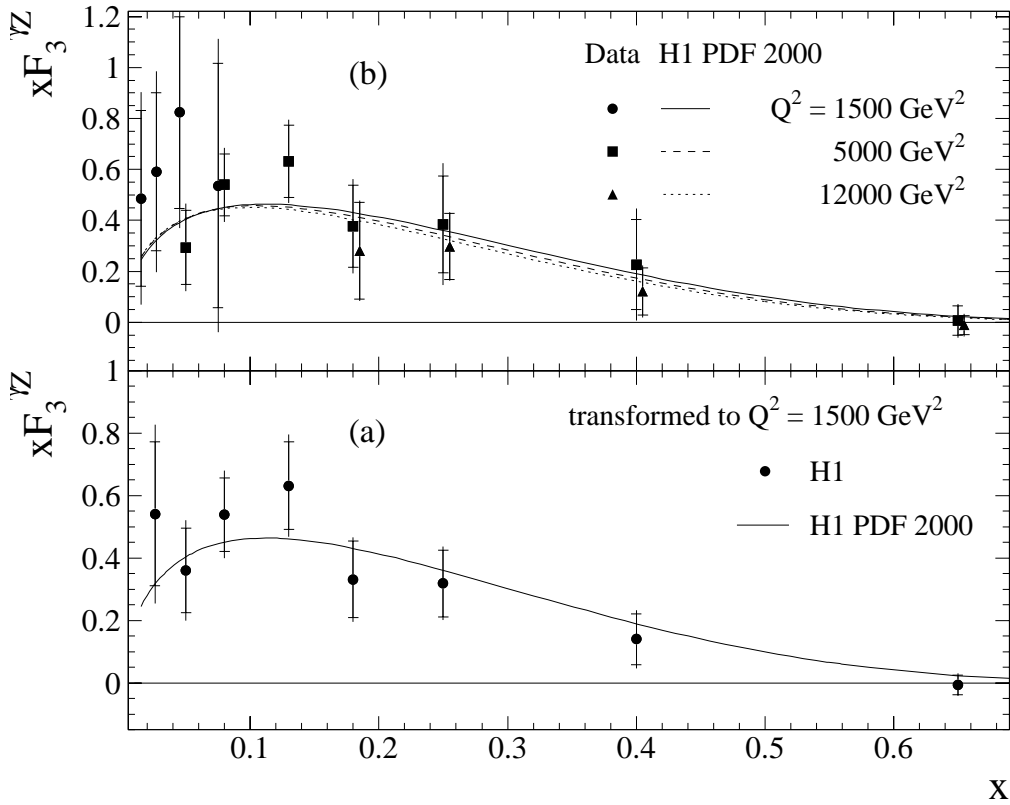


**Figure 9.4:**  $x$  dependence of  $xF_3^{\gamma Z}$  for three different  $Q^2$  values (a) compared with the predictions from the H1 2000 PDF fit. The averaged structure function  $xF_3^{\gamma Z}$  for a  $Q^2$  value corresponding to  $1500$  GeV<sup>2</sup> (b) is compared with the expectation determined from the H1 PDF 2000 fit. The normalisation uncertainties are included in the systematic errors.

measured  $xF_3^{\gamma Z}$  at these  $Q^2$  values can thus be averaged by taking weighted means and accounting for the small  $Q^2$  dependence. The two lowest  $x$  bins at  $x = 0.020$  and  $0.032$  are averaged as well. The  $xF_3^{\gamma Z}$  averaged for a  $Q^2$  value corresponding to  $1\,500\text{ GeV}^2$  is shown in table C.8 and in figure 9.4(b) compared with the expectation determined from the QCD fit.

The structure function  $xF_3^{\gamma Z}$ , depending on difference of the quark and anti-quark distributions (see eq. 1.32), determines both the shape and magnitude of the valence quark distributions independent of the sea quark distributions. The calculation from the QCD fit, in which the parton densities in the valence region are principally constrained by the NC and CC cross sections rather than the difference between the  $e^\pm p$  NC cross sections, gives a good description of the measurement. The level of agreement of the expectations with the data is checked using the sum rule<sup>2</sup> [113]:

$$\int_0^1 F_3^{\gamma Z} dx = (2e_u a_u N_u + 2e_d a_d N_d) \cdot \mathcal{O}(1 - \frac{\alpha_s}{\pi}) = \frac{5}{3} \cdot \mathcal{O}(1 - \frac{\alpha_s}{\pi}). \quad (9.5)$$

Here  $N_u$  and  $N_d$  are the numbers of  $u$  and  $d$  valence quarks, respectively. The term  $\mathcal{O}(1 - \alpha_s/\pi)$  represents the QCD radiative corrections [114]. The averaged structure function is integrated over the measured  $x$  range, yielding

$$\int_{0.026}^{0.650} F_3^{\gamma Z}(x, Q^2 = 1\,500\text{ GeV}^2) dx = 1.28 \pm 0.17(\text{stat.}) \pm 0.11(\text{syst.}),$$

which is in agreement with  $1.06 \pm 0.02$ , as predicted from the H1 PDF 2000 fit.

---

<sup>2</sup>The sum rule is determined by analogy with Gross Lewellyn-Smith sum rule [111] for neutrino nucleon scattering which is found to be valid [112].

## Chapter 10

# Electroweak Effects at High $Q^2$

The NC 99-00  $e^+p$  cross sections presented here complete the high  $Q^2$  cross section measurements by H1 in the first phase of HERA operation (HERA I). Together with the NC 94-97  $e^+p$  and 98-99  $e^-p$  results and the corresponding  $e^\pm p$  CC measurements, they provide a test of the electroweak part of the Standard Model.

”An electroweak summary” of the HERA I measurements is shown in figure 10.1. Here the single differential cross section,  $d\sigma/dQ^2$ , is shown for NC and CC processes in  $e^+p$  and  $e^-p$  scattering. The NC and CC  $e^+p$  cross sections from 94-97 and 99-00 data have been combined using the procedure described in [115] and labelled 94-00 in the figure.

The NC cross section measurements span six orders in magnitude and more than two orders in  $Q^2$ . At low  $Q^2$  the NC cross section exceeds the CC cross section by more than two orders of magnitude. The sharp increase of the NC cross section with decreasing  $Q^2$  is due to the dominating photon exchange cross section  $\propto 1/Q^4$ . In contrast, the CC cross section  $\sim [M_W^2/(Q^2 + M_W^2)]^2$  approaches a constant at low  $Q^2$ . The CC and NC cross sections are of comparable size at  $Q^2 \sim 10^4$  GeV<sup>2</sup> where the photon and  $Z^0$  exchange contributions to the NC process are also of similar size to those of  $W^\pm$  exchange. These measurements thus demonstrate unification of the electromagnetic and the weak interactions in deep inelastic scattering.

The Standard Model provides accurate description of all details of the NC and CC data behaviour up to the highest  $Q^2$ , i.e.  $Q^2 = 30\,000$  GeV<sup>2</sup>.

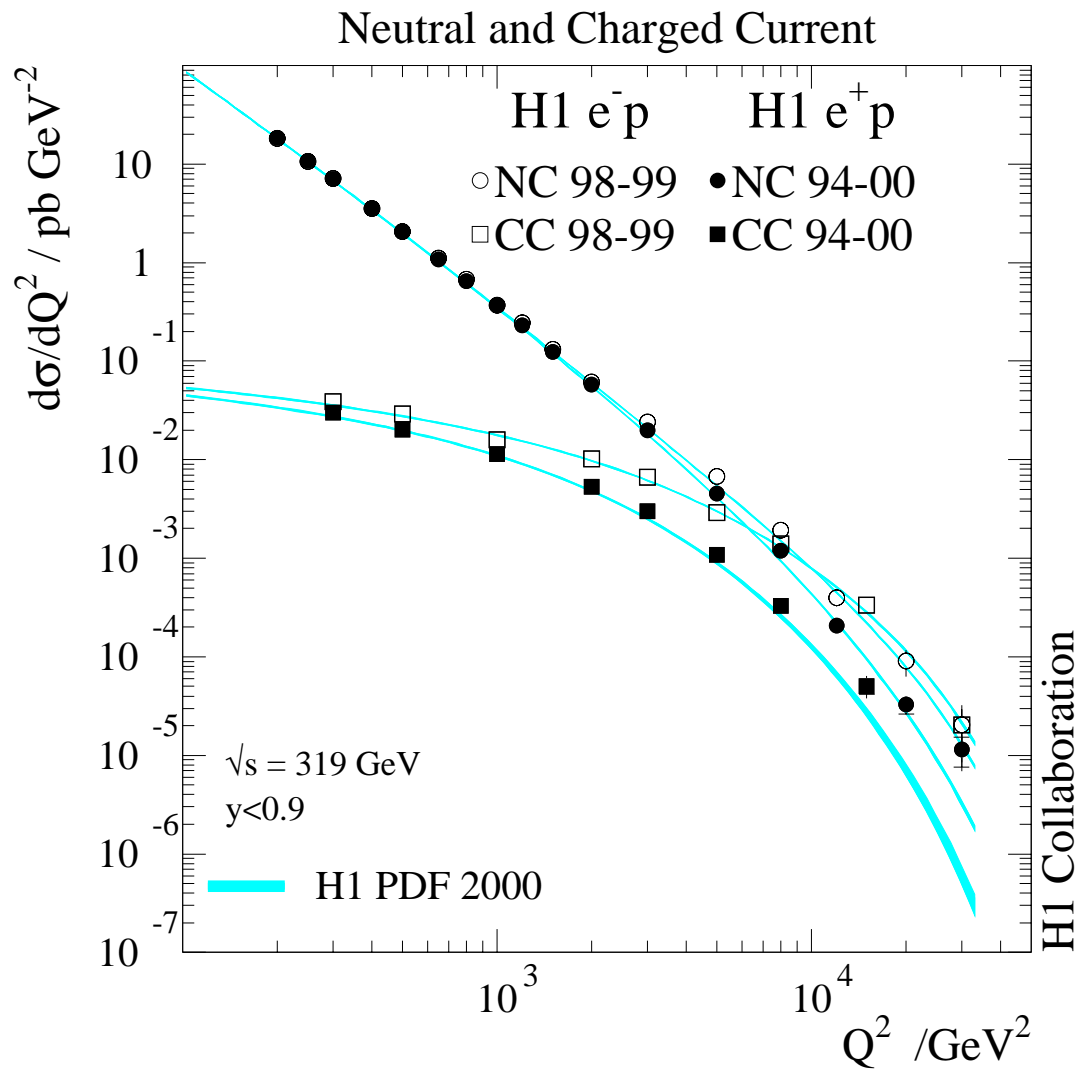


**Figure 10.1:** The  $Q^2$  dependences of the NC (circles) and CC (squares) cross sections  $d\sigma/dQ^2$  are shown for the combined 94-00  $e^+p$  (solid points) and 98-99  $e^-p$  (open points) measurements. The data are compared to the Standard Model expectations determined from the H1 PDF 2000 fit. The luminosity uncertainty is not included in the errors.

# Summary

In this thesis the measurements of the  $e^+p$  inclusive neutral current deep inelastic scattering cross sections have been presented. The measurements were performed in the domain of high momentum transfer squared  $Q^2$ , comparable with square of masses of  $Z^0$  and  $W^\pm$  bosons making possible tests of both components of the Standard Model, QCD and the electroweak theory.

The analysis was performed for the  $e^+p$  collisions at centre-of-mass energy  $\sqrt{s} = 319$  GeV. The data were taken within the H1 experiment in the 1999-2000 running period and correspond to an integrated luminosity of  $65.2 \text{ pb}^{-1}$ . The extension of the measurements to the high inelasticity region at low  $Q^2$  was performed using  $e^+p$  data as well as  $e^-p$  data taken in 1998-1999 running period at the same centre-of-mass energy and an integrated luminosity of  $16.4 \text{ pb}^{-1}$ .

Double and single differential cross sections are measured in  $x$  and  $Q^2$ :

- **Double differential cross section  $d^2\sigma/dx dQ^2$**

In the nominal analysis the  $e^+p$  double differential cross section is measured for  $100 < Q^2 < 30\,000 \text{ GeV}^2$  and  $0.002 < x < 0.65$ .

The accuracy of the measurement has reached a level of few percent in the medium  $Q^2$  range of  $Q^2 < 3\,000 \text{ GeV}^2$ , while in the region of very high  $Q^2$  the measurement is limited by the statistical precision of the data.

The obtained results are in a good agreement with previous measurements based on  $e^+p$  94-97 data at  $\sqrt{s} = 301$  GeV.

Both using  $e^+p$  and  $e^-p$  data, the cross section measurements are extended into the region of very high inelasticity  $y = 0.75$  for  $100 < Q^2 < 800 \text{ GeV}^2$ , allowing for the determination of the longitudinal structure function.

- **Single differential cross section  $d\sigma/dQ^2$**

The measured cross section covers a range of two orders in magnitude in  $Q^2$ ,  $200 < Q^2 < 30\,000 \text{ GeV}^2$  and falls by about six orders in magnitude. At highest  $Q^2$ , comparable with the  $W^\pm$  and  $Z^0$  boson masses squared, the NC cross section is of similar size with the CC cross section, illustrating the unification of the electromagnetic and weak forces in the deep inelastic scattering.



- **Single differential cross section  $d\sigma/dx$**

The cross section  $d\sigma/dx$  is measured for  $Q^2 > 1000 \text{ GeV}^2$  and also for the very high  $Q^2$  region  $Q^2 > 10000 \text{ GeV}^2$  up to the  $x = 0.65$ .

Using the measured double differential cross section the structure functions of the proton are determined:

- **Proton structure function  $F_2$**

The structure function  $F_2$ , which is the dominant contribution to the NC cross section, is measured for  $y < 0.6$ . At medium  $x$ , i.e.  $x \simeq 0.15$ ,  $F_2$  shows approximate scaling with  $Q^2$ , Bjorken scaling. Scaling violations in the positive direction at low  $x$  and in the negative direction at high  $x$  are observed. Both, the scaling and the scaling violations are well described by QCD predictions based on the DGLAP evolution equations.

- **Longitudinal structure function  $F_L$**

Using both  $e^+p$  and  $e^-p$  data the longitudinal structure function is determined from the measured cross section at  $y = 0.75$  in the range of  $110 < Q^2 < 700 \text{ GeV}^2$ . The results from both data sets are in mutual agreement, ruling out the extreme values allowed for  $F_L$ , i.e.  $F_L = 0$  and  $F_L = F_2$ . The measured  $F_L$ , directly sensitive to gluon distribution, is in a good agreement with the QCD prediction based on the gluon distribution derived from the scaling violations of  $F_2$ .

- **Structure function  $xF_3$**

The difference of the  $e^+p$  and the  $e^-p$  cross sections in the region of the very high  $Q^2$  is explored for the extraction of the structure function  $x\tilde{F}_3$  in the region of  $1500 < Q^2 < 12000 \text{ GeV}^2$  and  $0.2 < x < 0.65$ . This structure function is dominated by the  $\gamma Z^0$  interference term  $xF_3^{\gamma Z}$ . The structure function  $xF_3^{\gamma Z}$ , being a sensitive probe of the valence quarks in the proton, is explicitly derived from the measurements.

The Standard Model predictions based on the QCD fit to the H1 data, which partially uses the results presented in this thesis, provide consistent and detailed description of all measured cross sections and structure functions.

# Appendix A

## Details of QCD Analysis

The H1 PDF 2000 fit uses the NC and CC inclusive cross section measurements of the H1 experiment at low and high  $Q^2$  listed table A.1, partially including results of this thesis (see section 7.5). A fit including BCDMS  $\mu$ -proton and  $\mu$ -deuteron scattering data is performed for cross checks of fit to H1 data alone.

The analysis is performed in the  $\overline{MS}$  renormalisation scheme using the DGLAP evolution equations (see section 1.4, eqs. 1.24, 1.25) at NLO [34]. An approach is used whereby all quarks are taken to be massless, including the charm and bottom quarks. The bottom quark distribution,  $xb$ , is assumed to be zero for  $Q^2 < m_b^2$  where  $m_b$  is the bottom quark mass.

Fits are performed to the measured cross sections calculating the longitudinal structure functions to order  $\alpha_s^2$  and assuming the strong coupling constant to be equal to

| data set              | process    | $x$ range |        | $Q^2$ range         |                     | $\delta^{\mathcal{L}}$<br>(%) | ref. | comment                                       |
|-----------------------|------------|-----------|--------|---------------------|---------------------|-------------------------------|------|---|
|                       |            |           |        | (GeV <sup>2</sup> ) | (GeV <sup>2</sup> ) |                               |      |   |
| H1 minimum bias 97    | $e^+p$ NC  | 0.00008   | 0.02   | 1.5                 | 12                  | 1.7                           | [98] | $\sqrt{s} = 301$ GeV                          |
| H1 low $Q^2$ 96 – 97  | $e^+p$ NC  | 0.000161  | 0.20   | 12                  | 150                 | 1.7                           | [98] | $\sqrt{s} = 301$ GeV                          |
| H1 high $Q^2$ 94 – 97 | $e^+p$ NC  | 0.0032    | 0.65   | 150                 | 30 000              | 1.5                           | [32] | $\sqrt{s} = 301$ GeV                          |
| H1 high $Q^2$ 94 – 97 | $e^+p$ CC  | 0.013     | 0.40   | 300                 | 15 000              | 1.5                           | [32] | $\sqrt{s} = 301$ GeV                          |
| H1 high $Q^2$ 98 – 99 | $e^-p$ NC  | 0.0032    | 0.65   | 150                 | 30 000              | 1.8                           | [39] | $\sqrt{s} = 319$ GeV                          |
| H1 high $Q^2$ 98 – 99 | $e^-p$ CC  | 0.013     | 0.40   | 300                 | 15 000              | 1.8                           | [39] | $\sqrt{s} = 319$ GeV                          |
| H1 high $Q^2$ 98 – 99 | $e^-p$ NC  | 0.00131   | 0.0105 | 100                 | 800                 | 1.8                           | [29] | $\sqrt{s} = 319$ GeV;<br>high- $y$ data       |
| H1 high $Q^2$ 99 – 00 | $e^+p$ NC  | 0.0032    | 0.65   | 150                 | 30 000              | 1.5                           | [29] | $\sqrt{s} = 319$ GeV;<br>incl. high- $y$ data |
| H1 high $Q^2$ 99 – 00 | $e^+p$ CC  | 0.013     | 0.40   | 300                 | 15 000              | 1.5                           | [29] | $\sqrt{s} = 319$ GeV                          |
| BCDMS-p               | $\mu p$ NC | 0.07      | 0.75   | 7.5                 | 230                 | 3.0                           | [2]  | require $y_\mu > 0.3$                         |
| BCDMS-D               | $\mu D$ NC | 0.07      | 0.75   | 7.5                 | 230                 | 3.0                           | [2]  | require $y_\mu > 0.3$                         |

**Table A.1:** Data sets from H1 used in the H1 PDF 2000 fit and from BCDMS  $\mu$ -proton and  $\mu$ -deuteron scattering used in the H1+BCDMS fit. The original BCDMS data are used at four different beam energies imposing the constraint  $y_\mu > 0.3$ . The inelasticity  $y_\mu$  was defined using BCDMS beam energies. The normalisation uncertainties of each data set ( $\delta^{\mathcal{L}}$ ) are given as well as the kinematic ranges in  $x$  and  $Q^2$ .

$\alpha_s(M_Z^2) = 0.1185$  [27]. The analysis uses an  $x$  space program developed inside the H1 collaboration [116]. In the fit procedure, a  $\chi^2$  function defined in [98] is minimised. The minimisation takes into account correlations of data points caused by systematic uncertainties allowing the error parameters, including the relative normalisation of the various data sets, to be determined by the fit.

The initial parton distributions, i.e.  $xP = xg, xU, xD, x\bar{U}, x\bar{D}$ , are parameterised at  $Q^2 = Q_0^2$  in the following general form

$$xP(x) = A_q x^{B_q} (1-x)^{C_q} [1 + D_q x + E_q x^2 + F_q x^3]. \quad (\text{A.1})$$

The fit to the H1 data leads to the following set of parameterisations [117]:

$$\begin{aligned} xg(x) &= A_g x^{B_g} (1-x)^{C_g} \cdot [1 + D_g x] \\ xU(x) &= A_U x^{B_U} (1-x)^{C_U} \cdot [1 + D_U x + F_U x^3] \\ xD(x) &= A_D x^{B_D} (1-x)^{C_D} \cdot [1 + D_D x] \\ x\bar{U}(x) &= A_{\bar{U}} x^{B_{\bar{U}}} (1-x)^{C_{\bar{U}}} \\ x\bar{D}(x) &= A_{\bar{D}} x^{B_{\bar{D}}} (1-x)^{C_{\bar{D}}}. \end{aligned} \quad (\text{A.2})$$

At low  $x$  the valence quark distributions are expected to vanish. Thus the low  $x$  parameters  $A_q$  and  $B_q$  are required to be the same for  $xU, x\bar{U}$  and for  $xD, x\bar{D}$  as the sea quark and the anti-quark densities can be assumed to be equal. In the absence of deuteron data from HERA there is no distinction possible of the rise towards low  $x$  between  $xU$  and  $xD$ . Thus the corresponding  $B$  parameters are required to be equal, i.e.  $B_U = B_D = B_q$ . Further constraints are the conventional momentum sum rule and the valence quark counting rules.

In the H1 PDF 2000 fit the quark distributions  $xU, xD, x\bar{U}, x\bar{D}$  are determined. Further disentangling the individual quark flavour contributions to the sea is possible only with additional experimental information and/or assumptions. Assuming the strange and charm sea quark densities  $x_s$  and  $x_c$  can be expressed as fraction of  $f_s$  and  $f_c$  of the  $x\bar{D}$  and  $x\bar{U}$  at the starting scale of  $Q_0^2 = 4 \text{ GeV}^2$ , and  $\bar{d}/\bar{u} \rightarrow 1$  as  $x \rightarrow 0$ , one derives a further constraint used in the fit:  $A_{\bar{U}} = A_{\bar{D}} \cdot (1 - f_s)/(1 - f_c)$ .

The  $\chi^2$  value for each data set is given in table A.3 as well as the optimised relative normalisation as determined from the fit. The total  $\chi^2$  value<sup>1</sup> per degree of freedom ( $\chi^2/\text{ndf}$ ) is  $540/(621 - 10) = 0.88$ .

The parameters of the initial parton distributions are given in table A.4 (see also [118]) and the distributions are shown in section 1.7, figure 1.4.

---

<sup>1</sup>In the calculation of the  $\chi^2$ , the assumption is made that the uncorrelated errors among different data points within one data set stay uncorrelated with the corresponding data points from an independent data set.

| source of uncertainty                  | central value | variation       |
|--|---------------|-----------------|
| $Q_{min}^2 / \text{GeV}^2$             | 3.5           | 2.0 – 5.0       |
| $Q_0^2 / \text{GeV}^2$                 | 4.0           | 2.0 – 6.0       |
| $\alpha_s(M_Z^2)$                      | 0.1185        | 0.1165 – 0.1205 |
| $f_s$ , strange fraction of $x\bar{D}$ | 0.33          | 0.25 – 0.40     |
| $f_c$ , charm fraction of $x\bar{U}$   | 0.15          | 0.10 – 0.20     |
| $m_c / \text{GeV}$                     | 1.4           | 1.2 – 1.6       |
| $m_b / \text{GeV}$                     | 4.5           | 4.0 – 5.0       |

**Table A.2:** Model uncertainties considered in the QCD analysis.

| data set              | process   | data points | $\chi^2$<br>(unc. err.) | $\chi^2$<br>(corr. err.) | norm. |
|-----------------------|-----------|-------------|-------------------------|--------------------------|-------|
| H1 minimum bias 97    | $e^+p$ NC | 45          | 37.5                    | 5.9                      | 1.037 |
| H1 low $Q^2$ 96 – 97  | $e^+p$ NC | 80          | 71.2                    | 1.3                      | 1.008 |
| H1 high $Q^2$ 94 – 97 | $e^+p$ NC | 130         | 89.7                    | 2.1                      | 0.981 |
| H1 high $Q^2$ 94 – 97 | $e^+p$ CC | 25          | 18.0                    | 0.4                      | 0.981 |
| H1 high $Q^2$ 98 – 99 | $e^-p$ NC | 139         | 114.7                   | 1.0                      | 0.991 |
| H1 high $Q^2$ 98 – 99 | $e^-p$ CC | 27          | 19.5                    | 0.7                      | 0.991 |
| H1 high $Q^2$ 99 – 00 | $e^+p$ NC | 147         | 142.6                   | 2.6                      | 0.985 |
| H1 high $Q^2$ 99 – 00 | $e^+p$ CC | 28          | 32.4                    | 0.9                      | 0.985 |
| Total                 |           | 621         | 540                     |                          | –     |

**Table A.3:** For each data set used in the H1 PDF 2000 fit, the number of data points is shown, along with the  $\chi^2$  contribution determined using the uncorrelated errors (unc. err.). Each of the correlated error sources [29] leads to an additional contribution [98], which is listed as  $\chi^2$  (corr. err.). Also shown is the optimised normalisation of the data set as determined by the fit. The H1 NC 98 – 99  $e^-p$  and H1 NC 99 – 00  $e^+p$  data include the high- $y$  analyses.

The experimental accuracy of the initial distributions is typically a few percent in the bulk of the phase space of the H1 data. This accuracy has negligible dependence on

| $P$        | $A$    | $B$    | $C$  | $D$   | $F$  |
|------------|--------|--------|------|-------|------|
| $xg$       | 0.0183 | −0.872 | 8.97 | 3450. |      |
| $xU$       | 0.112  | −0.227 | 5.08 | 48.0  | 373. |
| $xD$       | 0.142  | −0.227 | 4.93 | 23.5  |      |
| $x\bar{U}$ | 0.112  | −0.227 | 7.28 |       |      |
| $x\bar{D}$ | 0.142  | −0.227 | 4.36 |       |      |

**Table A.4:** Parameters of the H1 PDF 2000 fit to the H1 data alone for the initial distributions at  $Q_0^2 = 4 \text{ GeV}^2$ . Equal parameter values reflect the constraints imposed by the fit. The uncertainties and their correlations are available in [118].

$Q^2$  but a strong dependence on  $x$ .

The model parameter uncertainties on the PDFs are determined in a similar manner to [98], i.e. by varying the parameters given in table A.2. The model uncertainties are relatively small with respect to those from experimental sources except at small  $x$  and low  $Q^2$ .

For cross check purposes the H1+BCDMS fit is performed [29, 119], which gives a  $\chi^2/\text{ndf} = 883/(1014 - 12) = 0.88$ . This fit gives consistent results with the H1 PDF 2000 fit [29]. The PDFs from the H1 PDF 2000 fit are also in very good agreement with with recent results from the MRST [30] and CTEQ [31], see figure 1.5 in section 1.4.

The cross sections and structure functions calculated using PDFs obtained by H1 PDF 2000 fit are used in the interpretation of the results of this thesis presented in sections 8-10.

# Appendix B

## Trigger Fiducial Cuts

| $\phi_{min}$           | $\phi_{max}$ | $z_{min}$ | $z_{max}$ |
|------------------------|--------------|-----------|-----------|
| Full run range:        |              |           |           |
| 135.0°                 | 157.5°       | -90 cm    | -60 cm    |
| 90.0°                  | 112.5°       | -90 cm    | -30 cm    |
| 90.0°                  | 112.5°       | -5 cm     | 20 cm     |
| -135.0°                | -112.5°      | -6 cm     | 20 cm     |
| -180.0°                | -157.5°      | -35 cm    | -5 cm     |
| 0.0°                   | 22.5°        | 30 cm     | 100 cm    |
| -67.5°                 | 0.0°         | -5 cm     | 20 cm     |
| 0.0°                   | 22.5°        | -5 cm     | 30 cm     |
| For run $\geq$ 262031: |              |           |           |
| 0.0°                   | 22.5°        | -60 cm    | -30 cm    |
| 0.0°                   | 22.5°        |           | -150 cm   |
| For run $\geq$ 265068: |              |           |           |
| 135.0°                 | 157.5°       | -120 cm   | -90 cm    |
| -22.5°                 | 45.0°        | -60 cm    | -35 cm    |
| -45.0°                 | 67.5°        | -60 cm    | -30 cm    |
| For run $\geq$ 269335: |              |           |           |
| 0.0°                   | 22.5°        | -115 cm   | -60 cm    |
| For run $\geq$ 276210: |              |           |           |
| 45.0°                  | 67.5°        | -115 cm   | -60 cm    |
| For $E_e < 11$ GeV     |              |           |           |
| 112.5°                 | 135.0°       |           | 130 cm    |
| 0.0°                   | 360.0°       | -114 cm   | -122 cm   |
| 0.0°                   | 360.0°       | -65 cm    | -58 cm    |

**Table B.1:** Regions excluded due to low trigger efficiency

# Appendix C

## Tables of Results

| $Q^2$ (GeV <sup>2</sup> )<br>Centre | $Q^2$ (GeV <sup>2</sup> )<br>limits | $\log \frac{Q^2}{\text{GeV}^2}$<br>limits | $x$<br>Centre | $x$<br>limits | $\log x$<br>limits |
|-------------------------------------|-------------------------------------|---|---------------|---------------|--------------------|
|                                     | 89.12                               | 1.95                                      |               | 0.0010        | -3.0               |
| 100                                 | 112.2                               | 2.05                                      | 0.0013        | 0.0016        | -2.8               |
| 120                                 | 141.2                               | 2.15                                      | 0.0020        | 0.0025        | -2.6               |
| 150                                 | 177.8                               | 2.25                                      | 0.0032        | 0.0040        | -2.4               |
| 200                                 | 223.9                               | 2.35                                      | 0.0050        | 0.0063        | -2.2               |
| 250                                 | 281.8                               | 2.45                                      | 0.0080        | 0.010         | -2.0               |
| 300                                 | 354.8                               | 2.55                                      | 0.0020        | 0.016         | -1.8               |
| 400                                 | 446.7                               | 2.65                                      | 0.020         | 0.025         | -1.6               |
| 500                                 | 562.3                               | 2.75                                      | 0.032         | 0.040         | -1.4               |
| 650                                 | 707.9                               | 2.85                                      | 0.050         | 0.063         | -1.2               |
| 800                                 | 891.2                               | 2.95                                      | 0.080         | 0.100         | -1.0               |
| 1000                                | 1122                                | 3.05                                      | 0.130         | 0.145         | -0.84              |
| 1200                                | 1412                                | 3.15                                      | 0.180         | 0.209         | -0.68              |
| 1500                                | 1778                                | 3.25                                      | 0.250         | 0.316         | -0.50              |
| 2000                                | 2239                                | 3.35                                      | 0.400         | 0.501         | -0.30              |
| 3000                                | 3548                                | 3.55                                      | 0.650         | 0.95          | -0.002             |
| 5000                                | 6000                                | 3.78                                      |               |               |                    |
| 8000                                | 10000                               | 4.000                                     |               |               |                    |
| 12000                               | 16680                               | 4.222                                     |               |               |                    |
| 20000                               | 27778                               | 4.444                                     |               |               |                    |
| 30000                               | 46334                               | 4.666                                     |               |               |                    |

Table C.1: Binning in  $x$  and  $Q^2$ .

| $Q^2$<br>(GeV <sup>2</sup> ) | $x$     | $y$   | $\tilde{\sigma}_{NC}$ | $\delta_{stat}$ (%) | $\delta_{sys}$ (%) | $\delta_{tot}$ (%) | $\delta_{unc}$ (%) | $\delta_{unc}^E$ (%) | $\delta_{unc}^h$ (%) | $\delta_{cor}$ (%) | $\delta_{cor}^{E+}$ (%) | $\delta_{cor}^{\theta+}$ (%) | $\delta_{cor}^{h+}$ (%) | $\delta_{cor}^{N+}$ (%) | $\delta_{cor}^{B+}$ (%) | $\delta_{cor}^{S+}$ (%) | $\phi_{NC}/Y_+$ | $F_2$ | $\Delta_{F_2}$ (%) | $\Delta_{F_3}$ (%) | $\Delta_{F_L}$ (%) |
|------------------------------|---------|-------|-----------------------|---------------------|--------------------|--------------------|--------------------|----------------------|----------------------|--------------------|-------------------------|------------------------------|-------------------------|-------------------------|-------------------------|-------------------------|-----------------|-------|--------------------|--------------------|--------------------|
| 100                          | 0.00131 | 0.750 | 1.450                 | 1.6                 | 3.6                | 4.0                | 3.5                | 0.6                  | 0.0                  | 0.7                | 0.4                     | -0.1                         | -0.1                    | 0.1                     | -                       | 1.1                     | 1.450           | -     | -                  | -                  | -                  |
| 100                          | 0.00200 | 0.492 | 1.388                 | 1.4                 | 2.7                | 3.1                | 2.1                | 0.8                  | 0.3                  | 1.8                | -0.3                    | 1.3                          | 1.3                     | 0.1                     | -0.9                    | -                       | 1.388           | 1.352 | 0.1                | 0.0                | -3.8               |
| 120                          | 0.00158 | 1.404 | 1.404                 | 1.8                 | 2.7                | 3.3                | 2.7                | 0.3                  | 0.0                  | 0.6                | -0.4                    | 0.2                          | 0.2                     | 0.1                     | -                       | 0.9                     | 1.404           | -     | -                  | -                  | -                  |
| 120                          | 0.00200 | 0.591 | 1.338                 | 1.5                 | 2.5                | 2.9                | 2.0                | 0.6                  | 0.3                  | 1.5                | -0.4                    | 0.8                          | 0.8                     | 0.2                     | -1.2                    | -                       | 1.338           | 1.396 | 0.2                | 0.0                | -5.8               |
| 120                          | 0.00320 | 0.369 | 1.220                 | 1.3                 | 2.2                | 2.6                | 1.8                | 0.4                  | 0.3                  | 1.4                | -0.3                    | 0.6                          | 0.6                     | 0.1                     | -0.5                    | -                       | 1.220           | 1.201 | 0.2                | 0.0                | -1.8               |
| 150                          | 0.00197 | 0.750 | 1.398                 | 2.0                 | 2.8                | 3.5                | 2.7                | 0.7                  | 0.1                  | 0.8                | -0.7                    | 0.3                          | 0.3                     | 0.1                     | -                       | 0.9                     | 1.398           | -     | -                  | -                  | -                  |
| 150                          | 0.00320 | 0.462 | 1.271                 | 1.2                 | 2.5                | 2.7                | 1.8                | 0.1                  | 0.7                  | 1.7                | -0.2                    | 1.5                          | 1.5                     | 0.2                     | -0.7                    | -                       | 1.271           | 1.244 | 0.2                | -0.1               | -3.0               |
| 150                          | 0.00500 | 0.295 | 1.077                 | 1.2                 | 1.9                | 2.3                | 1.7                | 0.3                  | 0.2                  | 0.9                | 0.3                     | 0.2                          | 0.2                     | 0.2                     | -0.1                    | -                       | 1.077           | 1.072 | 0.2                | 0.0                | -1.0               |
| 150                          | 0.00800 | 0.185 | 0.978                 | 1.7                 | 3.7                | 4.0                | 3.2                | 2.5                  | 0.7                  | 1.7                | -1.3                    | -1.0                         | -1.0                    | -0.1                    | 0.0                     | -                       | 0.978           | 0.914 | 0.1                | 0.0                | -0.3               |
| 200                          | 0.00263 | 0.750 | 1.284                 | 2.2                 | 2.7                | 3.5                | 2.6                | 0.2                  | 0.1                  | 0.9                | 0.2                     | 0.1                          | 0.1                     | 0.1                     | -                       | 0.7                     | 1.285           | -     | -                  | -                  | -                  |
| 200                          | 0.00320 | 0.615 | 1.273                 | 1.9                 | 2.5                | 3.1                | 2.1                | 0.5                  | 0.4                  | 1.3                | -0.4                    | 0.8                          | 0.8                     | 0.2                     | -0.3                    | -                       | 1.274           | -     | -                  | -                  | -                  |
| 200                          | 0.00500 | 0.394 | 1.090                 | 1.3                 | 2.4                | 2.7                | 1.9                | 0.7                  | 0.7                  | 1.4                | 0.4                     | 1.2                          | 1.2                     | 0.2                     | -0.3                    | -                       | 1.090           | 1.115 | 0.2                | -0.1               | -1.9               |
| 200                          | 0.00800 | 0.246 | 0.941                 | 1.3                 | 2.1                | 2.5                | 1.8                | 0.7                  | 0.4                  | 1.0                | 0.2                     | 0.6                          | 0.6                     | 0.3                     | 0.0                     | -                       | 0.942           | 0.946 | 0.2                | -0.1               | -0.6               |
| 200                          | 0.01300 | 0.152 | 0.817                 | 1.4                 | 1.9                | 2.3                | 1.7                | 0.3                  | 0.1                  | 0.7                | 0.2                     | 0.3                          | 0.3                     | 0.1                     | 0.0                     | -                       | 0.817           | 0.796 | 0.2                | -0.1               | -0.2               |
| 200                          | 0.02000 | 0.099 | 0.738                 | 1.6                 | 2.2                | 2.7                | 1.9                | 0.7                  | 0.2                  | 1.0                | -0.6                    | -0.5                         | -0.5                    | 0.4                     | 0.0                     | -                       | 0.738           | 0.683 | 0.2                | -0.1               | -0.1               |
| 200                          | 0.03200 | 0.062 | 0.594                 | 1.9                 | 3.5                | 3.9                | 3.0                | 2.2                  | 0.4                  | 1.8                | -1.3                    | -1.0                         | -1.0                    | 0.1                     | 0.0                     | -                       | 0.594           | 0.580 | 0.2                | -0.1               | 0.0                |
| 200                          | 0.05000 | 0.039 | 0.499                 | 2.2                 | 4.4                | 4.9                | 3.8                | 3.2                  | 0.5                  | 2.1                | -1.9                    | -0.3                         | -0.3                    | 0.7                     | 0.0                     | -                       | 0.499           | 0.499 | 0.2                | -0.1               | 0.0                |
| 200                          | 0.08000 | 0.025 | 0.388                 | 2.5                 | 4.7                | 5.4                | 4.2                | 3.4                  | 0.8                  | 2.3                | -1.8                    | -0.8                         | -0.8                    | 0.5                     | 0.0                     | -                       | 0.388           | 0.428 | 0.1                | 0.0                | 0.0                |
| 200                          | 0.13000 | 0.015 | 0.365                 | 2.9                 | 4.5                | 5.3                | 4.1                | 2.8                  | 1.7                  | 1.8                | -1.4                    | -1.0                         | -1.0                    | -0.6                    | 0.0                     | -                       | 0.365           | 0.362 | 0.1                | 0.0                | 0.0                |
| 200                          | 0.25000 | 0.008 | 0.273                 | 4.1                 | 6.4                | 7.5                | 4.8                | 4.7                  | 3.4                  | 4.2                | -1.0                    | -2.5                         | -2.5                    | -3.2                    | 0.0                     | -                       | 0.273           | 0.256 | 0.1                | 0.0                | 0.0                |
| 200                          | 0.40000 | 0.005 | 0.128                 | 5.5                 | 6.5                | 8.5                | 5.1                | 2.7                  | 1.6                  | 4.1                | -2.2                    | -0.6                         | -0.6                    | -3.4                    | 0.0                     | -                       | 0.128           | 0.140 | 0.1                | 0.0                | 0.0                |
| 250                          | 0.00328 | 0.750 | 1.250                 | 2.5                 | 2.9                | 3.8                | 2.7                | 0.3                  | 0.1                  | 1.1                | -0.3                    | 0.6                          | 0.6                     | 0.0                     | -                       | 0.8                     | 1.250           | -     | -                  | -                  | -                  |
| 250                          | 0.00500 | 0.492 | 1.138                 | 1.5                 | 2.5                | 2.9                | 1.9                | 0.5                  | 0.7                  | 1.6                | 0.5                     | 1.4                          | 1.4                     | 0.1                     | -0.5                    | -                       | 1.138           | 1.147 | 0.3                | -0.1               | -3.1               |
| 250                          | 0.00800 | 0.308 | 0.940                 | 1.5                 | 2.7                | 3.1                | 2.2                | 1.4                  | 0.5                  | 1.4                | 1.0                     | 0.8                          | 0.8                     | 0.3                     | -0.1                    | -                       | 0.940           | 0.970 | 0.3                | -0.1               | -1.0               |
| 250                          | 0.01300 | 0.189 | 0.843                 | 1.5                 | 2.0                | 2.5                | 1.9                | 0.7                  | 0.4                  | 0.7                | 0.1                     | 0.5                          | 0.5                     | 0.4                     | 0.0                     | -                       | 0.843           | 0.814 | 0.3                | -0.1               | -0.3               |
| 250                          | 0.02000 | 0.123 | 0.713                 | 1.5                 | 2.5                | 2.9                | 2.3                | 1.5                  | 0.2                  | 1.1                | 0.6                     | -0.2                         | -0.2                    | 0.2                     | 0.0                     | -                       | 0.714           | 0.696 | 0.3                | -0.1               | -0.1               |
| 250                          | 0.03200 | 0.077 | 0.582                 | 1.6                 | 2.2                | 2.8                | 2.1                | 1.1                  | 0.2                  | 0.8                | 0.3                     | -0.5                         | -0.5                    | 0.4                     | 0.0                     | -                       | 0.582           | 0.588 | 0.2                | -0.1               | 0.0                |
| 250                          | 0.05000 | 0.049 | 0.484                 | 1.8                 | 2.5                | 3.1                | 2.2                | 1.1                  | 0.1                  | 1.2                | 0.5                     | -0.5                         | -0.5                    | 0.7                     | 0.0                     | -                       | 0.484           | 0.503 | 0.2                | -0.1               | 0.0                |
| 250                          | 0.08000 | 0.031 | 0.391                 | 2.1                 | 2.6                | 3.3                | 2.2                | 0.7                  | 0.7                  | 1.4                | 0.2                     | -0.3                         | -0.3                    | 1.0                     | 0.0                     | -                       | 0.391           | 0.430 | 0.2                | -0.1               | 0.0                |
| 250                          | 0.13000 | 0.019 | 0.336                 | 2.3                 | 5.1                | 5.6                | 4.5                | 3.5                  | 1.8                  | 2.4                | 1.6                     | -1.2                         | -1.2                    | -1.1                    | 0.0                     | -                       | 0.336           | 0.361 | 0.2                | -0.1               | 0.0                |
| 250                          | 0.25000 | 0.010 | 0.247                 | 3.1                 | 5.7                | 6.5                | 4.8                | 4.8                  | 3.5                  | 2.2                | 3.0                     | 2.3                          | 2.3                     | -1.4                    | 0.0                     | -                       | 0.247           | 0.253 | 0.1                | 0.0                | 0.0                |
| 250                          | 0.40000 | 0.006 | 0.125                 | 4.3                 | 7.7                | 8.8                | 5.6                | 3.8                  | 2.7                  | 5.3                | 2.2                     | -1.5                         | -1.5                    | -4.4                    | 0.0                     | -                       | 0.125           | 0.137 | 0.1                | 0.0                | 0.0                |
| 300                          | 0.00394 | 0.750 | 1.189                 | 2.7                 | 2.8                | 3.9                | 2.7                | 0.2                  | 0.2                  | 0.8                | -0.2                    | 0.6                          | 0.6                     | 0.1                     | -                       | 0.7                     | 1.190           | -     | -                  | -                  | -                  |
| 300                          | 0.00500 | 0.591 | 1.167                 | 2.5                 | 2.5                | 3.6                | 2.4                | 0.5                  | 0.2                  | 1.0                | 0.3                     | 0.6                          | 0.6                     | 0.1                     | -0.5                    | -                       | 1.168           | 1.174 | 0.4                | -0.2               | -4.7               |
| 300                          | 0.00800 | 0.369 | 1.013                 | 1.7                 | 2.3                | 2.9                | 1.9                | 0.2                  | 0.6                  | 1.3                | 0.2                     | 1.2                          | 1.2                     | 0.1                     | -0.1                    | -                       | 1.014           | 0.990 | 0.3                | -0.2               | -1.4               |
| 300                          | 0.01300 | 0.227 | 0.845                 | 1.7                 | 2.3                | 2.9                | 2.1                | 0.7                  | 0.7                  | 1.1                | 0.6                     | 0.7                          | 0.7                     | 0.3                     | 0.0                     | -                       | 0.846           | 0.828 | 0.3                | -0.2               | -0.4               |
| 300                          | 0.02000 | 0.148 | 0.720                 | 1.7                 | 2.1                | 2.8                | 2.0                | 0.9                  | 0.2                  | 0.7                | 0.6                     | 0.1                          | 0.1                     | 0.3                     | 0.0                     | -                       | 0.721           | 0.706 | 0.3                | -0.1               | -0.2               |
| 300                          | 0.03200 | 0.092 | 0.619                 | 1.8                 | 2.4                | 3.0                | 2.2                | 1.2                  | 0.3                  | 1.0                | 0.7                     | -0.2                         | -0.2                    | 0.4                     | 0.0                     | -                       | 0.620           | 0.594 | 0.3                | -0.1               | -0.1               |
| 300                          | 0.05000 | 0.059 | 0.487                 | 2.0                 | 2.8                | 3.5                | 2.6                | 1.8                  | 0.1                  | 1.2                | 0.9                     | -0.5                         | -0.5                    | 0.4                     | 0.0                     | -                       | 0.487           | 0.507 | 0.3                | -0.1               | 0.0                |
| 300                          | 0.08000 | 0.037 | 0.430                 | 2.2                 | 2.8                | 3.6                | 2.5                | 1.2                  | 1.1                  | 1.2                | 0.6                     | 0.5                          | 0.5                     | 0.9                     | 0.0                     | -                       | 0.430           | 0.431 | 0.2                | -0.1               | 0.0                |
| 300                          | 0.13000 | 0.023 | 0.361                 | 2.3                 | 4.6                | 5.1                | 3.9                | 3.0                  | 1.5                  | 2.3                | 2.0                     | -0.9                         | -0.9                    | -0.2                    | 0.0                     | -                       | 0.362           | 0.361 | 0.2                | -0.1               | 0.0                |
| 300                          | 0.25000 | 0.012 | 0.254                 | 3.2                 | 7.7                | 8.4                | 6.2                | 4.7                  | 3.1                  | 4.7                | 3.2                     | -1.9                         | -1.9                    | -2.6                    | 0.0                     | -                       | 0.254           | 0.251 | 0.2                | 0.0                | 0.0                |
| 300                          | 0.40000 | 0.007 | 0.162                 | 4.3                 | 8.1                | 9.2                | 6.6                | 4.9                  | 2.6                  | 4.7                | 2.8                     | -1.5                         | -1.5                    | -3.2                    | 0.0                     | -                       | 0.162           | 0.135 | 0.1                | 0.0                | 0.0                |

**Table C.2:** The NC  $e^+p$  reduced cross section  $\tilde{\sigma}_{NC}(x, Q^2)$  shown with statistical ( $\delta_{stat}$ ), systematic ( $\delta_{sys}$ ) and total ( $\delta_{tot}$ ) errors. Also shown are the total uncorrelated systematic ( $\delta_{unc}$ ) errors and two of its contributions: the electron energy error ( $\delta_{unc}^E$ ) and the hadronic energy error ( $\delta_{unc}^h$ ). The effect of the other uncorrelated systematic errors is included in ( $\delta_{unc}$ ). In addition the correlated systematic error ( $\delta_{cor}$ ) and its contributions from a positive variation of one standard deviation of the error on the electron energy ( $\delta_{cor}^{E+}$ ) and polar angle ( $\delta_{cor}^{\theta+}$ ), of the hadronic energy error ( $\delta_{cor}^{h+}$ ), of the error due to noise subtraction ( $\delta_{cor}^{N+}$ ) and background subtraction ( $\delta_{cor}^{B+}$ ), and of the error due to charge symmetry background subtraction in the high- $y$  analysis ( $\delta_{cor}^{S+}$ ) are given. The normalisation uncertainty of 1.5% is not included in the errors. The NC structure function term scaled by the helicity factor  $Y_+$   $\phi_{NC}/Y_+$  is also given as well as the electromagnetic structure function  $F_2$  with the corrections  $\Delta_{F_2}$ ,  $\Delta_{F_3}$  and  $\Delta_{F_L}$  as defined in eq. 9.1. For  $Q^2 < 2000 \text{ GeV}^2$ , the extraction of  $F_2$  is restricted to the region of  $y < 0.6$  in which the sensitivity to  $F_L$  is small. The table continues on the next 2 pages.



| $Q^2$<br>(GeV <sup>2</sup> ) | $x$     | $y$   | $\tilde{\sigma}_{NC}$ | $\delta_{stat}$<br>(%) | $\delta_{sys}$<br>(%) | $\delta_{tot}$<br>(%) | $\delta_{unc}$<br>(%) | $\delta_{unc}^E$<br>(%) | $\delta_{unc}^h$<br>(%) | $\delta_{cor}$<br>(%) | $\delta_{cor}^{E+}$<br>(%) | $\delta_{cor}^{\theta^+}$<br>(%) | $\delta_{cor}^{h^+}$<br>(%) | $\delta_{cor}^{N^+}$<br>(%) | $\delta_{cor}^{B^+}$<br>(%) | $\delta_{cor}^{S^+}$<br>(%) | $\phi_{NC}/Y_+$ | $F_2$ | $\Delta F_2$<br>(%) | $\Delta F_3$<br>(%) | $\Delta F_L$<br>(%) |
|------------------------------|---------|-------|-----------------------|------------------------|-----------------------|-----------------------|-----------------------|-------------------------|-------------------------|-----------------------|----------------------------|----------------------------------|-----------------------------|-----------------------------|-----------------------------|-----------------------------|-----------------|-------|---------------------|---------------------|---------------------|
| 400                          | 0.00525 | 0.750 | 1.162                 | 2.9                    | 3.0                   | 4.2                   | 2.9                   | 0.0                     | 0.2                     | 0.9                   | 0.0                        | 0.4                              | 0.4                         | 0.0                         | 0.0                         | 0.6                         | 1.163           | 1.021 | 0.5                 | -0.3                | -2.7                |
| 400                          | 0.00800 | 0.492 | 1.065                 | 2.1                    | 2.8                   | 3.5                   | 2.2                   | 0.4                     | 0.8                     | 1.7                   | 0.4                        | 1.3                              | 1.3                         | 0.2                         | -0.3                        | —                           | 1.056           | 0.867 | 0.6                 | -0.4                | -1.3                |
| 400                          | 0.01300 | 0.303 | 0.902                 | 2.0                    | 2.6                   | 3.3                   | 2.3                   | 1.1                     | 0.3                     | 1.3                   | 1.0                        | 0.6                              | 0.6                         | 0.2                         | -0.1                        | —                           | 0.850           | 0.734 | 0.7                 | -0.4                | -0.4                |
| 400                          | 0.02000 | 0.197 | 0.734                 | 2.0                    | 2.2                   | 2.9                   | 2.0                   | 0.3                     | 0.5                     | 0.7                   | -0.2                       | 0.5                              | 0.5                         | 0.2                         | 0.0                         | —                           | 0.721           | 0.604 | 0.4                 | -0.3                | -0.3                |
| 400                          | 0.03200 | 0.123 | 0.602                 | 2.1                    | 2.5                   | 3.2                   | 2.2                   | 1.0                     | 0.3                     | 1.1                   | 1.0                        | 0.2                              | 0.2                         | 0.3                         | 0.0                         | —                           | 0.603           | 0.513 | 0.4                 | -0.2                | -0.1                |
| 400                          | 0.05000 | 0.079 | 0.508                 | 2.2                    | 2.8                   | 3.6                   | 2.4                   | 1.2                     | 0.1                     | 1.1                   | 1.2                        | -0.5                             | -0.5                        | 0.4                         | 0.0                         | —                           | 0.509           | 0.433 | 0.4                 | -0.2                | 0.0                 |
| 400                          | 0.08000 | 0.049 | 0.426                 | 2.4                    | 2.7                   | 3.7                   | 2.5                   | 0.8                     | 1.1                     | 1.5                   | 0.6                        | -0.4                             | -0.4                        | 0.6                         | 0.0                         | —                           | 0.427           | 0.360 | 0.3                 | -0.1                | 0.0                 |
| 400                          | 0.13000 | 0.030 | 0.356                 | 2.5                    | 3.0                   | 3.9                   | 2.6                   | 1.3                     | 0.9                     | 1.4                   | 1.2                        | -0.5                             | -0.5                        | -0.4                        | 0.0                         | —                           | 0.356           | 0.307 | 0.3                 | -0.1                | 0.0                 |
| 400                          | 0.25000 | 0.016 | 0.241                 | 3.5                    | 6.6                   | 7.5                   | 5.2                   | 3.3                     | 3.1                     | 4.0                   | 3.1                        | -1.8                             | -1.8                        | -1.5                        | 0.0                         | —                           | 0.241           | 0.245 | 0.4                 | -0.1                | 0.0                 |
| 400                          | 0.40000 | 0.010 | 0.152                 | 4.9                    | 7.5                   | 9.0                   | 5.5                   | 3.0                     | 2.7                     | 5.0                   | 2.8                        | -1.5                             | -1.5                        | -3.9                        | 0.0                         | —                           | 0.152           | 0.132 | 0.2                 | -0.1                | 0.0                 |
| 500                          | 0.00656 | 0.750 | 1.021                 | 3.3                    | 3.1                   | 4.5                   | 2.9                   | 0.1                     | 0.3                     | 1.0                   | 0.1                        | 0.5                              | 0.5                         | 0.1                         | —                           | 0.3                         | 1.022           | —     | —                   | —                   | —                   |
| 500                          | 0.00800 | 0.615 | 1.025                 | 3.6                    | 3.5                   | 5.0                   | 3.2                   | 1.2                     | 0.5                     | 1.5                   | -1.2                       | 0.7                              | 0.7                         | -0.1                        | -0.6                        | —                           | 1.026           | —     | —                   | —                   | —                   |
| 500                          | 0.01300 | 0.379 | 0.895                 | 2.4                    | 2.8                   | 3.7                   | 2.4                   | 0.5                     | 0.8                     | 1.5                   | 0.6                        | 1.2                              | 1.2                         | 0.2                         | -0.2                        | —                           | 0.896           | 0.867 | 0.6                 | -0.4                | -1.3                |
| 500                          | 0.02000 | 0.246 | 0.739                 | 2.4                    | 2.8                   | 3.7                   | 2.3                   | 0.8                     | 0.4                     | 1.7                   | 0.8                        | 0.5                              | 0.5                         | 0.2                         | 0.0                         | —                           | 0.739           | 0.734 | 0.7                 | -0.4                | -0.4                |
| 500                          | 0.03200 | 0.154 | 0.626                 | 2.4                    | 2.3                   | 3.3                   | 2.2                   | 0.4                     | 0.3                     | 0.6                   | 0.4                        | -0.2                             | -0.2                        | 0.3                         | -0.1                        | —                           | 0.626           | 0.612 | 0.6                 | -0.4                | -0.1                |
| 500                          | 0.05000 | 0.099 | 0.539                 | 2.5                    | 2.6                   | 3.6                   | 2.4                   | 0.8                     | 0.6                     | 1.2                   | 0.9                        | 0.3                              | 0.3                         | 0.6                         | 0.0                         | —                           | 0.539           | 0.517 | 0.5                 | -0.3                | 0.0                 |
| 500                          | 0.08000 | 0.062 | 0.413                 | 2.8                    | 3.1                   | 4.2                   | 2.6                   | 1.4                     | 0.1                     | 1.6                   | 1.4                        | -0.7                             | -0.7                        | 0.1                         | 0.0                         | —                           | 0.413           | 0.434 | 0.6                 | -0.3                | 0.0                 |
| 500                          | 0.13000 | 0.038 | 0.348                 | 3.4                    | 3.5                   | 4.9                   | 3.0                   | 1.6                     | 0.5                     | 1.8                   | 1.6                        | -0.3                             | -0.3                        | 0.8                         | 0.0                         | —                           | 0.348           | 0.359 | 0.4                 | -0.2                | 0.0                 |
| 500                          | 0.18000 | 0.027 | 0.304                 | 3.8                    | 4.1                   | 5.6                   | 3.6                   | 1.7                     | 1.4                     | 2.0                   | 1.7                        | -0.9                             | -0.9                        | -0.2                        | 0.0                         | —                           | 0.304           | 0.307 | 0.4                 | -0.2                | 0.0                 |
| 500                          | 0.25000 | 0.020 | 0.244                 | 5.0                    | 8.6                   | 9.9                   | 6.6                   | 4.0                     | 3.9                     | 5.5                   | 4.0                        | -2.4                             | -2.4                        | -2.9                        | 0.0                         | —                           | 0.244           | 0.245 | 0.4                 | -0.1                | 0.0                 |
| 500                          | 0.40000 | 0.012 | 0.158                 | 6.9                    | 8.7                   | 11.1                  | 7.2                   | 3.8                     | 3.3                     | 4.8                   | 3.7                        | -1.7                             | -1.7                        | -2.5                        | 0.0                         | —                           | 0.158           | 0.129 | 0.3                 | -0.1                | 0.0                 |
| 650                          | 0.00853 | 0.750 | 0.989                 | 3.8                    | 3.8                   | 5.4                   | 3.7                   | 0.5                     | 0.5                     | 0.9                   | -0.6                       | 0.5                              | 0.5                         | 0.1                         | —                           | 0.1                         | 0.990           | —     | —                   | —                   | —                   |
| 650                          | 0.01300 | 0.492 | 0.899                 | 3.0                    | 2.9                   | 4.2                   | 2.6                   | 0.6                     | 0.5                     | 1.4                   | 0.6                        | 0.9                              | 0.9                         | 0.2                         | -0.2                        | —                           | 0.900           | 0.887 | 0.9                 | -0.7                | -2.3                |
| 650                          | 0.02000 | 0.320 | 0.750                 | 2.9                    | 2.7                   | 4.0                   | 2.5                   | 0.3                     | 0.6                     | 1.0                   | 0.2                        | 0.8                              | 0.8                         | 0.1                         | 0.0                         | —                           | 0.751           | 0.748 | 0.8                 | -0.7                | -0.7                |
| 650                          | 0.03200 | 0.200 | 0.584                 | 2.9                    | 3.0                   | 4.1                   | 2.6                   | 1.1                     | 0.5                     | 1.4                   | 1.0                        | 0.4                              | 0.4                         | 0.3                         | 0.0                         | —                           | 0.585           | 0.621 | 0.9                 | -0.6                | -0.2                |
| 650                          | 0.05000 | 0.128 | 0.523                 | 2.9                    | 3.0                   | 4.2                   | 2.6                   | 1.0                     | 0.2                     | 1.4                   | 1.0                        | -0.3                             | -0.3                        | 0.2                         | 0.0                         | —                           | 0.524           | 0.522 | 0.8                 | -0.5                | -0.1                |
| 650                          | 0.08000 | 0.080 | 0.447                 | 3.2                    | 3.2                   | 4.5                   | 2.7                   | 1.1                     | 0.5                     | 1.6                   | 1.2                        | 0.2                              | 0.2                         | 0.3                         | 0.0                         | —                           | 0.447           | 0.436 | 0.7                 | -0.4                | 0.0                 |
| 650                          | 0.13000 | 0.049 | 0.358                 | 3.9                    | 3.3                   | 5.1                   | 3.1                   | 0.8                     | 1.0                     | 1.0                   | 0.5                        | -0.3                             | -0.3                        | 0.7                         | 0.0                         | —                           | 0.358           | 0.358 | 0.7                 | -0.3                | 0.0                 |
| 650                          | 0.18000 | 0.036 | 0.306                 | 4.3                    | 4.4                   | 6.2                   | 3.7                   | 1.8                     | 1.1                     | 2.3                   | 1.9                        | -0.9                             | -0.9                        | -0.2                        | 0.0                         | —                           | 0.306           | 0.305 | 0.6                 | -0.3                | 0.0                 |
| 650                          | 0.25000 | 0.026 | 0.246                 | 5.5                    | 8.7                   | 10.3                  | 6.9                   | 3.9                     | 4.2                     | 5.3                   | 4.2                        | -2.1                             | -2.1                        | -2.4                        | 0.0                         | —                           | 0.246           | 0.242 | 0.6                 | -0.2                | 0.0                 |
| 650                          | 0.40000 | 0.016 | 0.149                 | 8.5                    | 11.5                  | 14.4                  | 8.9                   | 4.9                     | 4.2                     | 7.4                   | 4.9                        | -2.1                             | -2.1                        | -4.8                        | 0.0                         | —                           | 0.149           | 0.126 | 0.5                 | -0.1                | 0.0                 |
| 800                          | 0.01050 | 0.750 | 0.948                 | 4.5                    | 4.4                   | 6.3                   | 4.2                   | 1.2                     | 0.2                     | 1.5                   | 0.9                        | 0.2                              | 0.2                         | 0.0                         | —                           | 0.2                         | 0.950           | —     | —                   | —                   | —                   |
| 800                          | 0.01300 | 0.606 | 0.797                 | 4.8                    | 3.7                   | 6.1                   | 3.6                   | 0.4                     | 0.2                     | 1.1                   | 0.4                        | 0.4                              | 0.4                         | 0.1                         | -0.2                        | —                           | 0.798           | —     | —                   | —                   | —                   |
| 800                          | 0.02000 | 0.394 | 0.795                 | 3.4                    | 3.2                   | 4.7                   | 2.9                   | 0.3                     | 0.8                     | 1.5                   | 0.3                        | 1.2                              | 1.2                         | 0.2                         | -0.1                        | —                           | 0.796           | 0.759 | 1.2                 | -1.0                | -1.2                |
| 800                          | 0.03200 | 0.246 | 0.576                 | 3.5                    | 2.8                   | 4.5                   | 2.7                   | 0.3                     | 0.4                     | 0.8                   | -0.4                       | 0.5                              | 0.5                         | 0.3                         | 0.0                         | —                           | 0.577           | 0.628 | 1.1                 | -0.9                | -0.3                |
| 800                          | 0.05000 | 0.158 | 0.540                 | 3.4                    | 2.7                   | 4.4                   | 2.7                   | 0.2                     | 0.4                     | 0.5                   | 0.3                        | 0.2                              | 0.2                         | 0.4                         | 0.0                         | —                           | 0.541           | 0.526 | 1.1                 | -0.8                | -0.1                |
| 800                          | 0.08000 | 0.099 | 0.451                 | 3.7                    | 3.5                   | 5.1                   | 3.1                   | 1.4                     | 0.1                     | 1.5                   | 1.3                        | -0.3                             | -0.3                        | 0.2                         | 0.0                         | —                           | 0.452           | 0.438 | 1.0                 | -0.6                | 0.0                 |
| 800                          | 0.13000 | 0.061 | 0.355                 | 4.6                    | 4.4                   | 6.4                   | 3.9                   | 1.8                     | 1.2                     | 2.1                   | 1.8                        | -0.4                             | -0.4                        | 0.3                         | 0.0                         | —                           | 0.355           | 0.358 | 1.0                 | -0.5                | 0.0                 |
| 800                          | 0.18000 | 0.044 | 0.309                 | 4.9                    | 4.4                   | 6.6                   | 3.9                   | 1.5                     | 1.2                     | 2.0                   | 1.7                        | -0.7                             | -0.7                        | -0.7                        | 0.0                         | —                           | 0.309           | 0.303 | 0.9                 | -0.4                | 0.0                 |
| 800                          | 0.25000 | 0.032 | 0.267                 | 6.1                    | 8.1                   | 10.2                  | 6.6                   | 3.7                     | 3.3                     | 4.7                   | 3.6                        | -2.1                             | -2.1                        | -2.1                        | 0.0                         | —                           | 0.267           | 0.240 | 0.8                 | -0.3                | 0.0                 |
| 800                          | 0.40000 | 0.020 | 0.123                 | 9.8                    | 8.9                   | 13.3                  | 7.9                   | 3.0                     | 3.7                     | 4.1                   | 3.1                        | -2.3                             | -2.3                        | -1.3                        | 0.0                         | —                           | 0.123           | 0.124 | 0.7                 | -0.2                | 0.0                 |
| 800                          | 0.65000 | 0.012 | 0.021                 | 16.4                   | 13.4                  | 21.2                  | 11.5                  | 4.1                     | 3.1                     | 6.9                   | 4.1                        | -0.6                             | -0.6                        | -5.3                        | 0.0                         | —                           | 0.021           | 0.016 | 2.5                 | -0.1                | 0.0                 |
| 1000                         | 0.01300 | 0.757 | 0.845                 | 5.2                    | 4.5                   | 6.9                   | 4.2                   | 0.8                     | 0.4                     | 1.7                   | 0.3                        | -0.4                             | -0.4                        | 0.0                         | -1.6                        | —                           | 0.846           | —     | —                   | —                   | —                   |
| 1000                         | 0.02000 | 0.492 | 0.776                 | 3.8                    | 3.3                   | 5.0                   | 2.9                   | 0.8                     | 0.9                     | 1.6                   | -0.7                       | 1.3                              | 1.3                         | 0.1                         | -0.2                        | —                           | 0.777           | 0.772 | 1.6                 | -1.6                | -1.9                |
| 1000                         | 0.03000 | 0.308 | 0.663                 | 3.9                    | 3.1                   | 5.0                   | 2.8                   | 0.7                     | 0.3                     | 1.5                   | 0.6                        | 0.5                              | 0.5                         | 0.2                         | -0.1                        | —                           | 0.664           | 0.636 | 1.5                 | -1.4                | -0.5                |
| 1000                         | 0.05000 | 0.197 | 0.555                 | 4.0                    | 3.1                   | 5.0                   | 2.8                   | 0.5                     | 0.8                     | 1.2                   | 0.5                        | 0.6                              | 0.6                         | 0.4                         | 0.0                         | —                           | 0.556           | 0.531 | 1.4                 | -1.2                | -0.2                |
| 1000                         | 0.08000 | 0.123 | 0.443                 | 4.2                    | 2.9                   | 5.1                   | 2.8                   | 0.4                     | 0.2                     | 0.8                   | 0.4                        | 0.2                              | 0.2                         | 0.3                         | 0.0                         | —                           | 0.444           | 0.440 | 1.4                 | -1.0                | 0.0                 |
| 1000                         | 0.13000 | 0.076 | 0.351                 | 5.4                    | 4.8                   | 7.2                   | 4.0                   | 2.4                     | 0.6                     | 2.7                   | 2.4                        | -1.0                             | -1.0                        | -0.4                        | 0.0                         | —                           | 0.351           | 0.358 | 1.3                 | -0.8                | 0.0                 |
| 1000                         | 0.18000 | 0.055 | 0.318                 | 5.8                    | 4.5                   | 7.3                   | 3.9                   | 1.6                     | 0.4                     | 4.2                   | 4.0                        | 0.6                              | 0.6                         | 1.0                         | 0.0                         | —                           | 0.319           | 0.302 | 1.2                 | -0.6                | 0.0                 |
| 1000                         | 0.25000 | 0.039 | 0.234                 | 6.8                    | 6.9                   | 9.7                   | 5.6                   | 3.3                     | 2.4                     | 4.0                   | 3.3                        | -2.0                             | -2.0                        | -1.1                        | 0.0                         | —                           | 0.234           | 0.238 | 1.2                 | -0.5                | 0.0                 |
| 1000                         | 0.40000 | 0.025 | 0.140                 | 10.0                   | 10.3                  | 14.3                  | 8.6                   | 4.7                     | 3.9                     | 5.7                   | 4.7                        | -1.9                             | -1.9                        | -2.3                        | 0.0                         | —                           | 0.140           | 0.122 | 1.0                 | -0.3                | 0.0                 |
| 1000                         | 0.65000 | 0.015 | 0.025                 | 17.4                   | 15.6                  | 23.4                  | 12.8                  | 3.8                     | 6.5                     | 8.9                   | 3.8                        | -3.7                             | -3.7                        | -7.1                        | 0.0                         | —                           | 0.025           | 0.016 | 3.5                 | -0.2                | 0.0                 |

| $Q^2$<br>(GeV <sup>2</sup> ) | $x$     | $y$   | $\tilde{\sigma}_{NC}$ | $\delta_{stat}$<br>(%) | $\delta_{sys}$<br>(%) | $\delta_{tot}$<br>(%) | $\delta_{unc}$<br>(%) | $\delta_{unc}^{E}$<br>(%) | $\delta_{unc}^h$<br>(%) | $\delta_{cor}$<br>(%) | $\delta_{cor}^{E+}$<br>(%) | $\delta_{cor}^{\theta+}$<br>(%) | $\delta_{cor}^{h+}$<br>(%) | $\delta_{cor}^{N+}$<br>(%) | $\delta_{cor}^{B+}$<br>(%) | $\delta_{cor}^{S+}$<br>(%) | $\phi_{NC}/Y_+$ | $F_2$ | $\Delta F_2$<br>(%) | $\Delta F_3$<br>(%) | $\Delta F_L$<br>(%) |
|------------------------------|---------|-------|-----------------------|------------------------|-----------------------|-----------------------|-----------------------|---------------------------|-------------------------|-----------------------|----------------------------|---------------------------------|----------------------------|----------------------------|----------------------------|----------------------------|-----------------|-------|---------------------|---------------------|---------------------|
| 1200                         | 0.02000 | 0.591 | 0.789                 | 4.8                    | 3.7                   | 6.0                   | 3.2                   | 0.4                       | 0.6                     | 1.9                   | 0.1                        | 1.5                             | 1.5                        | 0.1                        | -0.4                       | -                          | 0.791           | 0.783 | 2.1                 | -2.3                | -2.9                |
| 1200                         | 0.03200 | 0.369 | 0.633                 | 4.5                    | 2.8                   | 5.3                   | 2.5                   | 0.5                       | 0.9                     | 1.3                   | 0.4                        | 1.0                             | 1.0                        | 0.2                        | -0.1                       | -                          | 0.634           | 0.644 | 2.0                 | -2.1                | -0.8                |
| 1200                         | 0.05000 | 0.236 | 0.476                 | 4.8                    | 2.5                   | 5.4                   | 2.4                   | 0.6                       | 0.3                     | 0.9                   | 0.6                        | 0.2                             | 0.2                        | 0.1                        | 0.0                        | -                          | 0.476           | 0.536 | 1.9                 | -1.8                | -0.2                |
| 1200                         | 0.08000 | 0.148 | 0.475                 | 4.6                    | 2.5                   | 5.2                   | 2.3                   | 0.4                       | 0.2                     | 0.7                   | -0.4                       | 0.3                             | 0.3                        | 0.2                        | 0.0                        | -                          | 0.442           | 0.442 | 1.9                 | -1.4                | -0.1                |
| 1200                         | 0.13000 | 0.091 | 0.375                 | 5.8                    | 3.0                   | 6.5                   | 0.8                   | 0.4                       | 0.4                     | 1.0                   | 0.9                        | -0.2                            | -0.2                       | 0.5                        | 0.0                        | -                          | 0.375           | 0.359 | 1.7                 | -1.1                | 0.0                 |
| 1200                         | 0.18000 | 0.066 | 0.335                 | 6.6                    | 3.5                   | 7.5                   | 0.7                   | 0.8                       | 0.7                     | 1.6                   | 0.8                        | -0.5                            | -0.5                       | 0.3                        | 0.0                        | -                          | 0.336           | 0.302 | 1.7                 | -0.9                | 0.0                 |
| 1200                         | 0.25000 | 0.047 | 0.250                 | 7.4                    | 5.9                   | 9.4                   | 4.8                   | 2.9                       | 2.2                     | 3.4                   | 2.8                        | -1.8                            | -1.8                       | 0.5                        | 0.0                        | -                          | 0.251           | 0.237 | 1.6                 | -0.7                | 0.0                 |
| 1200                         | 0.40000 | 0.030 | 0.117                 | 11.9                   | 10.5                  | 15.8                  | 8.2                   | 3.9                       | 5.5                     | 6.5                   | 4.6                        | -2.6                            | -2.6                       | -3.7                       | 0.0                        | -                          | 0.117           | 0.120 | 1.4                 | -0.4                | 0.0                 |
| 1200                         | 0.65000 | 0.018 | 0.022                 | 21.3                   | 10.0                  | 23.6                  | 2.6                   | 2.6                       | 2.7                     | 3.6                   | 2.6                        | -1.5                            | -1.5                       | -1.4                       | 0.0                        | -                          | 0.022           | 0.015 | 3.9                 | -0.3                | 0.0                 |
| 1500                         | 0.02000 | 0.738 | 0.713                 | 6.4                    | 4.4                   | 7.8                   | 4.1                   | 1.9                       | 0.0                     | 1.5                   | 1.0                        | 0.2                             | 0.2                        | -0.1                       | -0.7                       | -                          | 0.715           | -     | -                   | -                   | -                   |
| 1500                         | 0.03200 | 0.462 | 0.625                 | 5.7                    | 4.0                   | 6.9                   | 3.5                   | 0.9                       | 1.1                     | 1.8                   | 0.7                        | 1.5                             | 1.5                        | 0.2                        | -0.1                       | -                          | 0.626           | 0.653 | 2.6                 | -3.1                | -1.3                |
| 1500                         | 0.05000 | 0.295 | 0.561                 | 5.2                    | 2.9                   | 5.9                   | 2.6                   | 0.6                       | 0.5                     | 1.3                   | 0.6                        | 0.5                             | 0.5                        | 0.2                        | 0.0                        | -                          | 0.562           | 0.541 | 2.5                 | -2.7                | -0.4                |
| 1500                         | 0.08000 | 0.185 | 0.439                 | 5.3                    | 3.1                   | 6.1                   | 2.6                   | 0.9                       | 0.4                     | 1.7                   | 1.0                        | 0.2                             | 0.2                        | 0.1                        | 0.0                        | -                          | 0.440           | 0.445 | 2.5                 | -2.2                | -0.1                |
| 1500                         | 0.13000 | 0.114 | 0.358                 | 6.4                    | 3.2                   | 7.2                   | 3.0                   | 1.1                       | 0.3                     | 1.3                   | 1.1                        | -0.3                            | -0.3                       | 0.3                        | 0.0                        | -                          | 0.358           | 0.359 | 2.2                 | -1.7                | 0.0                 |
| 1500                         | 0.18000 | 0.082 | 0.320                 | 7.4                    | 3.6                   | 8.2                   | 3.4                   | 0.7                       | 1.1                     | 1.3                   | 0.6                        | 0.5                             | 0.5                        | 0.3                        | 0.0                        | -                          | 0.320           | 0.301 | 2.2                 | -1.3                | 0.0                 |
| 1500                         | 0.25000 | 0.059 | 0.214                 | 8.1                    | 4.3                   | 9.2                   | 3.7                   | 1.3                       | 1.3                     | 2.2                   | 1.3                        | -1.7                            | -1.7                       | -0.5                       | 0.0                        | -                          | 0.214           | 0.235 | 2.1                 | -1.0                | 0.0                 |
| 1500                         | 0.40000 | 0.037 | 0.104                 | 12.7                   | 9.0                   | 15.5                  | 7.3                   | 4.1                       | 4.0                     | 5.3                   | 4.2                        | -1.9                            | -1.9                       | 2.1                        | 0.0                        | -                          | 0.104           | 0.119 | 1.8                 | -0.6                | 0.0                 |
| 1500                         | 0.65000 | 0.023 | 0.010                 | 35.4                   | 18.1                  | 39.7                  | 14.8                  | 8.0                       | 7.8                     | 10.4                  | 8.0                        | -5.2                            | -5.2                       | -3.8                       | 0.0                        | -                          | 0.010           | 0.015 | 4.4                 | -0.4                | 0.0                 |
| 2000                         | 0.03200 | 0.615 | 0.681                 | 6.2                    | 4.4                   | 7.6                   | 3.8                   | 1.1                       | 1.4                     | 2.2                   | 0.4                        | 2.1                             | 2.1                        | 0.1                        | -0.5                       | -                          | 0.683           | 0.667 | 3.8                 | -5.3                | -2.5                |
| 2000                         | 0.05000 | 0.394 | 0.471                 | 7.4                    | 4.2                   | 8.5                   | 3.8                   | 1.1                       | 0.9                     | 1.7                   | 1.1                        | 0.9                             | 0.9                        | 0.1                        | 0.0                        | -                          | 0.472           | 0.551 | 3.8                 | -4.7                | -0.7                |
| 2000                         | 0.08000 | 0.246 | 0.414                 | 6.5                    | 3.8                   | 7.6                   | 3.5                   | 1.0                       | 0.5                     | 1.3                   | 0.9                        | 0.7                             | 0.7                        | 0.2                        | 0.0                        | -                          | 0.415           | 0.450 | 3.5                 | -3.8                | -0.2                |
| 2000                         | 0.13000 | 0.152 | 0.374                 | 7.0                    | 4.1                   | 8.2                   | 3.8                   | 1.1                       | 0.5                     | 1.6                   | 1.0                        | -0.5                            | -0.5                       | 0.5                        | 0.0                        | -                          | 0.375           | 0.361 | 3.3                 | -2.8                | 0.0                 |
| 2000                         | 0.18000 | 0.109 | 0.313                 | 8.5                    | 4.8                   | 9.7                   | 4.4                   | 1.8                       | 0.6                     | 2.0                   | 1.9                        | -0.3                            | -0.3                       | 0.2                        | 0.0                        | -                          | 0.313           | 0.302 | 3.1                 | -2.2                | 0.0                 |
| 2000                         | 0.25000 | 0.079 | 0.226                 | 9.4                    | 5.6                   | 10.9                  | 4.9                   | 2.3                       | 0.9                     | 2.8                   | 2.1                        | -0.9                            | -0.9                       | 0.3                        | 0.0                        | -                          | 0.226           | 0.235 | 3.0                 | -1.7                | 0.0                 |
| 2000                         | 0.40000 | 0.049 | 0.119                 | 12.3                   | 11.4                  | 16.8                  | 9.5                   | 5.2                       | 5.0                     | 6.4                   | 5.4                        | -3.0                            | -3.0                       | -1.5                       | 0.0                        | -                          | 0.119           | 0.117 | 2.8                 | -1.1                | 0.0                 |
| 2000                         | 0.65000 | 0.030 | 0.026                 | 25.0                   | 21.2                  | 32.8                  | 17.3                  | 10.1                      | 7.0                     | 12.2                  | 9.4                        | -4.6                            | -4.6                       | -6.2                       | 0.0                        | -                          | 0.026           | 0.014 | 3.2                 | -0.7                | 0.0                 |
| 3000                         | 0.05000 | 0.591 | 0.563                 | 5.5                    | 4.3                   | 7.0                   | 3.8                   | 0.9                       | 1.1                     | 2.0                   | -0.3                       | 1.7                             | 1.7                        | 0.2                        | -0.6                       | -                          | 0.566           | 0.568 | 6.3                 | -10.0               | -1.7                |
| 3000                         | 0.08000 | 0.369 | 0.458                 | 6.1                    | 3.7                   | 7.1                   | 3.5                   | 0.8                       | 1.0                     | 1.1                   | 0.7                        | 0.9                             | 0.9                        | 0.2                        | 0.0                        | -                          | 0.459           | 0.461 | 6.0                 | -8.2                | -0.4                |
| 3000                         | 0.13000 | 0.227 | 0.327                 | 7.1                    | 3.7                   | 8.0                   | 3.5                   | 0.5                       | 0.6                     | 1.1                   | -0.9                       | -0.5                            | -0.5                       | -0.1                       | 0.0                        | -                          | 0.328           | 0.367 | 5.7                 | -6.1                | -0.1                |
| 3000                         | 0.18000 | 0.164 | 0.313                 | 7.7                    | 5.0                   | 9.2                   | 4.5                   | 2.4                       | 0.4                     | 2.4                   | 2.3                        | -0.5                            | -0.5                       | 0.3                        | 0.0                        | -                          | 0.314           | 0.304 | 5.4                 | -4.7                | 0.0                 |
| 3000                         | 0.25000 | 0.118 | 0.201                 | 9.7                    | 5.2                   | 11.0                  | 4.6                   | 2.1                       | 0.6                     | 2.4                   | 2.3                        | -0.7                            | -0.7                       | -0.2                       | 0.0                        | -                          | 0.201           | 0.235 | 5.1                 | -3.6                | 0.0                 |
| 3000                         | 0.40000 | 0.074 | 0.093                 | 12.3                   | 7.2                   | 14.2                  | 6.1                   | 3.5                       | 1.7                     | 3.8                   | 3.6                        | -1.2                            | -1.2                       | 0.0                        | 0.0                        | -                          | 0.093           | 0.115 | 4.6                 | -2.3                | 0.0                 |
| 3000                         | 0.65000 | 0.045 | 0.009                 | 30.2                   | 16.6                  | 34.4                  | 13.9                  | 7.1                       | 7.3                     | 9.1                   | 6.8                        | -5.2                            | -5.2                       | -2.7                       | 0.0                        | -                          | 0.009           | 0.014 | 5.7                 | -1.4                | 0.0                 |
| 5000                         | 0.08000 | 0.615 | 0.421                 | 6.9                    | 5.0                   | 8.5                   | 4.7                   | 2.8                       | 1.3                     | 1.7                   | 0.6                        | 1.4                             | 1.4                        | 0.2                        | -0.1                       | -                          | 0.424           | 0.483 | 11.0                | -20.1               | -1.4                |
| 5000                         | 0.13000 | 0.379 | 0.339                 | 8.0                    | 4.4                   | 9.2                   | 4.2                   | 1.1                       | 1.3                     | 1.3                   | -0.6                       | 1.1                             | 1.1                        | 0.3                        | 0.0                        | -                          | 0.341           | 0.380 | 10.4                | -15.2               | -0.3                |
| 5000                         | 0.18000 | 0.274 | 0.259                 | 9.2                    | 4.9                   | 10.5                  | 4.4                   | 1.1                       | 1.2                     | 2.3                   | 1.4                        | 1.3                             | 1.3                        | 0.3                        | -0.1                       | -                          | 0.260           | 0.313 | 9.9                 | -11.8               | -0.1                |
| 5000                         | 0.25000 | 0.197 | 0.266                 | 9.7                    | 8.3                   | 12.8                  | 7.8                   | 6.0                       | 1.9                     | 3.0                   | 2.5                        | -1.1                            | -1.1                       | 0.2                        | 0.0                        | -                          | 0.267           | 0.238 | 9.4                 | -8.8                | 0.0                 |
| 5000                         | 0.40000 | 0.123 | 0.118                 | 13.1                   | 7.6                   | 15.2                  | 7.2                   | 4.5                       | 1.4                     | 2.3                   | 2.1                        | -0.5                            | -0.5                       | -0.1                       | 0.0                        | -                          | 0.119           | 0.115 | 8.3                 | -5.5                | 0.0                 |
| 5000                         | 0.65000 | 0.076 | 0.007                 | 40.8                   | 16.2                  | 43.9                  | 15.0                  | 12.1                      | 4.7                     | 6.3                   | 4.2                        | -4.0                            | -4.0                       | -2.3                       | 0.0                        | -                          | 0.007           | 0.013 | 9.0                 | -3.4                | 0.0                 |
| 8000                         | 0.13000 | 0.606 | 0.382                 | 10.5                   | 5.6                   | 11.9                  | 5.4                   | 2.0                       | 0.9                     | 1.2                   | -0.7                       | 0.9                             | 0.9                        | 0.1                        | 0.0                        | -                          | 0.385           | 0.398 | 17.0                | -33.1               | -0.9                |
| 8000                         | 0.18000 | 0.438 | 0.334                 | 10.9                   | 5.8                   | 12.4                  | 5.5                   | 1.3                       | 1.7                     | 1.7                   | -0.9                       | 0.8                             | 0.8                        | 0.2                        | 0.0                        | -                          | 0.336           | 0.325 | 15.8                | -26.1               | -0.3                |
| 8000                         | 0.25000 | 0.315 | 0.239                 | 12.0                   | 7.7                   | 14.2                  | 7.5                   | 5.4                       | 0.7                     | 1.6                   | 1.3                        | 0.4                             | 0.4                        | 0.4                        | 0.0                        | -                          | 0.240           | 0.246 | 15.2                | -19.4               | -0.1                |
| 8000                         | 0.40000 | 0.197 | 0.094                 | 13.4                   | 13.4                  | 23.4                  | 12.7                  | 10.4                      | 2.3                     | 4.3                   | 3.7                        | -1.2                            | -1.2                       | -0.1                       | 0.0                        | -                          | 0.094           | 0.116 | 13.5                | -12.0               | 0.0                 |
| 8000                         | 0.65000 | 0.121 | 0.015                 | 31.6                   | 21.6                  | 38.3                  | 21.0                  | 17.8                      | 2.3                     | 5.1                   | 4.5                        | -1.3                            | -1.3                       | -1.3                       | 0.0                        | -                          | 0.015           | 0.013 | 14.5                | -7.3                | 0.0                 |
| 12000                        | 0.18000 | 0.656 | 0.266                 | 18.0                   | 4.8                   | 18.6                  | 4.6                   | 2.6                       | 0.6                     | 1.4                   | 0.6                        | 0.7                             | 0.7                        | 0.0                        | 0.0                        | -                          | 0.269           | 0.340 | 22.7                | -48.1               | -0.9                |
| 12000                        | 0.25000 | 0.473 | 0.104                 | 28.0                   | 5.4                   | 25.6                  | 5.2                   | 4.2                       | 1.5                     | 1.1                   | 0.6                        | 0.9                             | 0.9                        | 0.2                        | 0.0                        | -                          | 0.105           | 0.254 | 21.1                | -36.7               | -0.3                |
| 12000                        | 0.40000 | 0.295 | 0.056                 | 30.2                   | 10.3                  | 31.9                  | 9.9                   | 9.1                       | 0.6                     | 2.8                   | 2.6                        | -0.2                            | -0.2                       | 0.0                        | 0.0                        | -                          | 0.057           | 0.118 | 19.1                | -22.7               | -0.1                |
| 12000                        | 0.65000 | 0.182 | 0.016                 | 44.7                   | 21.7                  | 49.7                  | 21.0                  | 19.6                      | 2.6                     | 5.2                   | 3.8                        | -1.3                            | -1.3                       | -0.2                       | 0.0                        | -                          | 0.016           | 0.013 | 19.1                | -13.5               | 0.0                 |
| 20000                        | 0.25000 | 0.788 | 0.103                 | 39.7                   | 6.7                   | 40.3                  | 6.5                   | 3.9                       | 0.3                     | 2.0                   | 0.4                        | 0.1                             | 0.1                        | 0.0                        | -0.4                       | -                          | 0.106           | 0.266 | 29.5                | -71.9               | -1.0                |
| 20000                        | 0.40000 | 0.492 | 0.037                 | 50.0                   | 11.9                  | 51.4                  | 11.7                  | 10.7                      | 2.2                     | 2.0                   | 1.7                        | 1.1                             | 1.1                        | 0.1                        | 0.0                        | -                          | 0.037           | 0.121 | 26.7                | -48.0               | -0.2                |
| 20000                        | 0.65000 | 0.303 | 0.012                 | 70.7                   | 41.8                  | 82.2                  | 40.4                  | 40.2                      | 2.9                     | 10.8                  | 8.2                        | -0.5                            | -0.5                       | -0.1                       | 0.0                        | -                          | 0.012           | 0.013 | 26.2                | -28.6               | 0.0                 |
| 30000                        | 0.40000 | 0.738 | 0.171                 | 44.7                   | 7.9                   | 45.4                  | 7.5                   | 6.1                       | 0.4                     | 2.5                   | 1.8                        | 0.1                             | 0.1                        | 0.0                        | 0.0                        | -                          | 0.176           | 0.123 | 32.4                | -79.1               | -0.5                |

| $Q^2$<br>(GeV <sup>2</sup> ) | $d\sigma_{NC}/dQ^2$<br>(pb/GeV <sup>2</sup> )<br>$y < 0.9$ | $k_{cor}$ | $\delta_{stat}$<br>(%) | $\delta_{unc}$<br>(%) | $\delta_{cor}$<br>(%) | $\delta_{tot}$<br>(%) |
|------------------------------|--|-----------|------------------------|-----------------------|-----------------------|-----------------------|
| 200                          | $1.868 \cdot 10^1$   | 1.012     | 0.5                    | 1.4                   | 0.7                   | 1.7                   |
| 250                          | $1.077 \cdot 10^1$   | 1.009     | 0.6                    | 1.8                   | 0.8                   | 2.0                   |
| 300                          | $7.158 \cdot 10^0$   | 1.006     | 0.6                    | 1.8                   | 0.8                   | 2.0                   |
| 400                          | $3.562 \cdot 10^0$   | 1.000     | 0.8                    | 1.6                   | 0.9                   | 2.0                   |
| 500                          | $2.042 \cdot 10^0$   | 1.000     | 0.9                    | 1.6                   | 0.9                   | 2.1                   |
| 650                          | $1.062 \cdot 10^0$   | 1.000     | 1.1                    | 1.7                   | 1.2                   | 2.4                   |
| 800                          | $0.632 \cdot 10^0$   | 1.000     | 1.3                    | 1.7                   | 1.0                   | 2.4                   |
| 1000                         | $0.366 \cdot 10^0$   | 1.000     | 1.6                    | 2.7                   | 1.0                   | 3.3                   |
| 1200                         | $0.228 \cdot 10^0$   | 1.000     | 1.9                    | 2.5                   | 1.0                   | 3.3                   |
| 1500                         | $0.125 \cdot 10^0$   | 1.000     | 2.3                    | 2.7                   | 1.2                   | 3.7                   |
| 2000                         | $0.580 \cdot 10^{-1}$                                      | 1.000     | 2.8                    | 2.8                   | 1.4                   | 4.2                   |
| 3000                         | $0.193 \cdot 10^{-1}$                                      | 1.000     | 2.7                    | 2.7                   | 1.1                   | 4.0                   |
| 5000                         | $0.445 \cdot 10^{-2}$                                      | 1.000     | 3.7                    | 3.3                   | 0.9                   | 5.0                   |
| 8000                         | $0.122 \cdot 10^{-2}$                                      | 1.000     | 5.6                    | 5.1                   | 1.0                   | 7.6                   |
| 12000                        | $0.217 \cdot 10^{-3}$                                      | 1.000     | 11.8                   | 5.8                   | 1.2                   | 13.2                  |
| 20000                        | $0.242 \cdot 10^{-4}$                                      | 1.000     | 26.8                   | 10.8                  | 2.0                   | 28.9                  |
| 30000                        | $0.123 \cdot 10^{-4}$                                      | 1.000     | 38.8                   | 18.8                  | 4.8                   | 43.4                  |

**Table C.3:** The NC cross section  $d\sigma_{NC}/dQ^2$  for  $y < 0.9$  after correction ( $k_{cor}$ ) according to the Standard Model expectation for the kinematic cuts  $y < 0.63$  for  $Q^2 < 890$  GeV<sup>2</sup>. The statistical ( $\delta_{stat}$ ), uncorrelated systematic ( $\delta_{unc}$ ), correlated systematic ( $\delta_{cor}$ ), and total ( $\delta_{tot}$ ) errors are also given. The normalisation uncertainty of 1.5% is not included in the errors.

| $x$   | $d\sigma_{NC}/dx$ (pb)<br>$Q^2 > 1000$ GeV <sup>2</sup> , $y < 0.9$ | $\delta_{stat}$<br>(%) | $\delta_{unc}$<br>(%) | $\delta_{cor}$<br>(%) | $\delta_{tot}$<br>(%) |
|-------|---|------------------------|-----------------------|-----------------------|-----------------------|
| 0.013 | $0.130 \cdot 10^4$  | 6.0                    | 3.7                   | 3.4                   | 7.8                   |
| 0.020 | $0.253 \cdot 10^4$  | 3.0                    | 1.9                   | 1.4                   | 3.9                   |
| 0.032 | $0.216 \cdot 10^4$  | 2.5                    | 1.8                   | 1.1                   | 3.3                   |
| 0.050 | $0.148 \cdot 10^4$  | 2.4                    | 1.8                   | 1.1                   | 3.2                   |
| 0.080 | $0.969 \cdot 10^3$  | 2.3                    | 1.9                   | 1.1                   | 3.2                   |
| 0.130 | $0.549 \cdot 10^3$  | 2.7                    | 1.9                   | 1.0                   | 3.4                   |
| 0.180 | $0.369 \cdot 10^3$  | 3.0                    | 2.2                   | 1.3                   | 4.0                   |
| 0.250 | $0.204 \cdot 10^3$  | 3.4                    | 3.8                   | 2.6                   | 5.7                   |
| 0.400 | $0.626 \cdot 10^2$  | 4.9                    | 6.5                   | 4.6                   | 9.4                   |
| 0.650 | $0.575 \cdot 10^1$  | 10.2                   | 11.7                  | 7.4                   | 17.2                  |

**Table C.4:** The NC cross section  $d\sigma_{NC}/dx$  measured for  $y < 0.9$  and  $Q^2 > 1000$  GeV<sup>2</sup>. The statistical ( $\delta_{stat}$ ), uncorrelated systematic ( $\delta_{unc}$ ), correlated systematic ( $\delta_{cor}$ ), and total ( $\delta_{tot}$ ) errors are also given. The normalisation uncertainty of 1.5% is not included in the errors.

| $x$   | $d\sigma_{NC}/dx$ (pb)<br>$Q^2 > 10\,000 \text{ GeV}^2, y < 0.9$ | $\delta_{stat}$<br>(%) | $\delta_{unc}$<br>(%) | $\delta_{cor}$<br>(%) | $\delta_{tot}$<br>(%) |
|-------|--|------------------------|-----------------------|-----------------------|-----------------------|
| 0.130 | $0.391 \cdot 10^1$   | 34.1                   | 6.4                   | 5.1                   | 35.1                  |
| 0.180 | $0.806 \cdot 10^1$   | 17.5                   | 3.8                   | 1.4                   | 18.0                  |
| 0.250 | $0.375 \cdot 10^1$   | 20.9                   | 5.1                   | 1.1                   | 21.5                  |
| 0.400 | $0.186 \cdot 10^1$   | 22.4                   | 9.7                   | 2.4                   | 24.5                  |
| 0.650 | $0.037 \cdot 10^1$   | 33.3                   | 27.1                  | 6.7                   | 43.4                  |

**Table C.5:** The NC cross section  $d\sigma_{NC}/dx$  measured for  $y < 0.9$  and  $Q^2 > 10\,000 \text{ GeV}^2$ . The statistical ( $\delta_{stat}$ ), uncorrelated systematic ( $\delta_{unc}$ ), correlated systematic ( $\delta_{cor}$ ), and total ( $\delta_{tot}$ ) errors are also given. The normalisation uncertainty of 1.5% is not included in the errors.

| $Q^2$<br>( $\text{GeV}^2$ ) | $x$     | $y$   | $\tilde{\sigma}_{NC}$ | $\delta_{stat}$<br>(%) | $\delta_{sy}$<br>(%) | $\delta_t$<br>(%) | $\delta_u$<br>(%) | $\delta_u^E$<br>(%) | $\delta_u^h$<br>(%) | $\delta_c$<br>(%) | $\delta_c^{E+}$<br>(%) | $\delta_c^{\theta+}$<br>(%) | $\delta_c^{h+}$<br>(%) | $\delta_c^{N+}$<br>(%) | $\delta_c^{B+}$<br>(%) | $\delta_c^{S+}$<br>(%) |
|-----------------------------|---------|-------|-----------------------|------------------------|----------------------|-------------------|-------------------|---------------------|---------------------|-------------------|------------------------|-----------------------------|------------------------|------------------------|------------------------|------------------------|
| 100                         | 0.00131 | 0.750 | 1.366                 | 4.2                    | 4.6                  | 6.2               | 4.1               | 1.1                 | 0.1                 | 2.1               | -0.1                   | 0.1                         | 0.1                    | 0.1                    | 0.0                    | 1.2                    |
| 100                         | 0.00200 | 0.492 | 1.341                 | 3.3                    | 4.2                  | 5.3               | 3.3               | 0.3                 | 0.5                 | 2.6               | 0.4                    | 1.7                         | 1.7                    | 0.2                    | -1.0                   | 0.0                    |
| 120                         | 0.00158 | 0.750 | 1.341                 | 4.4                    | 3.3                  | 5.5               | 3.2               | 0.6                 | 0.2                 | 0.9               | 0.5                    | 0.3                         | 0.3                    | 0.1                    | -0.1                   | 1.0                    |
| 120                         | 0.00200 | 0.591 | 1.364                 | 3.4                    | 3.9                  | 5.2               | 3.3               | 0.8                 | 0.2                 | 2.1               | -0.4                   | 0.8                         | 0.8                    | 0.1                    | -1.2                   | 0.0                    |
| 120                         | 0.00320 | 0.369 | 1.220                 | 3.0                    | 3.9                  | 4.9               | 3.0               | 0.1                 | 0.1                 | 2.5               | 0.8                    | 0.3                         | 0.3                    | 0.0                    | -0.5                   | 0.0                    |
| 150                         | 0.00197 | 0.750 | 1.301                 | 4.7                    | 3.3                  | 5.7               | 3.0               | 0.5                 | 0.1                 | 1.3               | -0.5                   | 0.2                         | 0.2                    | 0.1                    | -0.1                   | 0.8                    |
| 200                         | 0.00263 | 0.750 | 1.174                 | 5.1                    | 3.3                  | 6.1               | 3.0               | 0.2                 | 0.2                 | 1.5               | -0.2                   | 0.6                         | 0.6                    | 0.0                    | -0.1                   | 0.8                    |
| 250                         | 0.00328 | 0.750 | 1.078                 | 6.2                    | 3.6                  | 7.2               | 3.4               | 0.5                 | 0.1                 | 1.3               | -0.3                   | 0.7                         | 0.7                    | 0.1                    | 0.1                    | 1.3                    |
| 300                         | 0.00394 | 0.750 | 1.110                 | 6.2                    | 3.5                  | 7.1               | 3.3               | 0.4                 | 0.1                 | 1.2               | -0.2                   | 0.6                         | 0.6                    | 0.0                    | 0.1                    | 0.8                    |
| 400                         | 0.00525 | 0.750 | 1.032                 | 6.8                    | 3.8                  | 7.8               | 3.5               | 0.8                 | 0.1                 | 1.5               | -0.1                   | 0.2                         | 0.2                    | 0.0                    | -0.1                   | 0.8                    |
| 500                         | 0.00656 | 0.750 | 1.041                 | 7.0                    | 3.9                  | 8.0               | 3.6               | 0.4                 | 0.4                 | 1.6               | 0.7                    | 0.6                         | 0.6                    | 0.1                    | 0.0                    | 0.3                    |
| 650                         | 0.00853 | 0.750 | 1.049                 | 7.7                    | 4.2                  | 8.8               | 3.9               | 0.7                 | 0.1                 | 1.6               | -1.2                   | 0.1                         | 0.1                    | 0.0                    | 0.0                    | 0.3                    |
| 800                         | 0.01050 | 0.750 | 0.921                 | 9.0                    | 4.8                  | 10.2              | 4.4               | 0.7                 | 0.2                 | 2.0               | 1.3                    | 0.3                         | 0.3                    | 0.0                    | -0.1                   | 0.2                    |

**Table C.6:** The NC  $e^-p$  reduced cross section  $\tilde{\sigma}_{NC}(x, Q^2)$  from the *high-y analysis* shown with statistical ( $\delta_{stat}$ ) and total ( $\delta_{tot}$ ) errors. Also shown are the total uncorrelated systematic ( $\delta_{unc}$ ) errors and two of its contributions: the electron energy error ( $\delta_{unc}^E$ ) and the hadronic energy error ( $\delta_{unc}^h$ ). The effect of the other uncorrelated systematic errors is included in ( $\delta_{unc}$ ). In addition the correlated systematic error ( $\delta_{cor}$ ) and its contributions from a positive variation of one standard deviation of the electron energy error ( $\delta_{cor}^{E+}$ ), of the polar electron angle error ( $\delta_{cor}^{\theta+}$ ), of the hadronic energy error ( $\delta_{cor}^{h+}$ ), of the error due to noise subtraction ( $\delta_{cor}^{N+}$ ), of the error due to background subtraction ( $\delta_{cor}^{B+}$ ), and of the error due to charge symmetry background subtraction in the high-y analysis ( $\delta_{cor}^{S+}$ ) are given. The normalisation uncertainty of 1.8% is not included in the errors.

| $Q^2$<br>(GeV <sup>2</sup> ) | $x$     | $y$  | $\phi_{NC}$ | $F_L$ | $\delta_{stat}$ | $\delta_{sys}$ | $\delta_{tot}$ |
|------------------------------|---------|------|-------------|-------|-----------------|----------------|----------------|
| $e^-p$ data                  |         |      |             |       |                 |                |                |
| 110                          | 0.00144 | 0.75 | 1.274       | 0.300 | 0.078           | 0.090          | 0.121          |
| 175                          | 0.00230 | 0.75 | 1.166       | 0.348 | 0.080           | 0.067          | 0.106          |
| 280                          | 0.00368 | 0.75 | 1.022       | 0.404 | 0.090           | 0.062          | 0.110          |
| 450                          | 0.00591 | 0.75 | 0.970       | 0.238 | 0.096           | 0.060          | 0.113          |
| 700                          | 0.00919 | 0.75 | 0.938       | 0.064 | 0.111           | 0.063          | 0.128          |
| $e^+p$ data                  |         |      |             |       |                 |                |                |
| 110                          | 0.00144 | 0.75 | 1.518       | 0.198 | 0.032           | 0.083          | 0.092          |
| 175                          | 0.00230 | 0.75 | 1.426       | 0.164 | 0.038           | 0.064          | 0.076          |
| 280                          | 0.00368 | 0.75 | 1.292       | 0.171 | 0.041           | 0.057          | 0.072          |
| 450                          | 0.00591 | 0.75 | 1.163       | 0.133 | 0.045           | 0.052          | 0.070          |
| 700                          | 0.00919 | 0.75 | 1.037       | 0.096 | 0.053           | 0.062          | 0.082          |

**Table C.7:** The NC structure function term  $\phi_{NC}(x, Q^2)$  and the structure function  $F_L$ , shown with its statistical ( $\delta_{stat}$ ), systematic ( $\delta_{sys}$ ) and total ( $\delta_{tot}$ ) absolute error. The total error includes a contribution arising from the model uncertainties in the calculated  $\tilde{F}_2$ . These are obtained by varying the assumptions of the H1 Low  $y$  QCD fit as listed in table A.2. The luminosity uncertainties of the  $e^+p$  and  $e^-p$  data sets are included in the systematic error.

| $Q^2$<br>(GeV <sup>2</sup> ) | $x$   | $x\tilde{F}_3$               | $\delta_{stat}$ | $\delta_{sys}$ | $\delta_{tot}$ |
|------------------------------|-------|------------------------------|-----------------|----------------|----------------|
| 1500                         | 0.020 | 0.0522                       | 0.037           | 0.025          | 0.045          |
| 1500                         | 0.032 | 0.0634                       | 0.033           | 0.026          | 0.042          |
| 1500                         | 0.050 | 0.0884                       | 0.040           | 0.027          | 0.049          |
| 1500                         | 0.080 | 0.0576                       | 0.051           | 0.034          | 0.062          |
| 5000                         | 0.050 | 0.0776                       | 0.038           | 0.024          | 0.045          |
| 5000                         | 0.080 | 0.1423                       | 0.032           | 0.020          | 0.038          |
| 5000                         | 0.130 | 0.1667                       | 0.037           | 0.022          | 0.043          |
| 5000                         | 0.180 | 0.0993                       | 0.042           | 0.024          | 0.049          |
| 5000                         | 0.250 | 0.1015                       | 0.050           | 0.038          | 0.063          |
| 5000                         | 0.400 | 0.0599                       | 0.046           | 0.035          | 0.058          |
| 5000                         | 0.650 | 0.0016                       | 0.015           | 0.008          | 0.017          |
| 12000                        | 0.180 | 0.1165                       | 0.079           | 0.022          | 0.082          |
| 12000                        | 0.250 | 0.1235                       | 0.054           | 0.016          | 0.056          |
| 12000                        | 0.400 | 0.0505                       | 0.038           | 0.018          | 0.042          |
| 12000                        | 0.650 | -0.0045                      | 0.015           | 0.009          | 0.018          |
| $Q^2$<br>(GeV <sup>2</sup> ) | $x$   | $x\overline{F}_3^{\gamma Z}$ | $\delta_{stat}$ | $\delta_{sys}$ | $\delta_{tot}$ |
| 1500                         | 0.026 | 0.54                         | 0.23            | 0.17           | 0.29           |
| 3250                         | 0.050 | 0.36                         | 0.13            | 0.09           | 0.16           |
| 3250                         | 0.080 | 0.54                         | 0.12            | 0.08           | 0.14           |
| 5000                         | 0.130 | 0.63                         | 0.14            | 0.08           | 0.16           |
| 8500                         | 0.180 | 0.33                         | 0.12            | 0.06           | 0.14           |
| 8500                         | 0.250 | 0.32                         | 0.12            | 0.05           | 0.12           |
| 8500                         | 0.400 | 0.14                         | 0.08            | 0.04           | 0.09           |
| 8500                         | 0.650 | -0.01                        | 0.32            | 0.02           | 0.04           |

**Table C.8:** The upper part of the table shows the generalised structure function  $x\tilde{F}_3$  with statistical ( $\delta_{stat}$ ), systematic ( $\delta_{sys}$ ) and total ( $\delta_{tot}$ ) absolute errors. The luminosity uncertainties of the  $e^+p$  and  $e^-p$  data are included in the systematic error. The lower part of the table shows the averaged structure function  $x\overline{F}_3^{\gamma Z}$  from those measured at different  $Q^2$  values to correspond to a  $Q^2$  value at 1500 GeV<sup>2</sup>.

## Appendix D

### Events in the H1 Detector

Following figures show the examples of the events in the H1 Detector from the 1999-2000 data taking. The NC events with highest  $Q^2$  are shown in figures D.1 and D.2. For all events the kinematic variables  $Q^2$ , Bjorken- $x$  and inelasticity  $y$ , as well as the energy  $E'_e$  and the polar angle  $\theta_e$  of the scattered electron are indicated. The examples of halo-muon and cosmic events are shown in figure D.3.

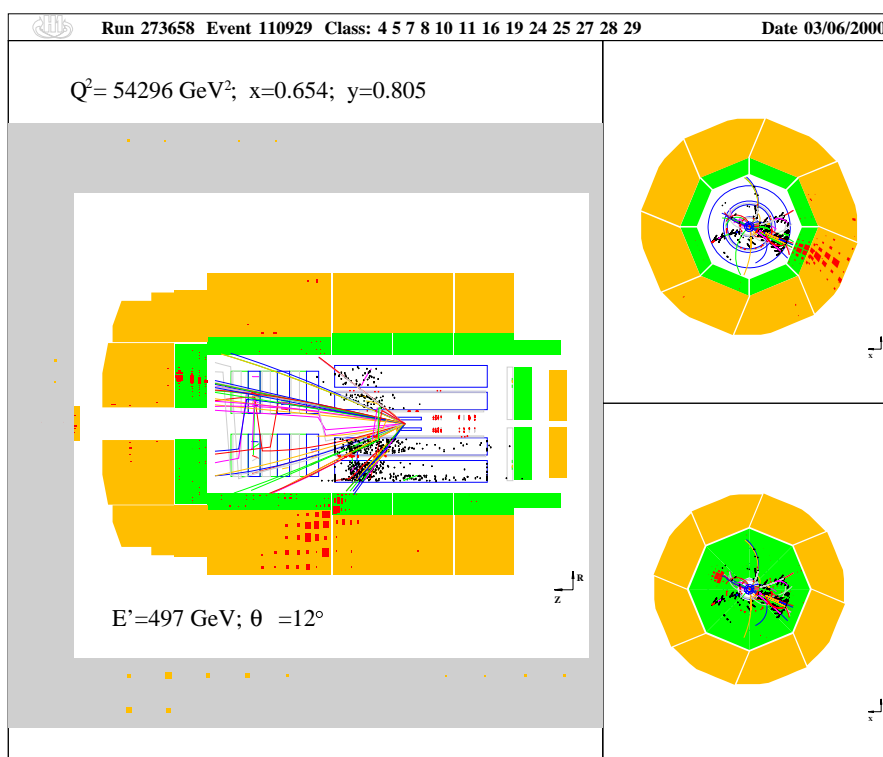


Figure D.1: Event with the highest  $Q^2$  in the 1999-2000 data taking.

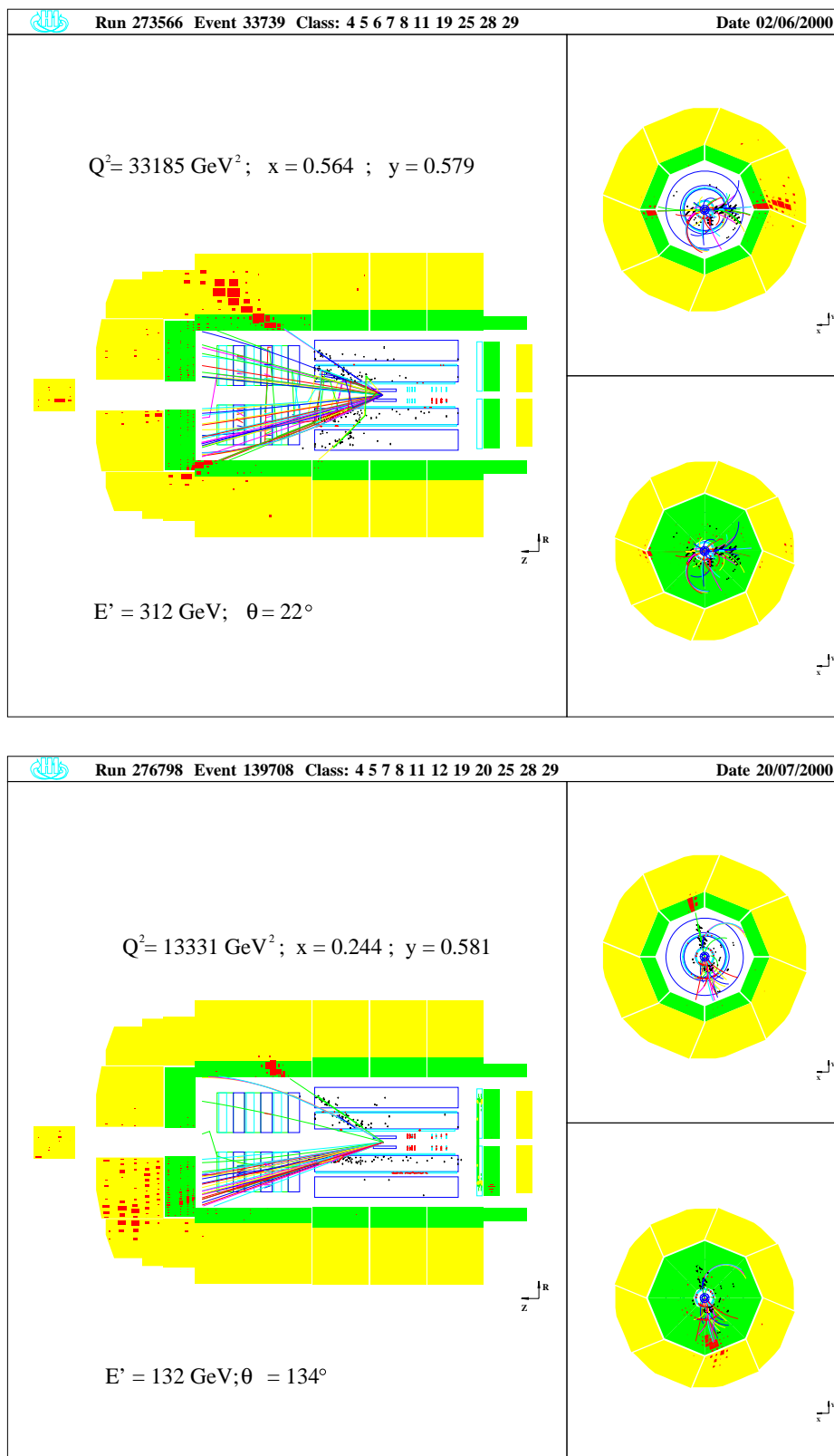


Figure D.2: Events in the highest  $Q^2$  kinematic region.



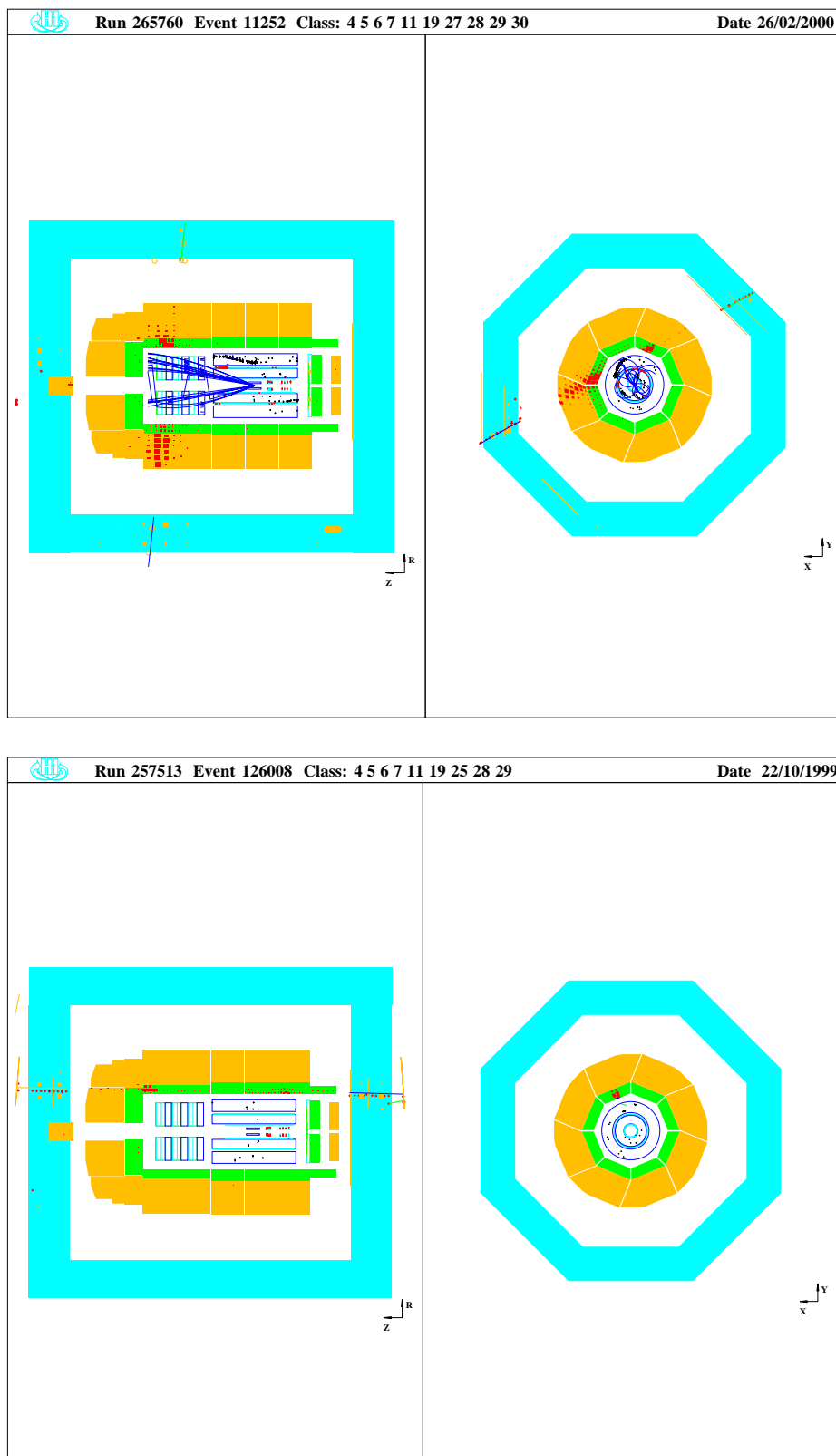


Figure D.3: Cosmic and halo-muon events in the H1 detector.

# Bibliography

- [1] E. Rutherford. The Scattering of  $\alpha$  and  $\beta$  Particles by Matter and the Structure of the Atom. *Philosophical Magazine*, **21**, page 669, 1911.
- [2] BCDMS Collaboration, A. C. Benvenuti et al. A High Statistics Measurement of the Proton Structure Functions  $F_2(x, Q^2)$  and  $R$  from Deep Inelastic Muon Scattering at High  $Q^2$ . *Phys. Lett.*, **B223**, page 485, 1989.
- [3] NMC Collaboration, M. Arneodo et al. Measurement of the proton and the deuteron structure functions  $F_2^p$  and  $F_2^d$ . *Phys. Lett.*, **B364**, pages 107–115, 1995.
- [4] S.A Rabinowitz et al. CCFR Collaboration. Measurement of the Strange Sea Distribution Using Neutrino Charm Production. *Phys. Rev. Lett.*, **70**, pages 134–137, 1993.
- [5] H. Abramowicz et al. CDHS Collaboration. Measurement of Neutrino and Antineutrino Structure in Hydrogen and Iron. *Z. Phys.*, **C25**, pages 29–43, 1984.
- [6] P. Berge et al. CDHS Collaboration. A measurement of differential cross-sections and nucleon structure functions in charged-current neutrino interactions on iron. *Z. Phys.*, **C49**, pages 187–223, 1991.
- [7] F. Halzen and A.D. Martin. QUARKS AND LEPTONS: An Introductory Course in Modern Particle Physics. John Wiley & sons, 1984.
- [8] I.J.R. Aitchison and A.J.G. Hey. Gauge Theories in Particle Physics. *Graduate student series in physics*. Adam Hilger, Bristol and Philadelphia, second edition, 1989.
- [9] L.N. Hand. Experimental Investigation of Pion Electroproduction. *Phys. Rev.*, **129**, pages 1834–1846, 1963.
- [10] R.P. Feynman. Photon-Hadron-Interaction. W.A.Benjamin, Inc., Advance Book Program, Reading Massachusetts, 1972.

- 
- [11] J.D. Bjorken and E.A. Paschos. Inelastic Electron-Proton and  $\gamma$ -Proton Scattering and the Structure of the Nucleon. *Phys. Rev.*, **185**, pages 1975–1982, 1969.
- [12] M. Gell-Mann. A schematic model of baryons and mesons. *Phys. Lett.*, **8**, pages 214–215, 1964.
- [13] C. Zweig. 1964. CERN-8192/TH 401.
- [14] E.D. Bloom et al. High-Energy inelastic  $ep$  Scattering at  $6^\circ$  and  $10^\circ$ . *Phys. Rev. Lett.*, **23**, pages 930–934, 1969.
- [15] M. Breidenbach et al. Observed Behavior of Highly Inelastic Electron-Proton Scattering. *Phys. Rev. Lett.*, **23**, pages 935–939, 1969.
- [16] C.G. Callan and D.J. Gross. High-Energy Electroproduction and the Constitution of the Electric Current. *Phys. Rev. Lett.*, **22**, pages 156–159, 1969.
- [17] Y.L. Dokshitzer. Calculation of structure functions of deep inelastic scattering and  $e^+e^-$  annihilation by perturbation theory in quantum chromo dynamics. *Sov. Phys. JTEP*, **46**, pages 641–653, 1977.
- [18] V.N. Gribov and L.N. Lipatov. Deep Inelastic  $ep$  Scattering in Perturbation Theory. *Sov. Journ. Nucl. Phys.*, **15**, pages 438–450, 1972.
- [19] V.N. Gribov and L.N. Lipatov.  $e^+e^-$ -Pair Annihilation and Deep Inelastic  $ep$  Scattering in Perturbation Theory. *Sov. Journ. Nucl. Phys.*, **15**, pages 675–684, 1972.
- [20] G. Altarelli and G. Parisi. Asymptotic Freedom in Parton Language. *Nucl. Phys.*, **B126**, pages 298–318, 1977.
- [21] G. Altarelli and G. Martinelli. Transverse Momentum of Jets in Electroproduction from Quantum Chromodynamics. *Phys. Lett.*, **B76**, page 89, 1978.
- [22] R.G. Roberts. The structure of the proton. Cambridge University Press, 1990.
- [23] A.M. Cooper-Sarkar et al. Measurement of the Longitudinal Structure Function and the small  $x$  Gluon Density of the Proton. *Z. Phys.*, **C39**, page 281, 1988.
- [24] A.M. Cooper-Sarkar et al. Measurement of  $F_L(x, Q^2)$  at Low- $x$  and Extraction of The Gluon Distribution. In W.Buchmüller and G. Ingelmann, *Proceedings of the Workshop: Physics at HERA*, volume 1, pages 155–170. DESY, 1992.
- [25] G. Ingelman and R. Rückl. Determination of Quark Distributions in  $ep$  Collisions. *Phys. Lett.*, **B201**, page 369, 1988.

- [26] M. Klein and T. Riemann. Electroweak Interactions Probing the Nucleon Structure. *Z. Phys.*, **C24**, page 151, 1984.
- [27] Particle Data Group, D.E. Groom et al. Review of Particle Physics. *Eur. Phys. J.*, **C15**, page 1, 2000.
- [28] A. Arbuzov, Dmitri Yu. Bardin, J. Bluemlein, L. Kalinovskaya, and T. Riemann. HECTOR 1.00 - A program for the calculation of QED, QCD and electroweak corrections to ep and IN deep inelastic neutral and charged current scattering. *Comput. Phys. Commun.*, **94**, pages 128–184, 1996.
- [29] H1 Collaboration, C. Adloff et al. Measurement and QCD Analysis of Neutral and Charged Current Cross Sections at HERA. DESY preprint: DESY 03-038 submitted to *Eur. Phys. J.* 04/03, 2003.
- [30] A.D. Martin, R.G. Roberts, W.J. Stirling, and R.S. Thorne. Partons and  $\alpha_s$  from Precise Deep Inelastic Scattering and Tevatron Jet Data. *Eur. Phys. J.*, **C23**, page 73, 2003.
- [31] J. Pumplin, D.R. Stump, J. Huston, H.L. Lai, P. Nadolsky, and W.K. Tung. New generation of parton distributions with uncertainties from global QCD analysis. *JHEP*, **07**, page 012, 2002.
- [32] H1 Collaboration, C. Adloff et al. Measurement of neutral and charged current cross-sections in positron-proton collisions at large momentum transfer. *Eur. Phys. J.*, **C13**, pages 609–639, 2000.
- [33] S. Chekanov et al. ZEUS Collaboration. A ZEUS next-to-leading-order QCD analysis of data on deep inelastic scattering. accepted by *Phys. Rev. D*.
- [34] W. Furmanski and R. Petronzio. Singlet Parton Densities Beyond Leading Order. *Phys. Lett.*, **B97**, page 437, 1980.
- [35] B. Heinemann. Measurement of Charged Current and Neutral Current Cross Sections in Positron-Proton Collisions at  $\sqrt{s} \simeq 300$  GeV. Dissertation, Universität Hamburg, 1999.  
also available at [http://www-h1.desy.de/publications/theses\\_list.html](http://www-h1.desy.de/publications/theses_list.html).
- [36] M. Böhm und H. Spiesberger. Radiative corrections to neutral current deep inelastic lepton nucleon scattering at HERA energies. *Nucl. Phys.*, **B294**, page 1081, 1987.
- [37] D. Bardin et al. Electroweak radiative corrections to Deep Inelastic Scattering at HERA: Neutral Current Scattering. *Z. Phys.*, **C42**, page 679, 1989.
- [38] H. Spiesberger et al. Radiative Corrections at HERA. In W. Buchmüller and G. Ingelmann, *Proceedings of the Workshop: Physics at HERA*, volume 2, pages 798–839. DESY, October 1992.

- 
- [39] H1 Collaboration, C. Adloff et al. Measurement of Neutral and Charged Current Cross Sections in Electron-Proton Collisions at High  $Q^2$ . *Eur. Phys. J.*, **C19**, page 269, 2001.
- [40] P. Schmüser. The Electron Proton Colliding Beam Facility HERA. *Nucl. Instrum. Meth.*, **A235**, pages 201–208, 1984.
- [41] H1 Collaboration, I. Abt et al. The H1 detector at HERA. *Nucl. Instrum. Meth.*, **A386**, pages 310–347, 1997.
- [42] H1 Collaboration, I. Abt et al. The tracking calorimeter and muon detectors of the H1 experiment at HERA. *Nucl. Instrum. Meth.*, **A386**, pages 348–396, 1997.
- [43] H1 Calorimeter Group, B. Andrieu et al. The H1 Liquid Argon Calorimeter System. *Nucl. Instrum. Meth.*, **A336**, pages 460–498, 1993.
- [44] H1 Spacal Group, R.-D. Appuhn et al. The H1 lead/scintillating-fibre calorimeter. *Nucl. Instrum. Meth.*, **A386**, pages 397–408, 1997.
- [45] M. Keller et al. A highly compact electromagnetic calorimeter for the VLQ spectrometer in H1 at HERA. *Nucl. Instrum. Meth.*, **A409**, pages 604–607, 1998.
- [46] M. Ruffer. Implementierung des Silizium-instrumentierten PLUG-Kalorimeters in den H1-Detektor. Dissertation, Hamburg University, 1992.
- [47] W.J. Willis et al. Liquid-Argon Ionization Chambers as Total-Absorption Detectors. *Nucl. Instrum. Meth.*, **120**, pages 221–236, 1974.
- [48] H1 Calorimeter Group, B. Andrieu et al. Beam tests and calibration of the H1 liquid argon calorimeter with electrons. *Nucl. Instrum. Meth.*, **A350**, pages 57–72, 1994.
- [49] H1 Calorimeter Group, B. Andrieu et al. Results from Pion Calibration Runs for the H1 Liquid Argon Calorimeter and Comparisons with Simulations. *Nucl. Instrum. Meth.*, **A336**, pages 499–509, 1993.
- [50] J. Bürger et al. The Central Jet Chamber of the H1 Experiment. *Nucl. Instrum. Meth.*, **A279**, pages 217–222, 1989.
- [51] S. Egli et al. The Central Inner z Drift Chamber of the H1 Experiment. *Nucl. Instrum. Meth.*, **A283**, pages 487–491, 1989.
- [52] P. Marage et al. Construction of a cylindrical MWPC for the central tracking detector of H1. *Nucl. Phys. Proc. Suppl.*, **16**, page 518, 1990.

- 
- [53] K. Müller et al. Construction and performance of a thin cylindrical multi wire proportional chamber with cathode pad readout for the H1-Experiment. *Nucl. Instrum. Meth.*, **A312**, pages 457–466, 1992.
- [54] S. Burke et al. Track finding and fitting in the H1 Forward Track Detector. *Nucl. Instrum. Meth.*, **A373**, pages 227–260, 1996.
- [55] G.A. Beck et al. Radial Wire Drift Chambers for the H1 Forward Track Detector at HERA: Design, Construction and Performance. *Nucl. Instrum. Meth.*, **A283**, pages 471–476, 1989.
- [56] W. Bethe and W. Heitler. On the Stopping of Fast Particles and on the Creation of Positive Electrons. *Proceedings of the Royal Society*, **A146**, pages 83–112, 1934.
- [57] H1 Collaboration. Luminosity Measurement in the H1 Experiment at HERA. In *Proceedings of the International Conference on High Energy Physics*, pages 17–26. DESY, 1996.
- [58] N. Gogitidze and S. Levonian. An Offline Luminosity Determination for the H1  $e^+p$  Data. H1–Note H1-01/96-471, DESY, 1996.
- [59] E. Elsen. Aspects of the H1 trigger and data acquisition system. Prepared for 2nd Annual Conference on Electronics for Future Colliders, Chestnut Ridge, N.Y., 19-21 May 1992.
- [60] H. Krehbiel. The H1 Trigger Decider: From Trigger Elements to L1-Keep. H1–Note H1-09/92-239, DESY, 1992.
- [61] G. Grindhammer et al. The First Level LAr Trigger Physics Requirement. H1–Note H1-TR-301, DESY, 1987.
- [62] C. Beigbeder. Level 2 Topological Trigger (L2TT) Hardware. H1–Note H1-07/98-547, DESY, 1998.
- [63] J.K. Köhne et al. Realization of a second level neural network trigger for the H1 experiment at HERA. *Nucl. Instrum. Meth.*, **A389**, pages 128–133, 1997.
- [64] B. Reisert. Elektron-Proton-Streuung bei hohen Impulsüberträgen am H1-Experiment bei HERA. Dissertation, Ludwig-Maximilians-Universität München, 2001. MPI-PhE/2000-26, also available at [http://www-h1.desy.de/publications/theses\\_list.html](http://www-h1.desy.de/publications/theses_list.html).
- [65] G.A. Schuller and H. Spiesberger. DJANGO: The Interface for the Event Generators HERACLES and LEPTO. In W. Buchmüller and G. Ingelmann, *Proceedings of the Workshop: Physics at HERA*, volume 3, pages 1419–1432. DESY, October 1992.

- 
- [66] H. Spiesberger A. Kwiatkowski and H.J. Mohring. HERACLES: An Event Generator for  $ep$  Interactions at HERA Energies including Radiative Processes: Version 1.0. *Comp. Phys. Comm.*, **69**, pages 155–172, 1992.
- [67] G. Ingelman. LEPTO Version 6.1 - The Lund Monte Carlo for Deep Inelastic Lepton-Nucleon Scattering. In W. Buchmüller and G. Ingelmann, *Proceedings of the Workshop: Physics at HERA*, volume 3, pages 1366–1394. DESY, October 1992.
- [68] B. Andersson et al. Coherence Effects in Deep Inelastic Scattering. *Z. Phys.*, **C43**, page 625, 1989.
- [69] L. Lonnblad. ARIADNE Version 4 – A program for simulation of QCD cascades implementing the color dipole model. *Comp. Phys. Comm.*, **71**, pages 15–31, 1992.
- [70] T. Sjöstrand and M. Bengtsson. The Lund Monte Carlo for Jet Fragmentation and  $e^+e^-$  Physics – Jetset Version 6.3 – An Update. *Comp. Phys. Comm.*, **43**, pages 367–379, 1987.
- [71] A.D. Martin, R.G. Roberts and W.J. Stirling. Parton distributions updated. *Phys. Lett.*, **B306**, pages 145–150, 1993. Erratum, *Phys. Lett.* **B309**, 1993, page 492.
- [72] T. Sjöstrand. High-energy-physics event generation with PYTHIA 5.7 and JETSET 7.4. *Comp. Phys. Comm.*, **82**, pages 74–89, 1994.
- [73] M. Glück, E. Reya and A. Vogt. Photonic parton distributions. *Phys. Rev.*, **D46**, pages 1973–1979, 1992.
- [74] A. Courau und P. Kessler. QED Compton scattering in high-energy electron - proton collisions. *Phys. Rev.*, **D46**, pages 117–124, 1992.
- [75] J.A.M. Vermaseren. Two Photon Processes at very high Energies. *Nucl. Phys.*, **B229**, page 347, 1983.
- [76] S. Baranov et al. A Generator for Lepton Pair Production. In W. Buchmüller and G. Ingelmann, *Proceedings of the Workshop: Physics at HERA*, volume 3, pages 1478–1482. DESY, October 1991.
- [77] J. Meyer. Guide for the H1 simulation program H1SIM. Internal Software–Note 03-11/89, DESY, 1989.
- [78] R. Brun et al. GEANT3 User’s Guide. *CERN-DD/EE-84-1*, 1987.
- [79] M. Peters. Die parametrisierte Simulation elektromagnetischer Schauer. Dissertation, MPI München, 1992.

- [80] M. Rudowicz. Hadronische Schauersimulation für den H1-Detektor. Dissertation, MPI München, 1992.
- [81] S. Bentvelsen et al. Reconstruction of  $(x, Q^2)$  and extraction of structure functions in neutral current scattering at HERA. In W. Buchmüller and G. Ingelmann, *Proceedings of the Workshop: Physics at HERA*, volume 1, pages 23–40. DESY, 1992.
- [82] A. Blondel and F. Jacquet. In U. Amaldi, *Proceedings of the Study of an ep Facility for Europe*, page 391. DESY 79/48, 1979.
- [83] U. Bassler and G. Bernardi. On the kinematic reconstruction of deep inelastic scattering at HERA. *Nucl. Instrum. Meth.*, **A361**, pages 197–208, 1995.
- [84] U. Bassler and G. Bernardi. Structure function measurements and kinematic reconstruction at HERA. *Nucl. Instrum. Meth.*, **A426**, pages 583–598, 1999.
- [85] P. Bruel. Recherche d'interactions au-delà du Modèle Standard à HERA. Dissertation, L'Université Paris XI Orsay, 1998.  
also available at [http://www-h1.desy.de/publications/theses\\_list.html](http://www-h1.desy.de/publications/theses_list.html).
- [86] A. Mehta et al. (DUK). Electron Finding Efficiency Using Track Based Finder. Presentations and Discussions on H1 HIP-meetings, 2000-2002.
- [87] S. Kermiche and J. Marks. LAr electromagnetic energy scale studies using NC DIS (1+1) jet and QED Compton events for the  $e^+p$  1994 H1 data. H1–Note H1-12/95-466, 1995.
- [88] R. Maraček. A Study of Quasi-Real QED Compton Events at HERA. Dissertation, Institute of Experimental Physics, Slovak Academy of Sciences Košice/Slovakia, 1998.  
also available at [http://www-h1.desy.de/publications/theses\\_list.html](http://www-h1.desy.de/publications/theses_list.html).
- [89] R. Stamen. Analyse quasireeller QED-Compton-Ereignisse. Diploma Thesis, Universität Dortmund, 1998.  
also available at [http://www-h1.desy.de/publications/theses\\_list.html](http://www-h1.desy.de/publications/theses_list.html).
- [90] V. Lendermann. Measurement of the QED Compton Scattering Cross Section with the H1 Detector at HERA. Dissertation, Universität Dortmund, 2001.  
also available at [http://www-h1.desy.de/publications/theses\\_list.html](http://www-h1.desy.de/publications/theses_list.html).
- [91] H.-P. Wellisch et al. Hadronic Calibration of the H1 LAr Calorimeter using Software Weighting Techniques. Technical Report MPI-PhE/94-03, MPI für Physik, 1994.
- [92] H. Abramowicz et al. The Response and the Resolution of an Iron-Scintillator Calorimeter for Hadronic and Electromagnetic Showers Between 10 GeV and 140 GeV. *Nucl. Instrum. and Meth.*, **180**, pages 429–439, 1981.



- 
- [93] H1 Collaboration, W. Braunschweig et al. Results from a Test of a Pb-Cu Liquid Argon Calorimeter. *Nucl. Instrum. and Meth.*, **A265**, pages 419–434, 1988.
- [94] H1 Collaboration, W. Braunschweig et al. Performance of a Pb-Cu Liquid Argon Calorimeter with an iron Streamer Tube Tail Catcher. *Nucl. Instrum. and Meth.*, **A275**, page 246, 1989.
- [95] H1 Calorimeter group, H. Oberlack. Compensation by software - single particles and jets in the H1 Calorimeter. In *Proceedings XXV International Conference on High Energy Physics, Singapore*, volume 2, page 1377, 1990.
- [96] P. Loch. Kalibration des H1 Fluessig-Argon Kalorimeters unter Berücksichtigung der Gewichtungsmethode für Teilchen-Jets. Dissertation, Hamburg University, 1992. DESY FH1K-92-02.
- [97] V. Chekelian. Simulation and Reconstruction in the H1 Liquid Argon Calorimetry. H1–Note H1-04/93-288, ITEP, 1993.
- [98] H1 Collaboration, C. Adloff et al. Deep-Inelastic Inclusive  $ep$  Scattering at Low  $x$  and a Determination of  $\alpha_s$ . *Eur. Phys. J.*, **C21**, page 33, 2001.
- [99] V. Arkadov. Measurement of Deep-Inelastic  $ep$  Scattering Cross Section using the Backward Silicon Tracker at the H1 Detector at HERA. Dissertation, Humboldt-Universität Berlin, 2000.  
also available at [http://www-h1.desy.de/publications/theses\\_list.html](http://www-h1.desy.de/publications/theses_list.html).
- [100] I. Negri et al. A Minimal Comprehensive Set of Muon Background Topological Finders for High  $P_T$  Physics Analysis. H1–Note H1-10/96-498, DESY, 1996.
- [101] E. Chabert et al. An Updated Phan Package for Cosmic and Halo Muon Topological Rejection in High  $P_T$  Physics Analysis. H1–Note H1-11/98-556, DESY, 1998.
- [102] A. Panitch. Measurement of the Proton Structure Function  $F_2(x, Q^2)$  with the H1 Detector at HERA. Dissertation, Universite Libre de Bruxelles, 1996.  
also available at [http://www-h1.desy.de/publications/theses\\_list.html](http://www-h1.desy.de/publications/theses_list.html).
- [103] A. Glazov. Measurement of the Proton Structure Functions  $F_2(x, Q^2)$  and  $F_L(x, Q^2)$  with the H1 Detector at HERA. Dissertation, Humboldt-Universität Berlin, 1997.  
also available at [http://www-h1.desy.de/publications/theses\\_list.html](http://www-h1.desy.de/publications/theses_list.html).
- [104] S. Levonian and A. Panitch. Treatment of the Proton Satellite Bunches in 1994 Data. Internal Report H1-05/95-454, 1995.
- [105] S. Levonian. Luminosity Summary Tables.  
[http://www-h1.desy.de/h1/www/h1det/lumi/summary\\_tables/summary.html](http://www-h1.desy.de/h1/www/h1det/lumi/summary_tables/summary.html).

- 
- [106] G.A. Schuler and H. Spiesberger. DJANGO: the interface for event generators HERACLES and LEPTO. In W. Buchmüller and G. Ingelman, *Proceedings of the Workshop: Physics at HERA*, volume 3, page 1419. DESY, 1992.
- [107] H. Spiesberger. EPRC: A program package for electroweak physics at HERA. In R. Klanner G. Ingelman, A. De Roeck, *Proceedings of the Workshop: Future Physics at HERA*, volume 1, page 227. DESY, 1996.
- [108] L. Bauerdick, A. Glazov, and M. Klein. Future Measurement of the Longitudinal Proton Structure Function at HERA. In *Proceedings of the Workshop: Future Physics at HERA*, pages 77–85, 1996.
- [109] C. Adloff et al. Determination of the Longitudinal Proton Structure Function  $F_L(x, Q^2)$  at low  $x$ . *Phys. Lett.*, **B393**, page 452, 1997.
- [110] S. Chekanov et al. ZEUS Collaboration. Measurement of high- $Q^2$  neutral current cross sections in  $e^-p$  deep inelastic scattering at HERA. Submitted to the Proceedings of the 31st International Conference on High Energy Physics.
- [111] D.J. Gross and C.H. Llewellyn-Smith. High-Energy Neutrino-Nucleon Scattering, Current Algebra and Partons. *Nucl. Phys.*, **B14**, pages 337–347, 1969.
- [112] CCFR Collaboration J.H. Kim et al. A measurement of  $\alpha_2(Q^2)$  from the Gross-Llewellyn Smith Sum Rule. *Phys. Rev. Lett.*, **81**, pages 3595–3598, 1998.
- [113] E. Rizvi and T. Sloan.  $x F_3^{\gamma Z}$  in charged lepton scattering. *Eur. Phys. J. direct*, **C3**, page N2, 2001.
- [114] S.A. Larin and J.A.M. Vermaseren. The  $\alpha_s^3$  corrections to the Bjorken sum rule for polarized electroproduction and to the Gross-Llewellyn Smith sum rule. *Phys. Lett.*, **B259**, pages 345–352, 1991.
- [115] Z. Zhang. New Insights into the Proton Structure with  $ep$  Collider HERA. Habilitation, Univesite de Paris-Sud, 2000.  
also available at [http://www-h1.desy.de/publications/theses\\_list.html](http://www-h1.desy.de/publications/theses_list.html).
- [116] C. Pascaud and F. Zomer. A fast and precise method to solve the Altarelli-Parisi equations in  $x$  space. *LAL preprint, LAL 95-05*, 1995.
- [117] B. Reisert. NLO QCD Fits Using H1 data. Presentations and Discussions on H1 HIP-meetings, 2001-2002.
- [118] See <http://www-h1.desy.de/psfiles/figures/d03-038.h1pdf2000.errcor> for the uncertainties on the parameters and their correlations.
- [119] See <http://www-h1.desy.de/psfiles/figures/d03-038.hbfit2000.results> for the details of the fit to H1 and BCDMS data.

# Acknowledgements

I would like to express my gratitude to Prof. Gerd Buschhorn for offering me the opportunity to work in the H1-group at MPI, for constant support and interest in my work, in particular in the last phase, during preparing this manuscript.

The success of this work I owe to Vladimir Chekelian. His interest and experience in all aspects of the analysis and his dedication to precision physics provided an guideline of invaluable importance. I am especially grateful that he, in spite of his overwhelming responsibilities as H1 physics coordinator, had time for very detailed proof-reading of this thesis.

I am greatly indebted to Burkard Reisert who I spent most of my time working with and learning from. His patience, encouragement and friendship have been precious to me since the beginning of my “PhD-time”.

I very much appreciate the time spent at DESY working together with colleagues within the H1 collaboration. Countless fruitful discussions in the HiP working group have been essential for bringing this analysis to its final point. Particularly, I would like to express my thanks to Eram Rizvi, Beate Heinemann, Andrew Mehta and Zhiqing Zhang for a successful teamwork. I am very grateful to Max Klein for many instructive and educative discussions.

Prof. Christian Kiesling I want to thank for continuous enlightening discussions about analysis and various physics topics. For a friendly atmosphere, very pleasant to work in, I owe thanks to members of MPI H1 group: Juraj Bracinik, Günter Grindhammer, Ludger Janauschek, Birger Koblitz, Ringailė Plačakytė, Christiane Risler, Zuzana Rurikova, Sebastian Schmidt, Thomas Schörner Sadenius, Ekaterini Tzamariudaki, Steffen Udluft, Biljana Vujičić and Jens Zimmermann. Special thanks belong to Christiane who always found time to “drag” me out of DESY during my stays in Hamburg. I am very grateful to Ludger and Ringailė for reading the draft of this thesis.

I am thankful to Denis Salihagić, who actually should be “blamed” for my interest in high energy physics, for advice and help he always offered. In particular for being very responsive, together with Uwe Leopold, in solving any kind of computing problems.

For ultimate help dealing with all administrative issues I would like to give thanks to Kristiane Preuss and Marlene Schaber.

Heartfelt thanks belong to people who enriched my life in Munich, with whom I shared all ups and downs during last three years, Svjetlana, Burkard and Cristina.

Last but not least, words of warmest gratitude belong to my family for their endless support and understanding, most of all to Jovana and Janko who have been most successful in cheering my spirit in the difficulties of past months.